

**DESIGN AND MANUFACTURING OF CONFORMAL ABLATIVE
HEATSHIELDS**

A Dissertation
Presented to
The Academic Faculty

By

Adam T. Sidor

In Partial Fulfillment
of the Requirements for the Degree
Doctor of Philosophy in the
School of Aerospace Engineering

Georgia Institute of Technology

August 2019

Copyright © Adam T. Sidor 2019

**DESIGN AND MANUFACTURING OF CONFORMAL ABLATIVE
HEATSHIELDS**

Approved by:

Dr. Robert D. Braun, Advisor
School of Aerospace Engineering
Georgia Institute of Technology

Dr. Graeme J. Kennedy, Co-Advisor
School of Aerospace Engineering
Georgia Institute of Technology

Dr. Julian J. Rimoli
School of Aerospace Engineering
Georgia Institute of Technology

Ms. Robin A.S. Beck
Entry Systems and Vehicle Development Branch
NASA Ames Research Center

Dr. Margaret M. Stackpoole
Thermal Protection Materials Branch
NASA Ames Research Center

Date Approved: November 30, 2018

To my family: my wife and sons, my parents, and my brother. I would not have gotten here without your endless support and encouragement.

ACKNOWLEDGEMENTS

Thanks to my advisor, Prof. Robert Braun, who has guided me through my academic career from the start. I am indebted to Prof. Braun for his support and his advocacy for me over the years. Thanks also to my co-advisor, Prof. Graeme Kennedy, who stepped in once Prof. Braun moved on from Georgia Tech and helped me to finish strong.

While many colleagues in the Space Systems Design Laboratory (SSDL) were integral to my work over the years, special thanks are due to Brad Steinfeldt and Grant Rossman, who provided invaluable feedback and friendship throughout this work, particularly while writing this dissertation. I would also like to thank the staff of the Aerospace Engineering Machine Shop (Scott Moseley, Greg Rogerson, and Henry Russell), who provided a great deal of practical assistance during my design work and fabricated all of the critical experimental tooling.

Several folks from NASA Ames Research Center were instrumental in the development and direction of my work. Robin Beck provided mentorship and guidance throughout this work, facilitating and supporting all of my research visits to NASA Ames. Dr. Mairead Stackpoole opened her lab to me for experimental work and lended her expert guidance to the processing and material characterization. Several current and former staff there were incredibly patient with me, answering innumerable questions and stepping in countless times with hands-on help: Tane Boghonian, Greg Gonzales, and Joe Wong.

The work presented here was funded by a NASA Space Technology Research Fellowship (NSTRF) under Grant #NNX14AL53H. I am grateful to NASA for their support through this fellowship, and I am particularly thankful for all those who helped to administer it over the years.

Finally, I would not be where I am, or the person I am, without my family. The overwhelming love, support, and faith of my parents have profoundly shaped me. For as long as I can remember, they have championed all of my endeavors and interests, encouraging and

enabling me to pursue my passion for learning and for space. Thank you, Mom and Dad. I have also been blessed with a brother who has been my undying defender throughout life, backing me up no matter what. Thank you, Rob, for being a great big brother.

To my sons, Micaiah and Theodore, you are undoubtedly too young to remember this period of life, but your lives have already indelibly marked mine. Raising you has been a joy and a privilege. I hope one day you will be able to look back at these words — and I want you to know how incredibly proud I am of you and how much I love you both.

Last, and most importantly, I want to thank my wife, Ruth. None of this, absolutely none, would have been possible without your love, support, encouragement, and devotion. You encouraged me to follow my passion returning to graduate school, and you worked tirelessly and selflessly to make it happen. You have been there for me, and our kids, every step of the way. It is a joy beyond words to walk side-by-side through life with you — through all its triumphs and challenges — and I look forward to continuing to do so until the end of our days. Thank you, Ruth — I love you.

TABLE OF CONTENTS

Acknowledgments	iv
List of Tables	xiii
List of Figures	xv
Nomenclature	xx
Summary	xxviii
Chapter 1: Background and Motivation	1
1.1 Background	1
1.1.1 What is a TPS?	1
1.1.2 Why do you need a TPS?	1
1.1.3 Types of TPS Materials	2
1.1.4 Composition of a Polymeric Ablative TPS	5
1.1.5 Manufacturing a Polymeric Ablative TPS	8
1.2 Conformal Ablators	11
1.2.1 Composition	12
1.2.2 Design and Fabrication	13
1.3 Liquid Composite Molding	19

1.3.1	Mold and Process Design	21
1.3.2	Numerical Modeling	23
1.4	Gap Analysis	29
1.4.1	Manufacturing Inefficiencies	29
1.4.2	Design Inefficiencies	30
1.4.3	Applicability of LCM	31
1.5	Study Overview and Objectives	31
1.6	Summary of Contributions	33
1.7	Outline of Thesis	34
Chapter 2: A Constitutive Model of Fiber Substrate Ablators for Conceptual Design		37
2.1	Introduction	37
2.2	Methodology and Results	40
2.2.1	Material Formulation and Processing	40
2.2.2	Properties of the Fiber Substrate before Processing	41
2.2.3	Properties of the Fiber Substrate after Processing	44
2.2.4	Properties of the Resin	49
2.2.5	Properties of the Composite Ablative Material	51
2.3	Uncertainty Analysis	55
2.3.1	Methodology	55
2.3.2	Results	57
2.4	Summary	61

Chapter 3: Vacuum Infusion Processing of a Low Density Conformal Ablator	64
3.1 Introduction	64
3.2 Motivation	65
3.3 Vacuum Infusion Processing	66
3.3.1 Overview of the Process	66
3.3.2 Comparison to Conventional Processing	67
3.3.3 Limitations of the Process	77
3.3.4 Summary	78
3.4 Experimental Methodology	78
3.4.1 Material Formulation	78
3.4.2 Overview of Development	78
3.4.3 Mold Design	80
3.4.4 Processing	82
3.4.5 Test Matrix	86
3.5 Analysis	87
3.5.1 Material Characterizations	87
3.5.2 Computational Methodology	90
3.6 Results and Discussion	91
3.6.1 Processing Results	91
3.6.2 Full Tiles	93
3.6.3 Cylindrical Coupons	97
3.7 Summary	106

Chapter 4: Objectives of the Design Methodology and its Inputs	108
4.1 Introduction	108
4.2 Overview and Objectives of the Design Methodology	109
4.2.1 Scope of the Present Work	110
4.3 Primary Inputs	112
4.3.1 TPS Geometry	112
4.3.2 Properties of the Fiber Substrate	112
4.3.3 Properties of the Resin Solution	114
4.3.4 Properties of the Cured Resin	115
4.3.5 Process and Design Parameters	116
4.3.6 Summary of Primary Inputs	118
4.4 Intermediate Inputs	118
4.4.1 Properties of the Fiber Substrate	119
4.4.2 Properties of the Resin Solution	121
4.4.3 Properties of the Composite Ablative Material	124
4.4.4 Summary of Intermediate Inputs	126
4.5 Summary	127
Chapter 5: Tasks of the Design Methodology	128
5.1 Introduction	128
5.2 Tile Layout	128
5.2.1 Tile Parametrization	129
5.2.2 Inputs	131

5.2.3	Optimization	131
5.2.4	Outputs	135
5.3	Mold and Process Design	135
5.3.1	Inputs	136
5.3.2	Optimization	136
5.3.3	Outputs	141
5.4	TPS Material Property Estimation	142
5.5	Summary	142
Chapter 6: Applications of the Design Methodology		144
6.1	Design of a Conformal PICA Heatshield	144
6.1.1	Tile Layout	146
6.1.2	Mold and Process Design	147
6.1.3	TPS Material Property Estimation	151
6.2	Design of Mold for Experimental Processing	152
6.2.1	Mold Design	152
6.2.2	Time to Fill Results	152
6.2.3	Discussion	154
6.3	Summary	155
Chapter 7: Summary and Future Work		157
7.1	Summary of Contributions	157
7.1.1	Formulation of A Constitutive Model of Fiber Substrate Ablators for Conceptual Design	157

7.1.2	Development and Demonstration of a Vacuum Infusion Process for Conformal Ablative TPS Materials	158
7.1.3	Development of a Methodology to Optimize a Conformal Ablative Heatshield Design	158
7.2	Suggestions for Future Work	159
7.2.1	Constitutive Model of Fiber Substrate Ablators	159
7.2.2	Vacuum Infusion Process for Conformal Ablative TPS Materials	161
7.2.3	Design Methodology to Optimize a Conformal Ablative Heatshield Design	163
Appendix A: Evaluation of Constituent Material Properties		168
A.1	Felt Substrate	168
A.1.1	Permeability	168
A.1.2	Porosity and Fiber Density	170
A.2	Resin	174
A.2.1	Dynamic Viscosity	174
Appendix B: Applicability of the Vacuum Infusion Process		178
B.1	Methodology	178
B.1.1	Geometry and Mold Design	178
B.1.2	Properties	178
B.1.3	Simulation	180
B.2	Results	180
B.3	Discussion	181
Appendix C: Computation of the Minimum Seam Angle		183

C.1	Methodology	183
C.2	Code	184
Appendix D: Further Details on the Mold Filling Simulation		186
D.1	Modified Mold Design Objective Function	189
D.1.1	Perimeter Velocity	189
D.1.2	Critical Velocity	190
D.1.3	Scaling Parameter Study	190
D.2	Mesh Generation	192
D.2.1	Mesh Generation	194
D.2.2	Mesh Parameter Study	195
D.2.3	Selection of Mesh Parameter	197
References		207

LIST OF TABLES

1.1	Overview of fabrication methods for polymeric ablative TPS materials. . . .	9
2.1	Properties of the cured resin.	41
2.2	Limiting cases of volume change during processing.	47
2.3	Expressions for TPS property estimation.	52
2.4	TPS properties: nominal and bounding values.	57
2.5	Inputs to uncertainty application, nominal values and one-sided deviations .	58
2.6	Uncertainty results for C-PICA fabricated from Felt 1	58
2.7	Correlation coefficients relating input and output uncertainties	60
3.1	Resin consumption for the example heatshield.	70
3.2	Matrix of test conditions.	86
3.3	Resin delivered during infusion and collected during curing.	92
3.4	Properties of the pre-process substrate and the final composite TPS tile (absolute and relative to theoretical values).	96
3.5	Summary of deviations from nominal tile geometry.	97
3.6	Summary of coupon thicknesses for each tile.	100
3.7	Mean and variation in coupon properties compared to theoretical predictions.	102
3.8	Comparison of TGA and furnace char yields	106

4.1	Summary of primary inputs to the design methodology.	117
4.2	Summary of intermediate inputs to the design methodology and relevant equations.	126
5.1	Summary of tiling constraints for OML segment <i>i</i>	134
5.2	Constraints on mold design.	141
6.1	Primary inputs for the example design.	145
6.2	Secondary quantities computed for the example design.	145
6.3	Summary of design constraints for the example.	146
6.4	Summary of optimal gate and vent positions and process parameters for each tile.	150
6.5	Estimated final TPS properties compared to reference values.	151
6.6	Time of flow arrival at pressure gauges and vent, experimental and simulated values.	154
A.1	Results of regression analyses with 95% CIs.	174

LIST OF FIGURES

1.1	An early blunt capsule design in supersonic flight testing	2
1.2	Ablative TPS surface and in-depth thermal response	3
1.3	Classification of thermal protection system materials.	4
1.4	Types of ablative TPS	6
1.5	A fiber filler ablator: Avcoat 5206 in fiberglass phenolic honeycomb reinforcement pre- and post-arcjet test	6
1.6	Examples of fiber substrates	6
1.7	A fiber substrate ablator: PICA installed as tiles on Mars Science Laboratory	7
1.8	Resin injection performed on Apollo and Orion Avcoat heat shields	10
1.9	Steps in the design and fabrication of a conformal ablative heatshield.	13
1.10	Seam designs demonstrated in C-PICA arcjet testing	16
1.11	Overview of the fabrication process for a conformal ablator	17
1.12	Two common LCM approaches	20
1.13	A double-sided, rigid aluminum mold for an RTM process	22
1.14	Numerical depiction of the mold filling problem.	28
1.15	Vacuum infusion processing of conformal ablators.	32
2.1	Description of TPS material properties: traditional and constitutive model approaches.	38

2.2	Material at each step in experimental processing (left to right): dry felt prior to processing, virgin TPS, and charred TPS.	41
2.3	Substrate areal density plotted against thickness.	43
2.4	Substrate porosity as a function of density.	44
2.5	Change in substrate density during processing.	48
2.6	Post-process resin density plotted against pre-process substrate density.	51
2.7	Virgin density as a function of pre-process substrate density.	53
2.8	Resin mass fraction as a function of pre-process substrate density.	54
2.9	Composite char yield as a function of pre-process substrate density.	54
2.10	Composite char yield with Y_R computed separately for each felt.	55
2.11	Distribution of virgin density with bounds.	59
2.12	Distribution of resin mass fraction with bounds.	59
2.13	Distribution of char yield with bounds.	60
3.1	Vacuum infusion processing of conformal ablators.	67
3.2	Example heatshield and tile geometry based on Mars Science Laboratory	68
3.3	Reductions in resin consumption, debris from demolding, and resin waste compared to the state of the art	71
3.4	Open processing impacts both oven cost and wear on interior surfaces.	72
3.5	Estimated vacuum pump cost compared for both processes.	73
3.6	Tooling design for the state of the art process.	75
3.7	Overview of VIP development from initial testing to final scale up.	79
3.8	Selected tile geometry on aeroshell (left) and expanded separately (right).	80
3.9	Exploded view of mold design (left) and detailed view of joint between the core and cavity sides (right)	81

3.10	Experimental steps: (1) cutting the raw substrate, (2) draping the substrate in the mold, (3) mold configured for infusion, and (4) mold, with lid installed, in oven for curing/drying.	83
3.11	System configuration for infusion.	84
3.12	System configurations for curing (left) and drying (right).	85
3.13	Core locations relative to part geometry and port locations.	87
3.14	Void formation during processing.	88
3.15	External tile surfaces after processing	94
3.16	Results of dimensional analysis for Sample 4	98
3.17	Drilled cores from Location 1.	98
3.18	Drilled cores from Location 10.	98
3.19	Properties of the cylindrical coupons.	101
3.20	Deviations from mean by location.	104
3.21	Thermogravimetric analysis of cores from Location 12.	105
4.1	Design methodology for tiling and fabricating a conformal heat shield. . . .	109
4.2	Front view of a symmetric tile layout with a single nose tile and two rings forming the conical flank.	111
4.3	A seam angle, $\beta_{j,j+1}$, illustrated on the previous tile layout example	116
4.4	Tomadakis and Robertson permeability model for a three-dimensional, random fiber network	121
5.1	Approach to generating tile layout for a sphere-cone geometry	130
5.2	An example OML geometry illustrating geometry definitions.	130
5.3	Transformation of (1) tile geometry to (2) scaled up substrate geometry to (3) two-dimensional flat pattern.	132

5.4	Illustration of the tile size optimization problem.	132
5.5	Example finite element mesh used to simulate mold filling	138
5.6	Example finite element mesh used to simulate mold filling	139
5.7	Results of a mold filling simulation and those results extracted along the perimeter.	140
6.1	Tile layout for the example heatshield.	146
6.2	Mold design results for nose tile.	147
6.3	Mold design results for the inner ring tile of the conical flank.	148
6.4	Mold design results for the outer ring tile of the conical flank.	148
6.5	Mold design results for experimental tooling.	153
6.6	Mold top showing selected gate and vent placement, and pressure gauge locations.	153
A.1	Illustration of through thickness and in plane sample orientations.	168
A.2	Experimental setup for measuring permeability	169
A.3	Permeability results for a single felt sample.	171
A.4	Saturated sample suspended in infiltrating liquid.	172
A.5	Regression analysis on substrate samples (nominal densities).	173
A.6	Experimental set up with rotational viscometer.	175
A.7	Viscosity results.	176
B.1	Variation of porosity and permeability with rayon-based substrate density. .	179
B.2	Correlation between viscosity and vapor pressure for a diluted phenolic resin solution.	180
B.3	Time to fill (in hours) for example designs.	181

C.1	MATLAB code used to compute the largest minimum seam angle between two adjacent rings in the tile layout.	184
D.1	Algorithm for computing the blocked length, p' , for one segment.	188
D.2	Scaling of objective function with increasing r_p	191
D.3	Scaling of objective function with increasing r_p	193
D.4	Mesh refinement for outer ring tile.	196
D.5	Convergence of the objective function for the nose tile.	196
D.6	Convergence of objective function for the outer ring tile.	197

NOMENCLATURE

Acronyms

C-C	Carbon-carbon
C-PICA	Conformal Phenolic Impregnated Carbon Ablator
C-SIRCA	Conformal Silicone Impregnated Reusable Ceramic Ablator
CI	Confidence Interval
CMCP	Chop Molded Carbon Phenolic
CP	Carbon Phenolic
cP	Centipoise
CV	Control volume
CV/FE	Control volume / finite element
EDL	Entry, Descent, and Landing
FRP	Fiber-reinforced plastic
IML	Inner mold line
LCM	Liquid composite molding
LIMS	Liquid Injection Molding Simulation
LRI	Liquid Resin Infusion
LSR	Least squares regression
MSL	Mars Science Laboratory
OML	Outer mold line
PAN	Polyacrylonitrile
PICA	Phenolic Impregnated Carbon Ablator
PPE	Personal protective equipment

PSO	Particle Swarm Optimization
RSS	Root sum square
RTM	Resin Transfer Molding
RTV	Room-temperature-vulcanizing silicone rubber
SCRIMP	Seeman Composite Resin Injection Molding Process
SIRCA	Silicone Impregnated Reusable Ceramic Ablator
SLA	Super Lightweight Ablator
SOTA	State of the art (or state-of-the-art)
SRIM	Structural Reaction Injection Molding
STF	Strain to failure
TGA	Thermogravimetric analysis
TPS	Thermal Protection System
TWCP	Tape Wound Carbon Phenolic
VaRTM	Vacuum-assisted Resin Transfer Molding
VBI	Viscosity blending index (in viscosity model)
VIP	Vacuum infusion process (or processing)

Greek Variables

α	Fractional volumetric shrinkage
β	Seam angle
β^{\min}	Minimum seam angle constraint
$\beta_{j,j+1}$	Seam angle between adjacent rings j and $j + 1$
$\beta_{j,j+1}^{\min}$	Minimum seam angle between adjacent rings j and $j + 1$
δ	Angular orientation of substrate flat pattern
$\Delta(\cdot)$	A change in variable (\cdot)
ϵ	Fraction length shrinkage
ϵ_M	Fractional thickness change after post-process machining
ϵ_{pre}	Fractional pre-process substrate compression

$\frac{\partial u}{\partial x}$	Shear velocity gradient
γ_j	Angular span of tile (or substrate) in ring j
γ_j^f	Angular span of substrate flat pattern in ring j
Γ_{gate}	Angular gate location (non-dimensional)
Γ_{gate}^*	Optimal angular gate location (non-dimensional)
Γ_{vent}^*	Optimal angular gate location (non-dimensional)
λ_{gate}	Radial gate location (non-dimensional)
λ_{gate}^*	Optimal radial gate location (non-dimensional)
λ_{vent}^*	Optimal radial gate location (non-dimensional)
μ	Dynamic viscosity
μ^*	Non-dimensionalized viscosity
μ_0	Reference viscosity (exponential viscosity model)
μ_g	Gas viscosity
ν	Kinematic viscosity
ϕ	Porosity
ϕ_p	Percolation threshold (in permeability model)
ρ	Density
ρ_{liq}	Density of infiltrating liquid
τ	Shear stress
ξ	Regression coefficient (porosity measurement)

Roman Variables

A	Surface area
F	Function of measurable quantities (permeability measurement)
K_g	Gas permeability
K_{xx}, K_{yy}, K_{zz}	Permeability in the x , y , and z Cartesian coordinate directions
L	Length
L_c	Characteristic part length

M	Molar mass
M	Number of OML segments
N_j	Number of tiles in ring j
N_{lb}	Lower bound on number of tiles in a ring
N_{ub}	Upper bound on number of tiles in a ring
P	Pressure
P_{atm}	Atmospheric pressure
P_{av}	Average pressure
P_{gate}	Gate pressure
P_{vac}	Vacuum pressure
P_{vap}	Vapor pressure
P_{vap}^*	Non-dimensionalized vapor pressure
P_{vent}	Vent pressure
Q	Total numbers of rings (tile geometries) in tile layout
Q_i^{\min}	Minimum number of rings in OML segment i
R	Gas constant
R	Radius of curvature
R^{\min}	Minimum radius of curvature constraint
R_n	Nose radius
R_{eq}	Radial distance from gate
R_{gate}	Gate radius
T	Temperature
T'	Reference temperature (exponential viscosity model)
T_f^{exp}	Experimental time to fill
T_f^{sim}	Simulated time to fill
T_{evac}	Evacuation time
T_f	Time to fill

$T_f(p_i)$	Time to fill at perimeter point i
V	Volume
V_{evac}	Evacuated volume
W	Width
X_i	i th input parameter
Y	Char yield
Z_j	j th output parameter
a	Geometry dependent parameter (in permeability model)
a_r	Part aspect ratio
b	Material-specific constant (permeability measurement)
c_s	Multiplicative factor describing material shrinkage
c_{el}	Multiplicative factor describing increase in element resolution near gate (mesh sizing parameter)
d	Diameter
f_f	Fill factor
f_{diff}	Average difference between objective function across all points in the design space (convergence criterion)
$f_{\text{obj},1}$	Tile layout objective function
$f_{\text{obj},2}$	Mold design objective function
l_j	Side length of tile in ring j
l_j^{max}	Maximum tile side length of ring j
l_j^{sub}	Side length of substrate in ring j
$l_{c,\text{gate}}$	Characteristic mesh element size near the gate
l_c	Characteristic mesh element size
m	Mass
m_{dry}	Dry sample mass
m_{sat}	Saturated sample mass
m_{sus}	Suspended sample mass

n_b	Number of points bounding blocked perimeter regions
n_d	Total number of points in discretization of the design space
n_p	Total number of perimeter points
n_{el}	Total number of elements along the perimeter (mesh sizing parameter)
p	Perimeter distance
p'	Blocked perimeter length
p_i	Perimeter distance at point i
p_j^*	Perimeter point j which bounds a blocked region
p_{total}	Total perimeter length
p'_{vel}	Velocity-based penalty to blocked length objective function
q	Volumetric fluid flux
q_{pump}	Pumping speed
r	Radial coordinate of OML
r_p	Scaling parameter for penalty function, p'_{vel}
$r_{1,c}$	Radial coordinate of circular nose segment
$r_{\rho_{comp}}$	Relative difference in composite density (as a percentage)
$r_{i,j}$	Correlation coefficient between input X_i and output Y_j
$r_{i,j}$	Radial coordinate of tile in ring j and OML segment i
$r_{i,j}^f$	Radial coordinate of substrate flat pattern in ring j and OML segment i
$r_{i,j}^{sub}$	Radial coordinate of substrate in ring j and OML segment i
$r_{w_{resin}}$	Relative difference in resin mass fraction (as a percentage)
t	Thickness
t_1, t_2	Spacer thicknesses
t_{cav}	Cavity thickness
t_{TPS}	TPS thickness
u	Macroscopic fluid velocity (scalar)

u^{crit}	Critical flow velocity
u^{perim}	Flow velocity at the perimeter
u_r	Radial flow velocity
v	Volume fraction
w	Mass fraction
x	Mole fraction
z	Height coordinate of OML
$z_{1,c}$	Height coordinate of circular nose segment
$z_{i,j}$	Height coordinate of tile j in OML segment i

Symbols

$[K]$	Permeability tensor
\bar{u}	Macroscopic fluid velocity (vector)
\bar{X}_i	Mean of i th input parameter
\bar{Z}_j	Mean of j th output parameter
\dot{m}	Mass flow rate
\mathcal{P}	Set of all perimeter points

Subscripts

$(\cdot)_c$	Property of component c in resin solution
$(\cdot)_{\text{char}}$	Property of the charred TPS
$(\cdot)_{\text{comp}}$	Property of the composite TPS material
$(\cdot)_{\text{fiber}}$	Property of a fiber comprising the substrate
$(\cdot)_{\text{IP}}$	In plane property
$(\cdot)_{\text{pore}}$	Property of the porous space
$(\cdot)_{\text{resin}}$	Property of the resin in the composite
$(\cdot)_{\text{R}}$	Property of the pure resin
$(\cdot)_{\text{sol}}$	Property of the resin solution
$(\cdot)_{\text{sub}}$	Property of the fibrous substrate

$(\cdot)_{TT}$ Through thickness property

Superscripts

$(\cdot)^+$ Upper bound on property

$(\cdot)^-$ Lower bound on property

$(\cdot)^{\text{areal}}$ Areal property

$(\cdot)^{\text{post}}$ Post-process property

$(\cdot)^{\text{pre}}$ Pre-process property

SUMMARY

Conformal ablators, first introduced in the early 2000s, are a type of rigid ablative thermal protection system that use flexible, rather than rigid, fibrous substrates. These materials are impregnated with resin in a mold to yield a part that is close to the final geometry and requires little post-process machining (a near net shape part). The lack of fiber connectivity through the thickness enables the TPS to tolerate larger strains than comparable rigid substrate ablators facilitating larger tiles and installation on most aeroshells without strain isolation. Reduced part count and simplified integration drive reductions in labor, cost and complexity.

Conformal ablators are currently fabricated using an open liquid impregnation process adapted from a technique developed for Lightweight Ceramic Ablators, such as Phenolic Impregnated Carbon Ablator, which leads to design and manufacturing inefficiencies. This work advances a new manufacturing technique for conformal ablators, vacuum infusion processing, that reduces resin consumption and streamlines clean up. The closed process also eliminates the need for an expensive atmosphere-controlled oven or vacuum chamber.

A design methodology, centered around a simulation of the mold filling process, is developed to tailor a conformal ablative heatshield to vacuum infusion processing. A constitutive model, combining properties of individual components, is formulated to estimate the properties of the composite TPS material. The methodology leverages this model, integrated with material selection, tile layout, and the mold filling simulation, to automate a conceptual conformal heatshield design. The approach allows rapid iteration on TPS composition and manufacturing constraints.

CHAPTER 1

BACKGROUND AND MOTIVATION

1.1 Background

1.1.1 What is a TPS?

A thermal protection system (TPS), or heat shield, forms the outermost layer of an entry system, protecting the structure and payload within from intense aerodynamic heating generated during flight through an atmosphere. It is a critical system without which a spacecraft would not withstand entry, descent, and landing (EDL).

1.1.2 Why do you need a TPS?

An entry vehicle at Earth orbital speeds contains specific kinetic energy around ~ 28 MJ/kg. A relatively small 10 kg capsule entering from low Earth orbit possesses a substantial amount of kinetic energy (280 MJ). The high velocity entry of the 46 kg Stardust Sample Return Capsule, 12.6 km/s relative to Earth, possessed kinetic energy an order of magnitude greater (3600 MJ). For some perspective, the kinetic energy of all the cars in the Indianapolis 500 driving at race speeds is approximately 92 MJ¹ — less than 3% of Stardust.

This energy must be entirely dissipated during a few short minutes of atmospheric deceleration. Energy dissipation is largely achieved through vehicle geometry. A blunt body creates a strong, detached bow shock that allows hot gas to convect around the capsule into the wake. Figure 1.1 shows an example of a blunt body in supersonic flight, from right to left, with a detached bow shock clearly visible in front of the vehicle. Thus, only a small fraction of the total flow energy is actually incident on the exterior of the capsule itself. Blunt body design, proposed by Harvey Allen in the early 1950s [2], reduced a previously

¹Thirty-three IndyCars weighing 1545 lbs and traveling at 200 mph.

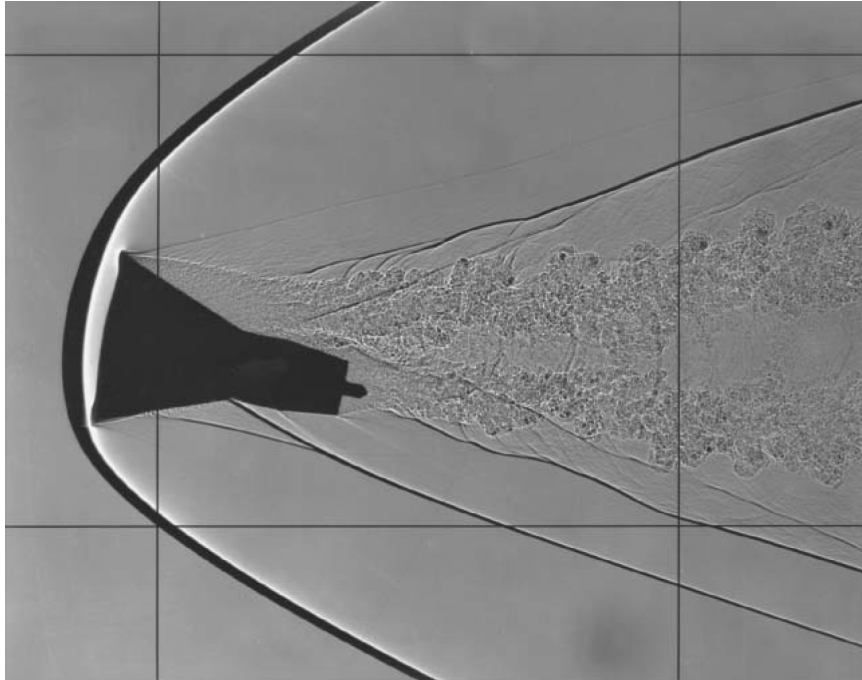


Figure 1.1: An early blunt capsule design in supersonic flight testing (Credit: Vincenti, et al. [1]).

intractable heating problem to merely a challenging one. At the vehicle stagnation point, heat fluxes still range from 10^1 to 10^4 W/cm² with integrated heat loads from 10^3 to 10^5 J/cm² [3]². A TPS must safely accommodate this heating while maintaining the internal structure and payload at an acceptable temperature.

1.1.3 Types of TPS Materials

TPS materials can be categorized into those that decompose during entry (ablative) and those that do not (reusable). Reusable TPS are appropriate for low heat flux, shallow and/or gliding entries such as that of the Space Shuttle. These materials withstand entry heating with little to no degradation allowing multiple uses. By comparison, ablative TPS are single-use systems that accommodate heating through reradiation, phase change, mass loss and passive transpiration cooling [3]. The combination of mechanisms, depicted in Figure 1.2, allows ablators to withstand severe entry heating.

²For comparison, the Sun's radiative energy flux at Earth is 1.361×10^{-1} W/cm², or about 100–100,000 times less, with a daily integrated heat load of 1.2×10^4 J/cm².

Convective and radiative flux from the hot flow heat the TPS surface. A portion of the incident energy is reradiated back into the flow while the remaining energy is conducted into the material. As the virgin material increases in temperature, it decomposes, absorbing energy, and forming pyrolysis gas which convects through the TPS material into the boundary layer. The gas, which absorbs additional energy from the hot char as it exits the TPS, alters the boundary layer such that convective heating is reduced (transpiration cooling, also called blowing). Active decomposition occurs in a layer called the pyrolysis zone, which progresses through the material thickness over time leaving behind a porous, carbonaceous char held together by the fiber reinforcement. The charred surface can undergo chemical reactions causing further mass loss (recession).

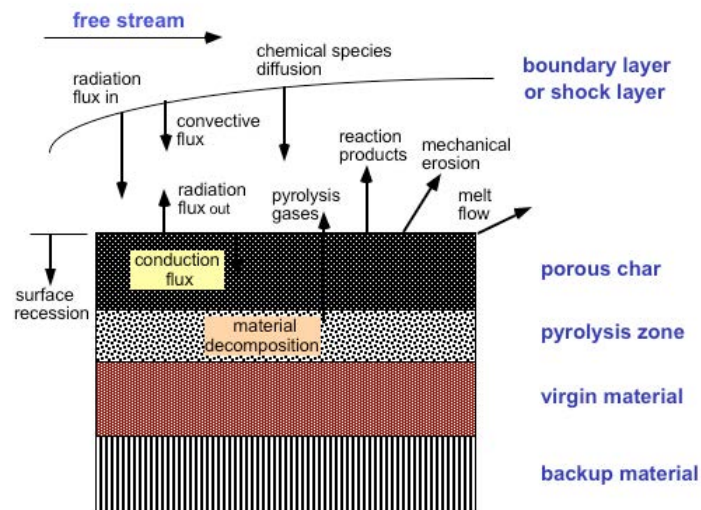


Figure 1.2: Ablative TPS surface and in-depth thermal response (Credit: Laub and Venkatesh [3]).

Ablative TPS materials may be differentiated into those containing a polymer (polymeric) and those that do not (non-polymeric). Non-polymeric ablators include metals, inorganic ceramics and ceramic composites. They also include carbon-carbon (C-C) composites, which are frequently used to protect rocket nozzle throats [4], though C-C was also employed as the forebody heatshield for the Genesis sample return capsule [5] and on the nose and wing leading edges of the Space Shuttle Orbiter [6].

Polymeric ablators comprise the largest class of ablative TPS and have been employed in the vast majority of entry vehicles to date [3, 4]. These materials can be differentiated based on the form of the fiber reinforcement, fiber filler or fiber substrate. Fiber substrate ablators may be further grouped into rigid substrate and flexible substrate materials. The latter encompasses both woven ablative TPS and conformal ablators, which are the focus of this work. Figure 1.3 depicts these classifications with conformals highlighted.

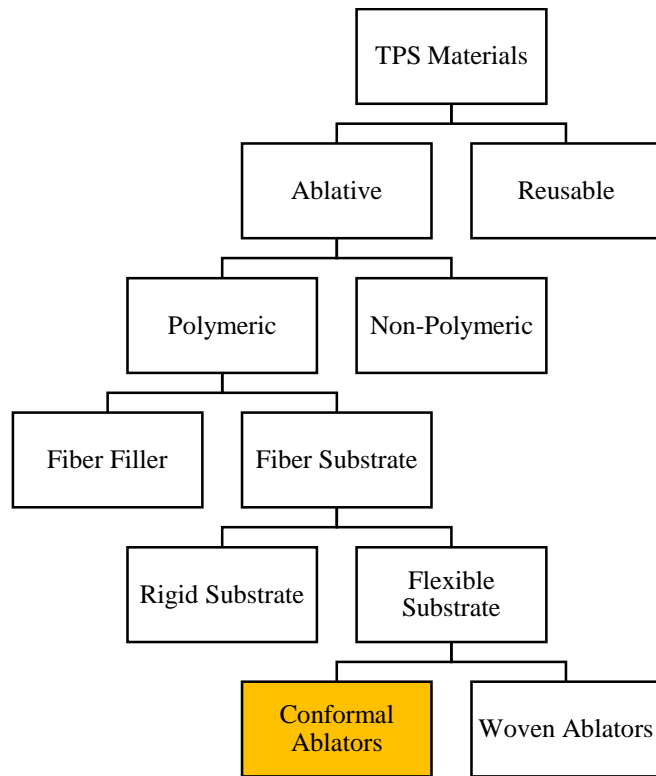


Figure 1.3: Classification of thermal protection system materials.

Other classifications can and have been made in the literature. Natali, et al. break down polymeric ablators similarly, though they note the difference between micron-scale materials (fiber-reinforced, heat shielding, and Lightweight Ceramic Ablators, or LCAs) and nanoscale materials (nanocomposites) [4]. Carbon/phenolic nanocomposites are further outlined by Tate, et al. [7]. Laub and Venkatapathy differentiate ablators into low, mid, and high density materials and note that peak heat flux and stagnation pressure capability are correlated with density [3].

Rasky and Tran make identical distinctions regarding the construction of polymeric ablators, but denote them as traditional ablators and LCAs [8]. This thesis replaces these terms with fiber filler and fiber substrate, respectively, which reflect the underlying construction. Fiber substrate ablators/LCAs were largely matured at NASA Ames Research Center in the 1990s [9, 10, 11, 12], providing a major advancement on the fiber filler/traditional ablators that previously dominated TPS technology. The next sections discuss these two subcategories of polymeric ablators further, starting with their compositions and then outlining different manufacturing techniques. Conformal ablators and their manufacturing are then presented in more detail.

1.1.4 Composition of a Polymeric Ablative TPS

Polymeric ablators consist of fibrous reinforcement in a polymer matrix — a composite material that blends the capabilities of its constituents. Decomposition of the polymer accommodates incident heat flux while the fiber network imparts mechanical strength. It was, in fact, this revelation that led to the invention, and subsequent adoption, of the ablative heat shield in the 1960s [13]. Reinforcing fibers are refractory materials with low thermal conductivity — silica and carbon are typical — and can be short, disconnected and distributed throughout the resin or can form a connected, monolithic substrate.

Fiber filler ablators (Figure 1.4, left) blend disconnected fibers in a mixture of polymer resin and fillers and often require additional structural reinforcement [17]. Avcoat [18], used as the primary TPS on both the Apollo and Orion capsules [19], and Super Lightweight Ablator (SLA) [20], used for a series of Mars landers beginning with Viking [21], are examples of this type of ablative material. Figure 1.5 depicts Avcoat 5206 in honeycomb reinforcement, before and after arcjet testing.

Fiber substrate ablators (Figure 1.4, right) combine a connected fibrous material — the substrate — with a liquid resin which is then cured to form a rigid composite [9]. These materials withstand high heat fluxes and surface pressures with better mass efficiency

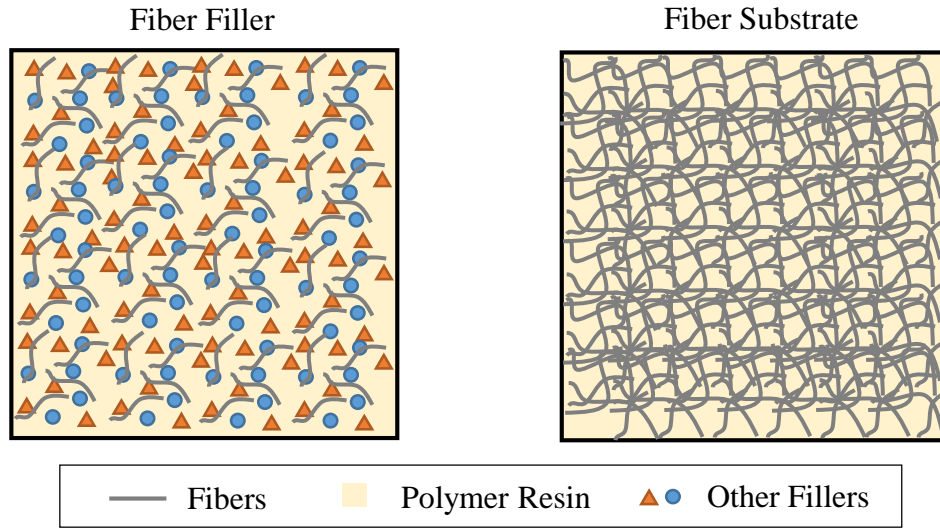


Figure 1.4: Types of ablative TPS (adapted from Rasky and Tran [8])

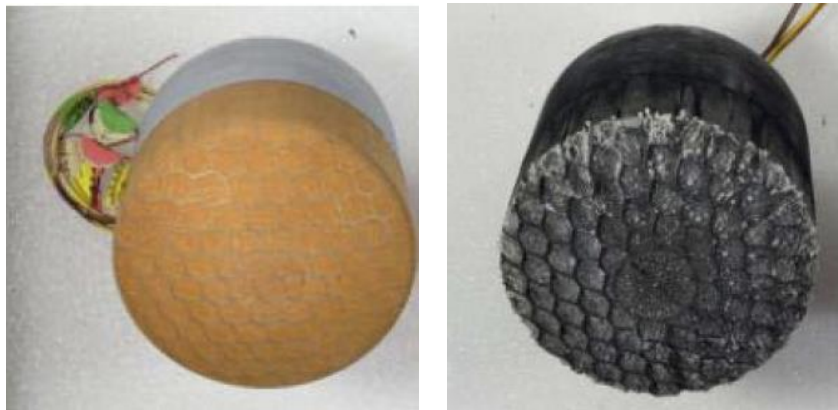


Figure 1.5: A fiber filler ablator: Avcoat 5206 in fiberglass phenolic honeycomb reinforcement pre- and post-arcjet test (Credit: Kowal [14])



Figure 1.6: Examples of fiber substrates (left to right): FiberForm® block, woven carbon, and carbon felt (Credits: FiberMaterials, Inc., Venkatapathy and Ellerby [15], and Gasch, et al. [16]).

than most fiber filler ablators [22]. Fibrous substrates may be ordered or disordered on a microscopic scale and take a variety of macroscopic forms. Figure 1.6 shows several examples: rigid preformed blocks [11], woven fabric [15, 23, 24], and felt [16]. Part size is limited by mechanical and thermal properties, requiring segmented, tiled designs for all but the smallest aeroshells (e.g., Stardust [25]) with gaps, and corresponding gap filling, between tiles to control tolerance. For example, the Mars Science Laboratory (MSL) heatshield, shown in Figure 1.7, used 113 tiles requiring extensive gap filling [26]. In many cases, tiles cannot be bonded directly to an aeroshell but require intermediate strain isolation to prevent mechanical failure [21].

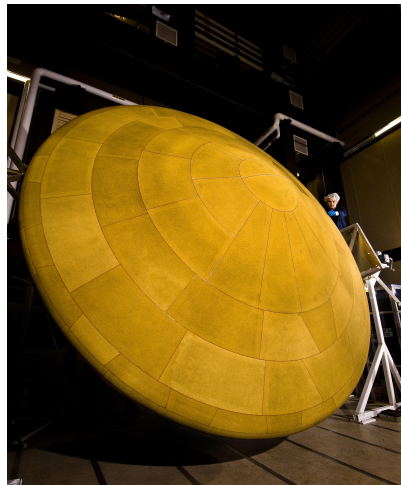


Figure 1.7: A fiber substrate ablator: PICA installed as tiles on MSL (Credit: NASA/JPL-Caltech/Lockheed Martin)

Fiber substrate ablators have been widely adopted since their invention in the 1990s [10]. Phenolic impregnated carbon ablator (PICA), one of the original LCAs, was employed as the primary heatshield on Stardust [25], MSL [21, 27], and OSIRIS-REx [28] and was considered for the Orion Crew Exploration Vehicle [29]. A related material, PICA-X, is flown on the SpaceX Dragon capsule [30]. Another variant, Silicone Impregnated Reusable Ceramic Ablator (SIRCA), was used on Mars Pathfinder [31], Mars Exploration Rover [32], and Mars Microprobe [33].

Polymer resins typically decompose endothermically, absorbing and rejecting incident

flow energy [3]. High emissivity char left behind by the decomposing polymer re-radiates an additional portion of this energy. High char yield, the proportion of the initial mass that remains as char, is desirable because it both aids re-radiation and reinforces the ablated material. Resins may be thermosets, polymers that crosslink and rigidize during curing at elevated temperature, or thermoplastics, long chain polymers that do not crosslink. Phenolic is undoubtedly the most widely used resin [4] found in a number of ablators including PICA, Carbon Phenolic (CP), Avcoat [18], and others. Fillers may be added to the matrix to control material and thermal properties. For example, SLA-561V consists of cork, silica and phenolic microballoons, and fibers in a silicone binder [20].

1.1.5 Manufacturing a Polymeric Ablative TPS

Manufacturing a polymeric ablative TPS involves combining, in some fashion, matrix and reinforcement into one material. Historically, this has been accomplished through a variety of processes described below and summarized in Table 1.1. Processes are differentiated based on construction.

Fiber Filler Ablators

Chop/Compression Molding Short, disconnected (chopped) fibers are combined with resin. The compound is loaded into a mold that applies pressure and heat to consolidate and cure the material. Resulting TPS are generally high density and heavy, suited for the most severe entries. Chop molded carbon phenolic (CMCP) was employed for the nosecone of the Galileo probe heat shield [34].

Spraying Polymer, fibers and, possibly, fillers are combined in a liquid mixture. This mixture is sprayed onto aeroshell surface and cured in place to form a rigid shell. This process is generally used for protection under less severe aerothermal environments. For example, a spray-on version of SLA-561V was used on the Space Shuttle external tank

Table 1.1: Overview of fabrication methods for polymeric ablative TPS materials.

Process	Description	Example(s)
Fiber Filler Ablators		
Chop / Compression Molding	Fiber and resin compound compressed and cured inside a mold	CMCP (Galileo nosecone [34])
Spraying	Liquid resin/fiber mixture sprayed and cured in place	SLA-561V (Space Shuttle, Pathfinder [35]), Prosiat (Huygens [36])
Injection / Packing	Liquid resin/fiber mixture injected or packed into a pre-bonded reinforcing structure then cured	Avcoat (Apollo [18], Orion [19]), SLA-561V (Pathfinder [35])
Fiber Substrate Ablators		
Filament / Tape Winding	Continuous fibers drawn through resin bath and onto mandrel	TWCP (rocket motor casings and payload shrouds [37], Galileo [34])
Liquid Impregnation	Liquid resin solution infused into a connected fibrous substrate	PICA (Stardust [25], MSL [21, 27], OSIRIS-REx [28]), C-PICA [38]

as well as the Mars Pathfinder backshell [35]. Prosoial, which formed the backshell of the Huygens probe, was also implemented in this fashion [36].

Injection/Packing Polymer, fibers and, possibly, fillers are combined in a liquid mixture. The mixture is injected, or packed, into a reinforcing structure prebonded to the aeroshell — an injection tool may be used (Figure 1.8). Then, the material is cured in place. Examples

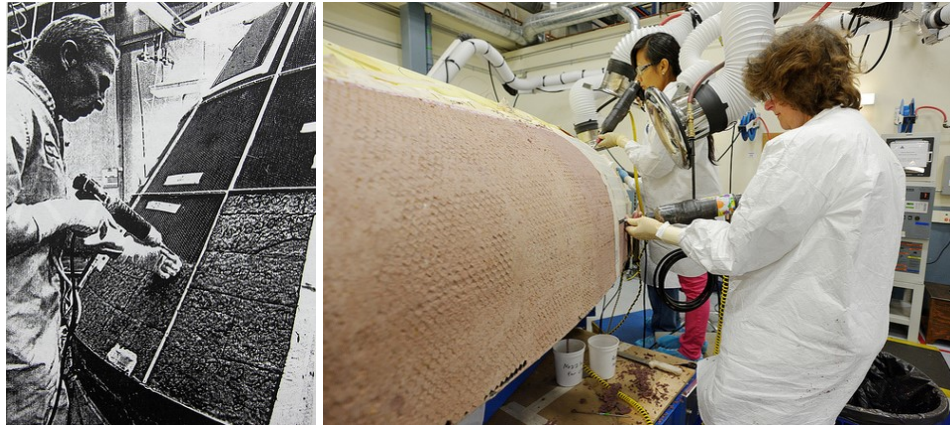


Figure 1.8: Resin injection performed on Apollo (left) and Orion (right) Avcoat heat shields (Credits: North American Aviation/Steve Jurvetson and Textron Systems/NASA).

of this type of manufacturing process include that of the Apollo [18] and Orion [19] Avcoat heat shields. A version of SLA-561V is manufactured this way for use in more severe environments (e.g., on the forebody of Mars Pathfinder [35]).

Fiber Substrate Ablators

Filament/Tape Winding Continuous fibers are drawn through a resin bath and onto a mandrel. The mandrel geometry forms the inner mold line of the part. The material is cured and then removed from the mandrel. Filament winding and tape winding use essentially the same process differing only in the form of the fibers: individual filaments, in the former, and wider/thicker tapes with multiple filaments, in the latter. This type of process is frequently employed for the TPS in rocket motor casings and payload shrouds, for example as tape wound carbon phenolic (TWCP) [37]. TWCP was also used on the frustrum of the Galileo

probe [34].

Liquid Impregnation Liquid impregnation is an open composite molding process pioneered to fabricate LCAs. Techniques are outlined in the patent for those materials [12]. Generally, a fiber substrate is slowly infiltrated by a liquid resin solution while under vacuum. Resin, which is typically diluted with solvent(s) to control loading and facilitate infusion, seeps into the porous substrate over time. Then, the infiltrated material is subjected to curing and drying processes to gel the polymer and remove solvent, respectively. Temperature and pressure profiles during curing and drying are resin-dependent. Multiple heat treatment cycles may be required to complete curing and solvent removal. In some cases, impregnation and curing/drying is carried out multiple times to increase resin loading. Pulci, et al. describes a similar approach applied to rigid graphitic substrates [39]. PICA is manufactured via liquid impregnation (e.g., the forebody heatshields of Stardust [25], MSL [21], and OSIRIS-REx [28]). Conformal ablators rely on a modified version of this technique [38].

1.2 Conformal Ablators

Unlike the rigid substrates of PICA and related materials, conformal ablators use flexible fibrous substrates such as felts or battings which, after processing, yield rigid TPS materials with higher strain to failure (STF) than their rigid substrate counterparts. The flexible substrates are conformed, infused, and cured in a mold to produce near net shape parts with consistent fiber orientation, which results in uniform thermal properties through the thickness. By contrast, a curved part machined from a rigid orthogonal block will have variable fiber orientation, and thus non-optimal through thickness properties (e.g., Mars Science Laboratory [21, 27]). Rigid substrates can be molded to align fibers but this requires additional preforming (e.g., Stardust [25] and OSIRIS-REx [28]). Conformal ablators achieve fiber alignment and resin infusion in a single process.

Near net shape manufacturing reduces post-process machining. Higher STF allows fabrication of larger TPS tiles, reducing part count, and installation directly on most aeroshells without strain isolation layers. In addition, higher STF may allow designers to eliminate gaps and gap fillers between tiles for small probe designs. Larger aeroshells may still require gaps and gap filling; however, increased tile size reduces the total length of these gaps. One study estimates that a conformal variant of PICA could reduce the number of tiles on the MSL forebody heat shield from 113 to less than 35 [40]. Reduced part count and simplified integration drive reductions in labor, cost, and complexity over comparable rigid substrate ablators [41, 42, 43, 44, 38, 45, 16] – advancements which are enabling for planetary and human missions [40, 46, 47].

1.2.1 Composition

The construction of conformal ablative TPS is similar to other fiber-reinforced plastics (FRPs) such as carbon fiber and fiberglass. Unlike these structural composites, however, conformals possess relatively low density and fiber fraction (around 10%) by design. Fiber consolidation/compaction, which is typical of FRPs, would increase thermal conductivity and compromise thermal performance in an ablator. In addition, resins are substantially diluted by solvents to control resin loading and allow infusion at lower pressures, producing a lightweight, porous material.

Conformal TPS variants include C-PICA and C-SIRCA (conformal analogs of PICA and SIRCA, respectively). C-PICA combines a high porosity rayon-based carbon felt insulator with phenolic resin and is suited to high heat fluxes. Designed as a drop in replacement for PICA, C-PICA has a similar density (~ 0.27 g/cc) but is more thermally efficient which can reduce TPS mass [45]. Recent work has focused on identifying alternative carbon felt substrates manufacturable in larger thicknesses and higher densities [16]. Scale up to larger curved parts (~ 0.6 m x 0.7 m) was planned for 2017 [48]. C-SIRCA is an RF-transparent material made from a silica-based felt and silicone resin [48]. Terminal Velocity Aerospace

leveraged these materials for the heat shield on its RED-Data2 miniature entry capsule [47, 45]. Elsewhere, AQ60/I is a proprietary material made of a silica felt impregnated with phenolic and has a density of around 0.3 g/cc [36]. Details of its manufacturing process are unclear, however, and tile size was limited on the Huygens forebody heatshield to $\sim 0.15 \text{ m} \times 0.20 \text{ m}$.

Note that woven ablative TPS, while similarly constructed, differ from conformal ablaters both in density ($\sim 0.38 \text{ g/cc}$ to 1.5 g/cc) and substrate compliance (the higher density substrates must be preformed to the desired shape prior to mold insertion and infusion) [23]. Felt-based conformals are of lower density ($< 0.3 \text{ g/cc}$) and are formed into shape and infused in the same process.

1.2.2 Design and Fabrication

The following section describes the steps to design and manufacture a conformal ablative heatshield, summarized in Figure 1.9. The process proceeds sequentially beginning with TPS material selection and sizing. The heatshield geometry is then segmented into a tiled design, based on material constraints, and molds are designed and fabricated for each tile. Those molds are then used to process the material, and, finally, the resulting tiles are integrated with the aeroshell. Some aspects of a conformal heatshield design, such as TPS sizing and tile layout, are not unique to conformals but are included below for completeness. Note also that descriptions of the mold design and processing are reversed for clarity in the discussion below.

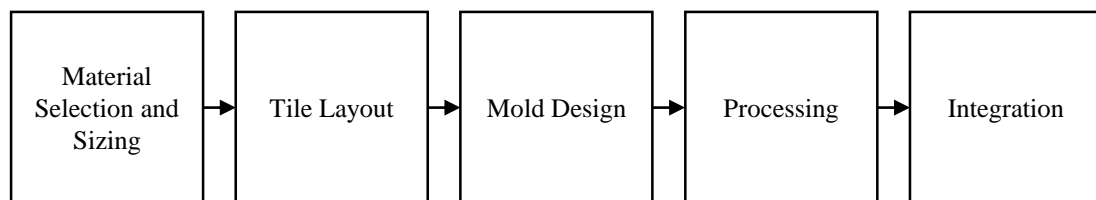


Figure 1.9: Steps in the design and fabrication of a conformal ablative heatshield.

Material Selection and Sizing

TPS material selection and sizing is dictated by the aerothermal entry environment. Relevant parameters for material selection include heat flux, shear rate and stagnation pressure. Material capability generally scales with TPS density, that is, higher density TPS can withstand harsher environments [3].

While material selection dictates peak instantaneous aerothermal conditions, integrated heat load sets TPS sizing. Typically, TPS thickness is determined by a bondline temperature limit, which is a limitation of the adhesive bond between TPS and aeroshell. As heat load increases so does TPS thickness. Margin is added to the sizing to accommodate uncertainty in the aerothermal environment and material properties. Traditional methods rely on either a worst-case stack up of uncertainties or a root sum square (RSS) method that considers uncertainties in the aerothermal environment and material response separately [49]. More rigorous, probabilistic uncertainty analysis have been developed more recently [50, 51, 52].

A database of material properties is necessary for evaluating TPS performance under aerothermodynamic heating. The material model — consisting of both thermochemical parameters (char yield; virgin and char densities, elemental compositions, and heats of formation; pyrolysis reaction rates and heats of reaction; and pyrolysis gas enthalpy and composition) and thermomechanical parameters (specific heats, thermal conductivities, and optical properties of both virgin and char material) [53] — forms an input to a thermal response model that predicts material behavior during entry. A subset of these properties relevant to, and within the scope of, this work are described here. Each factors into the energy balance describing the ablating material.

Composite (Virgin) Density, ρ_{comp} The density of the TPS material prior to decomposition (i.e., virgin material). This is referred to here as the composite density or virgin density.

Resin Mass Fraction, w_{resin} Resin mass fraction is the mass of resin in the virgin material as a fraction of total mass. The TPS material is typically modeled as a weighted combination of its constituents (resin and fiber).

Char Yield, Y_{comp} The remaining mass, as a percentage of initial mass, after complete pyrolysis of the polymer / conversion to char. The char yield of the composite TPS material is dependent on resin char yield, Y_{R} , as well as the relative proportions of resin and fibers.

Characterizing TPS properties and their uncertainties is crucial for successful heatshield design. Typically, an extensive experimental campaign is required in which data is accumulated from many samples across many different processing runs. An example of such a test campaign, for PICA, is described by Milos and Chen [54]. Property distributions can then be approximated from sample mean and variance. In some cases, experimental results may be supplemented with data from related materials as an approximation. For example, certain PICA properties were adjusted and scaled for C-PICA [38].

Tile Layout

Tile design and layout is strongly coupled to material selection. A combination of material and manufacturing constraints limit the part sizes and necessitate a tiled design for all but the smallest aeroshells. Fiber substrates are only available in certain sizes. For example, one carbon felt substrate used to fabricate C-PICA (Felt 1, described in Chapter 2) is available in widths of 41”–47” and thicknesses up to 0.88” nominally. In addition, substrate compliance, or lack thereof, limits how much they can bend and may impact heatshield design in areas of high curvature, such as the nose of an entry vehicle. Manufacturing constraints, such as tooling and oven dimensions, may also restrict tile size.

Tiled designs have the added complexity of handling seams between adjacent tiles. While a small conformal heatshield may be manufacturable without seams, large heat-

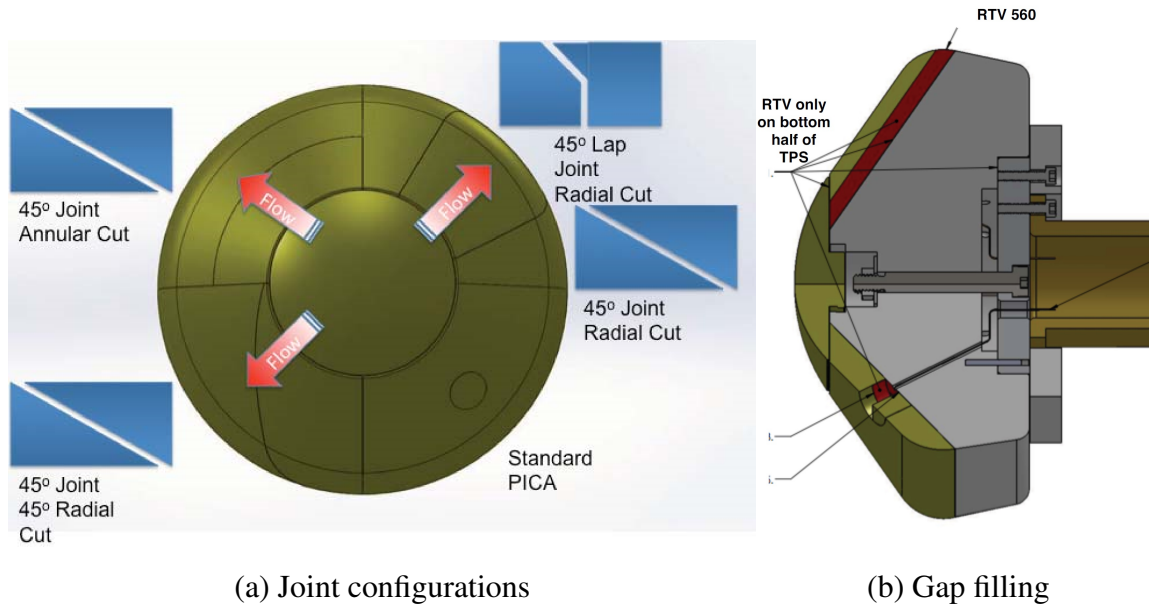


Figure 1.10: Seam designs demonstrated in C-PICA arcjet testing (Credit: Gasch, et al. [55]).

shields require gaps to manage part tolerances. These gaps must be filled in order to protect the underlying structure from exposure to the flow. Because gap fillers are exposed to the flow, joint design is an important driver of heatshield design. Five joint configurations were tested in C-PICA arcjet testing [55]. Four of these configurations are identified in Figure 1.10 (a). The fifth type, a perpendicular radial cut joining each quarter panel, was also found on the test article. RTV 560, a room-temperature-vulcanizing silicone rubber, spanning half the TPS thickness was applied to fill gaps between tiles (Figure 1.10 (b)).

Processing

Fabrication relies on a modified version of the liquid impregnation technique outlined earlier [16, 38, 56]. In general, there are a series of six steps for manufacturing a conformal ablator, summarized below and in Figure 1.11. Note that processing and machining are not shown in the figure due to the proprietary nature of these techniques, but general descriptions are provided. This outline is based on Refs. [38, 57].

1. Substrate preparation: Dry substrate material is cut and formed into the desired ge-

ometry.

2. Draping: Prepared substrate is placed over one side of the mold while the second side is clamped over top, securing it inside. Shims, typically of the same material, are sometimes used to absorb gaps with the tooling.
3. Processing: Substrate is infused with resin. Then, it undergoes heat treatment to cure the resin and remove solvent.
4. Mold removal: Cured and dried near net shape part(s) removed from the mold.
5. Machining: Excess material is removed and part(s) machined to the final geometry.
6. Installation: Finished TPS tile is ready for installation on an aeroshell.

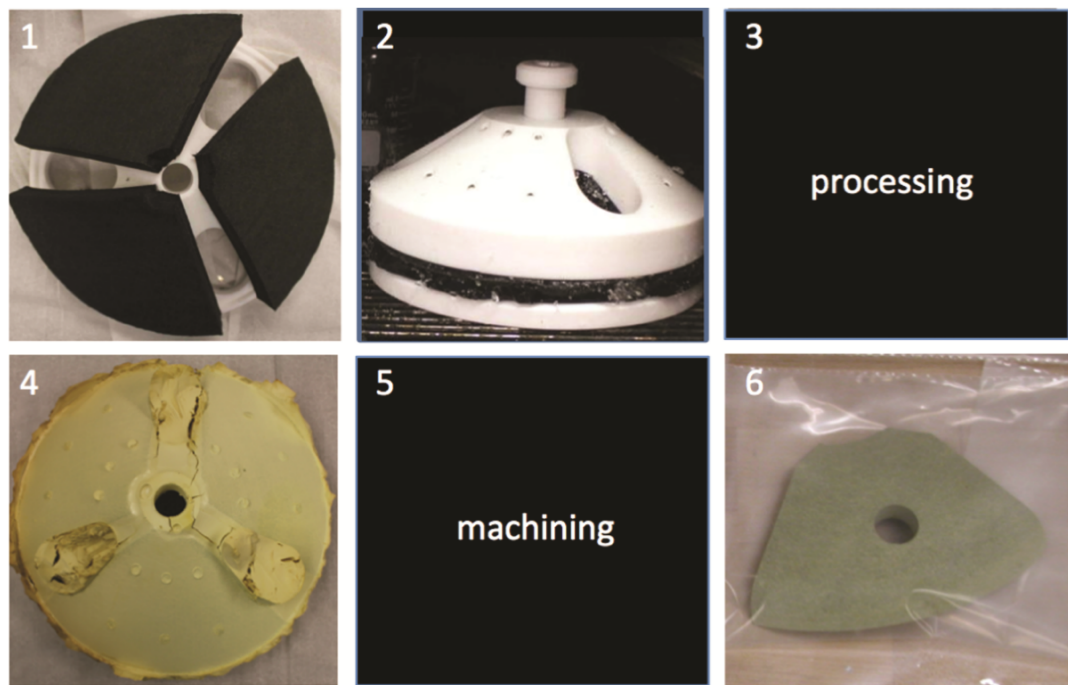


Figure 1.11: Overview of the fabrication process for a conformal ablator (Credit: Milos, et al. [38]).

Processing (Step 3) uses the liquid impregnation technique, but the fiber substrate is constrained in a matched mold to the desired geometry. The mold is placed in a larger

container and infiltrated by liquid resin while under vacuum. The process is carried out slowly (up to several hours for large parts) to ensure complete impregnation. The container with the immersed part is cured at high temperature, which causes the resin to polymerize. Then, the part is removed from the container and extracted from the now rigid resin yielding the near net shape part (Step 4). Removing excess resin requires careful cleaning and proper disposal, a time- and labor-intensive process. Once extracted, the bare part is heated a second time to remove residual solvent. For certain resin systems, a vacuum oven is required for both curing and drying to provide inert atmosphere and prevent oxidation.

Mold Design

Liquid impregnation is an open process. The mold is not closed, or sealed, but rather is partially open to its surroundings to allow resin to infiltrate the substrate while it is immersed. Molds require a large degree of open space to allow resin to enter the part. Some resin necessarily remains outside the substrate in this approach but is cured along with the part and then removed from the mold and discarded post-process. Note the small and large openings in the top and around the perimeter of the mold depicted in Figure 1.11, Step 2. The size and placement of these openings is important for ensuring adequate resin flow during impregnation so that no dry areas, or voids, are formed in the final material. Increasing open space in the mold can help to limit issues with poor flow but increases waste.

Integration

After processing, the near net shape tiles are machined to the precise geometry and then bonded to an aeroshell. While rigid substrate ablators require strain isolation layers between the tiles and the aeroshell, conformal ablators may be directly bonded to the structure. The temperature limit of this adhesive bond, the bondline, typically drives TPS sizing. RTV is frequently employed as a bonding agent, and its operating range limits the maxi-

imum bondline temperature to 250 °C. Gap filling, if required, also occurs during integration.

1.3 Liquid Composite Molding

Liquid composite molding (LCM) is a closed manufacturing process in which a fibrous substrate is impregnated with a liquid polymer resin and cured within a mold. LCM has existed in some form at least since the 1940s. Rudd, et al. identify the Marco method, designed as an improvement over hand layup for boat hulls, as the first use of LCM. A U.S. patent was granted for this process in 1950 [58]. In the Marco method, vacuum draws resin into a fibrous substrate that is sealed between a semi-flexible bag and a rigid mold. LCM soon expanded into the aerospace industry, for structural components, in the 1950s [59] and, subsequently, the rail, automobile and marine industries [60].

Today, LCM encompasses a variety of techniques: Resin Transfer Molding (RTM), Vacuum-assisted Resin Transfer Molding (VaRTM), gravity and vacuum infusion, structural reaction injection molding (SRIM), liquid resin infusion (LRI), Seemann Composite Resin Injection Molding Process (SCRIMP), and many other variants. Descriptions in this section are based on summaries by Rudd, et al. [61], Parnas, et al. [62], and Ermanni, et al. [63]. While each of these processes is a unique implementation of LCM, all operate on essentially the same principle: driving liquid resin into a dry, fiber preform through an applied pressure differential. Accordingly, they share common traits. Rudd, et al. identify these traits as a resin delivery system, a fiber handling system, a matched mold, and an approach for controlling resin flow and air removal. Parnas, et al. describe the extent, and importance, of resin flow as the trait that differentiates LCM from other composite manufacturing processes. While resin flow does occur in the other processes, managing this flow is uniquely critical to material quality and performance in LCM [62].

Tooling may be single- or double-sided. A single-sided mold is combined with a flexible material (e.g., a vacuum bag) to form the secondary surface. A double-sided tool

consists of two rigid, matched sides. Resin is injected into the dry fiber substrate at one or more ports, called gates. Residual air is vented at another port or along the periphery of the part as the flow advances. The resin can be cured after mold filling is complete or simultaneously with infusion to reduce cycle time.

Figure 1.12 depicts two LCM examples: RTM, on the left, and VaRTM, on the right. RTM uses a double-sided mold with resin typically injected at the center of the part. A peripheral joint allows air venting while restricting resin flow out of the cavity. VaRTM uses a single-side tool paired with a vacuum bag. Like RTM, resin is injected at the center of the part, but vacuum is applied at the periphery to assist resin flow. Note that the substrate may be preformed prior to mold insertion. Otherwise, the unformed substrate is draped over the tool surface immediately prior to injection.

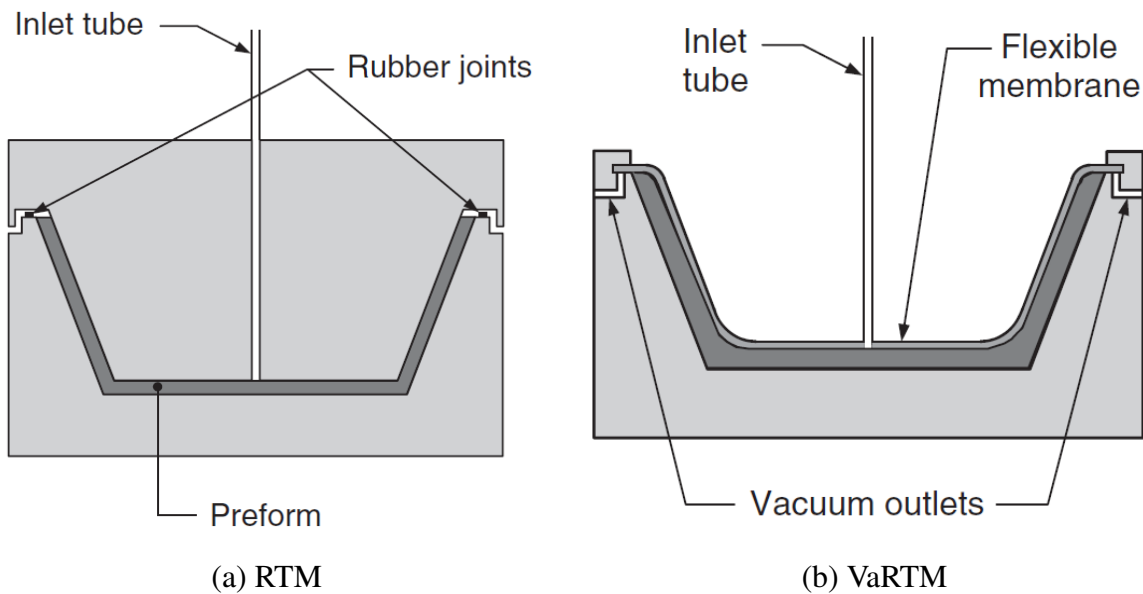


Figure 1.12: Two common LCM approaches (Credit: Ermanni, et al. [63]).

Rudd, et al. note that LCM is ideal for composites manufacturing due to:

1. Cost effectiveness over a range of production volumes
2. Application across a wide range of component types and geometries
3. Pre-placement of fiber substrate / control over fiber orientation

4. Part reproducibility

5. Ability to incorporate process automation if desired

Parnas, et al. indicate that LCM may not be cost effective for certain, simple part geometries, which are better suited to pultrusion and tape/filament winding. However, it is appropriate in most cases, and material performance can be nearly on par with hand layup / autoclave processing, which yields the highest strength composites [62].

Finally, and significant to this work, the mold filling process, which is deterministic, can be simulated using Darcy's Law, an empirical formula describing flow through a porous medium. Simulated flow patterns can aid mold design (e.g., locating a gate to avoid dry spots) and process design (e.g., evaluating resin arrival times). Significantly, this analysis can be carried out on a computer prior to tool fabrication preventing costly experimental trial and error. An overview of mold and process designs is presented in the next section followed by a description of the numerical simulation using Darcy's Law.

1.3.1 Mold and Process Design

Because resin flow is of primary importance in LCM — poor flow will yield poor part quality — much of the innovation, and variation, in LCM processes involves the method of resin delivery according to Parnas, et al. Some processes drive resin into the part with a pump or pressure pot (RTM, SRIM), others through vacuum (SCRIMP, vacuum infusion), and some a combination of both (VaRTM). Compression molding distributes resin through mold closure, pushing resin into the substrate with mechanical pressure.

In a double-sided tool, compression is applied to the mold through peripheral clamping or a press to consolidate the part and remove entrapped air. A single-sided tool is combined with a flexible material (e.g., vacuum bag) to form the second surface and provide consolidation pressure. Numerous approaches exist for injection and venting. In RTM and VaRTM, injection occurs at or near the center of the part with venting along the periphery of the mold as described above. In vacuum infusion, injection and venting are generally at

point locations within the mold and the periphery is fully sealed. To aid resin flow, distribution channels may be built into the tool or specialized distribution media may be layered on top of the primary substrate.

Mold material depends on application. For short production runs, plaster or a polymer laminate such as glass-fiber reinforced epoxy is appropriate. These materials are low cost but possess limited tool life. For longer production runs, metal, composite, or ceramic tooling is required for greater durability. Flexible tooling is generally elastomeric. An example of rigid tooling, a double-sided aluminum RTM mold, is shown in Figure 1.13. Note a characteristic “egg crate” structure to provide stiffness. Clamps are built into the periphery of the mold to compress the two sides.



Figure 1.13: A double-sided, rigid aluminum mold for an RTM process (Credit: JHM Technologies, Inc.).

Resin curing is accomplished through heating the mold and enclosed part. Perhaps the simplest approach is to place the entire assembly inside an oven, though this may present a challenge for particularly large parts. More sophisticated designs eliminate the oven altogether in favor of heating elements or liquid lines incorporated directly into the mold.

1.3.2 Numerical Modeling

Darcy's Law, an empirical relationship first outlined in 1856 [64], approximates flow through porous media. Numerical implementations of Darcy's Law to the LCM mold filling process have aided design in a range of processes: RTM [65], VaRTM [66], vacuum infusion [67], and SCRIMP [68] among others. In the literature, numerical simulation is frequently employed to optimize gate and vent locations as demonstrated by Jiang, et al. [69], Gokce, et al. [70], and Mathur, et al. [71]. Ruiz, et al. optimized injection flow rate to minimize microscopic and macroscopic voids [Ruiz2006]. Liu, et al. used a numerical model for real time process monitoring and control [72]. Application of Darcy's law to LCM is itself an extension of established work in soil mechanics and groundwater flows [73] originating with Darcy himself. Before describing the law and its implementation in LCM, relevant material properties appearing in the law are outlined first.

Relevant Material Parameters

The following parameters appear below in Darcy's Law and are required for simulating the mold filling process. The first two, porosity, ϕ , and permeability, $[K]$, are properties of the porous medium, or substrate. Note that ϕ and $[K]$ are continuum approximations of microscopic structure and can vary locally within a material. The last parameter, dynamic viscosity, μ , is a property of the infiltrating liquid.

Porosity, ϕ The empty, porous volume of the substrate, V_{pore} , as a fraction of its bulk volume, V_{sub} . Porosity is a unitless number between 0 and 1 (with one indicating a completely porous material):

$$\phi = \frac{V_{\text{pore}}}{V_{\text{sub}}} \quad (1.1)$$

Fibers occupy the other portion of the bulk volume, thus the fiber volume fraction, v_{fiber} , is related to porosity by $v_{\text{fiber}} = 1 - \phi$.

Permeability, $[K]$ A measure of the ease (or difficulty) with which a fluid flows through a porous medium. It is proportionality constant relating a pressure gradient to flow rate. Higher permeability corresponds to a higher flow rate. $[K]$ depends on substrate microstructure and, in certain cases, the fluid flowing through it. In three-dimensional Cartesian coordinates, $[K]$ is a rank 2 tensor:

$$[K] = \begin{bmatrix} K_{xx} & K_{xy} & K_{xz} \\ K_{yx} & K_{yy} & K_{yz} \\ K_{zx} & K_{zy} & K_{zz} \end{bmatrix} \quad (1.2)$$

Diagonal components, K_{xx} , K_{yy} , and K_{zz} , relate flow and pressure gradients in the same direction. Off-diagonal components relate flow rate to orthogonal pressure gradients. $[K]$ can be diagonalized to remove off-diagonal components. Furthermore, the materials of this work can be reduced to an in plane component parallel to the vehicle surface, K_{IP} , and a through thickness component perpendicular to the surface, K_{TT} . With these simplifications, the permeability matrix can be written

$$[K] = \begin{bmatrix} K_{IP} & 0 & 0 \\ 0 & K_{IP} & 0 \\ 0 & 0 & K_{TT} \end{bmatrix} \quad (1.3)$$

In SI units, K_{TT} and K_{IP} are on the order of 10^{-10} m^2 for the low density felts used in this thesis.

Dynamic Viscosity, μ A measure of a fluid's resistance to shear. Higher viscosity corresponds qualitatively to a thicker fluid. Quantitatively, it is a proportionality constant

relating a shear velocity gradient, $\frac{\partial u}{\partial x}$ to shear stress, τ :

$$\tau = \mu \frac{\partial u}{\partial x} \quad (1.4)$$

For a Newtonian fluid, μ is independent of shear rate. The SI unit for viscosity is the Pa·s, but an alternative unit, the poise, is also used frequently. One centipoise (cP), one hundredth of a poise, is equivalent to 10^{-3} Pa·s. In these units, μ is around 1 cP for water at room temperature.

Darcy's Law

In one dimension, Darcy's law relates a volumetric fluid flux, q , to the permeability of the medium, viscosity of the infiltrant, and a pressure change, ΔP , across a domain, L ,

$$q = \frac{K \Delta P}{\mu L} \quad (1.5)$$

Flux, q , has units of volume per time per area, or simply length per time. The macroscopic fluid velocity, u , which is the rate at which the flow front progresses through the medium, is the volumetric flux divided by porosity, which yields

$$u = \frac{K \Delta P}{\phi \mu L} \quad (1.6)$$

According to the equation, flow moves from high pressure to low pressure with a velocity proportional to substrate permeability and inversely proportional to liquid viscosity and porosity. Darcy's law averages complex microscopic flows through the pores of a medium into a single macroscopic, bulk velocity, u . The relationship is somewhat analogous to that of Fourier's law, relating heat conduction through a material to a temperature gradient. In

higher dimensions, Darcy's law becomes

$$\bar{u} = -\frac{[K]}{\phi\mu}\nabla P \quad (1.7)$$

where P is a pressure field (and the negative sign accounts for the directionality of the gradient). The bulk velocity, \bar{u} , is a vector and permeability, $[K]$, is now a matrix as described above. Combining this equation with conservation of mass for an incompressible fluid,

$$\nabla \cdot \bar{u} = 0 \quad (1.8)$$

yields an elliptic partial differential equation governing the pressure field in the saturated region.

Though originally an empirical formula, Darcy's law has been derived from an analysis of Stokes flow [74], which describes low Reynolds numbers flows [75]. Adaptations and extensions have attempted to address more complex phenomena not captured by the original formulation:

1. Forchheimer added a velocity-squared term to capture inertial resistance for high Reynolds number flows [76]. An alternative criterion derived from that work, the Forchheimer number, describes the relative contribution of inertial effects [77].
2. Klinkenberg showed that gas permeability varied with pressure and developed a correction to account for slippage in the porous material [78]. This correction has been used to approximate liquid permeability in the limit of continuum flow [79].
3. Brinkman introduced an additional term to Darcy's law in an attempt to address shearing along pore walls [80], but it has numerous shortcomings [81].

While Darcy's law is relatively simple in form, complication arises in its application to LCM processes. In some cases, the substrate is compacted to increase fiber density and eliminate voids (dry, unfilled regions) leading to permeability and porosity variation [66].

If the process is not isothermal (i.e. resin is heated during infusion to initiate curing), then thermal coupling arises due to the temperature dependence of μ . Separating mold filling and curing into distinct phases somewhat simplifies the task. Furthermore, maintaining the mold and resin at a single temperature (i.e., an isothermal process) removes temperature dependence, and temperature may be treated as a fixed input to the model, which is done in the present work.

Solution Approach

Solution of the mold filling problem, summarized by Rudd, et al. [61], involves an iterative procedure of (1) solving for the pressure field from the governing partial differential equation (Equations 1.7 and 1.8), (2) obtaining resulting fluid velocities at the flow front from Equation 1.7, (3) updating the location of the flow front, then (4) repeating until the mold is filled. In the literature, various approaches have been employed. Methods for solving the pressure field include finite difference, boundary element and finite element. Boundary conditions are typically specified by:

1. Constant pressure, constant flow rate, or a combination of both at the gate(s)
2. Zero gauge pressure along the flow front
3. Zero normal velocity along the mold wall

A single iteration of the simulation is illustrated in Figure 1.14. The initial saturated region (dark green) is defined by zero gauge pressure along the unrestricted flow front and zero normal velocity along the upper boundary of the domain. The gate may be defined by any of the boundary conditions described above. After solving for the pressure field, the flow front is advanced to the next time step (light green). The procedure is repeated until the saturated region completely fills the domain.

The time-varying geometry of the saturated region, and thus the solution domain, lends additional complexity to the problem. Both fixed and moving grids have been utilized for

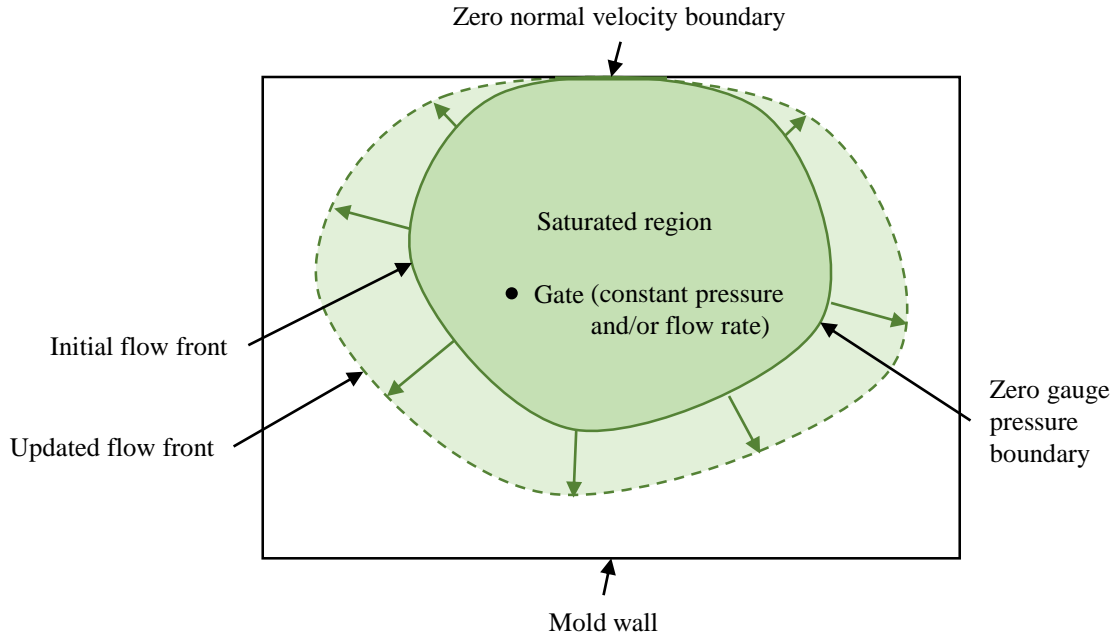


Figure 1.14: Numerical depiction of the mold filling problem.

flow front advancement. In the moving grid approach, the solution domain is re-meshed at each time step yielding an accurate flow front geometry at the expense of large computational cost. The fixed grid approach is substantially faster but the flow front shape is less accurate and violations of mass conservation can arise.

Control volume / finite element (CV/FE) methods first developed by Brusckie and Advani attempt to bridge the gap between fixed and moving grid methods [82]. This approach, which has now been widely adopted, ensures local conservation of mass while leveraging the computational efficiency of a fixed grid. Flow front advancement is achieved by tracking fluid flow into and out of control volumes (CV) around each mesh node. A fill factor, f_f , denotes the fraction of resin saturation within a CV allowing numerical representation of an empty node ($f_f = 0$), a fully saturated node ($f_f = 1$) and a partially saturated node ($0 < f_f < 1$). Logically, partially saturated nodes represent the approximate flow front location.

1.4 Gap Analysis

The current method of fabricating conformal ablators, relying on the liquid impregnation technique of older rigid substrate ablators, has several inefficiencies as seen in the previous discussions. These relate to both the manufacturing and the design processes for these materials. Cumulatively, these inefficiencies lead to added labor, time, and cost in making a conformal ablative heatshield and can impact material quality and consistency.

1.4.1 Manufacturing Inefficiencies

First, open processing is inherently wasteful because large openings in and around the mold are required to ensure adequate resin infiltration. More open space yields better resin flow and ensures full impregnation but generates more waste. Excess resin necessarily remains outside the substrate only to be discarded after curing. More than half of the resin may be wasted (as described in Chapter 3). Not only does this excess add to direct material costs, but it also negatively impacts other aspects of manufacturing.

Larger demands on resin consumption necessitate a larger inventory and the capacity to store it. Prior to processing, resin must be stored and, in some cases, at low temperatures to prevent composition changes. Waste generation significantly burdens both processing technicians and disposal facilities. Resin removal is messy and laborious. Materials are often hazardous and generate significant dust requiring careful cleaning and appropriate handling. Personal protective equipment (PPE) is necessary to mitigate health risks. Once removed, hazardous resin waste must then be disposed of in compliance with local, state, and federal regulations.

The open process requires atmosphere control (i.e., a vacuum oven or chamber) to prevent resin oxidation during curing and drying. Compared to conventional ovens, vacuum ovens are much more expensive and limited in size, a comparison presented in Chapter 3. Open processing also exposes the oven, or chamber, to resin and solvent which evaporates

and collects on the interior during processing. The oven, or chamber, must be frequently cleaned, and interior surfaces deteriorate over time.

1.4.2 Design Inefficiencies

Traditionally, mold design is a trial and error process informed by operator experience. No computational tool exists to support design and, thus, each new TPS geometry requires substantial design effort. Without a numerical tool, sizing and locating mold openings relies on best practices and engineering intuition but is not simulated prior to fabrication. Thus, non-optimal mold designs, which may yield poor material quality, can only be identified after fabrication and subsequent material characterization. Mold fabrication requires substantial upfront investment, and modifications to a tool may be costly or even impossible. Additionally, because a single processing run takes several days from start to finish, iterations incur a steep penalty on manufacturing time and cost.

Tile layout, which is coupled to manufacturing, also impacts processing. Tiles must be manufacturable while meeting design and process restrictions. Again, without a computational tool, these criteria are manually incorporated into heatshield design and then translated to tooling and processing. A change in material composition (e.g., alternate substrate dimensions) will necessitate a change to tile geometries and the subsequent mold designs.

Finally, no framework exists for efficiently estimating conformal ablative TPS material properties and their uncertainties. The current approach of experimentally quantifying material uncertainties is rigorous, but, due to the time and cost involved in TPS processing and testing, producing enough samples to obtain accurate statistical distributions is difficult, particularly during the conceptual phase of a flight project. Changes to material formulation alter resulting properties and uncertainties requiring a whole new set of property data.

1.4.3 Applicability of LCM

LCM appears to be well-suited to TPS manufacturing — a closed process produces little resin waste and numerical modeling enables mold and process design. Despite its potential, however, LCM has had limited usage in TPS manufacturing to date. Applications have primarily focused on using vacuum bagging to pack ablative resin into a reinforcing structure as an alternative to hand packing/injection for fiber filler ablators. Vacuum drawn on the bag applies compression to the layup, forcing resin into the cells of the reinforcement. This approach is described in a patent for Boeing Lightweight Ablator [83] and a related patent for the Boeing CST-100 [84]. A similar approach was developed for SRAM and Phen-Carb [85]. RTM processing of a thick (>0.25 inch) fully dense TPS material, 3D-MAT, was demonstrated in recent work [45, 23], the only known example employing LCM for a fiber substrate ablator. However, no simulation was employed in mold design, which could potentially impact material quality.

1.5 Study Overview and Objectives

In this work, a vacuum infusion process (VIP) was developed for conformal ablative TPS materials which injects resin directly into a fiber substrate within a closed, evacuated mold. Like state-of-the-art (SOTA) processing, VIP proceeds in three steps depicted in Figure 1.15: resin infusion (or mold filling), curing, and drying. Infusion is performed with the enclosed substrate under vacuum. Curing and drying are then carried out with a secondary lid to allow resin expansion. The process is described in more detail in Chapter 3.

VIP — a subset of LCM — addresses inefficiencies in the design and processing of conformal ablators. First, VIP injects resin into the fibrous substrate within a closed mold resulting in little to no waste and allowing use of a conventional, rather than vacuum, oven for curing and drying. Demolding and clean up are simplified because the part does not need to be extracted from surrounding excess, and there is less waste to dispose of. Second,

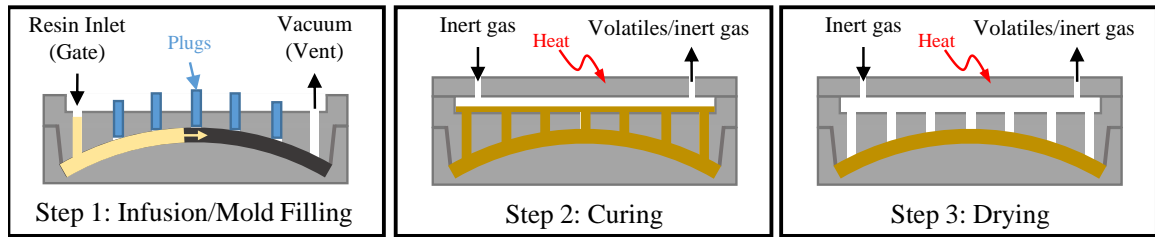


Figure 1.15: Vacuum infusion processing of conformal ablators.

Darcy's Law enables simulation of the mold filling step, which can identify areas of poor infusion and inform mold design. Design iteration on a computer enables high quality, well-infused TPS without costly experimental trial and error.

VIP was demonstrated on a representative conformal TPS material that combines a low density carbon felt with a dilute phenolic resin. VIP was first demonstrated on small, flat coupons and then scaled up to large, curved tiles forming the acreage of a large heatshield. Fabricated TPS materials were assessed through visual inspection and material characterization. Both global and local properties of the tiles were measured and analyzed to assess variability.

A computational framework was developed combining a Darcy's law simulation of mold filling with optimal tile layout and material property estimation. The latter included properties required for the mold filling simulation (substrate permeability and porosity, and resin viscosity and vapor pressure) and those describing the resulting TPS material (virgin density, resin mass fraction, and char yield). The framework forms the basis for a conceptual design methodology allowing rapid evaluation of changes to constituent materials, process parameters, and TPS geometry and their impact on manufacturing and TPS properties.

This study is the first to develop a LCM process for fabricating a conformal ablator and pair it with a methodology and simulation tool to perform automated heatshield design and material characterization. It advances the state of the art of conformal ablator manufacturing, design, and evaluation by integrating much of the design and fabrication

process shown in Figure 1.9. The approaches developed here are relevant to a range of conformal ablative materials, aeroshell geometries, and tile layouts. VIP is applicable not only to conformals but could also be used to manufacture related low density rigid substrate ablators such as PICA. The approach may be especially attractive for small, single piece heatshields around 1.5 m in diameter. Such a design may be fabricated with a single mold in VIP yielding significant reductions in resin waste. The mold filling simulation can also be useful as a standalone tool to design molds for unusual or complex tile geometries, such as those forming the shoulder of an entry vehicle.

1.6 Summary of Contributions

Advancements in this investigation include both experimental development of the VIP process and the computational framework to design and fabricate a heatshield using that process. Academic contributions to the state of the art are summarized here.

Formulation of A Constitutive Model of Fiber Substrate Ablators for Conceptual Design

A filamentary analog model of a fibrous substrate was combined with known properties of a resin to approximate a composite TPS material resulting in closed-form expressions for virgin density, resin mass fraction, and char yield. While not a replacement for experimental characterization, the approach reduces experimental burden and accelerates evaluation of alternative compositions when full experimental characterization is difficult or impractical such as during conceptual design. Uncertainty bounds formulated from the closed-form expressions help to quantify TPS variability and the constituent properties that drive it. Numerical uncertainties provide a useful sanity check on manufacturing to confirm that a fabricated material is within accepted tolerances.

Development and Demonstration of a Vacuum Infusion Process for Conformal Ablative TPS Materials

A vacuum infusion process was developed for conformal ablative materials that improves efficiency over the state-of-the-art method, reducing resin consumption and eliminating the need for an atmosphere-controlled oven or chamber. Less excess resin reduces the burden on processing technicians who clean tooling and discard the hazardous material. It also decreases the required inventory of the resin and other additives saving storage space. Switching to a conventional oven for processing significantly decreases equipment costs, especially when scaling to a large heatshield, and the oven is not exposed to harsh solvents which can affect longevity. Combined, these advancements make manufacturing of conformal ablative TPS simpler and more accessible.

Development of a Methodology to Optimize a Conformal Ablative Heatshield Design

A rigorous design methodology integrating material selection, tile layout, and processing was developed. The methodology improves on largely manual, segregated approaches tailored to a specific material and aeroshell geometry. A Darcy's law mold filling simulation was paired with an approach for tiling a heatshield geometry. Optimization of mold designs ensures consistent, high quality parts without voids. Material property estimation generalized the approach to a range of constituent materials and geometries enabling rapid conceptual design of a conformal ablative heatshield. A designer is freed to evaluate other aspects of heatshield design such as TPS material composition and its impact on processing and properties.

1.7 Outline of Thesis

Contributions of the thesis are organized into the following chapters:

Chapter 2 presents the constitutive model for fiber substrate ablators. The model combines properties of the underlying substrate and resin to estimate properties of the final TPS material. Substrate properties are modeled using a filamentary analog approach which

assumes smooth, cylindrical, uniform density fibers. Expressions for porosity, density, and material shrinkage follow from this approach. Resin properties in the composite TPS material are estimated from known properties of the pure resin. Then, substrate and resin properties are combined by assuming resin occupies only the porous space within the substrate resulting in closed-form equations describing properties of the composite material: virgin density, resin mass fraction, and char yield. Two felt variants were processed into several small C-PICA coupons for comparison to numerical models. Finally, bounds on TPS properties were computed from known input parameter uncertainties and confirmed by a Monte Carlo analysis. Results were then used to correlate input and output uncertainties to determine primary drivers of material variability.

Chapter 3 describes the vacuum infusion process for conformal ablators and contrasts it with the conventional process. Early development work, fabricating small 4 inch square, flat coupons, is reviewed. Then, results of a scale up to larger, curved C-PICA tiles, approximately 0.5 meters across, are presented. Aspects of design and processing are reviewed from mold configuration to substrate preparation and finally VIP. Results of material characterization indicated successful infusion and good material quality. Fabricated parts were visually inspected and sampled at several locations across the part. Virgin density, resin mass fraction, and char yield of both the bulk parts and the small coupons compare well to predicted values from the constitutive model of Chapter 2.

Chapter 4 introduces the design methodology for a conformal ablative heatshield. The complete methodology, encompassing both inputs and design tasks, is outlined followed by a detailed discussion of the inputs. Inputs are differentiated into primary and intermediate parameters. The latter are quantities that are typically unpublished or unavailable but are nonetheless required for subsequent mold filling analysis and TPS property estimation. Approaches for estimating these inputs are presented to speed early conceptual design. The final section compares these estimates with experimentally obtained values for C-PICA

constituent materials.

Chapter 5 completes the description of the design methodology. The beginning of the chapter discusses each design task: tile layout, mold and process design, and TPS property estimation. Iteration on tile layout yields a design that minimizes the total number of tiles subject to manufacturing constraints. Subsequent tile geometries feed into the mold and process design, which selects an optimal gate location and then generates relevant process metrics. The final design task uses the constitutive model of Chapter 2 to estimate TPS properties.

Chapter 6 demonstrates the integrated methodology on a 4.5-meter diameter, 70 degree sphere-cone, C-PICA heatshield. Then, mold design is carried out independently for the prescribed tile geometry of Chapter 3. Predicted mold flow is compared to the experimental process, linking the computational methodology to experimental work.

Chapter 7 summarizes the thesis and its contributions. Potential extensions of this work are suggested.

CHAPTER 2

A CONSTITUTIVE MODEL OF FIBER SUBSTRATE ABLATORS FOR CONCEPTUAL DESIGN

2.1 Introduction

Modeling TPS performance requires a database of properties describing material response under aerothermodynamic heating. These parameters, outlined in Chapter 1, include both thermomechanical and thermochemical properties. Due to material variability, uncertainty in these properties must also be factored into a design. Traditional methods rely on either a worst-case stack up of uncertainties or a RSS method that considers uncertainties in the aerothermal environment and material response separately [49]. These approaches often rely on ad hoc judgments of underlying uncertainties resulting in non-optimal designs. More rigorous, probabilistic uncertainty analyses have been developed more recently [50, 51, 52]. Carrying out a probabilistic analysis requires knowledge of parameter distributions. Monte Carlo simulation is then used to assess TPS material response uncertainty and appropriately size the heatshield to yield high confidence of success.

The material model is typically accumulated through an experimental campaign which tests many samples over many processing runs to obtain relevant statistical distributions. Such a time-consuming approach may not be appropriate or feasible in all scenarios, e.g., when a heatshield is undergoing rapid iteration during conceptual design, or when evaluating alternative formulations of a TPS material. A recent study, mentioned in Chapter 1, explored alternate felt substrates for C-PICA [16]. Changing the substrate of a given ablator requires a whole new set of property data to evaluate its performance. Full material characterization would not even be carried out until much later in development after down-selection to the final material(s). Changes to composition also impact resulting uncertain-

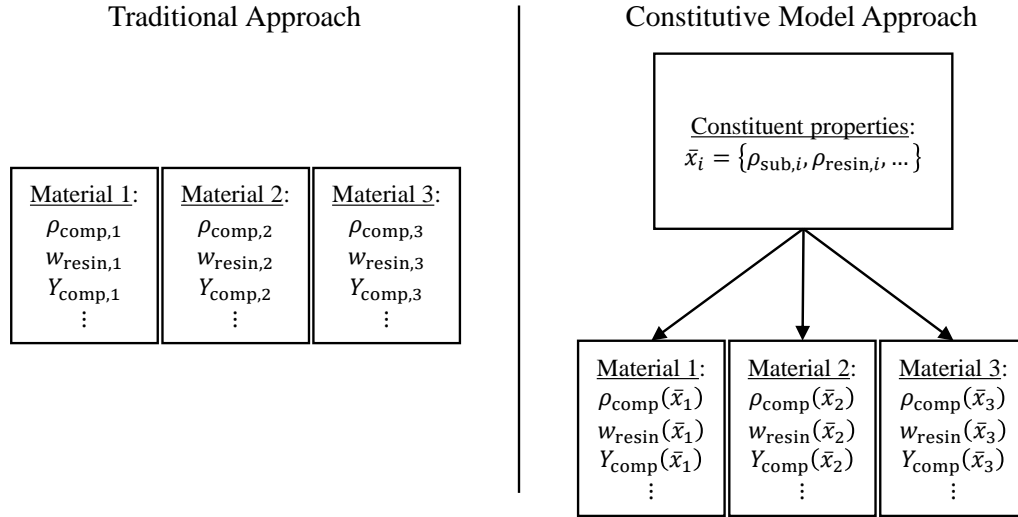


Figure 2.1: Description of TPS material properties: traditional and constitutive model approaches.

ties. Variation in a single input can affect multiple outputs — e.g., starting substrate density affects not only virgin density but also char yield, char density, thermal conductivity, and other parameters. These uncertainties are difficult to quantify without a full-fledged experimental campaign. Furthermore, capturing correlations between input and output properties could advance the understanding of what drives material variability.

This chapter adopts a constitutive model of the TPS material based on properties of the underlying substrate and resin. Rather than materials represented by distinct databases of properties, they are represented by a common set of constituent properties (Figure 2.1). Each TPS formulation is functionally dependent on these underlying properties. Composition changes can then be assessed by changing the properties of the constituents rather than through exhaustive testing of each unique formulation. This approach allows material property estimation when full experimental characterization is difficult or impractical. While it is not a replacement for accurate experimental characterization, the method reduces reliance on experiment in early design and materials development. For example, data from a known resin solution can be applied to another fiber substrate without further testing.

This chapter presents such a constitutive model of fiber substrate-based ablators. Sub-

strates are modeled using a filamentary analog method where fibers are assumed to be smooth, nonporous cylinders of uniform density distributed randomly through the material. The resin is described by its cured density, cure shrinkage, and char yield. These simplifications yield closed-form expressions describing the substrate, the resin, and the composite TPS material. Estimated TPS properties include virgin density, resin mass fraction, and char yield though these could potentially be extended to other relevant modeling parameters. Properties are shown to be functionally dependent on the underlying substrate density, resin density in the composite, and resin char yield.

Small samples of two C-PICA variants, possessing the same resin composition but different carbon felt substrates, were fabricated for comparison to numerical models. Virgin density and resin mass fraction were measured for each sample. Then, the materials were charred in a furnace at 1200 °C to obtain yields. In most cases, experimental results align well with numerical models though certain discrepancies are identified. Finally, bounds on TPS properties were computed from known input parameter uncertainties. Property distributions generated using Monte Carlo confirmed computed bounds. Results were then used to correlate input and output uncertainties to determine primary drivers of material variability.

The framework presented here is well suited for conceptual design and for rapidly evaluating the impact of changes to TPS composition. Development of new TPS materials could also benefit from this approach by allowing designers to identify the constituent properties driving variability. These properties could then be targeted for modification or manufacturing improvements to reduce variations. Numerical uncertainties can provide a useful sanity check on manufacturing to confirm that a fabricated material is within accepted tolerances. Out-of-tolerance properties may help identify a manufacturing problem or material defect. Finally, though not carried out here, statistical property distributions could be input into a larger probabilistic material response analysis to carry out TPS design.

2.2 Methodology and Results

2.2.1 Material Formulation and Processing

Present testing was carried out on two low density carbon felts manufactured from a rayon precursor. Felt 1 ranged in density from 0.07 g/cc to 0.10 g/cc with thicknesses ranging from 0.80 in to 0.96 in (2.0 cm to 2.4 cm). Felt 2 ranged in density from 0.10 g/cc to 0.12 g/cc with thicknesses between approximately 0.70 in and 0.95 in (1.9 cm and 2.4 cm). Both felt materials were infiltrated with C-PICA resin, a proprietary phenolic resin solution, using the conventional open liquid impregnation technique described in Chapter 1. Resin loading, as measured by the difference between virgin density and substrate density, is between 0.16 g/cc and 0.18 g/cc.

Felt cores were cut from larger billets using a 1 in (2.54 cm) cylindrical punch. Sixteen samples were taken from a single billet of Felt 1 and 22 samples were taken from a single billet of Felt 2 — 38 coupons in total. These cores were infused with resin in an open container at room temperature. Cores were placed between two plates to keep them submerged in the resin solution during processing. Thickness variation resulted in some samples being compressed slightly pre-process (by a few percent of their initial thickness) while others remained uncompressed, and the results below are differentiated accordingly. They were subsequently cured and dried at high temperature to produce the composite TPS material. Resulting TPS cores were then charred at 1200°C under inert atmosphere in a tube furnace to obtain yields. Processing steps, from initial dry felt to virgin TPS to charred TPS, are depicted in Figure 2.2. Mass and dimensions were recorded for each sample at each step of the experiment.

Relevant resin properties were drawn from eleven approximately 0.45” diameter samples of pure resin. These samples were obtained from holes in the tooling (expansion ports) during the processing of the four C-PICA tiles described in Chapter 3. Each tile produced several resin plugs, but only a few of these were intact after removal. In total, four samples



Figure 2.2: Material at each step in experimental processing (left to right): dry felt prior to processing, virgin TPS, and charred TPS.

were taken from Tile 2, three from Tile 3, and four from Tile 4. Tile 1 was ignored due to a deficiency in the experimental setup which was corrected in later runs.

Measured properties included cured density, ρ_R , one-dimensional shrinkage, ϵ_R , and char yield, Y_R . Shrinkage, ϵ_R , is the non-dimensional, fractional length change that occurs as the resin polymerizes. Mean values and observed ranges are presented in Table 2.1.

Table 2.1: Properties of the cured resin.

Property	Symbol	Mean	Range	Units
Cured density	ρ_R	0.30	0.28–0.33	g/cc
Fractional length shrinkage	ϵ_R	0.10	0.05–0.13	m/m
Char yield	Y_R	52	48–54	%

2.2.2 Properties of the Fiber Substrate before Processing

Methodology

Fibrous substrates are modeled as networks of smooth, nonporous cylindrical fibers with uniform density. Such an approach, the filamentary analog method, has been applied elsewhere to estimate porosity, permeability, and specific surface area of low density carbon felts similar to the present work [86, 87]. Employing the filamentary analog model simplifies preform properties to functions of density. Porosity, ϕ , the fraction of empty space in the substrate, is estimated as a ratio of apparent substrate density, ρ_{sub} , to fiber density,

ρ_{fiber} ,

$$\phi = 1 - \frac{\rho_{\text{sub}}}{\rho_{\text{fiber}}} \quad (2.1)$$

Note that ρ_{sub} is an average of the fiber mass, m_{fiber} , over the bulk volume and is strictly less than ρ_{fiber} . That is,

$$\rho_{\text{sub}} = \frac{m_{\text{fiber}}}{V_{\text{sub}}} \quad (2.2)$$

where V_{sub} , the bulk volume, includes the volume of the fibers, V_{fiber} , and volume of open, porous space, V_{pore} :

$$V_{\text{sub}} = V_{\text{fiber}} + V_{\text{pore}} \quad (2.3)$$

Porosity and substrate density are inversely proportional, ϕ decreases as ρ_{sub} increases. Fiber density, ρ_{fiber} , depends on precursor material and processing. Fiber density for Felt 1 was computed as 1.395 ± 0.055 g/cc in Appendix A.1, a value that is consistent with other data for rayon-based carbon fibers. Pierson suggests a historical range from 1.40 g/cc to 1.80 g/cc though the upper end encompasses high modulus fibers that are no longer manufactured [88]. Morgan lists current commercially available fibers from 1.35 g/cc to 1.44 g/cc [89].

Areal density, $\rho_{\text{sub}}^{\text{areal}}$, is assumed to be constant here because it is controlled during manufacturing of the felt materials under investigation. Figure 2.3, which shows areal density plotted against the initial, uncompressed thickness of each of the cores, confirms this assumption. Means for each felt (0.194 g/cm² for Felt 1 and 0.209 g/cm² for Felt 2) vary between the two materials as can be expected from different manufacturing processes. However, for a given felt, areal density shows little to no correlation with thickness. Standard deviation is also higher for Felt 2 (0.007 g/cm²) compared to Felt 1 (0.003 g/cm²).

Note that volumetric substrate density, and thus porosity, is dependent on compaction. Flexible substrates are typically processed to near net shape in a mold. Resulting compression increases substrate density and decreases porosity. Assuming constant areal density

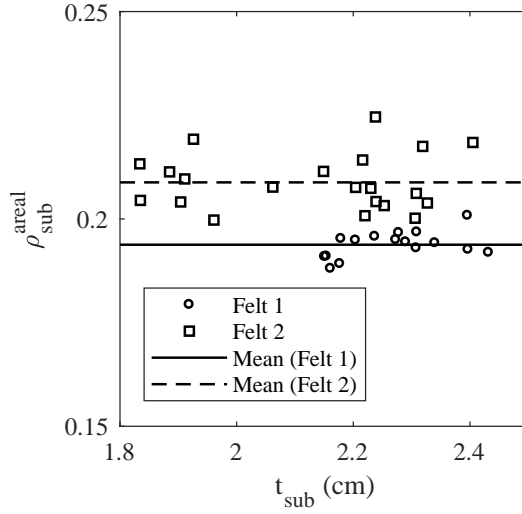


Figure 2.3: Substrate areal density plotted against thickness.

reduces substrate properties to a function of the material thickness:

$$\rho_{\text{sub}} = \frac{\rho_{\text{sub}}^{\text{areal}}}{t_{\text{sub}}} \quad (2.4)$$

The relevant porosity is that based on the pre-process, compressed thickness, t^{pre} . In a mold, this is equivalent to the distance between the two sides of the cavity. The pre-process substrate density is then,

$$\rho_{\text{sub}}^{\text{pre}} = \frac{\rho_{\text{sub}}^{\text{areal}}}{t_{\text{sub}}^{\text{pre}}} \quad (2.5)$$

with pre-process porosity

$$\phi^{\text{pre}} = 1 - \frac{\rho_{\text{sub}}^{\text{areal}}}{\rho_{\text{fiber}}} \frac{1}{t_{\text{sub}}^{\text{pre}}} \quad (2.6)$$

Results

Porosity was measured on 19 half-inch (1.27 cm) diameter cylindrical felt samples, different from the samples described above, described in Appendix A.1. Fourteen Felt 1 samples and five Felt 2 samples were tested taken from single billets of each respective material. Porosity was calculated using Archimedes principle — comparing dry mass and saturated

mass after infiltrating with water using a technique described in Appendix A.1. Resulting porosities are plotted against substrate density (Figure 2.4). The porosity model (Equation 2.1) shows good agreement with experimental data. The bounds reflect the range of fiber densities for Felt 1, 1.395 ± 0.055 g/cc. Felt 1 exhibits high variability around the nominal value whereas Felt 2 has little variation but is biased toward the upper bound. This may indicate a higher nominal fiber density for Felt 2, despite the same precursor material.

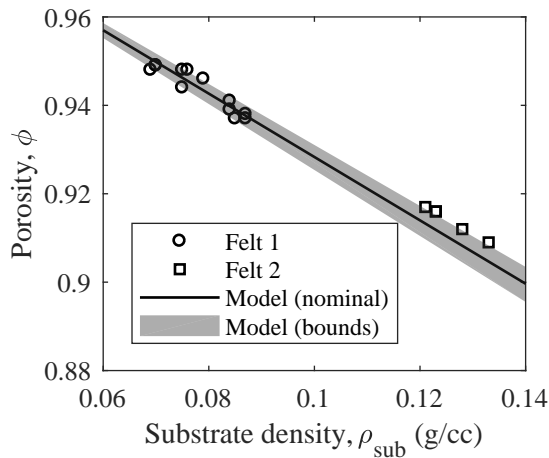


Figure 2.4: Substrate porosity as a function of density.

2.2.3 Properties of the Fiber Substrate after Processing

Methodology

In addition to mechanical compression, flexible substrates can undergo dimensional changes during processing due to shrinkage of the resin infiltrant. The carbon felts here provide little resistance to contraction through the thickness due to a lack of fiber connectivity in that direction. Resulting shrinkage is typically between 5% and 10% of the pre-process thickness, but may be lower with higher levels of compression. In plane shrinkage also occurs but to a lesser degree, typically from zero to 2% percent [90]. Due to this directional dependence, shrinkage is differentiated into through thickness and in plane components with fractional changes denoted ϵ_{TT} and ϵ_{IP} , respectively. Note that these are quantities of the composite

material and are thus a function of the combined substrate-resin system. In contrast, the one-dimensional shrinkage of the pure resin (in the absence of a substrate) is denoted ϵ_R and is assumed equal in all directions. Thus, the volumetric shrinkage of the pure resin, α_R , is

$$1 - \alpha_R = [1 - \epsilon_R]^3 \quad (2.7)$$

Assume momentarily that shrinkage occurs in one dimension alone. Then, the post-process volume of the composite material is related to the pre-process volume by

$$V_{\text{sub}}^{\text{post}} = V_{\text{sub}}^{\text{pre}} [1 - \epsilon] \quad (2.8)$$

where ϵ is the composite shrinkage in the chosen direction. Similarly, for the pure resin undergoing shrinkage in one dimension,

$$V_{\text{resin}}^{\text{post}} = V_{\text{resin}}^{\text{pre}} [1 - \epsilon_R] \quad (2.9)$$

where superscripts denote pre- and post-process quantities. Now, in the composite material, the volume of resin is taken to be equivalent to the pore space in the material, i.e., resin occupies the empty volume between fibers. Setting $V_{\text{resin}} = V_{\text{pore}} = \phi V_{\text{sub}}$,

$$\phi^{\text{post}} V_{\text{sub}}^{\text{post}} = \phi^{\text{pre}} V_{\text{sub}}^{\text{pre}} [1 - \epsilon_R] \quad (2.10)$$

This substitution effectively reduces the effect of resin shrinkage in the composite by the porosity. Combining this expression with Equation 2.8 yields

$$\phi^{\text{post}} [1 - \epsilon] = \phi^{\text{pre}} [1 - \epsilon_R] \quad (2.11)$$

Now, Equation 2.1 can be written in terms of mass for both the pre- and post-process substrate,

$$\phi^{\text{pre}} = 1 - \frac{m_{\text{sub}}}{V_{\text{sub}}^{\text{pre}} \rho_{\text{fiber}}} \quad (2.12)$$

$$\phi^{\text{post}} = 1 - \frac{m_{\text{sub}}}{V_{\text{sub}}^{\text{post}} \rho_{\text{fiber}}} \quad (2.13)$$

Note that substrate mass does not change during processing. Combining these expressions with Equation 2.8 yields a relationship between pre- and post-process porosity based on composite shrinkage alone,

$$\phi^{\text{post}} = \frac{\phi^{\text{pre}} - \epsilon}{1 - \epsilon} \quad (2.14)$$

Finally, combining Equations 2.11 and 2.14 and simplifying gives an expression for the one-dimensional composite shrinkage as a function of resin shrinkage assuming the substrate does not resist the volume change,

$$\epsilon = \phi^{\text{pre}} \epsilon_{\text{R}} \quad (2.15)$$

Intuitively, composite shrinkage scales with initial substrate porosity. Absent a substrate ($\phi^{\text{pre}} = 1$), the material is purely resin with a shrinkage equivalent to the resin shrinkage. As porosity decreases ($\phi^{\text{pre}} \rightarrow 0$), there is less porous volume, less infused resin, and less shrinkage. A nonporous substrate ($\phi^{\text{pre}} = 0$) possesses no resin and thus does not shrink.

Equation 2.15 can be used to bound results for these composite materials. The substrate may be either incompressible or compliant in each direction. That is, if incompressible, the substrate resists dimensional change and $\epsilon = 0$. If compliant, the substrate provides no resistance to such changes and ϵ follows from the equation. Shrinkage is differentiated into an in plane component, ϵ_{IP} , and a through thickness component, ϵ_{TT} . Three limiting cases are derived from this approach: (1) a fully incompressible substrate, (2) a partially compliant substrate, and (3) a fully compliant substrate (Table 2.2). The first case represents a rigid

fiber substrate (e.g., FiberForm) that does not shrink at all during processing ($\epsilon_{IP} = \epsilon_{TT} = 0$). The second case represents a material that shrinks through the thickness ($\epsilon_{TT} = \phi^{\text{pre}}\epsilon_R$) but not in plane ($\epsilon_{IP} = 0$) approximating the felt materials of this work. The last case is a theoretical upper bound on shrinkage where shrinkage occurs equally in all directions ($\epsilon_{IP} = \epsilon_{TT} = \phi^{\text{pre}}\epsilon_R$). Post-process substrate density, the density of the substrate alone ignoring the resin, can then be computed as

$$\rho_{\text{sub}}^{\text{post}} = \frac{\rho_{\text{sub}}^{\text{pre}}}{1 - \alpha} \quad (2.16)$$

with corresponding porosity

$$\phi^{\text{post}} = 1 - \frac{1}{1 - \alpha} \frac{\rho_{\text{sub}}^{\text{pre}}}{\rho_{\text{fiber}}} \quad (2.17)$$

where $1 - \alpha$ is the fractional volumetric change of the composite appearing in Table 2.2.

Experimental results should fall somewhere between the bounds provided by the fully incompressible and fully compliant cases, and near to that predicted by the second case, partially compliant, which approximates the through thickness compliance of these materials. However, it is important to note that these felts are not perfectly compliant through the thickness, resisting compression/shrinkage to some degree, which is not captured by the model.

Table 2.2: Limiting cases of volume change during processing.

Case	Description	ϵ_{TT}	ϵ_{IP}	$1 - \alpha$
1	Fully Incompressible	0	0	1
2	Partially Compliant	$\phi^{\text{pre}}\epsilon_R$	0	$1 - \phi^{\text{pre}}\epsilon_R$
3	Fully Compliant	$\phi^{\text{pre}}\epsilon_R$	$\phi^{\text{pre}}\epsilon_R$	$[1 - \phi^{\text{pre}}\epsilon_R]^3$

Results

Pre-process substrate density is plotted against post-process density in Figure 2.5. Felt samples that were compressed during processing are denoted by filled markers while uncompressed ones are denoted by open markers. Note that here and elsewhere resin shrinkage

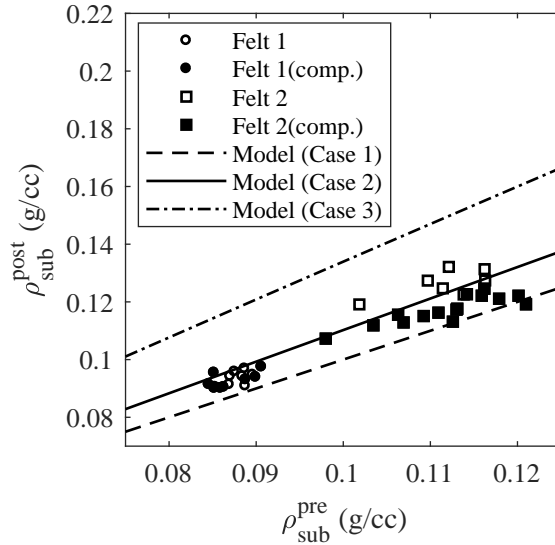


Figure 2.5: Change in substrate density during processing.

and fiber density are assumed to be nominal ($\epsilon_R = 0.10$ and $\rho_{fiber} = 1.395$ g/cc, respectively). Therefore, variation around the modeled lines is expected. Experimental results are near to expected bounds with most samples falling between Case 1 and Case 2. Because the fiber substrate provides some resistance through the thickness, shrinkage tends to be somewhat less than the theoretical value predicted by Case 2. Pre-process compression of the substrate may further suppress shrinkage (as deflection of the material increases, its stiffness increases). Compressed samples of Felt 2 shrunk less than the uncompressed samples. However, the relationship is less clear for Felt 1 samples. Note that one sample falls below Case 1, an apparent decrease in density. In this sample, negligible through thickness shrinkage (less than 1%, likely due to relatively high compression of that sample) was offset by a slight increase in the diameter. Note that in plane expansion was observed in another C-PICA investigation related to this work [90]. In that work, a 4-inch square sam-

ple fabricated using the SOTA method shrunk during curing but expanded during drying, yielding a 2% increase in area post-processing.

2.2.4 Properties of the Resin

Methodology

The resin undergoes both mass and volume change during processing. Mass loss occurs due to evaporation of solvent and/or reaction products. Volume change occurs as the solution expands due to heating and contracts due to crosslinking. Shrinkage is coupled to substrate compliance and mold boundary conditions. That is, any resistance to shrinkage reduces volume contraction leading to lower resin density. An incompressible substrate resists shrinkage as does bonding to a mold wall. Post-process resin density, $\rho_{\text{resin}}^{\text{post}}$, is a globally-averaged quantity such that

$$m_{\text{resin}} = \rho_{\text{resin}}^{\text{post}} \phi^{\text{post}} V_{\text{sub}}^{\text{post}} \quad (2.18)$$

where m_{resin} is the total resin mass in the TPS after processing. Note that $\rho_{\text{resin}}^{\text{post}}$ is averaged over the porous, not bulk, volume and is not a local resin density, which is somewhat higher due to clumping around the fibers.

With known properties of the pure resin, its cured density, ρ_{R} , and volumetric shrinkage, α_{R} , the density of the thermally expanded resin prior to shrinkage can be computed,

$$\rho'_{\text{R}} = [1 - \alpha_{\text{R}}] \rho_{\text{R}} \quad (2.19)$$

This quantity is not the physical density of the resin solution itself, which contains solvents that are removed in processing, but rather a theoretical quantity representing the density of solids that will remain in the processed material. Assuming the mass of solids present

within the substrate does not change as the material shrinks, this density is equivalent to

$$\rho'_R = \frac{m_{\text{resin}}}{\phi^{\text{pre}} V_{\text{sub}}^{\text{pre}}} \quad (2.20)$$

This approach assumes that the resin binds to the fibers instantaneously at the curing temperature, and then no further movement of solids into or out of the substrate occurs. In reality, curing occurs gradually and solvent evaporation carries away some resin throughout the process. Combining Equations 2.18–2.20, leads to an expression for the post-process resin density in the composite material,

$$\rho_{\text{resin}}^{\text{post}} = [1 - \alpha_R] \frac{\phi^{\text{pre}} V_{\text{sub}}^{\text{pre}}}{\phi^{\text{post}} V_{\text{sub}}^{\text{post}}} \rho_R \quad (2.21)$$

Substituting for volumetric shrinkage yields

$$\rho_{\text{resin}}^{\text{post}} = \frac{1 - \alpha_R}{1 - \alpha} \frac{\phi^{\text{pre}}}{\phi^{\text{post}}} \rho_R \quad (2.22)$$

Applying the limiting cases in Table 2.2 predicts constant $\rho_{\text{resin}}^{\text{post}}$ for Cases 1 and 2, respectively, $[1 - \epsilon_R]^3 \rho_R$ and $[1 - \epsilon_R]^2 \rho_R$. Using properties from Table 2.1, predicted densities are 0.22 g/cc and 0.24 g/cc, respectively.

Results

Results are compared to predicted values in Figure 2.6. Note that actual resin density does appear constant across substrate density as predicted with no dependence on pre-process compression. However, its value falls somewhat below the estimated values. Mean resin density across the samples is 0.187 g/cc, which is 15% below the Case 1 model and 22% below the Case 2 model. The discrepancy could be due to additional resin loss in the TPS during curing. Recall that ρ_R is drawn from pure resin samples. While the curing profiles were identical, it is possible that the pure resin samples solidified earlier in the cycle than

the TPS samples. The individual resin plugs were in direct contact with the aluminum tooling and were much smaller in volume than the resin container used to process these TPS samples. Thus, the TPS materials may have heated more slowly and experienced evaporation for a longer period of time, losing a larger amount of solids through the process. Practically then, this method provides an upper bound on resin density, one where little or no resin evaporation occurs. Previous results for the same material processed in a small, closed mold, which presumably better limited evaporation, agree more closely with prediction. In those samples, $\rho_{\text{resin}}^{\text{post}}$ was computed as 0.233 g/cc [90], which falls between values predicted by Cases 1 and 2.

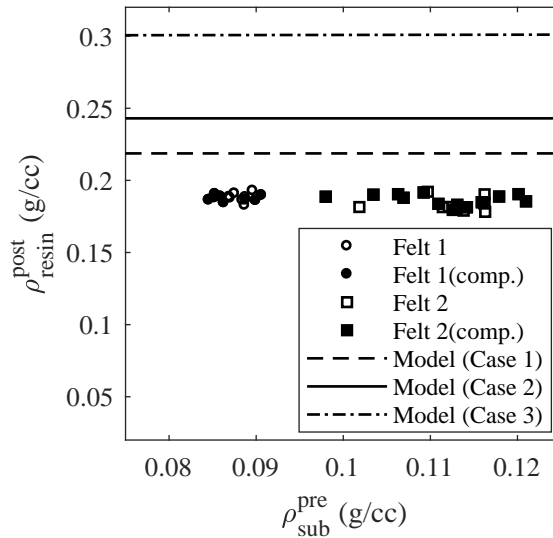


Figure 2.6: Post-process resin density plotted against pre-process substrate density.

2.2.5 Properties of the Composite Ablative Material

Methodology

Selected properties of the final TPS material — composite, or virgin, density, ρ_{comp} ; resin mass fraction, w_{resin} ; and char yield, Y_{comp} — can be computed from post-process substrate and resin densities, fiber density, and resin char yield. Assuming no substrate mass loss,

char mass is

$$m_{\text{char}} = m_{\text{sub}} + Y_{\text{R}}m_{\text{resin}} \quad (2.23)$$

Equations 2.18 and 2.23 reduce TPS properties to functions of density, which are summarized in Table 2.3. Note that post-process porosity, which appears in each model equation, is listed for clarity. These quantities can be related back to pre-process substrate density and the known resin properties using Equations 2.7, 2.16, 2.17, and 2.22 and material shrinkage from Table 2.2.

Table 2.3: Expressions for TPS property estimation.

Property	Symbol	Expression	Model
Post-process porosity	ϕ^{post}	$\frac{V_{\text{pore}}^{\text{post}}}{V_{\text{sub}}^{\text{post}}}$	$1 - \frac{\rho_{\text{sub}}^{\text{post}}}{\rho_{\text{fiber}}}$
Virgin density	ρ_{comp}	$\frac{m_{\text{sub}} + m_{\text{resin}}}{V_{\text{sub}}^{\text{post}}}$	$\rho_{\text{sub}}^{\text{post}} + \rho_{\text{resin}}^{\text{post}}\phi^{\text{post}}$
Resin mass fraction	w_{resin}	$\frac{m_{\text{resin}}}{m_{\text{sub}} + m_{\text{resin}}}$	$\frac{\rho_{\text{resin}}^{\text{post}}\phi^{\text{post}}}{\rho_{\text{comp}}}$
Composite char yield	Y_{comp}	$\frac{m_{\text{char}}}{m_{\text{sub}} + m_{\text{resin}}}$	$\frac{\rho_{\text{sub}}^{\text{post}} + Y_{\text{R}}\rho_{\text{resin}}^{\text{post}}\phi^{\text{post}}}{\rho_{\text{comp}}}$

Results

Virgin density is plotted against pre-process substrate density in Figure 2.7. Note that nominal resin density, $\rho_{\text{resin}}^{\text{post}}$, was assumed equal to the mean of all present samples, rather than that estimated from Equation 2.22, to better reflect actual results. Experimental data agrees well with that predicted by the model equation. Results largely fall near to Case 2 as expected, though the density of a few coupons was lower than anticipated (falling below the line for Case 1). These samples were compressed, likely reducing shrinkage and yielding results more in line with the rigid substrate. Virgin density increases with substrate density, though not one-to-one. The increase in substrate density is partially offset by reduced pore volume and, thus, less infused resin. Resin mass fraction also shows good agreement

with prediction with most results again between Cases 1 and 2, though a few compressed samples more closely align with Case 1 (Figure 2.8). Here, the relationship between mass fraction and substrate density is not linear. Resin mass fraction decreases with substrate density due to both increased substrate mass and reduced porosity.

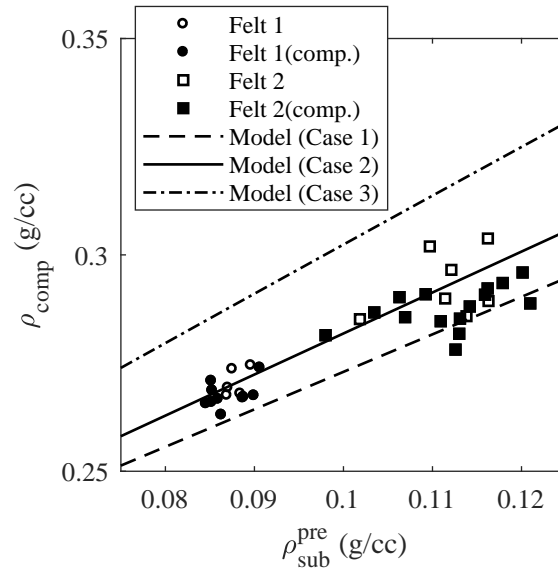


Figure 2.7: Virgin density as a function of pre-process substrate density.

Char yields vary more significantly from predicted values (Figure 2.9). An analysis of underlying resin char yield suggests a difference between the two substrate materials. Using Equation 2.23, Y_R was computed from the experimental data as $Y_R = 55.8 \pm 3.8\%$ for Felt 1 and $49.2 \pm 3.0\%$ for Felt 2. Ranges reflect the 95% confidence intervals (CIs). The discrepancy may stem from processing the two felts in different containers. While both were cured at the same time in the same oven, the temperature profiles would have varied slightly between the containers due to oven non-uniformity.

Applying the mean Y_R to its respective material yields better fits (Figure 2.10). Model predictions are those of Case 2 and bounds reflect the 95% CIs on Y_R . Large variation in resin char yield produces corresponding spread in the char yield of the composite itself.

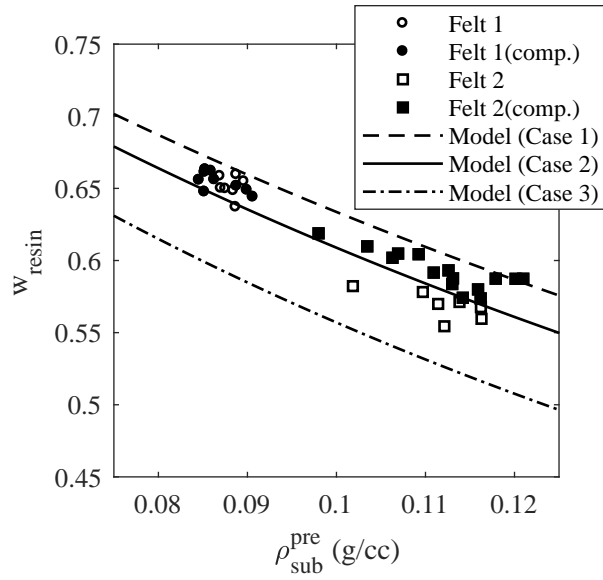


Figure 2.8: Resin mass fraction as a function of pre-process substrate density.

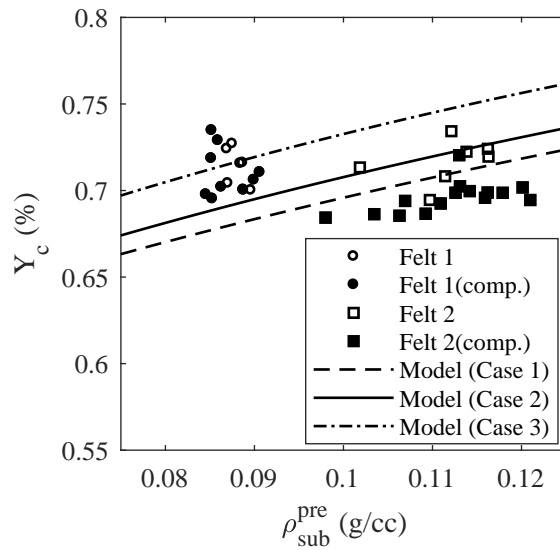


Figure 2.9: Composite char yield as a function of pre-process substrate density.

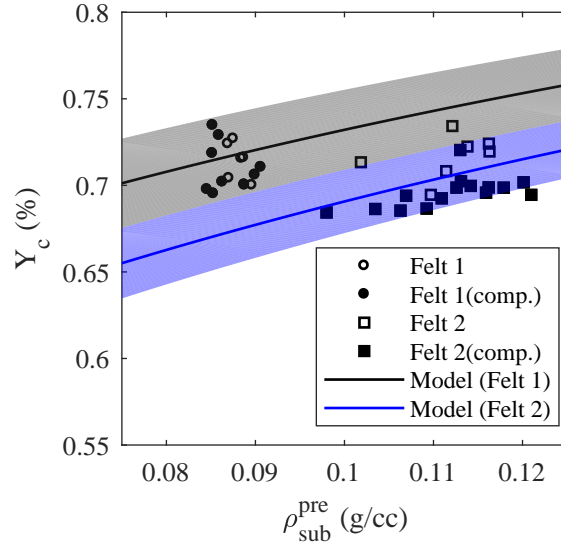


Figure 2.10: Composite char yield with Y_R computed separately for each felt.

2.3 Uncertainty Analysis

2.3.1 Methodology

Bounds on final TPS material properties can be computed from an analysis of input uncertainties. For this work, a known substrate with nominal thickness, t_{sub} , areal density, $\rho_{\text{sub}}^{\text{areal}}$, and fiber density, ρ_{fiber} , was assumed. Known resin properties include one-dimensional cure shrinkage, ϵ_R , post-process density in the composite, $\rho_{\text{resin}}^{\text{post}}$, and char yield, Y_R . All input variables, X_i , are assumed to fall within a range $[X_i - \Delta X_i, X_i + \Delta X_i]$. For example, substrate thickness ranges from $[t_{\text{sub}} - \Delta t_{\text{sub}}, t_{\text{sub}} + \Delta t_{\text{sub}}]$ where Δt_{sub} denotes the one-sided, symmetric deviation. Bounding values are indicated as the upper (+) or lower (-) bound. Flexible substrates are considered here, though a similar approach could be used for rigid materials.

The substrate is compressed to a uniform, constant starting thickness equal to the minimum substrate thickness,

$$t_{\text{sub}}^{\text{pre}} = t_{\text{sub}} - \Delta t_{\text{sub}} \quad (2.24)$$

to avoid gaps with the tool. From Equation 2.5,

$$(\rho_{\text{sub}}^{\text{pre}})^+ = \frac{(\rho_{\text{sub}}^{\text{areal}})^+}{t_{\text{pre}}} \quad (2.25)$$

$$(\rho_{\text{sub}}^{\text{pre}})^- = \frac{(\rho_{\text{sub}}^{\text{areal}})^-}{t_{\text{pre}}} \quad (2.26)$$

Volumetric shrinkage is allowed to vary between zero (Case 1) and $\phi^{\text{pre}}\epsilon_{\text{R}}$ (Case 2). This range approximately captures uncertainty observed in the experimental results. Shrinkage is numerically represented as

$$\alpha = c_s \phi^{\text{pre}} \epsilon_{\text{R}}, \quad c_s = [0, 1] \quad (2.27)$$

Nominal shrinkage is set to the middle of this range, $c_s = 0.5$. Bounds on final TPS properties are obtained by first rewriting the model equations in Table 2.3 in terms of independent parameters to remove cross-correlation. Deviations are then applied to each independent property in order to maximize (or minimize) the target property. Expressions for virgin density and resin mass fraction are rewritten by substituting Eqs. 2.16, 2.17, and 2.27 into the model equations and collecting terms:

$$\rho_{\text{comp}} = \left[1 + \left(\frac{\rho_{\text{sub}}^{\text{pre}}}{\rho_{\text{fiber}}} - 1 \right) c_s \epsilon_{\text{R}} \right]^{-1} \left[\rho_{\text{sub}}^{\text{pre}} + \rho_{\text{resin}} \left(1 - \frac{\rho_{\text{sub}}^{\text{pre}}}{\rho_{\text{fiber}}} \right) (1 - c_s \epsilon_{\text{R}}) \right] \quad (2.28)$$

$$w_{\text{resin}} = \left\{ \left[\rho_{\text{resin}}^{\text{post}} \left(\frac{1 - c_s \epsilon_{\text{R}}}{\rho_{\text{sub}}^{\text{pre}}} + \frac{c_s \epsilon_{\text{R}} - 1}{\rho_{\text{fiber}}} \right) \right]^{-1} + 1 \right\}^{-1} \quad (2.29)$$

Noting that $\rho_{\text{resin}}^{\text{post}} \phi^{\text{post}} = w_{\text{resin}} \rho_{\text{comp}}$ and $\rho_{\text{sub}}^{\text{post}} = (1 - w_{\text{resin}}) \rho_{\text{comp}}$, composite char yield can be rewritten as a function of resin mass fraction and resin char yield,

$$Y_{\text{comp}} = (Y_{\text{R}} - 1) w_{\text{resin}} + 1 \quad (2.30)$$

Applying appropriate deviations to the independent parameters to maximize (or minimize) these properties yields the set of expressions for nominal and bounding values in Table 2.4.

Table 2.4: TPS properties: nominal and bounding values.

Property / Bound	Expression
ρ_{comp}	$\left[1 + \left(\frac{\rho_{\text{sub}}^{\text{pre}}}{\rho_{\text{fiber}}} - 1\right) 0.5\epsilon_{\text{R}}\right]^{-1} \left[\rho_{\text{sub}}^{\text{pre}} + \rho_{\text{resin}} \left(1 - \frac{\rho_{\text{sub}}^{\text{pre}}}{\rho_{\text{fiber}}}\right) (1 - 0.5\epsilon_{\text{R}})\right]$
ρ_{comp}^+	$\left[1 + \left(\frac{(\rho_{\text{sub}}^{\text{pre}})^+}{\rho_{\text{fiber}}^+} - 1\right) \epsilon_{\text{R}}\right]^{-1} \left[(\rho_{\text{sub}}^{\text{pre}})^+ + \rho_{\text{resin}}^+ \left(1 - \frac{(\rho_{\text{sub}}^{\text{pre}})^+}{\rho_{\text{fiber}}^+}\right) (1 - \epsilon_{\text{R}})\right]$
ρ_{comp}^-	$\left[(\rho_{\text{sub}}^{\text{pre}})^- + \rho_{\text{resin}}^- \left(1 - \frac{(\rho_{\text{sub}}^{\text{pre}})^-}{\rho_{\text{fiber}}^-}\right)\right]$
w_{resin}	$\left\{ \left[\rho_{\text{resin}}^{\text{post}} \left(\frac{1 - 0.5\epsilon_{\text{R}}}{\rho_{\text{sub}}^{\text{pre}}} + \frac{0.5\epsilon_{\text{R}} - 1}{\rho_{\text{fiber}}} \right) \right]^{-1} + 1 \right\}^{-1}$
w_{resin}^+	$\left\{ \left[(\rho_{\text{resin}}^{\text{post}})^+ \left(\frac{1}{(\rho_{\text{sub}}^{\text{pre}})^-} - \frac{1}{\rho_{\text{fiber}}^+} \right) \right]^{-1} + 1 \right\}^{-1}$
w_{resin}^-	$\left\{ \left[(\rho_{\text{resin}}^{\text{post}})^- \left(\frac{1 - e_{\text{R}}}{(\rho_{\text{sub}}^{\text{pre}})^+} + \frac{e_{\text{R}} - 1}{\rho_{\text{fiber}}^-} \right) \right]^{-1} + 1 \right\}^{-1}$
Y_{comp}	$(Y_{\text{R}} - 1) w_{\text{resin}} + 1$
Y_{comp}^+	$(Y_{\text{R}}^+ - 1) w_{\text{resin}}^- + 1$
Y_{comp}^-	$(Y_{\text{R}}^- - 1) w_{\text{resin}}^+ + 1$

2.3.2 Results

Statistical Distributions

Results were generated for the C-PICA formulation based on Felt 1. Resin shrinkage and char yield were taken from Table 2.1. Additional input values and uncertainties are listed in Table 2.5. Substrate thickness was obtained from tolerances listed in the material datasheet for Felt 1. Areal density and post-process resin density were both drawn from the above experimental results. Areal density reflects the observed bounds of Felt 1 (Figure 2.3). Post-process resin density was derived from the bounds of all samples (Figure 2.6). Nomi-

nal values were set to the midpoint of their respective ranges. As above, fiber density was assumed to be in the range 1.395 ± 0.055 g/cc.

Table 2.5: Inputs to uncertainty application, nominal values and one-sided deviations

Category	Property	Nominal	One-sided deviation	Units
Substrate	t_{sub}	0.88 (2.235)	0.08 (0.203)	in (cm)
	$\rho_{\text{sub}}^{\text{areal}}$	0.194	0.006	g/cm ²
	ρ_{fiber}	1.395	0.055	g/cc
Resin	$\rho_{\text{resin}}^{\text{post}}$	0.187	0.007	g/cc

Bounds were computed from the expressions in Table 2.4 using the parameter values in Table 2.5. Property distributions were generated using a Monte Carlo simulation with 10 million points. Input variables were randomly selected from uniform distributions. Histograms of the output distributions are shown in Figures 2.11–2.13. Nominal values are denoted by the solid vertical line. Bounds indicate both the maximum extents computed from Table 2.4 and the range containing 95% of the data. Virgin density (Figure 2.11) and resin mass fraction (Figure 2.12) are close to normally distributed, albeit with flattened centers and truncated tails. Virgin density ranges from 0.259 g/cc to 0.287 g/cc with 95% of the data falling between 0.264 g/cc and 0.282 g/cc. Resin mass fraction ranges from 0.603 to 0.661 with 95% of the data in the range 0.614–0.652.

Composite char yields have a larger variance (Figure 2.13). Yields from 68%–70% are roughly equally probable due to the large uncertainty in resin char yield. This spread may explain the large variance observed in experimental char yields. Char yields range from 65.6% to 72.3% at the bounds while 95% of the data fall in the range 66.8%–71.1%. Nominal values and ranges for all properties are summarized in Table 2.6.

Table 2.6: Uncertainty results for C-PICA fabricated from Felt 1

Property	Units	Nominal	Full Range	95% of Data
ρ_{comp}	g/cc	0.273	[0.259, 0.287]	[0.264, 0.282]
w_{resin}	—	0.633	[0.603, 0.661]	[0.614, 0.652]
Y_{comp}	—	0.690	[0.656, 0.723]	[0.668, 0.711]

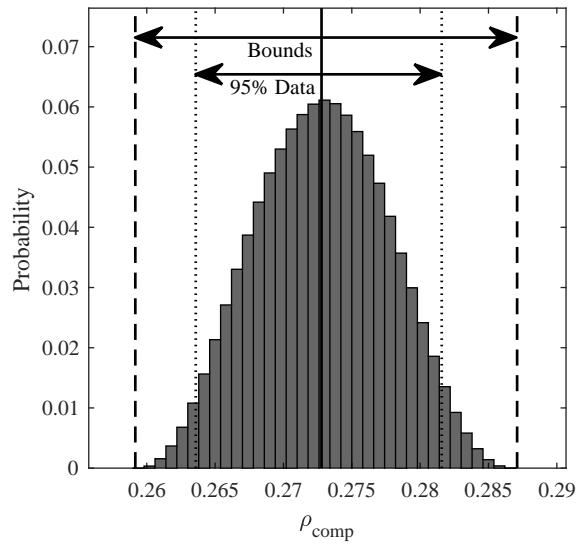


Figure 2.11: Distribution of virgin density with bounds.

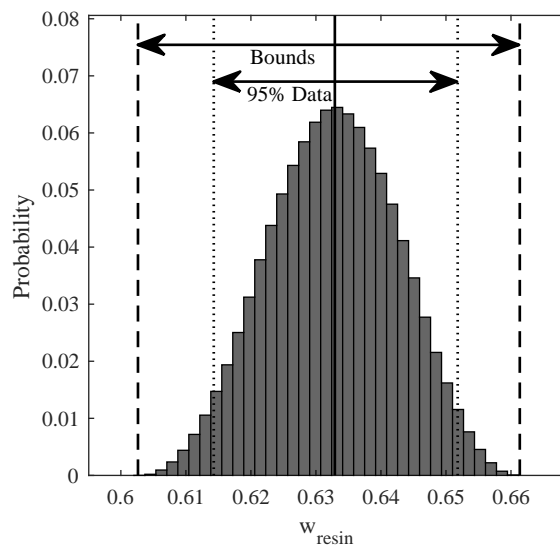


Figure 2.12: Distribution of resin mass fraction with bounds.

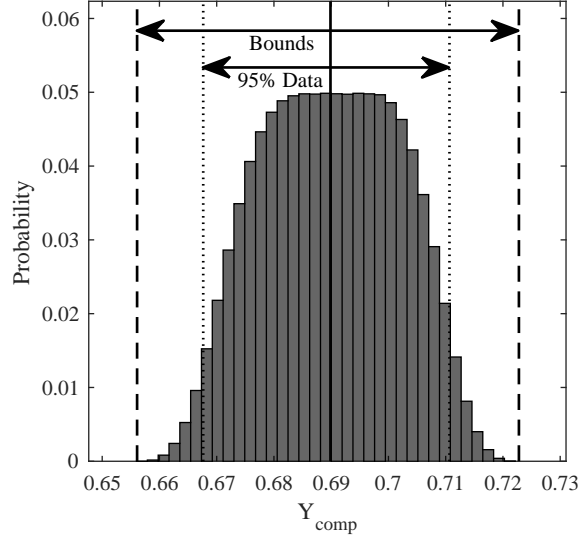


Figure 2.13: Distribution of char yield with bounds.

Linear Correlations

Linear correlations between individual input uncertainties and the output TPS properties were computed from Monte Carlo results using a linear regression analysis [51]. For the i th input, X_i , and j th output, Z_j , the correlation coefficient is calculated over k points,

$$r_{i,j} = \frac{\sum_k (X_{i,k} - \bar{X}_i) (Z_{j,k} - \bar{Z}_j)}{\left[\sum_k (X_{i,k} - \bar{X}_i)^2 \sum_k (Z_{j,k} - \bar{Z}_j)^2 \right]^{1/2}} \quad (2.31)$$

where \bar{X}_i and \bar{Z}_j are the respective means of input i and output j . Computed coefficients are shown in Table 2.7. Output variables appear in the leftmost column with correlations

Table 2.7: Correlation coefficients relating input and output uncertainties

	ρ_{fiber}	$\rho_{\text{sub}}^{\text{areal}}$	$\rho_{\text{resin}}^{\text{post}}$	α	Y_{R}
ρ_{comp}	0.066	0.33	0.79	0.52	0.00041
w_{resin}	0.04	-0.46	0.52	-0.72	0.00015
Y_{comp}	-0.016	0.18	-0.21	0.29	0.92

appearing across the corresponding row. Resin char yield has almost no effect on the variability of ρ_{comp} and w_{resin} , a logical result given that these properties are not functionally

related. Fiber density does not contribute significantly to variability in any of the output properties. Resin density is the primary driver in virgin density variability with secondary contributions from shrinkage and substrate areal density. Resin mass fraction is negatively correlated with shrinkage and areal density with α having the largest relative contribution. Unsurprisingly, variability in Y_{comp} is strongly correlated to variability in Y_{R} with smaller contributions from the other inputs.

2.4 Summary

In this chapter, a methodology was presented for estimating properties of a fiber substrate ablator from its constituents. This approach is well suited for conceptual design of thermal protection systems. The numerical approach presented herein improves on the traditional method, which relies on significant experimental characterization, by representing TPS materials through a limited set of constituent properties. This approach does not eliminate the need for experimental characterization. However, it does reduce experimental burden in the early stages of design allowing rapid iteration on ablator composition. The approach can be used to estimate both nominal properties and their uncertainties, which can aid thermal modeling and probabilistic heatshield design.

Substrate properties were estimated using a filamentary analog model of the material. This model, combined with resin parameters, allowed closed-form expression of composite TPS properties. Process shrinkage was estimated for three substrates of varying compliance. A model was then presented for estimating the resin density in the composite material from the properties of the pure resin and known shrinkage. Finally, virgin density, resin mass fraction, and char yield were computed from post-process substrate density, fiber density, resin density, and resin char yield.

Thirty eight one-inch cylindrical samples of a conformal carbon felt-phenolic TPS material were processed for comparison to numerical predictions. Two different fiber substrates, spanning densities from 0.08–0.12 g/cc, were used. Mass and dimensions of the

pre-process substrate and the post-process TPS samples were measured to obtain substrate density, resin density, virgin density, and resin mass fraction. These samples were then charred in a furnace to obtain char yields. Experimental results generally showed good agreement with prediction. Most data fell between predictions for the idealized incompressible (Case 1) and partially compressible (Case 2) substrates — a result of some through thickness resistance to dimensional change. Pre-process compression appeared to increase resistance to shrinkage, skewing results toward Case 1 in a few samples. Post-process resin density deviated from that predicted by the model due to resin evaporation during curing. Nonetheless, resin density was constant across substrate density as expected. Char yield showed a large degree of spread around the predicted values due to apparent variability in resin char yield. The material based on Felt 1 exhibited a slightly higher resin char yield than that based on Felt 2. Considering each population separately provides better agreement with the model equation. Differences in temperature profile may have contributed to this discrepancy, and further analyses to that end are suggested in Chapter 7.

Analysis of the model equations yielded bounds on the TPS properties which are useful for understanding material variability. Monte Carlo simulation confirmed the validity of these bounds. A linear regression analysis was then used to estimate the contributions of input variability to that of the output properties. Variability in virgin density was driven primarily by variability in resin density with additional contributions from substrate density and material shrinkage. Resin mass fraction was driven by material shrinkage with secondary contributions from resin and areal densities. Uncertainty in the composite char yield was strongly correlated to variability in resin char yield with lesser effects from the other inputs.

The results of this chapter are foundational to both the experimental work of Chapter 3 and the computational methodology of Chapters 4–6. TPS fabricated in the study of Chapter 3 are validated against predicted properties and uncertainties presented here. These models are then used to estimate TPS properties in Chapter 5, the final design task of the

methodology, allowing evaluation of the final heatshield material.

CHAPTER 3

VACUUM INFUSION PROCESSING OF A LOW DENSITY CONFORMAL ABLATOR

3.1 Introduction

This chapter describes a new vacuum infusion process (VIP) for conformal ablators that improves efficiency over the SOTA process, reducing resin consumption and waste, equipment cost, and processing time. The closed process scales efficiently because it does not require an evacuated oven or chamber for processing, and purging and backfilling are done within the mold cavity.

The first section outlines the SOTA and discusses challenges implementing LCM for conformal ablators. VIP itself is described, including how it addresses these challenges, followed by an analysis of its advantages and limitations. The next section discusses the experimental methodology in this investigation, briefly outlining preliminary development processing small, flat coupons of C-PICA using a partial implementation of VIP. Then, the remainder of the chapter discusses a full demonstration of VIP scaled up to larger, curved tiles approximately 0.5 meters across. Vent pressure, curing conditions, and drying configuration were varied during the course of the current investigation. Resulting TPS materials were characterized through visual inspection, dimensional analysis, and property evaluation. The fabricated tiles were well-infused in depth with voidage limited to the external surfaces. Material properties generally aligned well with predictions from the material model of Chapter 2 though differences in post-process resin density, stemming from resin evaporation during curing, appeared to cause some variation. Accounting for this difference yielded similar variation across all tiles.

The process demonstrated here was developed for conformal ablators but could be ex-

tended to other TPS materials as well. VIP can be applied to materials possessing a similar substrate density and resin viscosity, such as PICA and other low density rigid substrate ablators, with little modification. Higher density substrates, which are less permeable and pose greater resistance to resin flow, may benefit from pressurizing the resin delivery above atmospheric pressure, which was the limit here. Less dilute resins, with correspondingly higher viscosity, could be preheated to similarly assist flow.

3.2 Motivation

Conventional conformal ablator processing, described in Section 1.2.2, relies on a modified liquid impregnation technique where a matched mold containing a fiber substrate is slowly infiltrated under vacuum in a large, open container. The process is slow (up to several hours for large parts) and inefficient (producing significant excess resin waste). Additionally, certain resin systems, like phenolic, require a vacuum oven or chamber to provide inert atmosphere.

Direct injection of resin into a closed mold — as in a LCM process — appears to be a solution to these shortcomings. However, unlike typical structural composites which are compacted during processing to yield high fiber fraction and low porosity, conformals are lightweight and porous by design. Substrates are lightly compressed during processing (yielding only $\sim 10\%$ fiber fraction by volume), and resins are substantially diluted to control loading and allow infusion at lower pressures. While conformal ablators are porous on a microscopic scale, larger macroscopic voids must be prevented. Large regions without resin offer little thermal protection. No pyrolysis occurs without resin, and no reinforcing carbonaceous char is formed. Thus, voids reduce energy absorption and may compromise the structural integrity of the TPS. Finally, most ablative resins oxidize in air, requiring inert atmosphere during processing.

Combined, these factors pose unique challenges for LCM of a conformal ablator:

1. Air removal must be achieved without compaction, which compresses and shrinks

entrapped air bubbles in a typical LCM process. Vacuum infusion typically addresses this problem by fully evacuating the cavity prior to mold filling, and a cavity pressure of 1 torr is suggested to ensure low voidage in VIP [61]. However, such a low pressure could easily fall below the vapor pressure of these diluted resins and cause boiling along the flow front leading to bubble entrapment and unpredictable flow.

2. Resin expansion and evaporation during curing and drying must be accommodated while also facilitating removal of evaporated solvent. Lengthy heating cycles more or less require that these occur without manual intervention.
3. The interior of the mold must provide inert atmosphere during curing and drying to avoid resin oxidation.

These challenges were addressed by the VIP developed in this investigation, which is described next.

3.3 Vacuum Infusion Processing

3.3.1 Overview of the Process

The VIP developed in this investigation was designed to: (1) constrain the part to near net shape with minimal compaction of the fiber substrate, (2) facilitate air removal while maintaining vent pressure above the resin vapor pressure, and (3) allow resin expansion and solvent evaporation during heat treatment within a closed, inert atmosphere. Like the SOTA process, VIP proceeds in three steps: resin infusion (also called mold filling), curing, and drying. Unlike the SOTA process, VIP is carried out within a closed mold.

Figure 3.1, which was originally presented as Figure 1.15 in Chapter 1, depicts each of the processing steps. The substrate is first draped and enclosed within a double-sided rigid mold with a single gate and a single vent. In Step 1, vacuum is applied at the vent to evacuate internal air. Vent pressure is maintained above the resin vapor pressure to prevent boiling. Resin, driven by atmospheric pressure, enters the substrate at the gate.

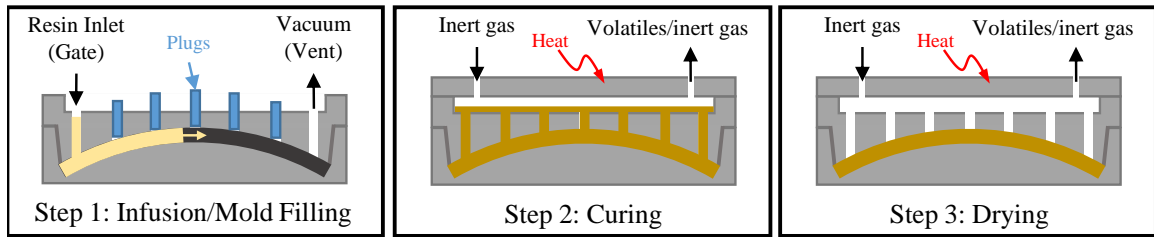


Figure 3.1: Vacuum infusion processing of conformal ablators.

Full saturation is critical to material quality. Trapped air will lead to partial saturation and voidage. Evacuation of the cavity limits this risk but not completely. Because the vacuum level is relatively high, residual internal air must be continuously vented during filling. If an unsaturated region of the mold is blocked from the vent by advancing resin flow, air cannot be properly evacuated, becoming trapped and forming a void in the material. Proper gate and vent locations, the subject of the methodology in Chapters 4 and 5, are crucial to venting, ensuring that blockage does not occur during mold filling.

Once the substrate is saturated, plugs sealing the mold top are removed and a secondary lid installed to enclose the chamber above the part. In Step 2, this assembly is then heated to cure the resin. As the material heats up, some resin expands into the upper chamber and cures there. After curing, the excess is removed and discarded, the secondary lid is re-installed, and the mold is subjected to a second heating cycle to remove residual solvent and dry the part in Step 3. Inert gas is flowed through the mold during both curing and drying, preventing resin oxidation and carrying away volatiles generated during processing.

3.3.2 Comparison to Conventional Processing

Compared to SOTA processing, VIP improves efficiency, reducing resin consumption and waste while streamlining clean up and disposal. It also eliminates the need for an atmosphere-controlled oven, or chamber, and a large vacuum pump to evacuate it, simplifying processing equipment and facilitating larger tile sizes. Additionally, VIP allows numerical simulation of the mold filling process, which can inform mold design and ensure high ma-

terial quality. The two processes are compared and contrasted in the following section with examples illustrating improvements over the SOTA.

Examples are partially based on an analysis of a representative heatshield, shown in Figure 3.2, based on the MSL forebody geometry. The outer mold line (OML) is a 4.5-meter diameter, 70 degree sphere-cone [26, 91]. The tile layout was modified to a symmetric layout with a single nose tile and two concentric rings of tiles, approximately 1 meter across, covering the flank. Like MSL, TPS thickness, t_{TPS} , in this configuration is uniformly 1.25 inches (3.18 cm) across the aeroshell. Typical conformal ablative TPS properties are assumed based on experimental results in this investigation: pre-process substrate porosity, $\phi^{\text{pre}} = 0.93$, through thickness shrinkage, $\epsilon_{\text{TT}} = 0.06$, and 20% resin thermal expansion by volume.

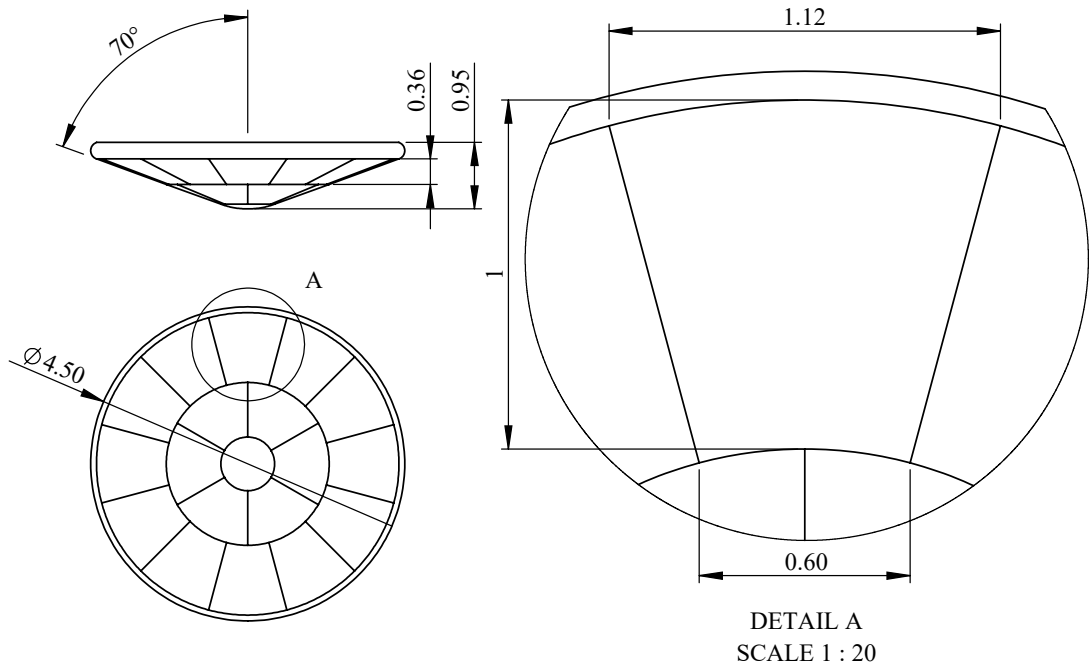


Figure 3.2: Example heatshield and tile geometry based on MSL (dimensions in meters).

Other aspects of the comparison (processing time and clean up) draw on experience with both methods during this work. Oven and vacuum pump costs were compared using data for commercially available equipment. Tooling cost for processing the 0.5-meter tiles

in this investigation was compared with that from a similarly-sized part made using the SOTA process. Finally, computational methods for simulating infusion were contrasted.

Resin Consumption and Waste

Accounting for shrinkage, the pre-process substrate thickness for the example heatshield is 1.33 inches (3.38 cm). In VIP, additional shims made of the same substrate material add approximately 10% to this thickness, 1.46 inches (3.71 cm) in total. For the SOTA process, no shims are added, and a 0.5 inch (1.27 cm) thick, matched mold encloses the substrate with a custom tray matching its outer dimensions. Shoulder tiles, which are a small percentage of the overall volume, are neglected in this example.

The tile in the outer ring, highlighted in Detail A in Figure 3.2, has a final bulk volume of 29.5 L. With VIP, resin is injected directly into the part with little to no excess, consuming an amount of resin approximately equal to the pre-process porous volume (32.0 L). In contrast, the SOTA method consumes nearly twice that volume of resin (55.2 L) due to large empty spaces above and below the curved part. A larger mold could occupy more of this empty volume, and thus displace more resin, but some amount of open space is still required around the mold to allow resin to flow freely.

Higher curvature only exacerbates the problem. The SOTA process more than doubles the resin consumption of VIP for the inner ring and nose tiles. VIP yields reductions of 62% and 68%, respectively, for these parts. Table 3.1 summarizes resin consumption for each of the three tiles. For the entire heatshield (excluding the shoulder), VIP reduces resin consumption by 50% over the SOTA process, a total volume of 544 L. With resin solutions on the order of \$10 dollars per liter, material cost is reduced by several thousands of dollars.

Excess resin complicates clean up in SOTA processing as the surrounding resin must be chipped away to expose the mold and enclosed part, which takes a significant amount of time and generates a substantial mess because the resin is brittle, producing small dust particles that coat the work area. VIP shortens and simplifies clean up because the mold

Table 3.1: Resin consumption for the example heatshield.

	Final Bulk Volume (L)	Resin Consumption		
		SOTA (L)	VIP (L)	Reduction (%)
Nose Tile	15.2	51.4	16.6	68%
Inner Ring Tile	21.5	61.8	23.3	62%
Outer Ring Tile	29.5	55.2	32.0	42%
Full Heatshield	498	1085	541	50%

is not encased in resin. The little excess residing in the expansion chamber above the part is easily discarded after disassembling the secondary lid. For the 0.5-meter tiles fabricated in this investigation, clean up time was about two-thirds less than a similar volume part processed in the SOTA method (20 minutes versus upwards of an hour for the conventional process).

In the example, cured resin occupies a volume of approximately 1302 L in the SOTA or 649 L in VIP. Of that total, 463 L remains within the tiles while the rest resides externally and must be cleaned up post-curing. Note that in VIP some of the resin waste is contained in the shims. Resin waste is approximately 839 L in the SOTA and 186 L in VIP, a factor of four difference. Discarding this material would require four 55-gallon hazardous waste drums in the SOTA. VIP requires not quite one full drum. In addition to cured resin waste, the volume of evaporated solvent, which is collected during processing, is also reduced in VIP.

Figure 3.3 contrasts resin consumption, demolding, and waste for the two processes. Relative consumption and waste are based on the analysis above. Photos depict the aftermath of demolding two TPS parts of similar volume. Note the significant mess resulting from SOTA processing. In summary, for this example, VIP reduces:

1. Resin consumption by 50%
2. Resin waste by 78%

3. Clean up time by approximately two-thirds

Results from recent processing of a large, curved C-PICA panel using the SOTA process suggest that waste may be even more than that estimated here. That work, partially described in Ref. [47], used approximately 80 L of resin solution to process a 21 L panel, about one-third more than that estimated above for the inner ring tile, which is a similar volume, and about three times that of the comparable VIP process.

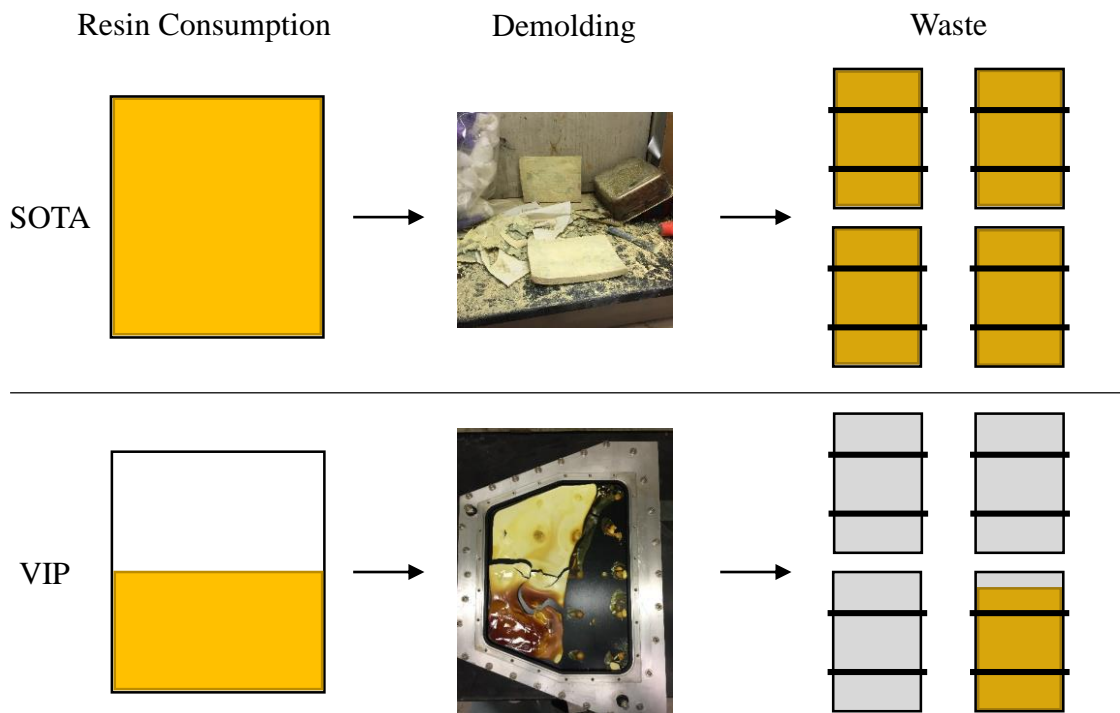
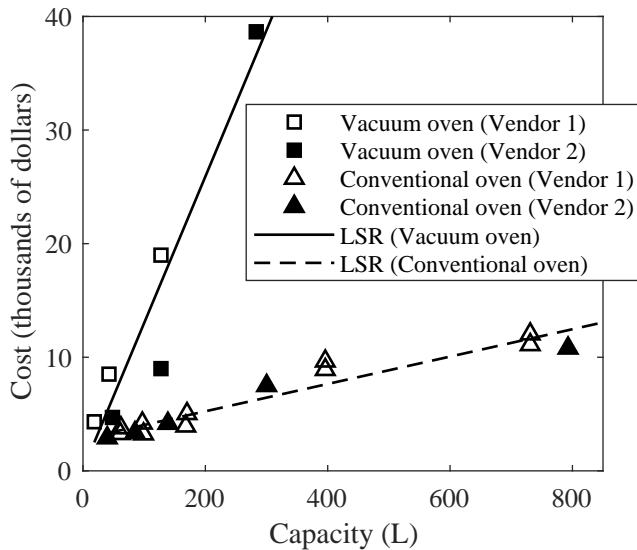


Figure 3.3: Improvements in resin consumption, clean up, and waste compared to the state of the art.

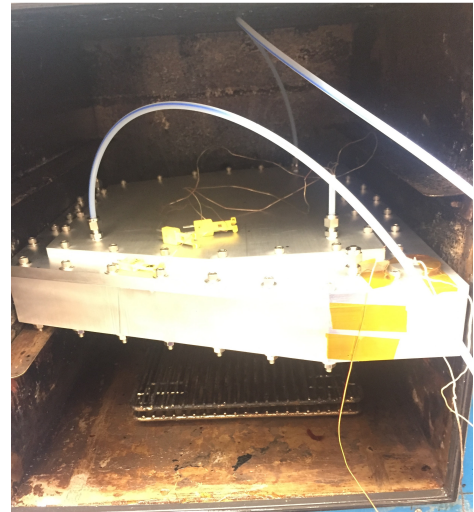
Processing Equipment and Associated Impacts

Oven TPS can be processed in a conventional, rather than vacuum, oven in VIP because the mold interior provides inert atmosphere. The switch to a conventional oven reduces cost and limits long term oven degradation. Figure 3.4 explores these impacts. Figure 3.4(a) compares publicly available cost data for two well known vendors of both conventional and

vacuum ovens, Vendor 1¹ and Vendor 2². Both product lines allow programmable temperature control, which is necessary for curing and drying. A linear least squares regression (LSR) of the data is shown for each oven type. Conventional ovens are both cheaper and available in larger capacities. Marginal cost is an order of magnitude smaller for conventional ovens (\$12 vs. \$130 per additional liter on average) and maximum capacities are more than twice as large (800 L vs. 300 L). For the largest vacuum oven, cost is five times that of the similarly-sized conventional oven. Larger oven capacity may facilitate production of larger tiles.



(a) Cost comparison between vacuum and conventional ovens



(b) Interior of an oven used to process phenolic-based TPS

Figure 3.4: Open processing impacts both oven cost and wear on interior surfaces.

In addition to higher cost, open processing exposes the oven to evaporated resin and solvent requiring frequent cleaning and damaging interior surfaces. Figure 3.4(b) shows discoloration and flaking inside an oven used to process a phenolic-based TPS material. Solvents are contained within the mold in VIP and not exposed to the surrounding oven.

¹Thermo Scientific™, Lindberg/Blue M™ and Heratherm™ product families, URL: <https://www.fishersci.com/>, accessed: October 22, 2018

²CascadeTek™, TVO and TFO product families, URL: <https://www.cascadetek.com/>, accessed: October 22, 2018.

The SOTA process may use a vacuum chamber placed inside a conventional oven as an alternative to a vacuum oven, but this configuration does not significantly improve the picture. The vacuum chamber adds additional equipment cost while similarly limiting part size. Given the same conventional oven, VIP still allows a larger maximum tile size and avoids the extra piece of equipment.

Vacuum Pump VIP further improves efficiency because only the mold interior must be evacuated, rather than the entire vacuum oven or chamber, which can accelerate purging and backfilling (a reduction in labor) or reduce pump capacity (a reduction in equipment cost). Figure 3.5 investigates the latter alternative. On the left, pump cost is compared against pumping capacity for a well known pump vendor³. A linear LSR model fitted to the data was used to estimate pump costs for the two processes as a function of the tile surface area, A_{comp} , in Figure 3.5(b).

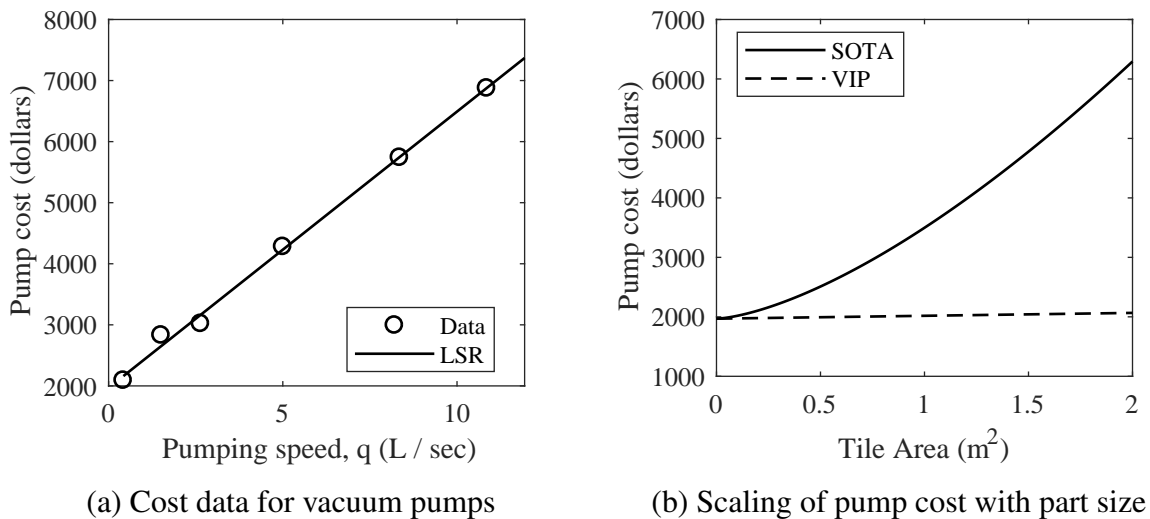


Figure 3.5: Estimated vacuum pump cost compared for both processes.

The theoretical required pumping speed, q_{pump} , was computed from the equation [92],

$$q_{pump} = \frac{V_{evac}}{T_{evac}} \ln \frac{P_{atm}}{P_{vac}} \quad (3.1)$$

³Welch Vacuum, DuoSeal Product Family, URL: <https://welchvacuum.com/products/duoseal-1400>. Accessed: October 22, 2018.

where V_{evac} is the volume to be evacuated, T_{evac} is the evacuation time, P_{atm} is atmospheric pressure, and P_{vac} is the desired vacuum pressure. Equation 3.1 describes evacuation of a chamber in the range 1–1000 mbar. The computed pumping speed, q_{pump} , was assumed equal to the pump specification, which assumes no leaks, no flow restrictions through tubing, and no additional sources of gas. As such, the calculation provides an estimate under ideal conditions. Evacuation time was fixed to an arbitrary value ($T_{\text{evac}} = 10$ min) and vacuum pressure to a value typical of current processing, which is within the range of applicability of Equation 3.1.

For VIP, evacuated volume, V_{evac} , was assumed to be equal to the tile volume,

$$V_{\text{evac}} = A_{\text{comp}} t_{\text{TPS}} \quad (3.2)$$

where tile thickness, t_{TPS} , is again 1.25 inches (3.18 cm). For the SOTA, V_{evac} was equal to

$$V_{\text{evac}} = (A_{\text{comp}})^{3/2} \quad (3.3)$$

This expression assumes that the vacuum oven or chamber scales similarly in all three dimensions, driven by tile area, leading to the cubic relationship. Figure 3.5(b) suggests little difference in cost below 0.5 m² but a significant increase for the SOTA at larger sizes. Pump cost could be offset by extending evacuation time in the SOTA process. However, VIP limits both evacuation time and pump cost, which further improves scale up.

Mold/Tooling While a rigorous evaluation of tooling costs between the two processes has not been performed, two examples are presented here for comparison. Tooling for the curved tiles processed in this work, with a 0.40 m x 0.56 m footprint, consisted of three aluminum pieces that cost \$4700 to procure, machine, and coat. The SOTA scale up mentioned earlier processed a tile with a footprint of approximately 0.63 m x 0.60 m using the tooling shown in Figure 3.6 [47]. A third part not shown in the figure, the tank,

was required for holding resin during infiltration. Combined, these parts cost between \$8000 and \$9000 to manufacture. The SOTA method benefits from not needing to fully enclose the substrate. VIP requires additional width around the perimeter of the part to accommodate a joint between the two sides of the mold. Thus, while the overall tooling was of a similar size between these two examples, the SOTA produced a larger tile. However, cost was also slightly more for SOTA processing. Therefore, it appears that tooling cost is of the same order of magnitude between the two processes, and it may in fact be slightly cheaper for VIP.

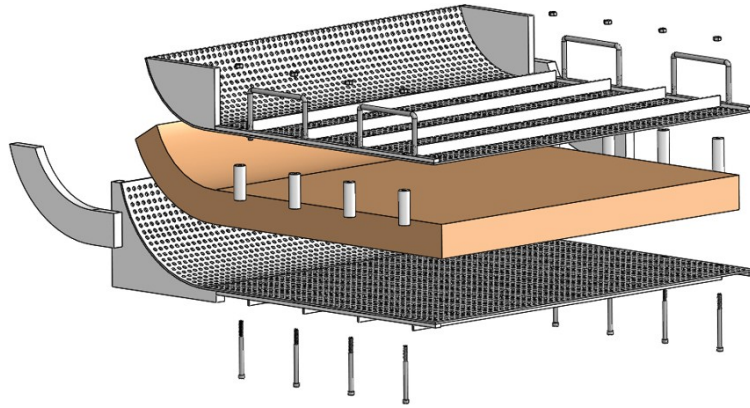


Figure 3.6: Tooling design for the state of the art process (Credit: Beck, et al. [47]).

Processing Time

In addition to reducing clean up time, VIP shortens the length of infusion and, potentially, curing and drying. Shorter cycle times can not only speed up production of a heatshield but can also allow faster evaluation of alternative material formulations during early stage development. Infusion is sped up because infiltration is driven by a large pressure gradient unlike the open process where resin slowly seeps into the fiber substrate as it fills the surrounding container. The 0.5-meter tiles described later in this chapter, which were approximately 4L in volume, were infused in 5–9 minutes. Similarly sized TPS processed using the SOTA process required about an hour to infuse, which is about an order of mag-

nitude longer. Totaling infusion and clean up, VIP required approximately 25–30 minutes versus over 2 hours for the SOTA.

Speeding up curing and drying, which account for the bulk of total processing time, can further benefit cycle time. There is less resin and, therefore, less thermal mass in VIP. Thus, while not investigated in this thesis, it may be possible to accelerate temperature ramping as well as shorten the hold time at the final curing temperature relative to the SOTA. Drying might also be accelerated using higher gas flow rates, which are feasible given the smaller cavity volume of the closed process.

Part Quantity

In this thesis, VIP was carried out on single parts only, and scale up focused on increasing part size, rather than quantity. While a higher quantity capability matching the SOTA has yet to be demonstrated, VIP will likely scale at least as well given the arguments above: larger and cheaper ovens, smaller vacuum pumps, and a more efficient process. Ideas for simultaneously processing multiple tiles using VIP are suggested in Chapter 7.

Computational Design

The mold filling process of VIP can be simulated using a numerical application of Darcy's law, which leads to two advances over the state of the art: (1) it allows mold design without experimental trial and error, and (2) it can generate relevant process metrics such as infusion time. While modeling the current process to the same end may be possible, it would appear to be significantly more complicated. Absent the strong pressure gradient that dominates flow in LCM, the open process is influenced by other, no longer negligible, forces (e.g., gravity and capillary forces).

Adaptations of the classical Lucas-Washburn equation, which describes capillary flow through parallel tubes [93], have been used to model imbibition of porous media [94] including that of fibrous fabrics [95]. In the latter, Pezron, et. al. vertically suspended pieces

of fabric and then brought them into contact with an infiltrating liquid. The authors found that absorption was dominated by two distinct filling processes, in depth and along the surface, not described by Lucas-Washburn alone. Infiltration of a conformal ablator adds complexity in both geometry (three-dimensional, curved shapes) and boundary conditions (multiple interfaces between the substrate and surrounding empty space). Thus, modeling the SOTA process appears to be significantly more complicated. Regardless of the possibility, such an approach is not used currently. Therefore, the availability, and heritage, of Darcy's law simulations for modeling infusion in VIP is a distinct advantage over the state of the art.

3.3.3 Limitations of the Process

While VIP is well-suited to the low viscosity resins and high porosity, high permeability substrates typical of conformal ablators, the relatively small pressure gradient of vacuum alone may not be suitable for infiltrating higher density TPS or higher viscosity resin solutions. A supplemental study in Appendix B investigated the range of applicability of VIP for similarly formulated materials (rayon-based carbon substrates infused with phenolic resin) by varying substrate density and resin viscosity. Mold filling was simulated on an approximately 1 m x 1 m tile using the approach in Chapters 5 and 6. Infusion times less than 8 hours, the length of a standard work day, were considered feasible.

With the current resin formulation, VIP is feasible up to a pre-process substrate density of $\sim 0.2\text{--}0.25$ g/cc depending on part thickness. Based on the constitutive model of the previous chapter, such a composition would yield nominal virgin density around 0.4 g/cc. The applicable range shrinks as resin dilution decreases (and viscosity increases). For the base resin without dilution, which possesses a viscosity over eight times that of the current formulation, substrate density is limited to approximately 0.1 g/cc. Post-process resin density would be correspondingly higher without dilution. Despite limitations of the current implementation, VIP could likely be extended to higher density TPS materials

through additional modifications discussed in Chapter 7.

3.3.4 Summary

Vacuum infusion processing of conformal ablators leads to improvements in efficiency — reducing waste, labor, and cost compared to the state of the art — and introduces a computational design capability for conformal ablative heatshields. The entire process is closed, rather than open. Resin is injected directly into the substrate with little excess, and air removal is achieved without compacting the substrate ensuring a low density, mass efficient TPS material. Combined with a switch to a conventional oven, as well as smaller evacuated volumes, these advances enable quick and efficient fabrication of large tiles.

While a tiled example was considered here, VIP may also be suited to small, single piece heatshields (~1.5 m diameter). Flexible substrates can facilitate such a single piece design, but SOTA processing would again lead to large inefficiencies. With VIP, the entire forebody (or aft) heatshield could be formed and processed using a single mold yielding significant reductions in resin consumption and waste.

3.4 Experimental Methodology

3.4.1 Material Formulation

All testing was carried out on a C-PICA formulation consisting of a low density carbon felt, Felt 1 from Chapter 2, and the phenolic resin solution also described in that chapter. Recall that the felt is nominally 0.9 in (2.29 cm) thick with a density of 0.09 g/cc. Resin loading is approximately 0.18 g/cc resulting in a TPS density of around 0.27 g/cc.

3.4.2 Overview of Development

Testing of the vacuum infusion process began with partial implementations on small samples in 2016 and 2017, culminating in scale up to the full process during 2018 (Figure 3.7). Preliminary development of the VIP process (2016) was carried out using a benchtop-sized

mold to process flat, four-inch (10 cm) square coupons. Initial testing infused carbon felt in the closed mold, but carried out curing and drying with the mold open as in the SOTA process. Properties of these materials showed good agreement with that fabricated using the SOTA method. While voids were present on external part surfaces, VIP-fabricated materials were uniformly infiltrated through the thickness. Additional testing which applied only partial, rather than full, vacuum at the vent resulted in trapped air pockets and significant in depth voidage, demonstrating the significance of vent pressure to material quality.

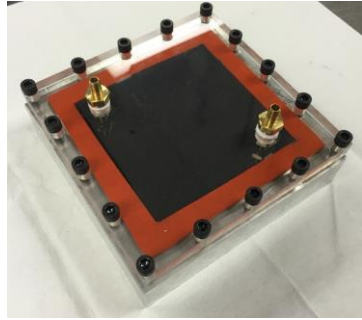

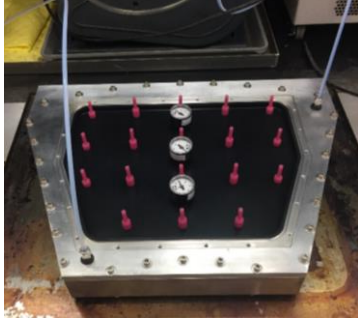
2016	2017	2018
		
<p>Infusion: closed Curing: open Drying: open</p>	<p>Infusion: closed Curing: open and closed Drying: open</p>	<p>Infusion: closed Curing: closed Drying: open and closed</p>

Figure 3.7: Overview of VIP development from initial testing to final scale up.

Subsequent testing (2017) extended VIP to alternate curing configurations (both closed and open) [90]. However, the closed curing configurations proved unsuccessful, allowing air into the mold and causing some resin oxidation. Drying was again done outside the mold, open to the oven atmosphere. Voidage on external surfaces proved to be an issue in this testing as well, but, again, most TPS materials were generally well infused in depth. The one exception was a sample cured under reduced pressure, which showed significant in depth voidage. Otherwise, bulk physical properties, virgin density and resin mass fraction, compared favorably to the standard material.

Changes were then implemented to address problems in the small scale testing. Solvent bubbles appeared at the vent during infusion, indicating bubble formation somewhere within the cavity. The gate design was changed to limit resin flashing at the inlet, which may have contributed, and an approach for regulating vent pressure was introduced to prevent boiling along the flow front. For curing and drying, instead of a completely sealed system during curing and drying, inert gas was flowed through the mold to provide positive internal pressure and prevent air ingress. With these changes, the complete VIP process was then demonstrated on large, curved tiles (2018). The remainder of this chapter discusses the results of that scale up.

3.4.3 Mold Design

Part geometry was based on the 4.5-meter diameter, 70 degree sphere-cone heatshield shown in Figure 3.2. A flank tile adjacent to the nose with an angular span of 45 degrees was selected for processing (Figure 3.8). The tile is approximately 0.56 m x 0.40 m. While

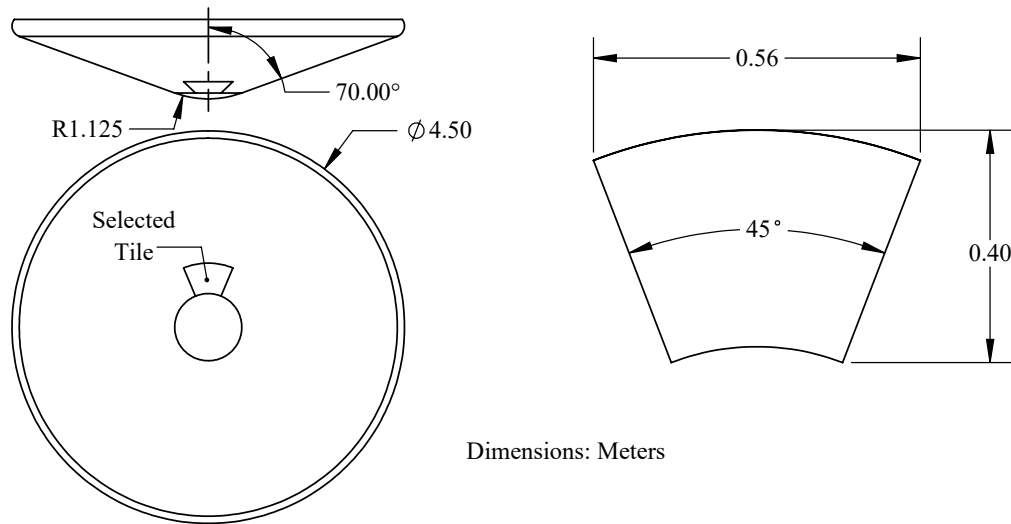


Figure 3.8: Selected tile geometry on aeroshell (left) and expanded separately (right).

tile size was limited by available oven dimensions, it still represented a significant scale up from earlier work, a 20 times increase in volume over the small samples. Furthermore, the demonstrated approach can be rather easily scaled to even larger parts given a sufficiently

large oven. Indeed, this is one of the aforementioned advantages of VIP.

A three-part aluminum mold was used to process the TPS tiles (Figure 3.9). The cavity in the bottom mold part forms the inner mold line (IML) as well as the tile edges. The core, machined in the top part, forms the OML. The distance between the two sides is 1 in (2.54 cm). A cross-section of the joint design is depicted in the figure. Offset drafts on the cavity and core side converge to zero clearance at the OML. This design, based on guidelines summarized by Rudd, et al. [61], prevents resin from escaping the cavity and flowing around the substrate (in a phenomenon called racetracking). The interior of the mold was

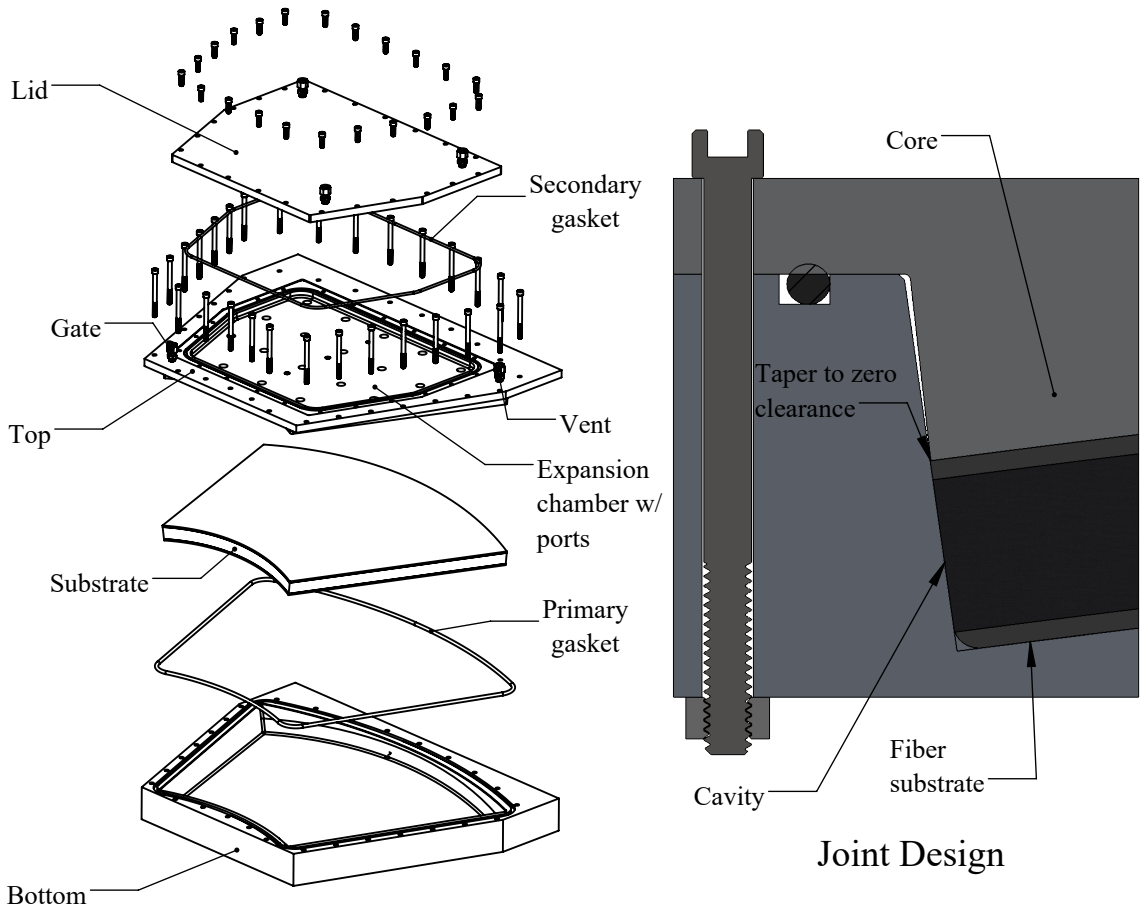


Figure 3.9: Exploded view of mold design (left) and detailed view of joint between the core and cavity sides (right)

coated with PTFE to facilitate release. A planar gasket sealed the mold around its perimeter

and was clamped by bolts spaced uniformly along its length. Gate and vent locations, optimized via the numerical simulation presented as a design example in Chapter 6, were at opposite corners of the part. For infusion, resin and vacuum lines were connected via compression fittings in the top part. Holes in the top/core (expansion ports) allowed resin expansion and volatile removal during curing and drying but were sealed during infusion by pull through plugs. The 0.5 inch (1.27 cm) diameter expansion ports, 18 holes in total, spanned the part surface in a rectangular grid, nominally spaced 3.5 in (8.9 cm) apart. Three pressure gauges also installed in the top during infusion (not depicted in the figure) were used to measure cavity pressure and identify flow front arrival. Experimental arrival times are compared to theoretical ones from the mold filling simulation in Chapter 6. For curing and drying, the lid was installed above the expansion chamber in the top part with a second gasket sealing that volume. Fittings in the lid were used to connect the mold interior to inert gas, vacuum, and exhaust during curing and drying.

3.4.4 Processing

This section outlines fabrication using the above design to infuse, cure, and dry several C-PICA tiles. Steps in the process are depicted in Figure 3.10 and described below.

Preparation

Substrates were first cut from several pieces of the raw felt by converting the curved, three-dimensional tile shape to its corresponding flat, two-dimensional pattern. For each tile, two thin felt spacers were also layered above and below the main substrate in an attempt to limit resin evaporation from the tile surface. Two cutting methods were used, a 75-W laser cutter for the thin felt materials and a water jet cutter for the main substrate (Figure 3.10, top left). The latter was employed because the laser cutter was not able to fully penetrate the thick felt. The water jet was operated at low pressure and without abrasive additives to avoid substrate contamination, and the felt was weighted down along the cutting path to

limit movement during operation. The resin solution was mixed according to the standard formulation and stored prior to processing.

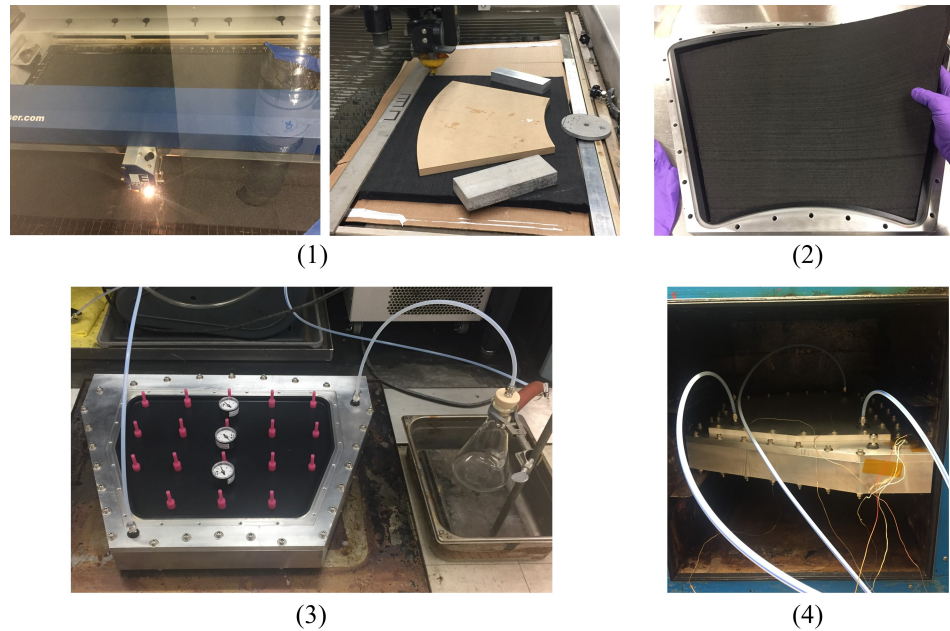


Figure 3.10: Experimental steps: (1) cutting the raw substrate, (2) draping the substrate in the mold, (3) mold configured for infusion, and (4) mold, with lid installed, in oven for curing/drying.

Substrates were then draped in the mold cavity with the main substrate sandwiched between the thin felt spacers (Figure 3.10, top right). The gasket was installed in the perimeter groove and pull through plugs inserted into the top mold part to seal the cavity. Finally, the top and bottom mold parts were bolted together. The assembly, with substrate inside, was then connected to the vacuum and resin lines (Figure 3.10, bottom left). The vacuum line was connected first to a resin trap, to collect overflow, and then to the pump. Valves in both lines controlled flow within the system. Vacuum was pulled on the cavity and maintained for several hours to remove any trapped moisture within the substrate.

Infusion

Prior to infusion, the resin line was placed at the bottom of a resin reservoir which was open at the top. Figure 3.11 depicts the experimental configuration. Vacuum was regulated

to a selected vent pressure and, then, the resin valve was opened to allow resin to flow into the cavity. With infusion started, the pressure gauges were monitored to identify flow front position, and resin arrived at the vent approximately 5–9 minutes later. At that point, the resin trap was allowed to fill slightly before shutting off flow.

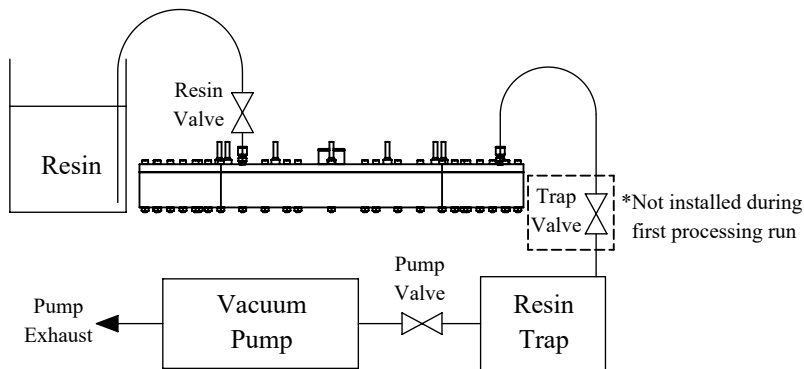


Figure 3.11: System configuration for infusion.

In the first processing run, no valve was installed between the vent and the resin trap. Therefore, resin flow was stopped by closing the resin valve, which resulted in slightly less than full saturation. Subsequent processes added a valve upstream of the trap to stop further collection allowing resin to continue filling the cavity until the internal pressure equalized with the ambient pressure before finally closing the resin valve.

Curing

After infusion, the pull through plugs were removed from the mold top, and the exposed holes were filled with additional resin to ensure that the substrate remained fully submerged. The gate and vent fittings were capped sealing those ports. The lid was then installed above the expansion chamber with the secondary gasket. Fittings in the lid were connected to the vacuum pump, an inert gas line, and an exhaust line and placed inside an oven. Figure 3.12 depicts the experimental set up, which is also shown in the bottom right of Figure 3.10.

Inert gas was flowed continually through the mold during curing to prevent resin oxida-

tion and to carry released volatiles out of the system. Evaporated resin and solvent traveled out the exhaust line and collected in a trap. Exhaust flow was regulated by a manual valve, which was periodically adjusted to maintain a desired internal pressure. However, continual monitoring was infeasible due to the length of the process resulting in imprecise control.

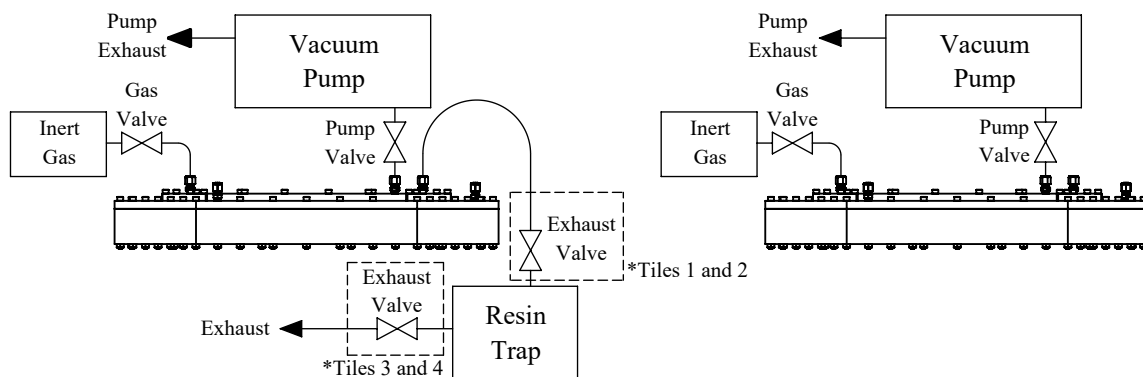


Figure 3.12: System configurations for curing (left) and drying (right).

The exhaust valve was installed upstream of the resin trap during the first two processing runs (Tiles 1 and 2) but downstream of the trap for the latter two runs (Tiles 3 and 4) in an attempt to better regulate exhaust flow and internal pressure. Both locations are depicted in the figure. After curing, the lid was removed, and excess resin was cleaned from the expansion chamber and expansion ports.

Drying

The first two tiles were dried at the same time using the conventional, open approach with the oven providing inert atmosphere. The first tile was dried outside of the mold, oriented horizontally and supported along the sides, while the second tile was dried inside the mold with the lid off to expose the part to the oven atmosphere. The latter two samples, Tiles 3 and 4, were dried within the mold with the lid installed, depicted on the right in Figure 3.12. Inert gas was flowed through the closed mold as it was during curing. However, gas and evaporated solvent were removed through the vacuum line here rather than the exhaust line, which was not used. All parts were within 2%–3% of their fully dry mass after undergoing

a standard drying profile. Shims were dried along with the tiles.

3.4.5 Test Matrix

Four C-PICA tiles were fabricated in the present testing under a variety of test conditions summarized in Table 3.2. Vent pressure was varied between runs as were curing and drying configurations. Vent pressure was nondimensionalized by the measured vapor pressure of the resin solution, discussed in the next chapter. Thus, a vent pressure less than one indicates a pressure below the solution vapor pressure, which was true of Tile 1.

Test conditions were adjusted to address issues observed in prior runs. For example, after noting resin boiling during the first infusion, vent pressure was set higher in subsequent runs in an attempt to suppress bubbling. The exhaust valve was moved downstream of the resin trap because evaporated resin collecting in the valve made flow control difficult during curing of the first two tiles.

Due to the lack of precise control, internal pressure was not well-regulated and is thus indicated by a range in Table 3.2. Curing pressure was purposely increased for the last tile in an attempt to limit resin evaporation. Drying was performed with the part open to the oven (open) or sealed within the mold (closed). The first tile was dried out of the mold, while the others were constrained inside, in order to assess any impact on the final part geometry. Tiles 3 and 4 were dried with the system sealed and, thus, represent a full implementation of VIP.

Table 3.2: Matrix of test conditions.

Tile No.	Infusion	Curing		Drying	
	Vent Pressure (non-dimensional)	Internal Pressure (psi)	Exhaust Valve Location	Open / Closed	In / Out of Mold
1	0.75	1–4	Upstream	Open	Out of mold
2	1.5	1–6	Upstream	Open	In mold
3	7.5	1–6	Downstream	Closed	In mold
4	2.5	3–10	Downstream	Closed	In mold

3.5 Analysis

3.5.1 Material Characterizations

Full tiles and small cylindrical cores removed from the tiles were characterized through visual inspection, dimensional analysis, and material property evaluation. Figure 3.13 depicts the core locations relative to expansion ports and the gate and vent. Eleven 1-inch (2.54 cm) diameter cores were removed: eight from the perimeter (one in each corner and one at the midpoint of each side) and three in the center of the part. Perimeter locations were selected due to the possibility of air entrapment in those regions. Locations 1 and

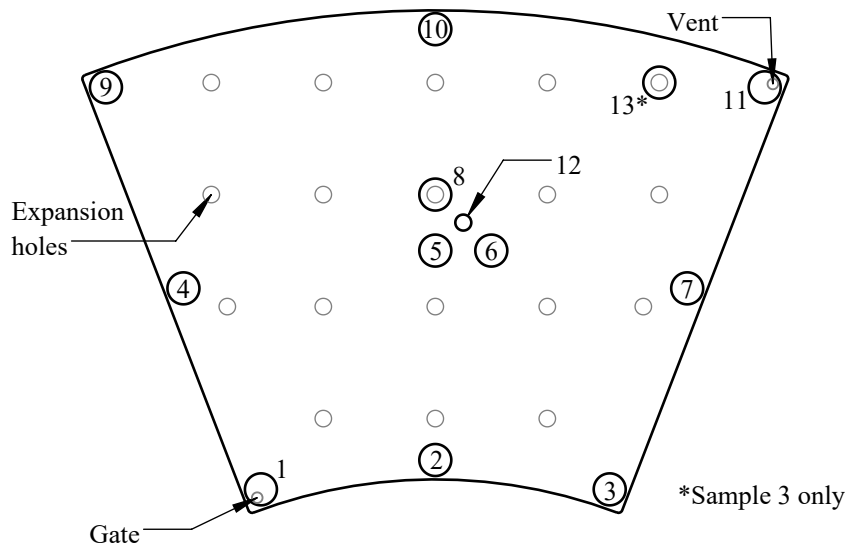
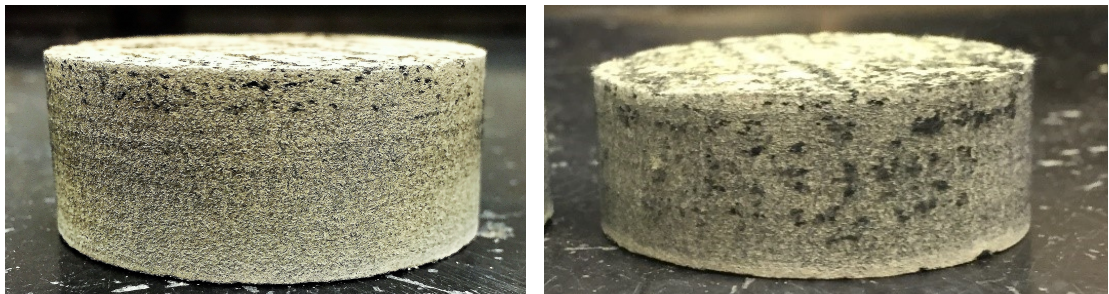


Figure 3.13: Core locations relative to part geometry and port locations.

11 were directly under the gate and the vent, respectively. Central locations were selected to investigate the effect of expansion ports on material properties. Location 8 was directly underneath one of these ports while Locations 5 and 6 were for a nearby comparison. An additional 0.5-inch (1.27 cm) core was also removed in this region (Location 12). This coupon was split in half to investigate variation through the thickness using thermogravimetric analysis (TGA). A final 1-inch (2.54 cm) diameter core (Location 13) was removed from the third tile to investigate extensive surface voidage in that area.

Visual Inspection

Visual inspection assessed the uniformity of resin infusion, presence (or absence) of voids, and substrate delamination. Cured phenolic, characteristically yellow in color, should be distributed through the thickness filling all open pore volume within the substrate. Voids, darker dry areas lacking resin, are undesirable because they offer little thermal protection. Substrate delamination, when felt layers separate due to curing stresses as the resin shrinks, compromises mechanical strength.



(a) Surface voidage due to solvent evaporation

(b) In depth voidage due to air trapped during mold filling

Figure 3.14: Void formation during processing.

Two types of voids are typically encountered during processing. Smaller voids along the top surface stem from solvent evaporation during curing (Figure 3.14, left). Premature solvent evaporation causes the resin to “collapse”, that is, to no longer be suspended in solution leaving a layer of small dry spots near the top surface. Larger voids in depth result from air entrapment during infusion (Figure 3.14, right). The latter sample exhibits both in depth and surface voidage. Note that surface voidage is frequently found on the VIP-produced parts, but it typically does not extend far in depth and can be removed in post-process machining.

Mass and Dimensions

Dry substrate masses and dimensions, both the primary substrate and shims, were recorded prior to processing. Thicknesses were measured at each corner and the midpoint of each

side and compared to the same locations on the post-process TPS tile. Perimeter dimensions were also measured pre- and post-process to estimate in plane shrinkage. Pre-process felt surface area was reduced by the average in plane shrinkage to estimate the post-process TPS surface area. Note that the full tiles were not sanded prior to measurement. Thus, computed properties were influenced by areas of voidage on the external surfaces. However, this voidage was small, typically less than 5% of the total thickness.

In contrast, cylindrical cores were sanded until all surface voidage was removed and then subjected to additional drying to ensure complete solvent removal. Sanding approximated the post-process machining that would be carried out on an actual TPS tile, leaving the well-infused in depth material. Coupon thicknesses were measured before and after sanding to estimate the depth of the evaporation layer. Masses were recorded after additional drying. The 0.5-inch (1.27 cm) core from Location 12 was sanded, dried, and then segmented in half.

Finally, full three-dimensional tile geometries were captured using a laser scanner and compared to a 0.76 inch (1.93 cm) thick tile with the nominal OML and IML curvature. Due to differences in the starting substrate thickness, final tile thicknesses also varied, but 0.76 in was selected as a baseline. Laser scanning was performed after core removal. Resulting holes, accounting for between 5% and 6% of the total surface area, were excluded from the analysis.

Composite TPS Properties

Virgin densities and resin mass fractions were estimated for both the full tiles and each of the 1-inch coupons. Tile masses were adjusted by the mass loss observed during additional drying of the cylindrical coupons. Char yields were obtained on the cylindrical coupons by heating to 1200°C in an inert furnace (3°C/min with a 30 minute hold). Assuming identical resin composition, the char yield of the composite is related to the amount of phenolic present in the material. Higher resin loading results in greater relative mass loss during

charring and a lower char yield. Thus, variation in char yield can indicate differences in resin loading.

3.5.2 Computational Methodology

Material properties were compared to expected values using the material model of Chapter 2 with additions relevant to the current investigation outlined below.

Properties of the Substrate

Substrate density was estimated by assuming constant areal density across the material and adjusting for shrinkage. That is, the areal density of the substrate in the composite was taken as the mass of the dry, pre-process felt, m_{sub} , divided by the surface area of the final composite TPS part, $A_{\text{comp}}^{\text{post}}$,

$$\rho_{\text{sub}}^{\text{areal}} = \frac{m_{\text{sub}}}{A_{\text{comp}}^{\text{post}}} \quad (3.4)$$

and the post-process substrate density as the ratio of the areal density, $\rho_{\text{sub}}^{\text{areal}}$, and coupon (composite) thickness, t_{comp} ,

$$\rho_{\text{sub}}^{\text{post}} = \frac{\rho_{\text{sub}}^{\text{areal}}}{t_{\text{comp}}} \quad (3.5)$$

Recall that post-process substrate density is that of the fiber material alone, ignoring the resin.

Because substrates were compressed between the two shims, the pre-process thickness of the substrate itself was not known precisely. An estimate was made by assuming uniform compression of both the spacers and the substrate — that is, all layers were compressed by the same fraction,

$$\epsilon_{\text{pre}} = \frac{t_{\text{cav}}}{t_1 + t_{\text{sub}} + t_2} \quad (3.6)$$

where t_{cav} is the thickness of the mold cavity, and t_1 , t_2 , and t_{sub} are the uncompressed thicknesses of the two spacers and the substrate, respectively. Thus, the pre-process sub-

strate thickness, as compressed in the mold, was estimated by:

$$t_{\text{sub}}^{\text{pre}} = \epsilon_{\text{pre}} t_{\text{sub}} = t_{\text{cav}} \frac{t_{\text{sub}}}{t_1 + t_{\text{sub}} + t_2} \quad (3.7)$$

Properties of the Composite TPS Material

Theoretical values for virgin density, resin mass fraction, and composite char yield were estimated using the expressions in Table 2.3 of Chapter 2 and compared to measured quantities. Material parameters were drawn from the experimental results of that chapter: $\rho_{\text{fiber}} = 1.395 \pm 0.055$ g/cc, $Y_{\text{R}} = 52.5 \pm 4.5\%$, and $\rho_{\text{resin}}^{\text{post}} = 0.187 \pm 0.008$.

3.6 Results and Discussion

3.6.1 Processing Results

Four C-PICA tiles were processed and characterized using the approaches described above. All infusions were carried out near room temperature with the resin solution temperature between 18°C and 23°C. Some bubble formation occurred during all infusions — bubbles were observed at the vent line prior to arrival of the main flow front. The quantity of bubbles was largest during infusion of the first tile, where a vent pressure below the vapor pressure of the resin caused boiling. Fewer bubbles were present in the latter infusions, which had higher vent pressures.

Table 3.3 summarizes relevant metrics from each process. Resin delivered to the mold cavity during infusion was obtained by comparing initial and final volumes in the resin reservoir. The volume of evaporated solution, collected in the exhaust line trap during curing, was measured at the end of curing. Based on its color, the collected solution clearly contained resin, in addition to solvent. These metrics are discussed next.

Table 3.3: Resin delivered during infusion and collected during curing.

Tile No.	Resin Delivered (L)	Evaporated Solution	
		(L)	(%)
1	3.81	0.65	17
2	3.92	0.50	13
3	3.93	0.73	19
4	3.90	0.63	16

Resin Delivery

The volume of delivered resin was nearly identical between Tiles 2–4 despite differences in vent pressure, a result indicating that the cavity was vented well and residual air was successfully evacuated throughout mold filling. Air trapped by advancing flow would leave unsaturated regions in the cavity, reducing the volume of delivered resin by the volume of the air pockets. Therefore, resin volume would depend on air density in the cavity and, thus, vent pressure. That is, in a poorly vented mold, higher vent pressure leaves more residual air in the cavity resulting in larger trapped pockets and less delivered resin. Instead, in this testing, delivered resin volumes were similar, for all but the first tile, suggesting little difference in infiltration at the present vacuum levels.

Infusion of Tile 1 was adversely affected by both low vent pressure and the lack of a valve between the vent and the resin trap. Boiling along the flow front likely caused significant bubble entrapment within the cavity. Resin flow was shut off upstream of the mold, then vacuum was released at the resin trap. Resin in the vent line flowed back into the cavity but not enough to fully saturate the substrate resulting in less delivered resin.

Evaporated Resin Solution

Resin evaporation was less for Tile 2 (13% of total resin volume) than the other tiles (16%–19% of total resin volume), a result that appears to be correlated to the curing conditions. The valve was placed upstream of the trap during curing of Tiles 1 and 2 and downstream of the trap for Tiles 3 and 4. Evaporated solution collected inside the valve and constricted

flow in the upstream location during processing of Tile 2, which made flow control somewhat challenging but may have helped to limit evaporation. The valve was moved to the downstream location to avoid this issue, but this configuration led to overall higher gas flow rates which may have contributed to more evaporation despite higher internal pressures. Differences in resin loss appeared to alter the post-process resin density in the TPS, which is discussed in the following sections.

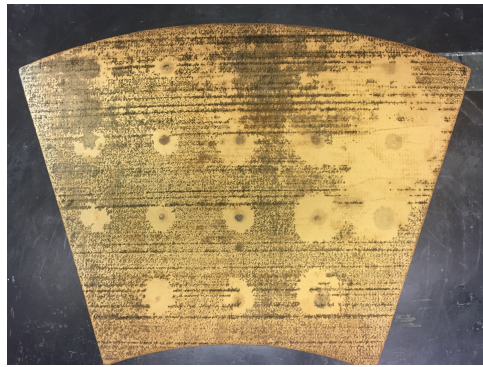
3.6.2 Full Tiles

Visual Inspection

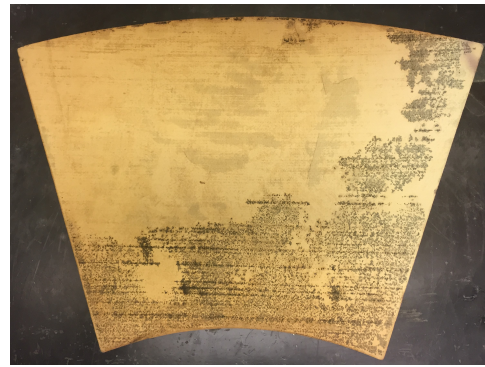
Figure 3.15 shows the front (OML) and back (IML) of the TPS tiles post-processing. Surface variation typical of VIP is evident. Front views are oriented with the gate in the bottom left and the vent at the top right while the back views are flipped with the gate in the bottom right and the vent in the top left. Photos of Tiles 3 and 4 were obtained after core removal and, thus, resulting holes are visible. Differences in coloration are apparent both within each tile as well as between tiles. Tile 1 was markedly darker than the other samples due to drying outside of the mold. Tiles 2–4, dried inside the mold, remained lighter in color. Within individual parts, there were several irregularly-shaped stains which may be from solvent and/or resin byproducts collecting on part surfaces. Differences in coloration did not appear to affect material properties.

Surface voids appear to stem from the two sources identified earlier, resin evaporation during curing and bubble entrapment during mold filling, though they seem to be coupled here. Resin evaporation is evident on the OML surface of Tiles 3 and 4, both around the expansion ports and along the top edge (Figures 3.15(e) and (g)). Inert gas flowed from the inlet, at the top left, to the exhaust, at the top right, which may explain higher evaporation along the top. This type of voidage does not appear around the expansion ports in Tiles 1 and 2, which had relatively lower gas flow.

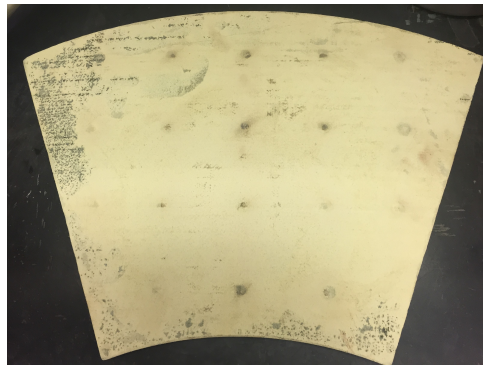
Other voids appear to be localized near the gate and adjacent sides (i.e., the bottom right



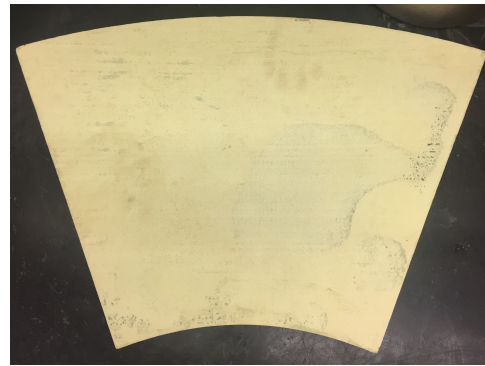
(a) Tile 1 (front)



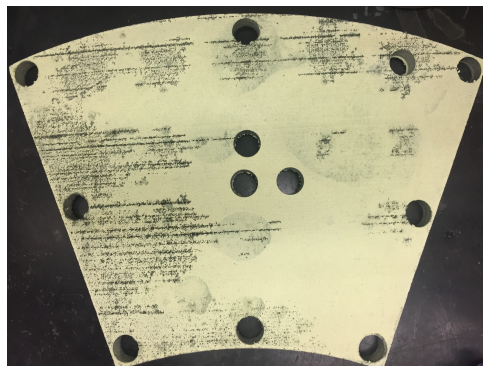
(b) Tile 1 (back)



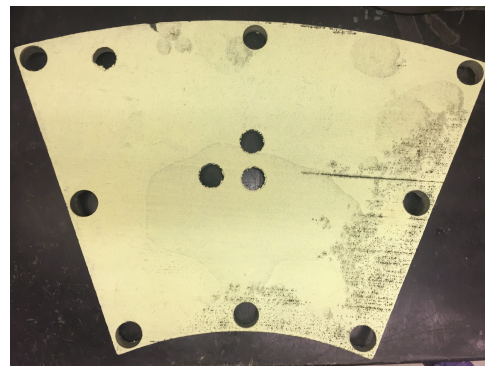
(c) Tile 2 (front)



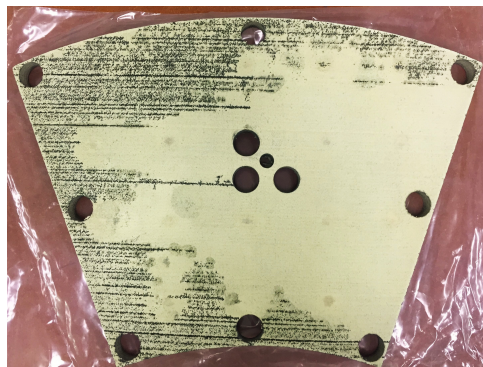
(d) Tile 2 (back)



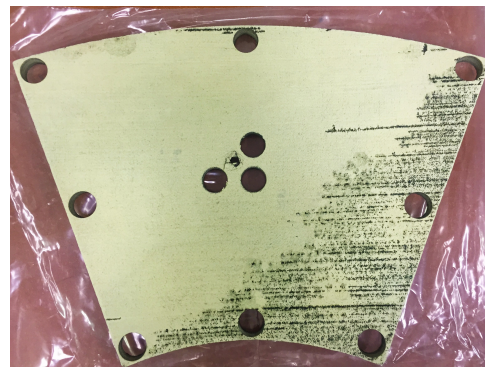
(e) Tile 3 (front)



(f) Tile 3 (back)



(g) Tile 4 (front)



(h) Tile 4 (back)

Figure 3.15: External surfaces of all tiles post-processing without sanding.

corner on the back surface). While the exact cause of this voidage is unknown, it may stem from large pore spaces at the surface of the felt trapping resin bubbles during infusion. This voidage is particularly pronounced along horizontal lines, which correspond to low points (valleys) in the felt surface. Closing the resin trap valve, which allowed the cavity to continue filling while it equilibrated with atmospheric pressure, appeared to collapse most, but not all, of these bubbles in Tiles 2–4. Tile 1 lacked the trap valve, which resulted in significantly more voidage remaining across both surfaces.

As discussed above, vent pressure did not significantly change the volume of delivered resin between Tiles 2–4. Therefore, any bubble entrapment was likely similar across these infusions. However, surface voidage is clearly more prevalent on Tiles 3 and 4 than Tile 2. Thus, it appears that resin evaporation drives most of the surface voidage. Trapped bubbles exacerbate the problem because they leave voids as the material cures providing a path for volatiles. This mechanism may help to further explain voidage appearing primarily along valleys on the surfaces of Tiles 3 and 4 (Figures 3.15(f) and (h)).

Part Shrinkage and Bulk Properties

Properties of the pre-process substrate and the final TPS tiles are presented in Table 3.4. Virgin density and resin mass fraction were computed from bulk part dimensions and compared to theoretical values. The latter quantities are given as relative differences, $r_{\rho_{\text{comp}}}$ and $r_{w_{\text{resin}}}$. In all cases, the substrate was compressed to a pre-process thickness of approximately 0.8 in (2.0 cm). Pre-process substrate density was roughly 0.1 g/cc for all tiles. Final tile thicknesses ranged from 0.75 in (1.91 cm) to 0.76 in (1.93 cm) with post-process substrate densities between 0.103 g/cc and 0.107 g/cc. Shrinkage was averaged across thickness and in plane measurements, respectively, to yield the fractional length changes shown in the table. Post-process resin density was estimated by rearranging the equation for virgin density in Table 2.3.

Shrinkage through the thickness ($\epsilon_{\text{TT}} = 0.01\text{--}0.04$) tended to be higher than in plane

Table 3.4: Properties of the pre-process substrate and the final composite TPS tile (absolute and relative to theoretical values).

Tile No.	Pre-Process Substrate	Shrinkage		Post-Process Composite TPS					
	$\rho_{\text{sub}}^{\text{pre}}$ (g/cc)	ϵ_{TT} —	ϵ_{IP} —	$\rho_{\text{sub}}^{\text{post}}$ (g/cc)	$\rho_{\text{resin}}^{\text{post}}$ (g/cc)	ρ_{comp} (g/cc)	w_{resin} —	$r_{\rho_{\text{comp}}}$ %	$r_{w_{\text{resin}}}$ %
1	0.100	-0.04	-0.01	0.106	0.191	0.283	0.62	1.3	0.8
2	0.102	-0.01	-0.01	0.105	0.191	0.282	0.63	1.5	0.9
3	0.101	-0.04	-0.02	0.107	0.183	0.276	0.61	-1.2	-0.8
4	0.099	-0.03	-0.01	0.103	0.185	0.275	0.62	-0.5	-0.3

($\epsilon_{\text{TT}} = 0.01\text{--}0.02$) but not substantially so because these felts were already fairly compressed within the mold prior to processing (about 7%–14% of the uncompressed thickness). Therefore, the substrates appeared to resist much of the through thickness shrinkage. In Chapter 2, ϵ_{TT} was estimated as $\phi^{\text{pre}} \epsilon_{\text{R}}$ for these materials. Substituting previous results for resin shrinkage and noting that $\phi^{\text{pre}} = 0.93$ in this test yields a higher predicted value ($\epsilon_{\text{TT}} = 0.06\text{--}0.14$).

Bulk virgin densities and resin mass fractions are all within about a percent of their theoretical values. Tiles 1 and 2 have slightly elevated resin loading, $\rho_{\text{resin}}^{\text{post}}$, compared to theory leading to higher ρ_{comp} and w_{resin} . In contrast, Tiles 3 and 4 have slightly reduced resin loading with correspondingly lower ρ_{comp} and w_{resin} . Between tiles, post-process resin density was approximately 3–4% higher in the first two tiles relative to the latter two, which may stem from differences in resin evaporation and shrinkage. Less resin evaporated during processing of Tile 2, which likely increased resin content in the final material. While more resin evaporated during Tile 1 processing, it also shrank more through the thickness than Tile 2, offsetting the effect on density.

Dimensional Analysis

Figure 3.16 shows deviations between Tile 4 and the nominal tile geometry (left) and their distribution (right). Contour lines denote the relative deviation. Gray areas correspond to

the drilled holes excluded from the analysis. Material directly under the expansion ports was raised around 0.06–0.12 cm relative to the surrounding area due to little substrate compression there. The average deviation was -0.06 cm indicating that the mean part thickness was less than nominal. Results for the other tiles, summarized in Table 3.5, were similar.

Table 3.5: Summary of deviations from nominal tile geometry.

Tile No.	Mean (cm)	Std. Dev. (cm)
1	-0.06	0.05
2	-0.08	0.04
3	-0.04	0.04
4	-0.06	0.04

Variation in tile thickness yield slight differences in the mean deviation, but the difference, less than half a millimeter, was small. Standard deviation was also largely the same across all tiles (0.04–0.05 cm). These results suggest that there was no improvement in dimensional tolerance drying inside of the mold (Tiles 2–4) versus outside of the mold (Tile 1). Drying inside the mold can prevent large changes to part geometry (i.e., warping) but not small ones because the tile is not fully constrained by the mold cavity after cure shrinkage. Therefore, any dimensional changes during drying were small enough to be unaffected by the mold.

3.6.3 Cylindrical Coupons

Visual Inspection

Cylindrical coupons were well infused at all locations with no observable voids through the thickness. Surface voidage did not extend significantly in depth for any of the tiles. Cores from Location 1 and Location 10 are depicted in the figures below. Location 1 was directly below the gate (Figure 3.17) while Location 10 was near to an expansion port along the top edge (Figure 3.18). Despite significant surface voidage in both locations, phenolic appeared to be uniformly distributed through the thickness with voidage limited

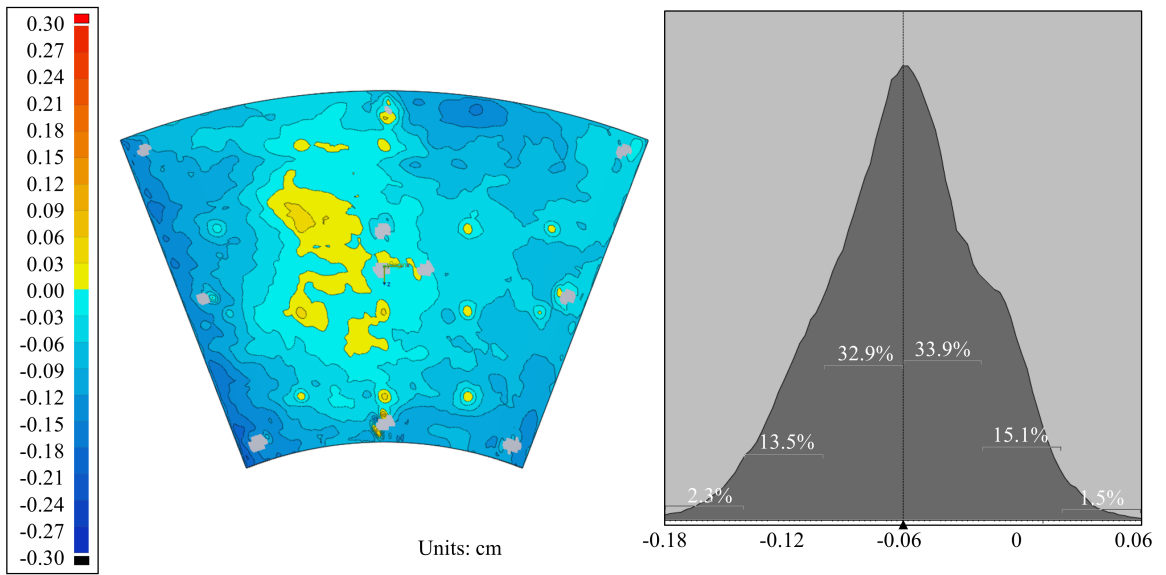


Figure 3.16: Dimensional analysis for Sample 4: map of deviations across the OML surface (left) and their distribution on both OML and IML surfaces (right).

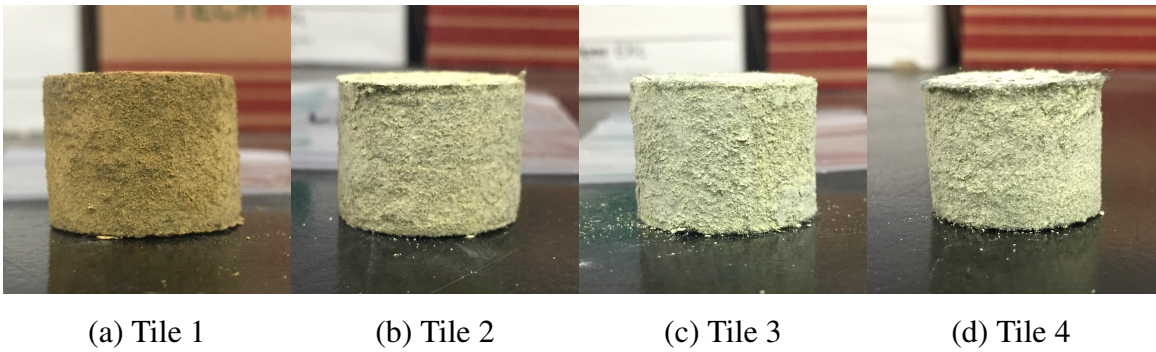


Figure 3.17: Drilled cores from Location 1.

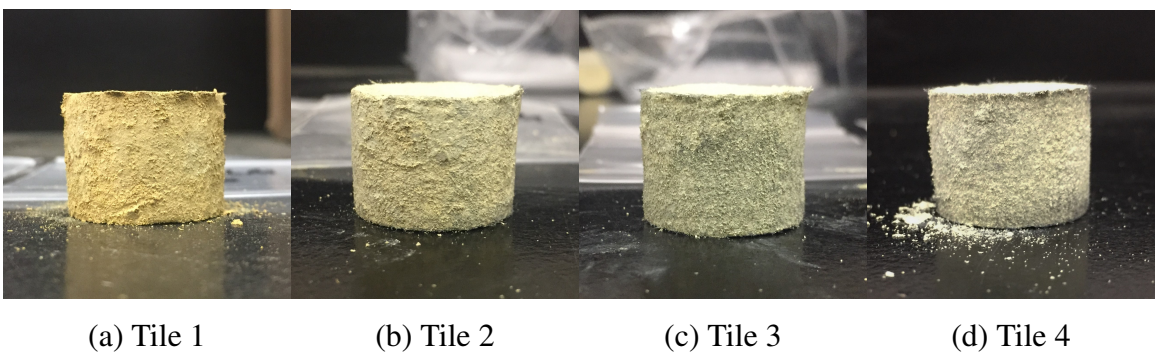


Figure 3.18: Drilled cores from Location 10.

to a thin surface layer only. Other locations demonstrated similar infusion, and no substrate delamination was found in any of the coupons.

Dimensions and Properties

Thickness Analysis Figure 3.19 (a) shows typical thickness reduction, Δt_{comp} , of 0.05–0.1 cm after removal of surface voidage, though a few coupons had larger reductions. Location 1 on Tiles 3 and 4 had the largest reduction, $\Delta t = 0.20\text{--}0.25$ cm. Location 2 on Tiles 1 and 4 and Location 8 on Tile 4 were slightly elevated with Δt_{comp} around 0.15 cm. Bubble entrapment near the gate may have contributed to increased surface voidage at Locations 1 and 2. High resin evaporation under the expansion port likely contributed to more pronounced surface voidage at Location 8 on Tile 4, but there was little effect on the other tiles at that location.

Coupon thicknesses are summarized in Table 3.6, which presents the minimum, mean, and standard deviation for each tile. Here, minimum thickness roughly dictates tile thickness after post-process machining. By this measure, Sample 2 yields the most usable material (1.83 cm). However, the other samples are only slightly thinner at minimum (1.74–1.76 cm). Mean thickness is similar across all samples ranging from 1.83 cm to 1.88 cm. Sample 2 possessed the smallest standard deviation whereas Sample 1, 3, and 4 had higher deviations. This result appears to be correlated to the overall amount of resin evaporation during processing. Again, the volume of evaporated solution was lower for Tile 2 than all other parts (Table 3.3). Higher rates of evaporation for Tiles 1, 3, and 4 may have contributed to both the lower minimum thicknesses (because evaporation occurs at the surface) and larger variances (because evaporation was not uniform across the part).

Material Properties by Location Figure 3.19(b)–(d) shows virgin density, resin mass fraction, and composite char yield for each coupon. Summary statistics for each tile, and comparison to theoretical predictions, are shown in Table 3.7. Theoretical values were

Table 3.6: Summary of coupon thicknesses for each tile.

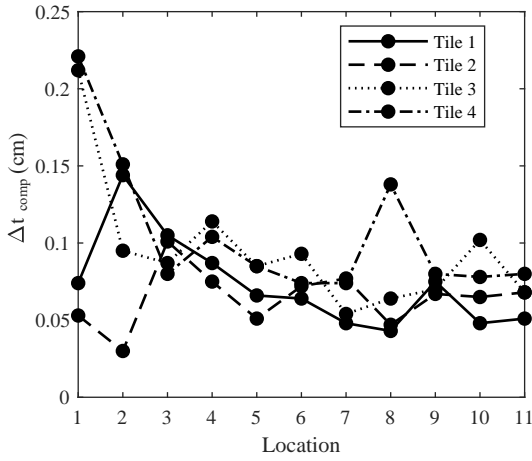
Tile No.	Minimum (cm)	Mean (cm)	Std. Dev. (cm)
1	1.75	1.84	0.04
2	1.83	1.86	0.02
3	1.76	1.88	0.05
4	1.74	1.83	0.05

computed from the mean post-process substrate density of all coupons within a tile. Standard deviations were derived from the uncertainty distributions found in Chapter 2. The relative difference between mean and nominal quantities is reported as a percentage of the theoretical value whereas standard deviations are compared as a ratio of the experimental to the theoretical span. Thus, a value of 100% indicates identical standard deviations.

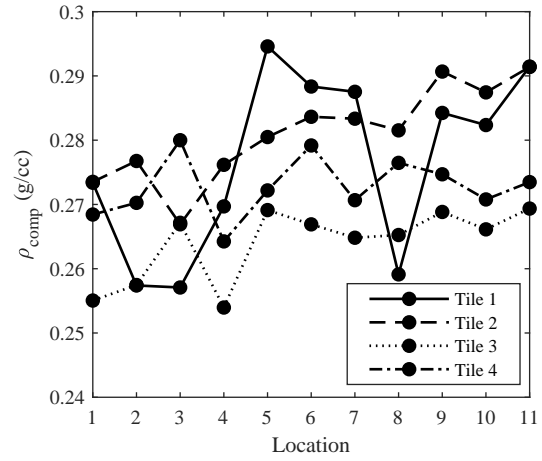
Virgin density and resin mass fraction, which are closely coupled, vary similarly across each tile with ρ_{comp} ranging between 0.254 g/cc and 0.295 g/cc and w_{resin} between 0.57 and 0.64. Tile means ranged from 0.264 g/cc to 0.281 g/cc and from 0.61 to 0.63, respectively. Mean virgin densities here are somewhat less than their corresponding bulk values above, which may be a result of selected core locations not being representative of the entire tile. Tile 3 had the largest difference between mean coupon density (0.264 g/cc) and the bulk tile density (0.274 g/cc). Other tiles align more closely with their bulk properties.

Char yields, plotted in Figure 3.19(d), ranged from 69.5% to 76.9%, but the majority of samples possessed char yields between 70% and 73% and average values mirror a narrower range. Location 11 of Tile 4 may have picked up debris mass during charring artificially inflating this value.

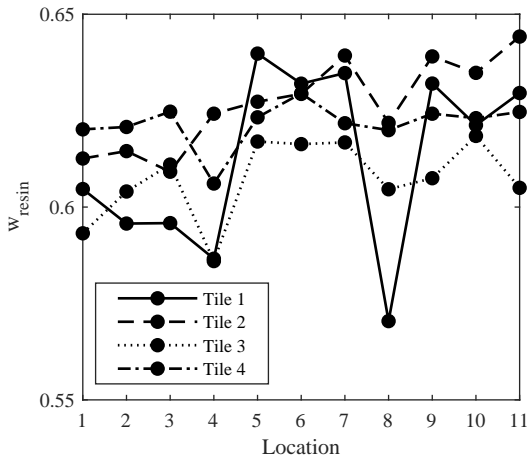
Tile 1 properties varied widely across the part with low resin loading near the gate (Locations 1–4) and under the expansion port (Location 8). Partial saturation of the substrate likely led to these material deficiencies. Tiles 2–4 demonstrated more consistent results. Virgin density and resin mass fraction were much less variable (standard deviations about half that of Tile 1). However, the lower resin loading of Tiles 3 and 4 is again evident here



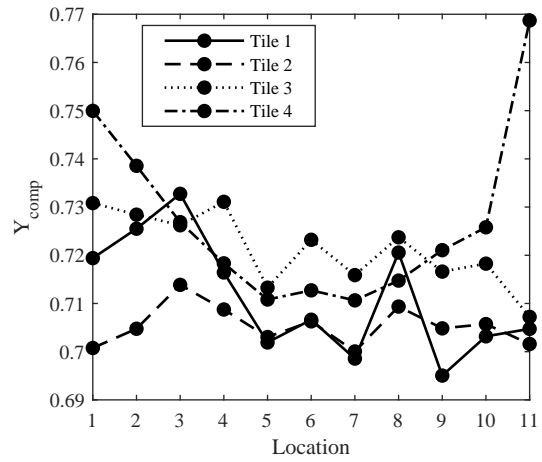
(a) Thickness reduction



(b) Composite (virgin) density



(c) Resin mass fraction



(d) Composite char yield

Figure 3.19: Properties of the cylindrical coupons.

Table 3.7: Mean and variation in coupon properties compared to theoretical predictions.

Tile No.	Experimental					
	Virgin Density		Resin Mass Fraction		Char Yield	
	Mean (g/cc)	Std. Dev. (g/cc)	Mean —	Std. Dev. —	Mean %	Std. Dev. %
1	0.277	0.014	0.61	0.02	71.1	1.2
2	0.281	0.007	0.63	0.01	70.5	0.4
3	0.264	0.006	0.61	0.01	72.1	0.8
4	0.273	0.005	0.62	0.01	72.7	1.8
	Theoretical					
	Nominal (g/cc)	Std. Dev. (g/cc)	Nominal —	Std. Dev. —	Nominal %	Std. Dev. %
1	0.280	0.005	0.62	0.01	70.7	1.2
2	0.278	0.005	0.62	0.01	70.4	1.2
3	0.277	0.005	0.63	0.01	70.3	1.2
4	0.276	0.005	0.63	0.01	70.2	1.2
	Relative					
	Mean* (%)	Std. Dev.** (%)	Mean* (%)	Std. Dev.** (%)	Mean* (%)	Std. Dev.** (%)
1	-1.1	280	-1.6	200	0.6	100
2	1.1	140	1.6	100	0.1	33
3	-4.7	120	-3.2	100	2.6	67
4	-1.1	100	-1.6	100	3.6	150

*The difference between the experimental mean and the theoretical value as a percentage of the theoretical value

**The ratio of the experimental deviation to the theoretical deviation as a percentage

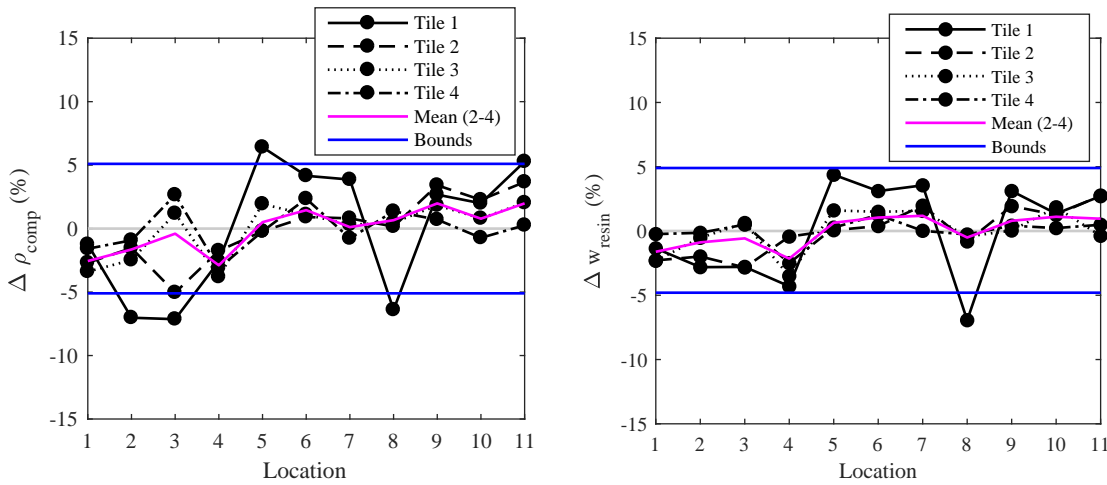
— leading to lower densities and elevated char yields compared to Tiles 1 and 2. Properties at Location 13 did not deviate significantly from the other coupons of Tile 3 despite substantial surface voidage ($\rho_{\text{comp}} = 0.262 \text{ g/cc}$, $w_{\text{resin}} = 0.61$, $Y_{\text{comp}} = 71\%$), and the depth of that voidage was also comparable (0.08 cm). Because visual inspection did not show any significant in depth voidage, it is unlikely that deviations in mean properties stem from differences in infiltration but rather from resin evaporation during curing, as stated earlier. Resin loss was higher during curing of Tiles 3 and 4 likely reducing post-process resin density in those parts.

Still, resin loading appears to be relatively consistent with predictions for Tiles 1, 2, and 4. Relative differences are within about 1% of nominal. Tile 3 possessed the largest deviations with virgin density and resin mass fraction falling -4.7% and -3.2% below their respective theoretical values. In Tile 4, these quantities were also somewhat below prediction, but less so than Tile 3, indicating that higher curing pressure may have suppressed evaporation as intended. Tile 1 also possessed slightly depressed resin loading here, contrary to estimates from the bulk part, but, this aligns with higher resin evaporation compared to Tile 2.

Mean char yields were in line with predictions for Tiles 1 and 2 but elevated for Tiles 3 and 4. Tile 4 was influenced by a potentially erroneous data point noted above. The outlier also produced larger than predicted variance in char yield in that part (1.8% vs. 1.2%). Neglecting Location 11 yields a standard deviation (1.3%) closer to the theoretical value. Tiles 2 and 3 have comparatively lower variation in char yield. Variation in density and resin loading appears to be near to that expected from the theoretical model for Tiles 2–4, with Tile 4 possessing the least variation in these quantities. The large variation in Tile 1 properties is again evident here — standard deviations are about twice predicted by theory.

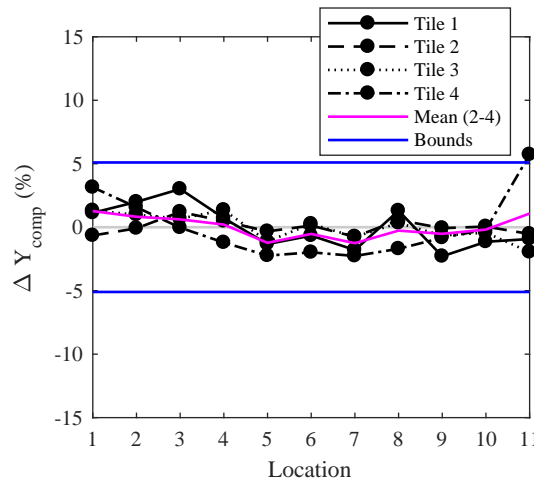
Deviation from Mean Properties by Location Despite differences in absolute properties stemming from variations in resin density, Figures 3.20(a)–(c) show relatively similar

variation relative to their means. In the figures, black lines denote the percentage difference relative to the mean of a given tile. Zero lines (gray) are included to assist in differentiating positive and negative deviations. Bounds are based on the uncertainty predictions from the Chapter 2 model (Table 2.4). Tiles 2–4 were averaged to produce the magenta line. Tile 1 was neglected in this average due to aforementioned issues with the experimental setup.



(a) Composite (virgin) density

(b) Resin mass fraction



(c) Composite char yield

Figure 3.20: Deviations from mean by location.

In general, resin loading was depressed, relative to the mean, near the gate and along the bottom edge of the tile. Locations 1–4 tended toward lower virgin density, lower resin mass fraction, and slightly elevated char yield. Location 3, which was in the bottom right corner

of the tile, was an exception to this rule. Locations further away from the gate and including the vent exhibited the reverse trend — higher virgin density, higher resin loading, and lower char yield. A slight reduction in resin loading existed under the expansion port relative to the surrounding volume, but not to a significant degree. Apart from Tile 1, deviations were generally within a few percentage points of the mean and within theoretical uncertainties. The one exception was Location 11 on Tile 4 with a char yield outside expected bounds. However, density and resin mass fraction were nominal at that location suggesting that the yield was indeed artificially inflated by debris mass.

Thermogravimetric Analysis TGA results for Location 12 are shown in Figure 3.21 differentiated into the top half (black lines) and bottom half (magenta lines). Mass loss curves are plotted as a percentage of the initial mass, which was taken at 150°C to account for slight variation in sample dryness. Sample masses were between 300 mg and 375 mg. Final TGA yields in Table 3.8 were obtained at 1200°C and compared to yields from Locations 5, 6, and 8, which were in close proximity.

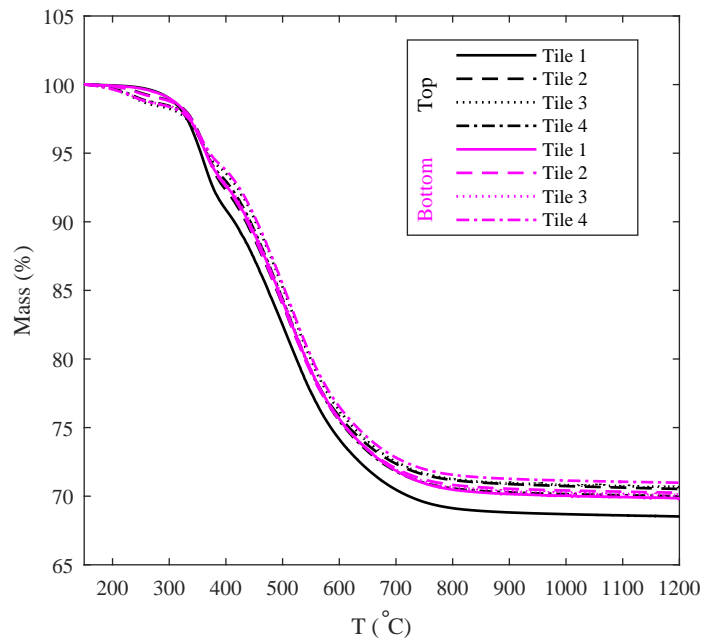


Figure 3.21: Thermogravimetric analysis of cores from Location 12.

Tile 1 exhibited the greatest through thickness variation with final char yield of 68.5% at the top and 69.8% at the bottom, a difference of 1.4%. Other tiles exhibited a smaller spread (1% or less) between top and bottom, and all were between 70% and 71%. Tile 2 yielded the most consistent results through the thickness with a difference of only 0.3%.

Table 3.8: Comparison of char yields derived from TGA (Location 12) and from furnace results (Locations 5, 6, and 8).

Tile No.	Core Locations				
	12 / top	12 / bottom	5	6	8
1	68.5%	69.9%	70.2%	70.7%	72.1%
2	70.5%	70.2%	70.3%	70.6%	70.9%
3	70.6%	70.2%	71.3%	72.3%	72.4%
4	70.0%	71.0%	71.1%	71.3%	71.5%

Tile 1 did not exhibit any appreciable mass loss between 200°C and 300°C, unlike the other tiles which lost around 2% in that range. Differences to resin composition may have resulted from drying Tile 1 outside of the mold. If the resin were not fully cured prior to drying, further evaporation could perhaps alter composition. Nonetheless, the tiles processed in the mold showed little through thickness variation in char yield which is promising for the VIP process.

Furnace yields appeared to be slightly elevated compared to TGA yields, especially at Location 8. Deviation at Location 8 likely resulted from reduced resin loading under the expansion port noted previously. Still, results were within approximately $\pm 2\%$, matching uncertainties from Chapter 2.

3.7 Summary

This chapter presented a new vacuum infusion process for conformal ablaters, which reduces resin consumption and waste, simplifies clean up, eliminates the need for a vacuum oven or chamber, and ultimately reduces labor and cost. Preliminary testing on small samples eventually led to the successful scale up to 0.5-meter curved C-PICA tiles in this

investigation. Though voidage appeared on external surfaces, fabricated TPS tiles were generally well infused in depth. No substrate delamination was observed in any samples. Material properties compared favorably with theoretical predictions, though Tiles 1 and 2 tended toward higher resin loading than Tiles 3 and 4 leading to elevated virgin density and resin mass fraction and reduced char yield. Because there was no significant in depth voidage in any samples, differences in material properties were likely driven by curing conditions and their corresponding effect on post-process resin density. With consistent and well-controlled curing conditions, it is likely that properties would be more uniform between parts.

Within each tile, properties were fairly consistent varying only a few percent from the mean. Resin loading tended to be depressed near the gate and elevated elsewhere. Resin loading was also depressed, though not significantly, directly under the expansion port. TGA found little difference in char yield between the top and bottom of the tile. Tile 1 was again the exception here, exhibiting larger variations in properties through the thickness and in plane likely due to poorer saturation during infusion.

The results of this chapter demonstrate the importance of proper gate and vent positioning. Tiles 2–4 were all similarly well infused, despite variation in vent pressure, because residual air inside the cavity could be evacuated throughout infusion with little or no entrapment. A poorly placed gate can result in air being trapped by advancing flow, preventing full saturation of the substrate. The mold filling simulation, which is described in Chapter 5, is thus crucial to mold design and forms the backbone of the final contribution of this thesis, a methodology to design a conformal ablative heatshield. Chapter 4 introduces the methodology and its inputs followed by the design tasks and their outputs in Chapter 5. Finally, two design examples using the methodology are presented in Chapter 6, including the design of the experimental mold shown in this chapter.

CHAPTER 4

OBJECTIVES OF THE DESIGN METHODOLOGY AND ITS INPUTS

4.1 Introduction

Chapter 3 described VIP, a new process for making conformal ablative TPS materials. VIP not only improves manufacturing efficiency over the SOTA but also allows computational design of the mold filling process using an application of Darcy's law described in Chapter 1. A mold filling simulation can identify potential dry spots during infusion, ensuring high quality TPS with no voids. However, a conformal heatshield consists of multiple tiles each requiring a potentially unique mold design. Connecting the mold filling simulation with a tile layout procedure can tailor a heatshield to VIP, generating the minimal set of tile geometries and the mold designs required to fabricate them. Such a methodology, integrating material selection, tile layout, and processing to produce a configuration optimized for VIP, forms the final contribution of this thesis.

This chapter introduces the methodology, outlining its inputs, subsequent design tasks, and their outputs, then discusses the scope of the current implementation. The remainder of the chapter is devoted to describing the inputs, which are divided into primary parameters, known a priori, and intermediate parameters, which can be estimated. The former quantities include TPS geometry, constituent material properties, and process parameters. Models for estimating intermediate inputs, derived properties of the substrate, resin, and the composite TPS material, are based on the constitutive model of Chapter 2. Those results are extended in this chapter to additional parameters (substrate permeability, resin viscosity, and resin vapor pressure) relevant to the mold filling simulation and the process design. Predicted properties are compared to experimental results for C-PICA.

4.2 Overview and Objectives of the Design Methodology

The design methodology, depicted in Figure 4.1, combines a Darcy's law simulation of the mold filling process with a tile layout tailored to VIP. It encompasses three sequential tasks: (1) generating a tile layout for the specified heatshield geometry, (2) producing a VIP mold design for each tile geometry, and (3) estimating relevant properties of the fabricated TPS material. These design tasks, shown on the right in the figure, form the core of the methodology. Full exploration of the design space is carried out during tiling to select the optimal tile layout. Mold designs are optimized using particle swarm optimization (PSO). The outputs/objectives of each step are listed below each heading.

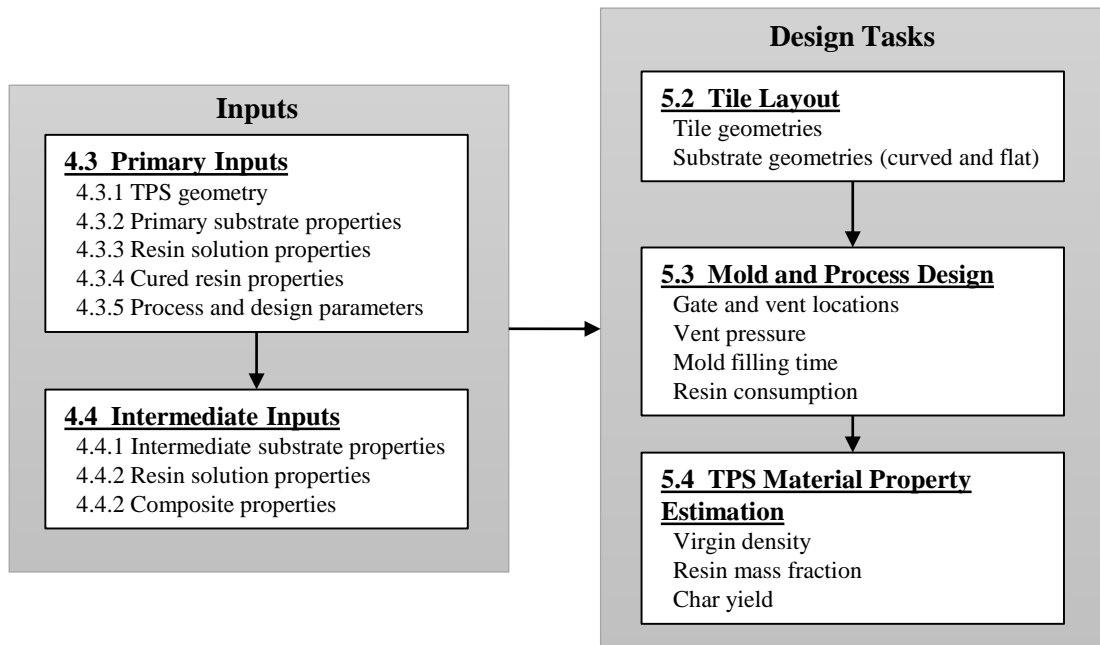


Figure 4.1: Design methodology for tiling and fabricating a conformal heat shield.

Tiling yields the minimal set of tile geometries spanning the aeroshell subject to constraints on manufacturing. Corresponding substrate geometries are generated by scaling up the tile geometries to account for process shrinkage, then flattening them to produce two-dimensional cutting patterns. Mold and process design iterates on the mold filling simulation in order to find gate and vent positions that minimize the risk of air entrapment

and void formation. Metrics for the selected design are also output from this step (total filling time and resin consumption) as well as the vent pressure. Finally, in the last step, results from Chapter 2 are used to estimate the virgin density, resin mass fraction, and char yield of the fabricated TPS material. Each task is discussed in more detail in Chapter 5 in sections corresponding to the numbers in Figure 4.1.

Required inputs to the methodology, on the left in Figure 4.1, precede the design tasks. These are differentiated into primary and intermediate inputs. The former are quantities or aspects of the design that must be known a priori (though some approaches for obtaining these quantities are suggested below) while the latter can be estimated to simplify early conceptual design where experimental data may be scarce. Inputs are discussed in detail in corresponding sections below after noting some limitations of the current implementation.

4.2.1 Scope of the Present Work

The methodology itself is generally applicable to any aeroshell geometry and TPS material. However, the present work is limited to conical aeroshells with a blunted, spherical nose flying at zero angle of attack. Thus, the stagnation point falls on the nose of the vehicle, and generated tile layouts are symmetric like the one depicted in Figure 4.2. TPS thickness is assumed to be uniform across the heatshield. The spherical nose must be manufacturable from a single tile. Otherwise, the nose tile is considered infeasible. Details of the seam geometry are also neglected — each tile is assumed to butt up against the next at a perpendicular joint with an orthogonal seam — and shoulder tiles are not considered.

Alternative tile layouts (e.g., asymmetric designs, non-uniform TPS thicknesses, shoulder tiles, and large nose tiles) cannot be generated automatically in the current implementation but could be designed externally and then treated as an input to the mold filling simulation. Thus, mold designs, process metrics, and estimated TPS properties can still be generated for these designs. However, note that, in this case, the number of unique tile geometries should be minimized to limit the number of molds that must be fabricated.

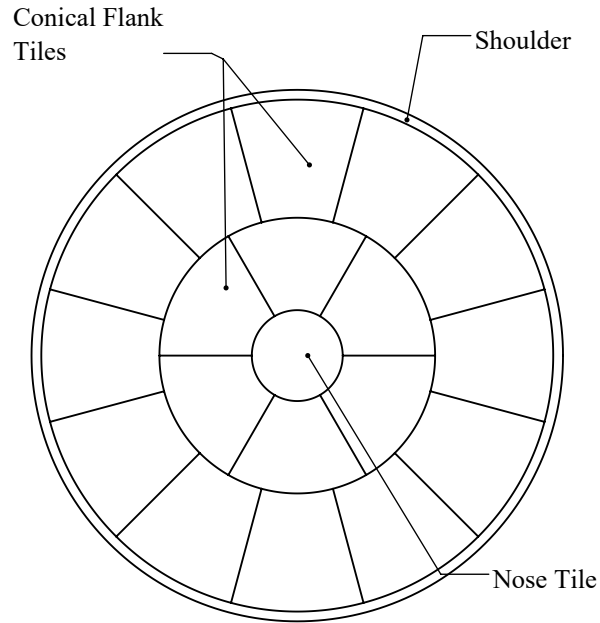


Figure 4.2: Front view of a symmetric tile layout with a single nose tile and two rings forming the conical flank.

In the future, layout rules could be extended to allow automated tiling of these additional configurations.

Molds are limited to single gate, single vent designs where injection and venting occur at point locations (though the gate is modeled as a two-dimensional circular source in the simulation). This configuration proved sufficient for infusing the TPS materials and geometries under consideration here (Chapter 3).

Finally, the methodology does not investigate expansion port size, number, or placement. The previous chapter described a rectangular grid of 0.5 in (1.27 cm) diameter expansion holes spaced 3.5 in (8.9 cm) apart in the experimental mold. This arrangement yielded good results, i.e., flow of resin and volatiles did not appear to be impeded during curing or drying. However, other arrangements and spacing could be studied as suggested in Chapter 7.

4.3 Primary Inputs

Primary inputs to the methodology include design inputs (TPS geometry), material inputs (properties of the constituent materials), and process and design parameters. These inputs are not estimated in the present work and, therefore, must be known a priori from external sources or analyses, some of which are suggested here.

4.3.1 TPS Geometry

TPS geometry is specified as a two-dimensional OML geometry and a TPS thickness, t_{TPS} . Ideally, a given geometry should be feasible for manufacturing. For example, the desired TPS thickness must not exceed that which is achievable with the specified substrate and any curvature should not be less than a minimum radius of curvature to ensure uniform draping of the substrate without wrinkling (drapeability, considered below). The methodology identifies such infeasibilities — by comparing t_{TPS} to the maximum manufacturable thickness, $t_{\text{comp}}^{\text{max}}$, and the radius of curvature of each tile to the minimum, R^{min} — but requires the designer to supply an alternate material or a different manufacturing technique to rectify them.

4.3.2 Properties of the Fiber Substrate

Bulk Properties

Required substrate properties include bulk dimensions (width, W_{sub} , length, L_{sub} , and thickness, t_{sub}), and areal density, $\rho_{\text{sub}}^{\text{areal}}$. Fiber substrates are only available, or manufacturable, in certain sizes. For example, Felt 1 is available up to a thickness of about 1 inch (2.54 cm) and widths between 41 and 47 inches (104 to 119 cm). Areal density is assumed constant as in previous chapters, though the equations below could easily be reformulated in terms of the volumetric density. To compute uncertainties using the results of Chapter 2, the variation in thickness, Δt_{sub} , and areal density, $\Delta \rho_{\text{sub}}^{\text{areal}}$, must also be supplied. These

quantities are often available from the manufacturer.

Fiber Properties

Properties of the the individual fibers composing the substrate — fiber density, ρ_{fiber} and diameter, d_{fiber} — are less available but can be approximated for carbon fiber materials given a known precursor. Rayon-based substrates, typical in ablative TPS due to low thermal conductivity, are commonly in the range 1.35 g/cc to 1.44 g/cc as was noted previously [89]. Using micro-tomography, Panerai, et al. measured fiber diameters around 10–12 μm for Felt 1 but noted that cross sections are lobular, not circular, and possess a hollow central lumen. This work simplifies the fiber cross section to a circular cross section with diameter, d_{fiber} , and average density, ρ_{fiber} .

Drapeability

Drapeability generally describes the ability of a fabric to conform to a desired shape. High curvature can lead to wrinkling, which can cause unpredictable, and undesirable, mold flow (i.e., racetracking) as well as reduce usable thickness. Draping, and wrinkling, of fabric materials are complex phenomena influenced by both microscopic and macroscopic properties.

Modeling draping in LCM is an area of considerable research in itself. A kinematic pin and joint model is frequently used to predict deformation and wrinkling of woven materials [96]. This model assumes fibers are pinned together and can rotate freely at these intersections giving rise to shearing. Fiber directions are assumed to lie in one of only two initial directions, warp and weft. Such a model has been used to assess change in substrate permeability due to deformation [97]. Finite element methods which treat the material as a continuum are an alternative to the kinematic approach, but these methods tend to be computationally intensive [98].

Nonwoven materials pose a problem for the kinematic approach due to disordered,

entangled fibers. Thus, fibers can undergo a variety of other deformations including uncurling, disentanglement, and pull-out. Furthermore, failure mechanisms operate at vastly different length scales. Martinez-Hergueta, et al. incorporated these effects in a multiscale constitutive model to predict deformation of needled nonwoven fabrics similar to the felts in this thesis [99]. Cherouat, et al. used an approach similar to the pin-joint model but allowed filament elongation at high shear angles to approximate nonwoven behavior [98].

This methodology forgoes a complicated draping simulation in favor of a simple minimum radius of curvature constraint, R^{\min} , to ensure uniform draping. Above this minimum, there is assumed to be no substrate wrinkling. The minimum radius of curvature is assumed to be known a priori; the quantity used later in Chapter 6 is based on guidance from the felt manufacturer. If the curvature of a tile violates this constraint, then it cannot be fabricated, and an alternate process or material must be selected. Future extensions of the methodology, discussed further in Chapter 7, could include an accurate draping simulation along the lines of the prior work to improve the mold filling simulation and material property predictions.

4.3.3 Properties of the Resin Solution

Resin solutions are a mixture of components including resin, solvent, and potentially other fillers. The methodology requires two properties of the resin solution, dynamic viscosity and vapor pressure, both important parameters for mold filling. Mixture quantities are estimated in the next section by weighted averages based on volume, weight, or mole fractions of the components. Thus, in addition to resin composition itself (e.g., component amounts by volume, v_c , by weight, w_c , and by mole, x_c), individual component properties must be known: viscosity (either the kinematic viscosity, ν_c , or dynamic viscosity, μ_c), vapor pressure, $P_{\text{vap},c}$, and density, ρ_c , of each component c must be supplied. Component viscosities and vapor pressures can be obtained from chemical databases or material datasheets.

4.3.4 Properties of the Cured Resin

Density and Dimensional Changes

The resin undergoes both mass and volume change during processing. Mass loss occurs due to evaporation of solvent, reactants, and products. Volume change occurs as the solution expands due to heating and contracts due to crosslinking. Contraction of the resin system is coupled to the substrate present (which may resist shrinkage and prevent some or all contraction) and mold boundary conditions (bonding to the mold walls also prevents contraction). Section 2.2.4 reduced post-process resin density, $\rho_{\text{resin}}^{\text{post}}$, to a function of two inputs: ρ_{R} , and its volumetric shrinkage during processing, α_{R} .

The quantities ρ_{R} and α_{R} are properties of the pure resin where there is no resistance to volume change, which may not hold in actual processing. An experimental approximation can be made by curing a given resin within a container possessing non-bonding walls. For example, PTFE coating, with its chemical resistance and non-stick properties, can achieve the desired boundary conditions. The necessary quantities are then obtained from measurement of pre- and post-cured mass and dimensions. Deviations in these quantities, $\Delta\rho_{\text{R}}$ and $\Delta\alpha_{\text{R}}$ are also necessary to predict uncertainty using the approach described previously in Chapter 2.

Char Yield

Resin char yield, Y_{R} , is highly dependent on composition and processing. This quantity may be measured experimentally. However, in the absence of experimental results, historical data may be useful (e.g., as compiled by Williams and Curry [100] and Parker and Winkler [101]). The latter reference contains char data for phenolic resins. It may also be estimated using computational techniques. For example, Parker and Winkler present a method for predicting phenolic char yield as a function of resin composition and degree of crosslinking. A similar approach is presented by Wang, et al. [102]. Still other work uses

a kinetics model of phenolic pyrolysis to predict char formation[103]. In addition to the nominal value, variation in char yield, ΔY_R , must also be supplied in accordance with the uncertainty estimation in Chapter 2.

4.3.5 Process and Design Parameters

Gate Design

Gate design includes geometry and an appropriate boundary condition to reflect the process setup. This work used a constant pressure boundary condition with gate pressure, P_{gate} , set to the ambient atmospheric pressure, P_{atm} , to reflect the process set up.

Minimum Seam Angle

A minimum seam angle, β^{min} , prevents seam alignment between adjacent tiles, a requirement typical of tiled heatshields (e.g., see the tile design for the Mars Science Laboratory heatshield [26]). A single angle between adjacent seams, $\beta_{j,j+1}$, is depicted on the represen-

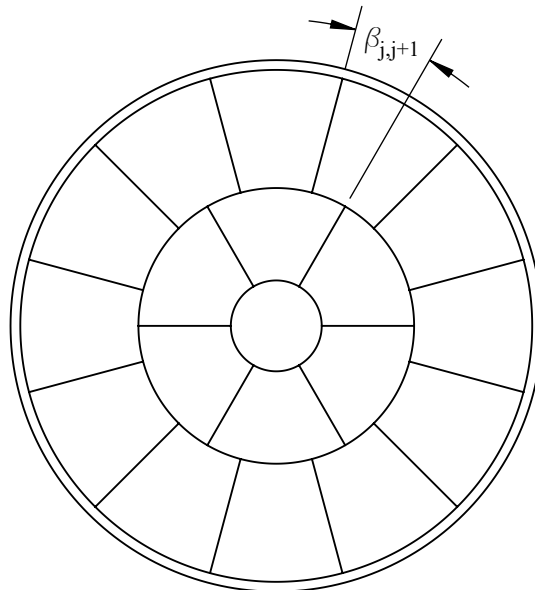


Figure 4.3: A seam angle, $\beta_{j,j+1}$, illustrated on the previous tile layout example (Figure 4.2).

Table 4.1: Summary of primary inputs to the design methodology.

Category	Parameter	Symbol(s)	Description
TPS Geometry	OML	—	A two-dimensional curve describing the external surface of the TPS
	TPS Thickness	t_{TPS}	Desired thickness of the TPS after processing
Fiber Substrate	Dimensions	$W_{\text{sub}}, L_{\text{sub}}$	Width and length of the substrate material
	Thickness	$t_{\text{sub}}, \Delta t_{\text{sub}}$	Nominal substrate thickness (and its variation)
	Areal density	$\rho_{\text{sub}}^{\text{areal}}, \Delta \rho_{\text{sub}}^{\text{areal}}$	Nominal substrate areal density (and its variation)
	Fiber density	$\rho_{\text{fiber}}, \Delta \rho_{\text{fiber}}$	Density of the fibers comprising the substrate averaged over their cross-section
	Fiber diameter	d_{fiber}	Diameter of the fibers comprising the substrate
	Min. radius of curvature	R^{min}	Curvature requirement to prevent substrate wrinkling
Resin Solution	Composition	v_c, w_c, x_c	Volume, weight, and mole fractions of solution components
	Viscosities	ν_c or μ_c	Kinematic or dynamic viscosity of solution components
	Vapor pressure	$P_{\text{vap},c}$	Vapor pressure of solution components
Cured Resin	Density	$\rho_{\text{R}}, \Delta \rho_{\text{R}}$	Density of the pure resin (and its variation) after curing
	Volumetric shrinkage	$\alpha_{\text{R}}, \Delta \alpha_{\text{R}}$	Shrinkage of the pure resin (and its variation) during curing
	Char yield	$Y_{\text{R}}, \Delta Y_{\text{R}}$	Char yield of the pure resin (and its variation)
Process and Design	Gate geometry	—	Geometry of the gate, specified here as a circle with radius, R_{gate}
	Gate pressure	P_{gate}	Pressure at the gate, specified here as P_{atm}
	Minimum seam angle	β^{min}	Constraint on the minimum angular offset between adjacent radial seams

tative heatshield in Figure 4.3. The minimum angle constraint is enforced for all adjacent seams during tile layout.

4.3.6 Summary of Primary Inputs

Table 4.1 summarizes the primary inputs, their symbols (where appropriate), and descriptions. Quantities are differentiated by category, corresponding to the subsection headings above.

4.4 Intermediate Inputs

The second set of inputs are intermediate material properties — properties that are functionally dependent on those above and are required for subsequent mold filling analysis and TPS property estimation. They are divided into properties of the substrate, properties of the resin solution, and properties of the combined substrate and resin after processing (i.e., the composite). Any of these properties may be experimentally measured and treated as additional inputs to the methodology. As a result, some inputs identified above may no longer be required.

Alternatively, these properties can be numerically estimated using simplified models below to speed design evaluation. Some of these models were previously derived in Chapter 2, and those equations are referred to here where appropriate. Additions to these results presented in this section include estimates of substrate permeability and resin viscosity, which appear in Darcy’s Law, and resin vapor pressure, which limits the vent pressure during processing. These models are compared to experimental values for C-PICA to demonstrate the validity of the approximations on a preliminary basis. Finally, an additional result describing the maximum manufacturable TPS thickness, $t_{\text{comp}}^{\text{max}}$, constrains TPS thickness during tile layout.

4.4.1 Properties of the Fiber Substrate

Density

In addition to the areal substrate density, multiple volumetric substrate densities appear in this methodology: the uncompressed density, ρ_{sub} ; the compressed density in the mold prior to processing, $\rho_{\text{sub}}^{\text{pre}}$; and the density after processing, $\rho_{\text{sub}}^{\text{post}}$. Practically, molds must be designed to the minimum substrate thickness to ensure there are no gaps between the fiber material and the tooling, which can lead to racetracking. Therefore, the uncompressed substrate, with thickness variance Δt_{sub} , is compressed to a uniform pre-process thickness (also Equation 2.24):

$$t_{\text{sub}}^{\text{pre}} = t_{\text{sub}} - \Delta t_{\text{sub}} \quad (4.1)$$

With known areal density, $\rho_{\text{sub}}^{\text{areal}}$, the compressed, pre-process volumetric density is given by (also Equation 2.5):

$$\rho_{\text{sub}}^{\text{pre}} = \frac{\rho_{\text{sub}}^{\text{areal}}}{t_{\text{sub}}^{\text{pre}}} \quad (4.2)$$

and post-process density by (also Equation 2.16):

$$\rho_{\text{sub}}^{\text{post}} = \frac{\rho_{\text{sub}}^{\text{pre}}}{1 - \alpha} \quad (4.3)$$

where α is the volumetric shrinkage of the substrate. Results for α , discussed previously in Chapter 2, are repeated later in this chapter.

Porosity

Porosity is estimated by (also Equation 2.1):

$$\phi = 1 - \frac{\rho_{\text{sub}}}{\rho_{\text{fiber}}} \quad (4.4)$$

where the pre- or post-process substrate density may be substituted to estimate the corresponding porosity. Recall that post-process substrate properties do not refer to the composite material but rather the substrate alone absent the resin.

Permeability

Kozeny-Carman relations have long been used to estimate the permeability of porous media [104]. Originally formulated for a bed of packed spheres, Kozeny-Carman has since been expanded to other porous structures. This methodology uses an extension to an arbitrary randomly-oriented, three dimensional fiber mat by Tomadakis and Robertson [105]. Nondimensional permeability is estimated:

$$\frac{K}{d_{\text{fiber}}^2} = \frac{\phi}{32 \ln^2 \phi} \frac{(\phi - \phi_p)^{a+2}}{(1 - \phi_p)^a [(a + 1)\phi - \phi_p]^2} \quad (4.5)$$

where ϕ_p , the percolation threshold, and a are numerically derived quantities dependent on geometry. For 3-D randomly overlapped fibrous media, these quantities are $\phi_p = 0.037$ and $a = 0.661$. Note that the notation has been adapted from the original to fit the nomenclature of this thesis.

Results Figure 4.4 presents estimated permeability as a function of porosity for several fiber diameters. Figure 4.4(a) depicts permeability across the full range of porosities, while Figure 4.4(b) shows a narrower range relevant to the high porosity materials of this thesis. Experimental results, discussed below, are included in the righthand plot. Note that porosity here is that of the substrate compressed within the mold, ϕ^{pre} , so that K corresponds to the material as infused. A truly random fiber network produces isotropic permeability, but fiber organization in the actual material may yield variation between the in plane, K_{IP} , and through the thickness, K_{TT} , components. However, the thinness of TPS tiles effectively limits the dependence on K_{TT} and allows use of a single value for permeability. This topic is addressed further in Chapter 5.

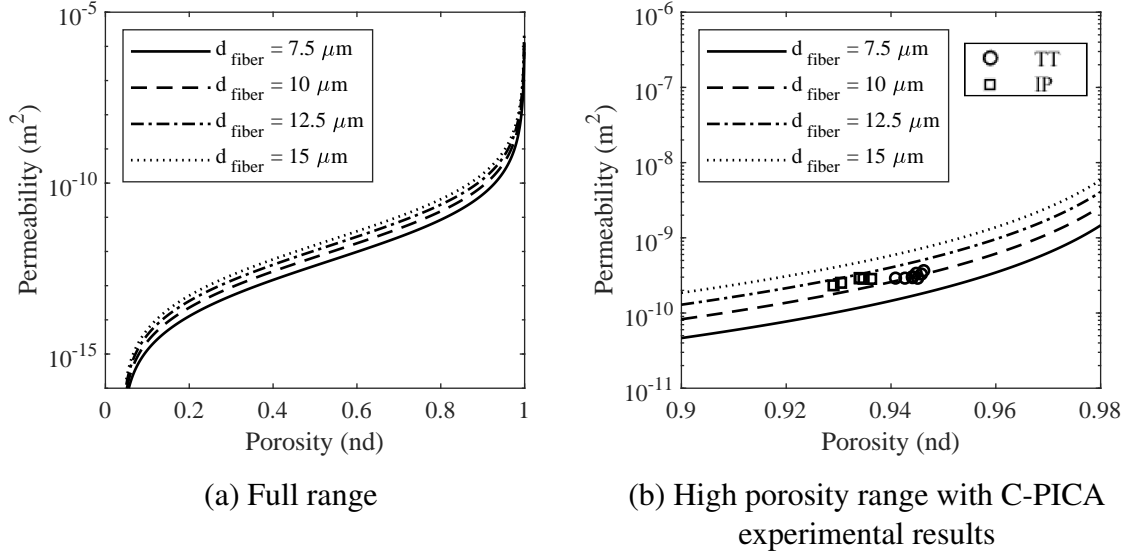


Figure 4.4: Tomadakis and Robertson permeability model [105] for a three-dimensional, random fiber network.

Permeability was measured by flowing air through cylindrical cores cut from Felt 1 using the methodology described in Appendix A.1. Cores were oriented in both directions, through thickness and in plane. Because the test fluid was a gas, the Klinkenberg correction was used to obtain permeability in the limit of continuum (liquid) flow. Results, plotted in Figure 4.4, compare well to theoretical values from the Tomadakis and Robertson model. Permeability was found to be between $2 \times 10^{-10} \text{ m}^2$ and $4 \times 10^{-10} \text{ m}^2$ for these samples, falling between $d_{\text{fiber}} = 10 \mu\text{m}$ and $12.5 \mu\text{m}$ which roughly corresponds to the range suggested by Panerai, et al. for this felt. Permeability appears to be slightly lower through the thickness than in plane. TT samples are clustered closer to the line corresponding to $d_{\text{fiber}} = 10 \mu\text{m}$.

4.4.2 Properties of the Resin Solution

The following properties are quantities for the resin mixture averaged over its components. It is important to note that component properties must be specified at the infusion temperature, which is room temperature in the current process. Extrapolating to other temperatures may be possible with knowledge of component properties as functions of temperature.

Furthermore, an ideal solution is assumed, i.e., interaction between unlike molecules can be neglected and mixture properties are functions of the individual components weighted by their relative proportions. Because the C-PICA resin formulation is proprietary, experimental and theoretical results are compared on a relative basis, rather than providing actual values. Experimental methodologies in this section are described in more detail in Appendix A.2

Dynamic Viscosity

This work leverages the Chevron model, originally developed to approximate the viscosity of petroleum blends, which uses a volume fraction weighted sum of component viscosities. This mixing rule, and several others, were reviewed by Centeno, et al. [106]. The Chevron method was found to yield good results at low viscosities while having a fairly simple formulation, which led to its selection here. The Chevron model employs a viscosity blending index (VBI) for each component of the mixture,

$$\text{VBI}_c = \frac{\log \nu_c}{3 + \log \nu_c} \quad (4.6)$$

The VBI of the mixture is a weighted sum of the component VBI_c ,

$$\text{VBI}_{\text{sol}} = \sum_c v_c \text{VBI}_c \quad (4.7)$$

where v_c is the volume fraction of a component in the solution. Rearranging Equation 4.6 yields an expression for the kinematic viscosity of the solution as a function of the mixture VBI,

$$\nu_{\text{sol}} = 10^{\left(\frac{3\text{VBI}_{\text{sol}}}{1-\text{VBI}_{\text{sol}}}\right)} \quad (4.8)$$

Finally, dynamic viscosity, not kinematic viscosity, is required for Darcy’s law and can be computed given the resin solution density, ρ_{sol} ,

$$\mu_{\text{sol}} = \nu_{\text{sol}}\rho_{\text{sol}} \quad (4.9)$$

If not known, ρ_{sol} can be approximated using an average of its components based on mole or weight fractions.

Results C-PICA resin viscosity was measured using a rotational viscometer over temperatures ranging from 16°C to 29°C. Portions of two separately mixed resin solutions were measured, and the data were fitted using an exponential model. The fitted model was then used to obtain nominal viscosity at 25°C, which was nondimensionalized to $\mu_{\text{sol}}^*=1$. The Chevron approach predicts slightly lower resin viscosity, $\mu_{\text{sol}}^*=0.87$. A weight fraction-based average of the solution components was used to estimate ρ_{sol} for the viscosity prediction. Minor components, comprising less than 1% of the solution in total by volume, were neglected in the approximation. Even with the simplification, the model prediction is only 13% below the measured value.

Vapor Pressure

Resin boiling effectively limits vent pressure in VIP. If the pressure is too low, boiling will occur along the flow front and may lead to entrapped gas bubbles and voidage, a problem for the first tile in Chapter 3. Resulting bubbles can be compressed after saturation, but not completely, thus it is still beneficial to limit their formation during infusion. Vapor pressure is estimated using Raoult’s law, the sum of component vapor pressures weighted by mole fraction [107],

$$P_{\text{vap,sol}} = \sum_c P_{\text{vap},c}x_c \quad (4.10)$$

The process pressure should not fall below the vapor pressure of the solution to avoid boiling. Thus, for simulation purposes, the vent pressure, P_{vent} , is set equal to $P_{\text{vap,sol}}$. In reality, vapor pressure may deviate from that predicted by Raoult's law due to the suppression or enhancement of intermolecular forces between unlike molecules. It is also complicated by the fact that individual components may possess varying volatility and do not behave as a uniform compound with a single boiling point. Thus, this method provides a first order approximation but would likely need to be adjusted in subsequent processing. In any case, the results of Chapter 3 indicated that a range of vent pressures in the vicinity of the solution boiling point yielded similar material quality.

Results Vapor pressure was measured by slowly evacuating an approximately 500 mL container of C-PICA resin until boiling was observed. Pressure was controlled by a vacuum regulator which was set to ramp down from atmospheric pressure over several minutes. There was some ambiguity in the actual boiling point (likely due to varying component volatility discussed above). Large bubbles indicative of boiling occurred at a low pressure, nondimensionalized here to $P_{\text{vap,sol}}^* = 1$, but small bubbles initially formed and percolated through the solution at about three times that pressure. The lower pressure was taken as the solution boiling point / vapor pressure, and relative to this quantity, Raoult's law agrees quite closely, $P_{\text{vap,sol}}^* = 0.97$. Minor solution components were again neglected in the estimation, comprising less than 1% of the solution in total by mole.

4.4.3 Properties of the Composite Ablative Material

Resin Density in the Composite

Resin density in the composite post-processing, $\rho_{\text{resin}}^{\text{post}}$, is coupled to the overall material shrinkage and functionally depends on the shrinkage and density of the pure resin. That is, a stiff substrate yields little volume contraction, and thus lower resin density, compared to

a compliant substrate. This parameter is estimated by (also Equation 2.22):

$$\rho_{\text{resin}}^{\text{post}} = \frac{1 - \alpha_{\text{R}}}{1 - \alpha} \frac{\phi^{\text{pre}}}{\phi^{\text{post}}} \rho_{\text{R}} \quad (4.11)$$

Recall that $\rho_{\text{resin}}^{\text{post}}$ is averaged over the post-process porous volume. Thus, it is not a measure of the local resin density but rather the density if the resin were uniformly distributed throughout the porous volume. This expression assumes that no bonding occurs with the mold walls, which is true of nonstick coated surfaces.

It was noted in Chapters 2 and 3 that post-process resin density is dependent on curing conditions, specifically the evaporation of solids from the solution during curing. Thus, while this approach bounds $\rho_{\text{resin}}^{\text{post}}$, the resin density will likely be lower in actual processing. In Chapter 2, experimental resin density was 15% to 22% below this prediction depending on assumptions on substrate compliance. Resin density was similarly depressed for the tiles processed in Chapter 3. Experimental results, if available, provide a better approximation and improve predictions of final TPS properties.

Dimensional Changes during Processing

Shrinkage of the resin system during processing changes overall part dimensions, which are differentiated into an in plane component, ϵ_{IP} , and a through thickness component, ϵ_{TT} . These quantities, which are fractional length changes, can be approximated as functions of the pure resin shrinkage and the substrate porosity as outlined in Section 2.2.3. The expressions in Table 2.2 can then be used to approximate shrinkage according to the substrate compliance. Total volumetric shrinkage is then,

$$1 - \alpha = (1 - \epsilon_{\text{TT}})(1 - \epsilon_{\text{IP}})^2 \quad (4.12)$$

Through thickness shrinkage leads to a post-process composite thickness of

$$t_{\text{comp}} = t_{\text{sub}}^{\text{pre}} (1 - \epsilon_{\text{TT}}) \quad (4.13)$$

However, margin must be added to account for post-process removal of surface voidage. Therefore, TPS thickness is reduced by an additional fractional change, ϵ_{M} , due to post-process machining:

$$t_{\text{comp}}^{\text{max}} = t_{\text{sub}}^{\text{pre}} (1 - \epsilon_{\text{TT}}) (1 - \epsilon_{\text{M}}) \quad (4.14)$$

This equation, used later in Chapter 5, constrains the maximum tile thickness.

4.4.4 Summary of Intermediate Inputs

Table 4.2 summarizes the intermediate inputs, their symbols, and the relevant equations for estimating them. Quantities are again differentiated by category, corresponding to the subsection headings above.

Table 4.2: Summary of intermediate inputs to the design methodology and relevant equations.

Category	Parameter(s)	Symbol(s)	Equation(s)
Fiber Substrate	Pre-process density	$\rho_{\text{sub}}^{\text{pre}}$	4.1–4.2
	Post-process density	$\rho_{\text{sub}}^{\text{post}}$	4.3
	Pre- and post-process porosity	$\phi^{\text{pre}}, \phi^{\text{post}}$	4.4
	Permeability	K	4.5
Resin Solution	Dynamic viscosity	μ_{sol}	4.6–4.9
	Vapor pressure	$P_{\text{vap,sol}}$	4.10
Composite Material	Post-process resin density	$\rho_{\text{resin}}^{\text{post}}$	4.11
	Volumetric shrinkage	α	4.12
	Maximum thickness	$t_{\text{comp}}^{\text{max}}$	4.13–4.14

4.5 Summary

This chapter introduced an integrated design methodology combining tile layout, process design, and property estimation for conformal ablative heatshields. Inputs to the methodology, which were discussed in detail, describe the heatshield geometry, process parameters, and the TPS formulation itself. Primary inputs, which must be known a priori, were outlined first and included bulk substrate properties, fiber properties, resin solution composition, and cured resin properties. Process and design parameters were also specified, including the gate design (geometry and boundary condition) and a minimum seam angle constraint to prevent alignment of adjacent tile seams.

Intermediate inputs were discussed next. These quantities, which are required for carrying out the subsequent design tasks, included properties describing the substrate (density, porosity, and permeability), resin solution (viscosity and vapor pressure), and composite TPS (post-process resin density and shrinkage). Results from Chapter 2 were leveraged in estimating several of these quantities. Additions presented here included permeability estimation for random, three dimensional fiber mats using a model by Tomadakis and Robertson, mixture viscosity estimation using the Chevron volume blending approach, and vapor pressure estimation via Raoult's law. Predicted properties agreed well with preliminary experimental results for C-PICA.

CHAPTER 5

TASKS OF THE DESIGN METHODOLOGY

5.1 Introduction

This chapter completes the description of the conformal heatshield design methodology, outlining approaches for the design tasks introduced in the previous chapter: tile layout, mold and process design, and TPS property estimation. The latter task once again uses estimations derived previously in this thesis (Chapter 2). Objective functions, defined in this chapter, quantify the “goodness” of the tile layout and mold designs. Tile layout minimizes the total number of tiles, yielding a minimal set of tile geometries. Then, molds are designed for each of the geometries to minimize the blocked length, a measure of air entrapment during infusion. Constraints ensure that the design is manufacturable given material selection and process parameters. The design tasks are discussed in the following sections, laying out the inputs, solution approaches, and outputs for each step. Section numbers correspond with those shown in the methodology outline in Figure 4.1.

5.2 Tile Layout

Tiling converts an untiled heatshield geometry (the input) into segmented, manufacturable tiles (the output) based on a set of layout rules (constraints). Recall that blunted conical or biconical geometries are within the scope of this work. Some constraints are implicitly enforced by the approach described below; other constraints are explicitly applied in the optimization. The optimal design is that with the minimum total number of tiles (the objective function). In the present approach, each tile requires one VIP run, and each tile geometry requires one tooling set. Minimizing these quantities can limit costs (both non-recurring and recurring) and manufacturing time (because there are fewer tiles to process).

In addition, fewer tiles greatly simplifies aeroshell integration due to fewer seams and less gap filling.

5.2.1 Tile Parametrization

Tiling proceeds radially outward from the nose of the vehicle forming axisymmetric, concentric rings. Each ring is divided into an integer number of identical tiles (thus, each ring requires only one mold to fabricate). Each segment of the OML is treated separately starting with the nose. For example, tiling a biconic aeroshell proceeds from the nose to the first conical segment and then the second conical segment (Figure 5.1). Tiles do not span these segments. Thus, a seam exists at the boundary between adjacent segments. Each segment is operated upon to generate the optimal tile layout for that segment producing a layout consisting of M OML segments each composed of Q_i^{\min} rings. Q_i^{\min} is the minimum number of rings required to tile segment i and is computed by assuming a number of tiles in each ring equal to the maximum value, N_{ub} , which yields the most coverage radially along the flank. The number of rings is then increased sequentially from one, stopping with the first feasible solution, which is set to Q_i^{\min} .

OML geometries consist of the circular nose segment and one or more linear segments forming the conical flank(s). Geometry is specified by a radial and height position relative to the vehicle nose, $(r_{i,j}, z_{i,j})$. Subscripts denote segment and ring indices, $i \in [1, M + 1]$ and $j \in [1, Q_i^{\min}]$, respectively. Segment geometries are defined by start and endpoints: $(r_{i,1}, z_{i,1})$ and $(r_{i+1,1}, z_{i+1,1})$. The circular nose segment also includes a center, $(r_{1,c}, z_{1,c})$, and radius of curvature, R_n (Figure 5.2). Within each segment, ring j spans from $(r_{i,j}, z_{i,j})$ to $(r_{i,j+1}, z_{i,j+1})$. The nose design, formed as a single tile if possible, is trivial. If the nose cannot be formed from a single tile, design of the flank continues, but an alternate material or manufacturing process must be considered for the nose tile. The following discussion describes the optimization procedure applied to each subsequent conical segment i .

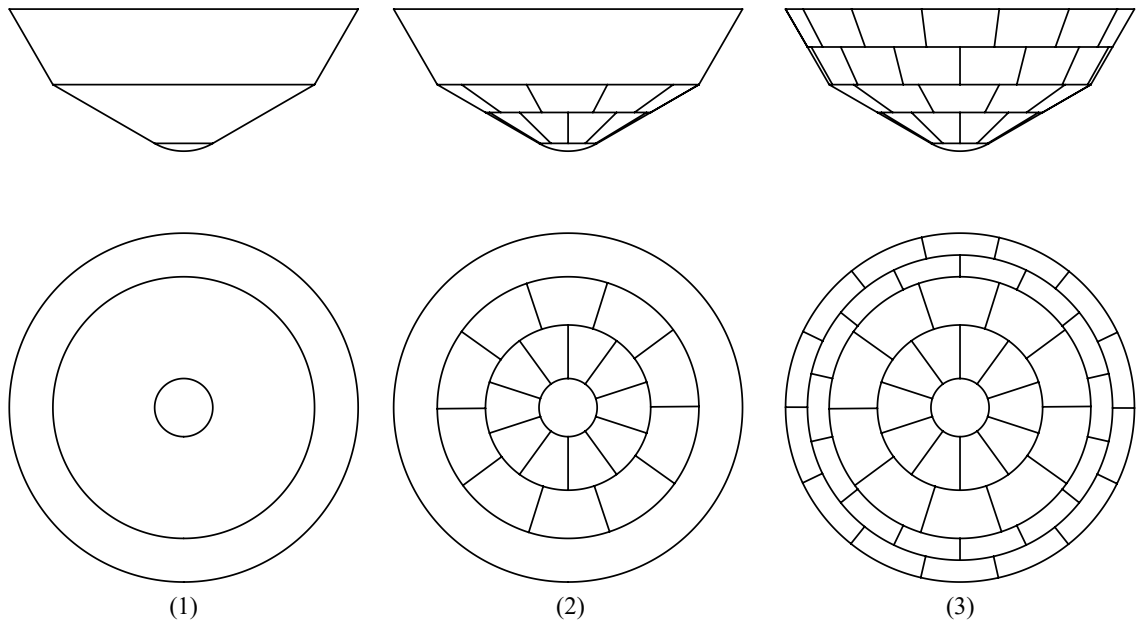


Figure 5.1: Approach to generating tile layout for a biconic aeroshell: (1) nose tile, (2) 1st conical flank, and (3) 2nd conical flank.

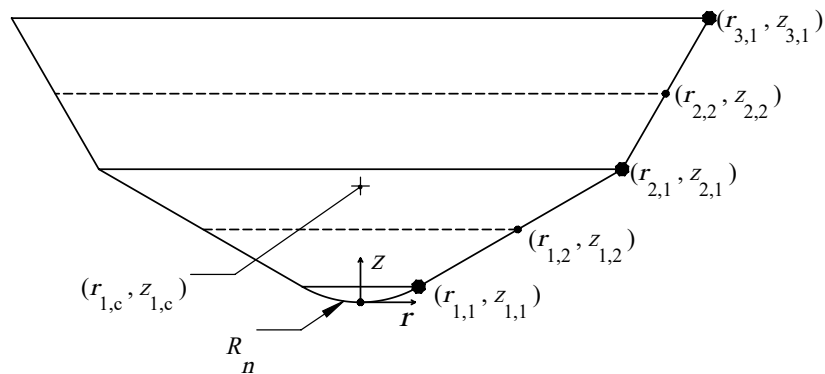


Figure 5.2: An example OML geometry illustrating geometry definitions.

5.2.2 Inputs

Inputs to the optimization include TPS geometry (OML segment geometry and desired TPS thickness, t_{TPS}), substrate geometry ($W_{\text{sub}}, L_{\text{sub}}$), and processing characteristics ($t_{\text{comp}}^{\text{max}}$, maximum processed material thickness, and ϵ_{IP} , in plane shrinkage). Finally, the minimum radius of curvature, R^{min} , and minimum seam angle, β^{min} , are required to enforce their respective constraints.

5.2.3 Optimization

Independent Variables

The independent design variables are the numbers of tiles in each concentric ring. Moving from the innermost to the outermost ring, these are denoted by $N_j, j \in [1, Q_i^{\text{min}}]$.

Dependent Variables

Dependent variables, computed quantities following from the design specification, include the dimensions of the curved tile as installed on the heatshield, the dimensions of the curved substrate, and the dimensions of the corresponding substrate once flattened. For example, the angle the curved tile spans on the heatshield, $\gamma_j = 2\pi/N_j$, is scaled up to a corresponding angle spanned by the substrate, γ_j^{sub} , and then transformed to a flat pattern angle, γ_j^f . Other parameters are similarly transformed (Figure 5.3). Note that these transformations are functionally dependent on segment geometry as well as the in plane material shrinkage during processing.

A sub-optimizer maximizes substrate side length l_j^{sub} given γ_j^f and $r_{i,j}^f$ by varying its angular orientation relative to one side of the substrate, δ (Figure 5.4). The problem is constrained by the substrate dimensions (width, W_{sub} , and length, L_{sub}), i.e. the flat pattern must reside within the rectangular footprint of the material. Thus, the maximum side length for a given orientation, $l_j^{\text{sub}} = l_j^{\text{sub}}(\delta)$, is contingent on the corner locations and, possibly,

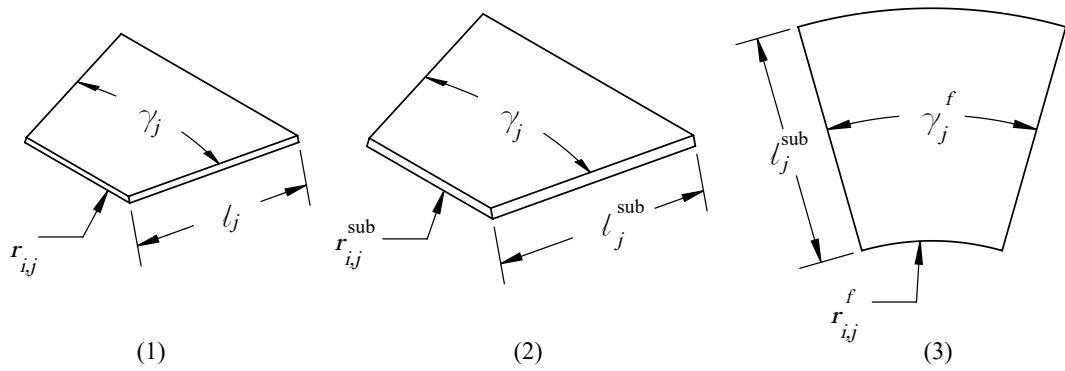


Figure 5.3: Transformation of (1) tile geometry to (2) scaled up substrate geometry to (3) two-dimensional flat pattern.

the outer radial arc.

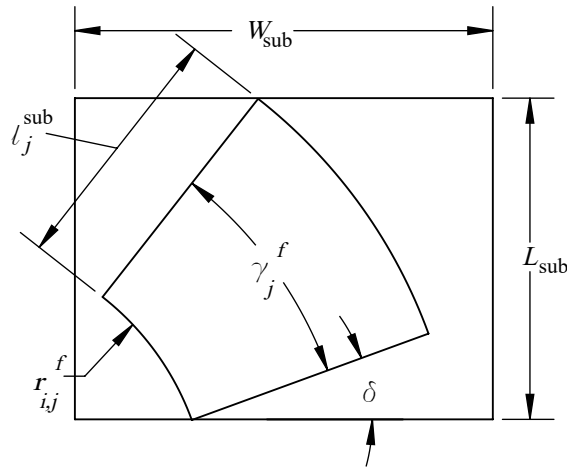


Figure 5.4: Illustration of the tile size optimization problem.

While a strictly geometric approach to the tile size problem does exist, it requires evaluating many cases in a network of conditional statements. Thus, optimization was selected for its relative simplicity over enumerating every possible geometric case. Once determined, maximum substrate length is then transformed back to a maximum tile length, l_j^{\max} , scaling by the shrinkage. That quantity, l_j^{\max} , is connected to the OML geometry through $l_j^{\max} = \sqrt{(r_{i,j+1} - r_{i,j})^2 + (z_{i,j+1} - z_{i,j})^2}$. Thus, the starting coordinate of each ring depends on that of the preceding one. In this way, tile layout is built radially outward.

Objective Function

The objective function minimized by the optimization routine is simply the sum of all N_j ,

$$f_{\text{obj},1} = \sum_{j=1}^{Q_i^{\min}} N_j \quad (5.1)$$

Constraints

The layout is subject to several constraints (Table 5.1) that ensure the design is manufacturable within size and curvature limitations and that seams of adjacent rings do not align. Manufacturing constraints are applied, first, by two inequalities: $t_{\text{TPS}} \leq t_{\text{comp}}^{\max}$ and $r_{i,j}^{\text{sub}} \geq R^{\min}$, $j = [1, Q_i^{\min}]$. The first inequality ensures that TPS thickness is not larger than that of the processed material. If this constraint is violated, the methodology terminates as no design would be feasible. Either the TPS thickness must be adjusted or another substrate must be selected. The second inequality enforces the limit on curvature. This inequality compares the minimum radius of curvature for each tile to the material constraint. If this second inequality is violated, the infringing tile(s) is (are) flagged, but the optimization continues. Flagging warns the designer that this tile geometry may present a challenge for VIP due to substrate wrinkling. An alternate design, material, or process may be required in these cases to avoid wrinkling. To ensure the set of N_j can fully span the OML segment, the sum of all l_j^{\max} must be greater than or equal to the total segment length, $\sqrt{(r_{i+1,1} - r_{i,1})^2 + (z_{i+1,1} - z_{i,1})^2}$.

The minimum seam angle constraint, β^{\min} , prevents radial seams of adjacent rings from being aligned. There are multiple seam angles between two adjacent rings j and $j + 1$, up to two adjacent seams per inner ring seam, or $2N_j$. Seams angles also depend on relative positioning (i.e., one ring can be rotated relative to the other). For example, $N_j = N_{j+1}$ could yield a minimum seam angle of zero (with all seams aligned) or $\frac{\pi}{N_j}$ (half the angular span of each tile). The latter quantity is the value used by the methodology, $\beta_{j,j+1}^{\min}$, the

largest possible minimum seam angle. This computation is described further in Appendix C. The minimum seam angles between all rings, i.e., all $\beta_{j,j+1}^{\min}$ $j \in [1, Q_i^{\min} - 1]$, must be larger than the minimum, or the design is infeasible. Finally, side constraints are imposed on the N_j to practically limit the design space.

Table 5.1: Summary of tiling constraints for OML segment i .

Description	Variable(s)	Constraint
Thickness	t_{TPS}	$t_{\text{TPS}} \leq t_{\text{comp}}^{\max}$
Radius of Curvature	$r_{i,j}$	$r_{i,j}^{\text{sub}} \geq R^{\min}, j \in [1, Q_i^{\min}]$
Segment Length	l_j^{\max}	$\sum_{j=1}^{Q_i^{\min}} l_j^{\max} \geq \sqrt{(r_{i+1,1} - r_{i,1})^2 + (z_{i+1,1} - z_{i,1})^2}$
Seam Angle	$\beta_{j,j+1}^{\min}$	$\beta_{j,j+1}^{\min} \geq \beta^{\min}, j \in [1, Q_i^{\min} - 1]$
Number of Tiles in Ring	N_j	$N_{\text{lb}} \leq N_j \leq N_{\text{ub}}$

Solver

The tile layout problem is a discrete one (i.e., a limited set of N_j), and the seam angle constraint significantly reduces the feasible design space. Thus, only a small subset of all possible designs typically needs to be fully evaluated, and, even then, the computation is quite fast. Thus, a full exploration of the design space is carried out, assuming t_{TPS} is feasible, generating every possible set of N_j that obeys the side constraints, N_{lb} and N_{ub} . The minimum seam angle is computed for each design, and those smaller than the constraint, β^{\min} , are eliminated. Resulting designs are then evaluated according to the radius of curvature and segment length constraints (Table 5.1). Designs violating the former constraint are flagged while designs violating the latter constraint are removed. Finally, the design that minimizes $f_{\text{obj},1}$ is selected from among the remaining feasible set. In the example presented later, the optimal tile layout was generated in only a few seconds in parallel with relatively modest processing power¹. Larger aeroshells, with several rings of

¹A single 6-core Intel Xeon E5-1650 v4 processor.

tiles, extend computation time but still only require a few minutes at most.

5.2.4 Outputs

Two outputs follow from the tiling procedure described above – the set of unique tile geometries and the corresponding substrate geometries required to make them. That is, for a tile layout design comprised in total of $Q = \sum_i Q_i^{\min}$ rings, there are Q tile geometries and Q substrate geometries. Recall that the substrate is scaled up from the final tile geometry to account for process shrinkage. Furthermore, the substrate geometries yielded by the procedure consist of both the two-dimensional flat pattern, used for cutting the substrate from the raw material, and the three-dimensional curved geometry, used in simulating the infusion process. The latter output is the subject of the next step outlined below.

5.3 Mold and Process Design

The next step of the methodology takes the set of substrate geometries generated above and simulates mold filling to produce an optimal mold design for each tile. Mold filling is simulated on the curved substrate geometry as it is draped in the mold. Designs are limited to single gate, single vent configurations as mentioned earlier. Generally speaking, the “best” designs are those that prevent voids from air entrapment during infusion, and the objective function quantifying that metric is discussed below. Leveraging the fact that TPS tiles are typically much smaller through the thickness than in plane, infusion is simulated on a two-dimensional shell to speed iteration. This simplification neglects through the thickness variation in substrate properties due to draping, but these variations are typically small for the materials and geometries here. Mold filling is simulated using Liquid Injection Molding Simulation (LIMS), a CV/FE simulation developed at the University of Delaware [82, 108], to compute the time of resin arrival across the part (time to fill, T_f).

5.3.1 Inputs

Inputs to the mold and process design steps include substrate geometry, material properties, and process settings. As described above, substrate geometry is that of the three-dimensional, curved material and is scaled up from the tile geometry to account for process shrinkage. Material properties include the porosity and permeability of the substrate, and the dynamic viscosity of the resin – the parameters appearing in Darcy’s law (Equation 1.6). Note that substrate quantities are for the material compressed in the mold. Thus, these are the pre-process quantities of the substrate: ϕ^{pre} and its corresponding K .

The final inputs form the boundary conditions for mold filling. These parameters are the gate design and the vent pressure. A circular, constant pressure gate with fixed radius, R_{gate} , is used here. Gate pressure is atmospheric pressure minus vent pressure, P_{vent} , where vent pressure is set to the vapor pressure of the resin solution.

5.3.2 Optimization

Independent Variables

Independent design variables describe the position of the gate relative to the curved substrate geometry: non-dimensional radial, λ_{gate} , and angular, Γ_{gate} , locations defined as fractions of substrate length, l_j^{sub} , and angular span, γ_j^{sub} ,

$$\lambda_{\text{gate}} = \frac{l_{\text{gate}}}{l_j^{\text{sub}}} \quad (5.2)$$

$$\Gamma_{\text{gate}} = \frac{\gamma_{\text{gate}}}{\gamma_j^{\text{sub}}} \quad (5.3)$$

where both quantities can range from [0,1]. Note that the vent is implicitly assumed to be located at the last point reached by the flow. Thus, vent location is not controlled by the optimization but is instead dependent on the other simulation parameters.

Mesh Generation

Two-dimensional finite element meshes are automatically generated in gmsh using meshing rules generalized to an arbitrary tile geometry and gate location. Element sizes scale proportionally with tile size maintaining an approximately constant number of elements along the perimeter, n_{el} . Elements are concentrated near the gate to capture rapid flow advancement in that region. Element sizing and mesh convergence are discussed further in Appendix D. An example mesh generated using the selected spacing rules ($n_{el} = 200$) is depicted in Figures 5.5 and 5.6. The former, a top down view, shows element clustering at the gate while the latter, a side view, shows part curvature.

According to Šimáček and Advani, the 2-D shell approximation is appropriate for most simulation tasks, assuming the aspect ratio of the part is small [108]. The authors note that the relevant aspect ratio, a_r is not simply geometric (i.e., part thickness divided by its length) but must be adjusted by the ratio of in plane and through thickness permeability,

$$a_r = \frac{t^{\text{pre}} \sqrt{\frac{K_{\text{IP}}}{K_{\text{TT}}}}}{L_c} \quad (5.4)$$

Beyond a characteristic length, L_c , flow is essentially two-dimensional with no pressure gradient (and no flow velocity) through the thickness. Šimáček and Advani do not identify a specific constraint on the aspect ratio, only suggesting that full 3-D modeling may be necessary when this adjusted part thickness is comparable to the planar dimensions. In this work, where K_{IP} and K_{TT} are of approximately the same order of magnitude, Equation 5.4 can be reduced to the geometric aspect ratio, and a_r is around 0.02 to 0.03, assuming parts approximately 1 meter across with thickness, t^{pre} , of 1 inch (2.54 cm). Three-dimensional modeling is not carried out during optimization to speed iteration, but it is performed after gate selection to compute time to fill in the actual process, which is not accurately generated in the 2-D simulation.

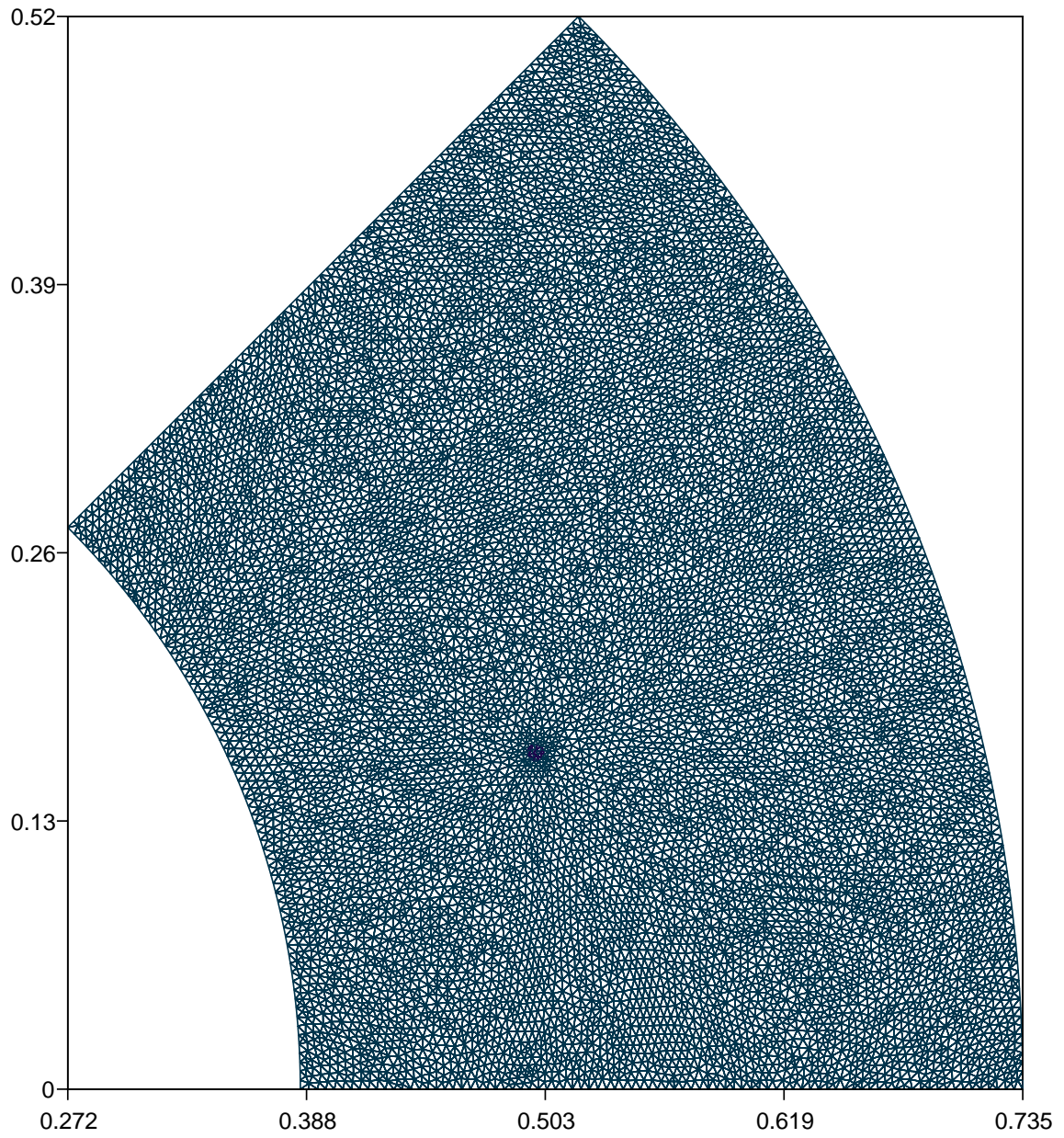


Figure 5.5: An example two-dimensional finite element mesh used to simulate mold filling (top view).

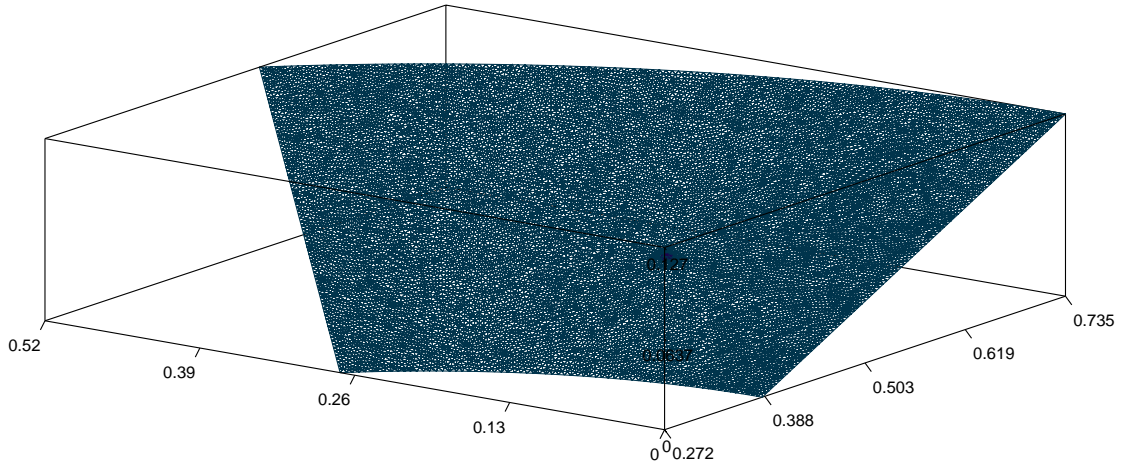


Figure 5.6: An example two-dimensional finite element mesh used to simulate mold filling (side view).

Objective Function

Each mold design is evaluated according to the objective function,

$$f_{\text{obj},2} = \frac{p'}{p_{\text{total}}} \quad (5.5)$$

where p' is the length of the perimeter blocked from the vent during processing and p_{total} is the total perimeter length. Thus, $f_{\text{obj},2}$ ranges from $[0,1]$ and reflects the proportion of the perimeter that is blocked (i.e., unfilled with no path for air to escape through the vent).

Practically, $f_{\text{obj},2}$ quantifies the degree of air entrapment during infusion, which can lead to incomplete filling and voidage. Minimizing $f_{\text{obj},2}$ limits this risk, ensuring complete saturation of the substrate. Mold filling is simulated on the specified design, and then time to fill is extracted for nodes along the perimeter of the part. This yields the time to fill as a function of distance along the perimeter, $T_f(p)$, which is operated upon to compute p' (Figure 5.7). Note that two curves are plotted, one for each direction around the perimeter. Each curve begins and ends at the same location and time – the first and the last point reached by the flow, respectively. Blocked regions correspond to a pair of perimeter points

with the same time to fill $T_f(p_{j+1}^*) = T_f(p_j^*)$, where $p_{j+1}^* > p_j^*$. That is, the flow front has reached two different locations on the perimeter at the same time. The length of all blocked regions are summed to yield the total blocked length.

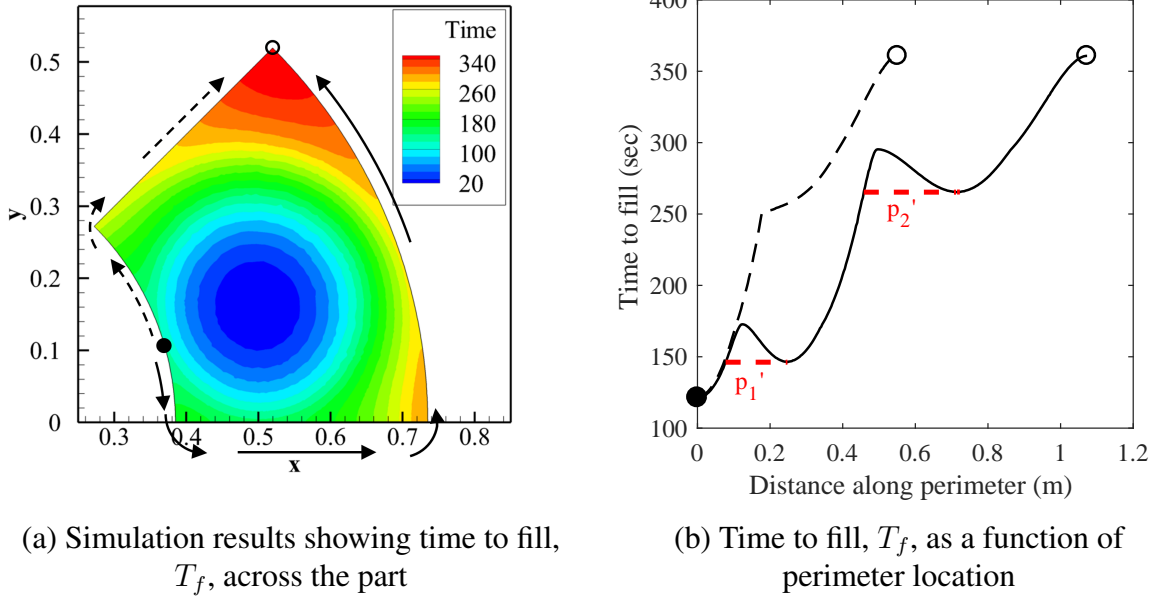


Figure 5.7: Results of a mold filling simulation and those results extracted along the perimeter.

This definition of blocked length was extended to include regions on the perimeter where flow arrives at nearly the same time, which is also a concern in processing. An additional term added to p' , which is discussed in Appendix D, addresses this issue. The computational algorithm is also outlined in more detail there.

Constraints

Gate location is constrained so that it falls within the two-dimensional footprint of the tile. A keepout area offset by R_{gate} from the perimeter enforces this requirement. The mathematical constraints are summarized in Table 5.2. Note that the upper bound on Γ_{gate} leverages the fact that tiles are symmetric down the midline and thus only one half of the tile need be considered. Angular position is generated such that $\Gamma = 0$ corresponds to a

gate tangent to the side of the tile irrespective of λ_{gate} .

Table 5.2: Constraints on mold design.

Description	Variable	Type	Constraint
Radial position	λ_{gate}	Side	$\frac{R_{\text{gate}}}{l_{\text{sub}}} < \lambda_{\text{gate}} < 1 - \frac{R_{\text{gate}}}{l_{\text{sub}}}$
Angular position	Γ_{gate}	Side	$0 \leq \Gamma_{\text{gate}} \leq 0.5$

Solver

Because the objective function, $f_{\text{obj},2}$, is computed from a numerical simulation with limited resolution, results are discontinuous and non-differentiable which pose a problem for traditional gradient-based methods. Furthermore, the design space frequently possesses several local optima which should be rejected in favor of the global optimum. Particle swarm optimization (PSO), a metaheuristic method, was selected as the solver because it does not use the gradient, performs broad exploration of the design space, and does not rely on a discretization of the design space. It can also be run in parallel to speed design evaluation. Though global optimality is not guaranteed, in practice, PSO was found to converge to the global optimum quickly (on the order of a few minutes) in the example problems below using the processor identified previously¹. PSO was implemented in MATLAB using the `particleswarm` function with a swarm size of 20 particles. Function tolerance, which controls convergence and ultimately termination of the algorithm, was set to 1×10^{-3} which is just below the resolution of the objective function at the selected element sizing (see Appendix D.2). Iteration was terminated after 10 successive generations where the relative change in the minimum objective value was less than the function tolerance.

5.3.3 Outputs

The optimal gate location, denoted $(\lambda_{\text{gate}}^*, \Gamma_{\text{gate}}^*)$, minimizes $f_{\text{obj},2}$ for the given geometry, material and process parameters. Optimal vent location, $(\lambda_{\text{vent}}^*, \Gamma_{\text{vent}}^*)$, is subsequently

set to the last point reached by the flow. Mold filling is then simulated on the full three-dimensional geometry using the selected gate location to obtain total infusion time and resin consumption. Additional thickness must be added to the 3-D geometry to account for top and bottom shims. These quantities, as well as vent (or vapor) pressure, which was estimated in Chapter 4, are important parameters both for the designer and for those processing the material. For example, knowing mold filling time helps a process technician anticipate when flow must be shut off, and vent pressure indicates the setting for the vacuum pump during processing. From a broader perspective, mold filling time and resin consumption impact the overall process timeline and cost. Relevant properties of the fabricated TPS material are also important outputs for the designer, and these quantities are the subject of the last step of the methodology.

5.4 TPS Material Property Estimation

In the final step, selected properties of the fabricated composite TPS material (virgin density, ρ_{comp} ; char yield, Y_{comp} and resin mass fraction, w_{resin}) are computed using the constitutive model in Chapter 2. That chapter reduced these properties to functions of known, or previously computed, densities. Nominal values are computed using expressions in Table 2.3 with bounds generated from those in Table 2.4.

5.5 Summary

This chapter described an integrated approach to tile layout, mold design, and TPS material property estimation for a conformal heatshield. Optimal tile layouts for sphere-cone aeroshells were generated that minimize the total of tiles while meeting constraints on tile size, curvature, and minimum seam angle. A simple, but fast, solution approach was implemented which evaluated the feasibility of the entire design space then selected the best design. Resulting geometries were then fed to a Darcy's law-based simulation to design a mold for processing each tile using VIP. Gate locations were evaluated by an objective

function, the blocked length, quantifying the degree of air entrapment during infusion. Particle swarm optimization identified the gate that minimized this function and, thus, best limited the risk of air entrapment. Vents were located at the last point reached by resin flow. Finally, results from Chapter 2 were used to estimate the virgin density, resin mass fraction, and char yield of the final TPS material.

Combined with the previous chapter, the results of this chapter form a powerful, conceptual framework for evaluating and manufacturing conformal ablative heatshields. The integrated, automated methodology improves on state-of-the-art approaches, which rely on segregated, manual, ad hoc methods tailored to a specific material and aeroshell geometry. Heatshield designs, and the molds to manufacture them, can be automatically generated for a range of materials and geometries reducing design time and freeing the designer to rapidly evaluate alternative compositions and their impact on processing and properties. In the next chapter, the methodology is demonstrated on two design scenarios.

CHAPTER 6

APPLICATIONS OF THE DESIGN METHODOLOGY

This chapter presents two applications of the design methodology, which demonstrate the capability of the integrated, yet decoupled, approach. First, the full methodology – from material specification to tile layout to tooling – was applied to the design of a 4.5-meter diameter, 70 degree sphere-cone conformal PICA heatshield. Second, mold design was independently demonstrated on a prescribed tile geometry, that selected for experimental processing in Chapter 3. Optimal gate and vent locations were translated to the mold design shown previously in that chapter. Theoretical flow times were compared against the experimental process to assess simulation accuracy.

6.1 Design of a Conformal PICA Heatshield

Heatshield design was based on the MSL forebody geometry shown previously in Figure 3.2 (a 4.5-meter diameter, 70 degree sphere-cone [26, 91]) and the C-PICA formulation used throughout this work. TPS thickness was set to $t_{\text{TPS}} = 0.75$ inches in order to obey the maximum manufacturable thickness for this material, $t_{\text{comp}}^{\text{max}}$. Substrate size was 1 meter by 1 meter. Reflecting typical results from Chapter 3, shrinkage was 1% in plane and 4% through the thickness with post-process reduction of 1% due to machining. Some resin quantities again appear as the nondimensional values from Chapter 4. Estimated resin properties were used here, but experimental quantities may improve the accuracy of the simulation. Post-process resin density and resin char yield were drawn from Chapter 2 results ($\rho_{\text{resin}}^{\text{post}} = 0.187$ g/cc and $Y_{\text{R}} = 52\%$). Other parameters for the design are summarized in Table 6.1, which lists primary inputs, and Table 6.2, which lists secondary inputs.

Table 6.3 indicates the constraints on the design. Minimum radius of curvature, R^{min} , was based on a manufacturer recommendation for this felt ($R^{\text{min}} = 0.15$ m). The lower and

upper bounds on the number of tiles, N_{lb} and N_{ub} , respectively, were selected to practically limit the design space. It is not feasible to conform a single annular tile, $N_{lb} = 1$, to the three-dimensional shape without significant wrinkling. Above $N_{ub} = 60$, tile size is so narrow as to be counterproductive. In any case, these bounds did not affect the resulting optimum and could be adjusted for other designs as necessary.

Table 6.1: Primary inputs for the example design.

Category	Parameter	Value	Units
Substrate	W_{sub}	1.0	m
	L_{sub}	1.0	m
	t_{sub}	0.88	in
	Δt_{sub}	0.08	in
	ρ_{sub}^{areal}	0.194	g/cm ²
Resin	ρ_{fiber}	1.395	g/cc
	d_{fiber}	11	μ m
	ρ_{resin}^{post}	0.187	g/cc
Composite	Y_R	52	%
	ϵ_{TT}	0.04	m/m
	ϵ_{IP}	0.01	m/m
Process	ϵ_M	0.01	m/m
	R_{gate}	0.125	in
	P_{gate}	101325	Pa

Table 6.2: Secondary quantities computed for the example design.

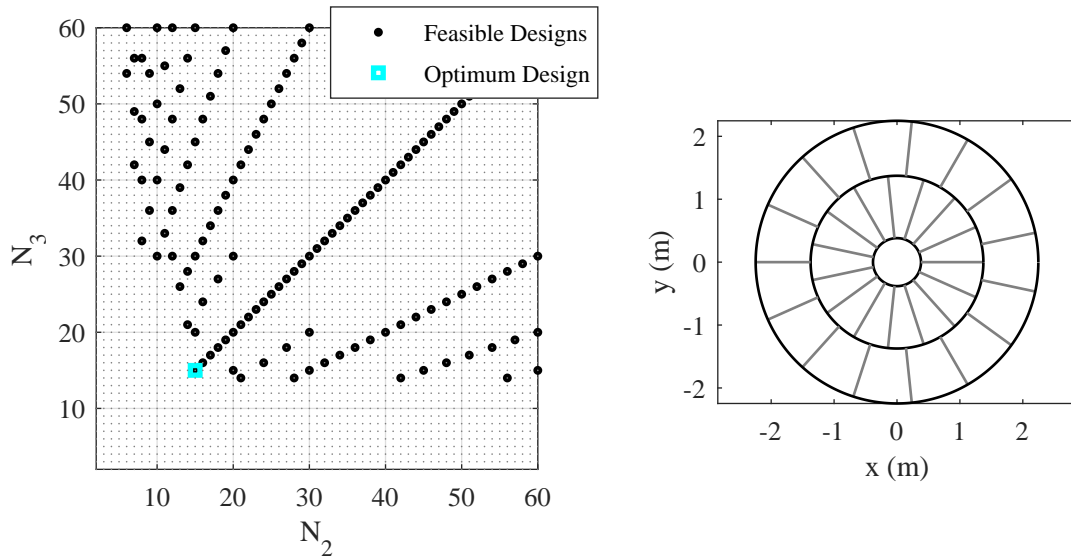
Category	Parameter	Value	Units
Substrate	ρ_{sub}^{pre}	0.095	g/cc
	ϕ^{pre}	0.93	–
	K	2.34×10^{-10}	m ²
Resin	μ_{sol}^*	0.87	–
	$P_{vap,sol}^*$	0.97	–

Table 6.3: Summary of design constraints for the example.

Description	Variable(s)	Value	Units
Maximum TPS Thickness	$t_{\text{comp}}^{\text{max}}$	0.76	in
Minimum Radius of Curvature	R^{min}	0.15	m
Minimum Seam Angle	β^{min}	3	deg
Minimum Number of Tiles in Ring	N_{lb}	2	non-dimensional
Maximum Number of Tiles in Ring	N_{ub}	60	non-dimensional

6.1.1 Tile Layout

The optimal tile design consists of a single nose tile, and a flank formed from two rings of 15 tiles each ($N_1 = 1$, $N_2 = 15$, and $N_3 = 15$). The design space for the nose is trivial – the nose is small enough to be fabricated from a single piece of the substrate material. The



(a) Design space

(b) Optimal layout (front view)

Figure 6.1: Tile layout for the example heatshield.

design space for the conical segment is depicted in Figure 6.1(a) with N_3 plotted against N_2 . Feasible designs are plotted with the design minimizing $f_{\text{obj},1}$ highlighted. Note that the feasible space is bounded on the left and the bottom by, respectively, $N_2 = 6$ and $N_3 = 14$. That is, no design spans the conical segment if either N_2 or N_3 falls below its respective bounding value. Note also that the minimum seam angle constraint substantially reduces

the number of feasible designs, and these designs tend to fall along lines where N_2 and N_3 are integer multiples of one another (e.g., $N_2 = N_3$, $N_2 = 2N_3$, etc.). Figure 6.1(b) depicts a front view of the optimal layout with $N_2 = 15$ and $N_3 = 15$. The seam angle offset is trivial in this case, as $N_2 = N_3$. Therefore, the each radial seam in the outer ring is offset from the inner ring by the angle $\frac{\pi}{N_2}$. This layout, and the corresponding substrate geometries (three, in total), were passed to the next step for mold and process design.

6.1.2 Mold and Process Design

Results of mold and process design for each of the three tile geometries, depicted in Figures 6.2 – 6.4, are discussed below. In each case, the full design space was generated first followed by solution of the optimal gate location using PSO, shown in the plots on the left. Mold filling was then simulated on the three-dimensional geometry using the selected gate location. Those results are depicted in the plots on the right, which show contours of flow position over time (time to fill, T_f , in seconds) on the tile geometry. These locations and final processing parameters are summarized in Table 6.4.

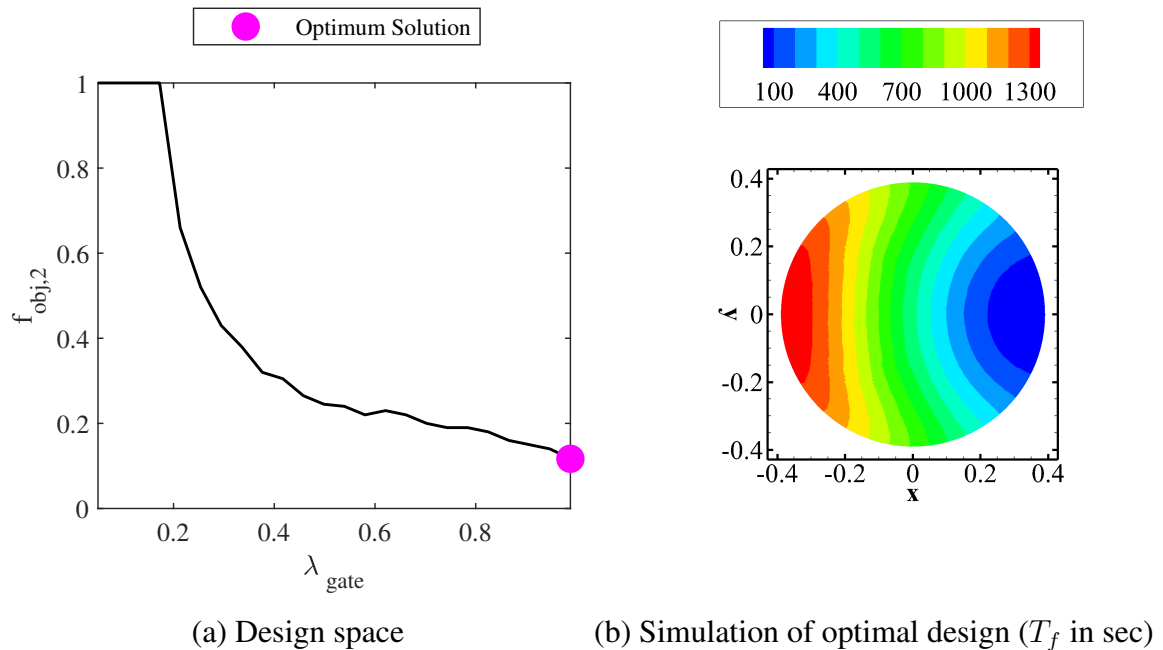
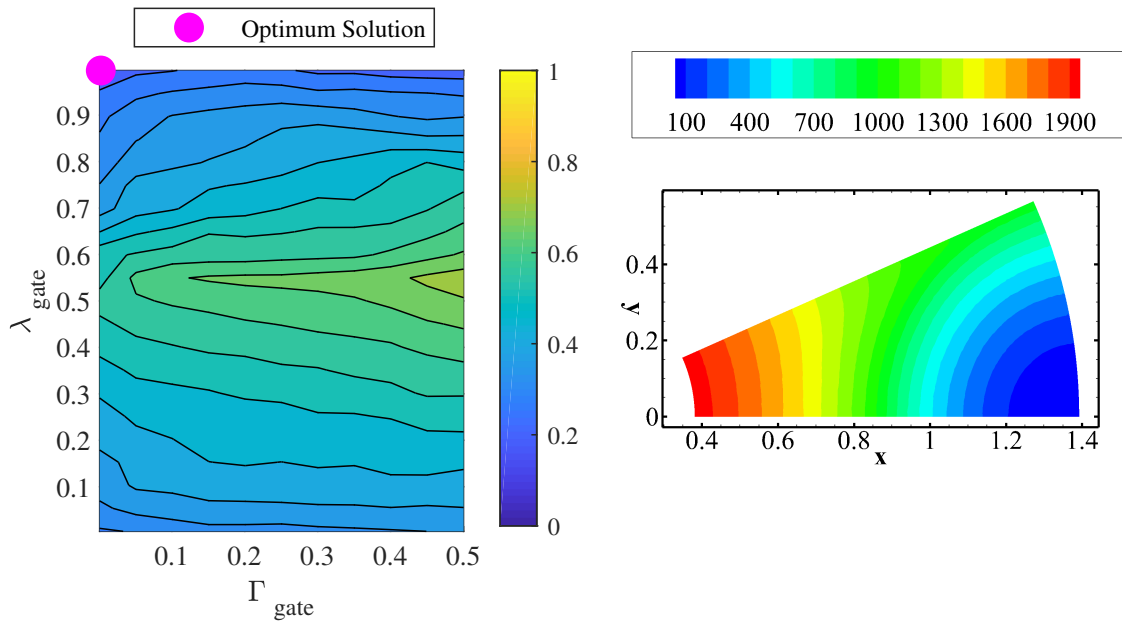


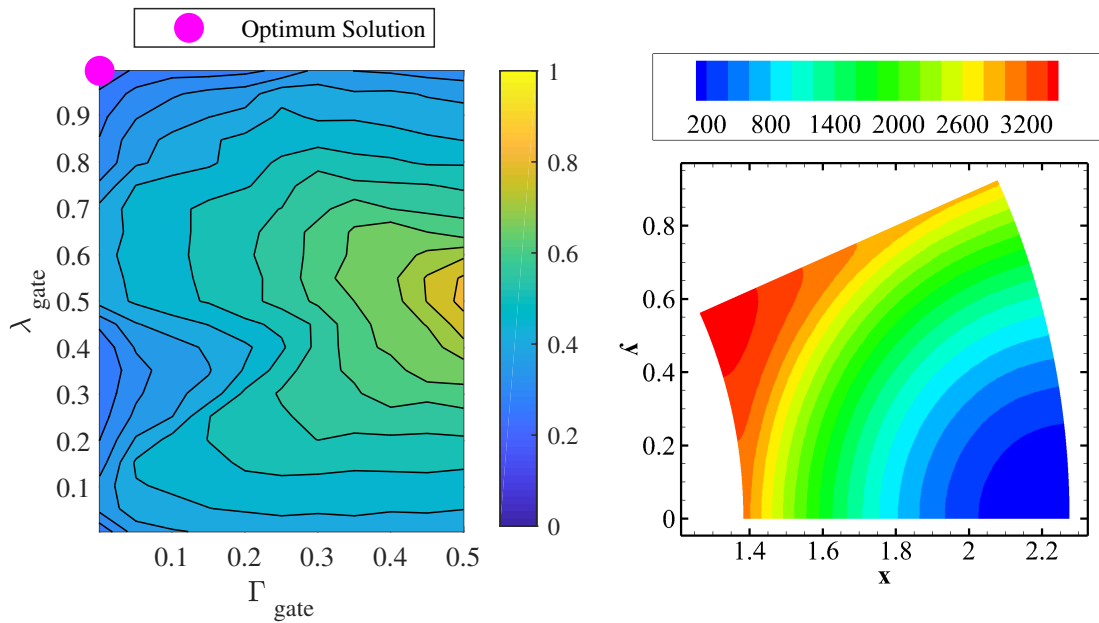
Figure 6.2: Mold design results for nose tile.



(a) Design space

(b) Simulation of optimal design (T_f in sec)

Figure 6.3: Mold design results for the inner ring tile of the conical flank.



(a) Design space

(b) Simulation of optimal design (T_f in sec)

Figure 6.4: Mold design results for the outer ring tile of the conical flank.

Nose Tile

Figure 6.2 depicts results for the nose tile. Due to symmetry, there is no dependence on Γ_{gate} and only λ_{gate} was varied. In this case, λ_{gate} was defined as a fraction of arc length, from the stagnation point ($\lambda_{\text{gate}} = 0$) to the outer radius ($\lambda_{\text{gate}} = 1$). The value of the objective function is $f_{\text{obj},2} = 1$ with a centrally located gate $\lambda_{\text{gate}} < 0.16$, decreasing and reaching a minimum at the perimeter ($f_{\text{obj},2} = 0.12$). The optimal gate location is on the edge ($\lambda_{\text{gate}}^* = 0.988$) with the vent directly opposite ($\lambda_{\text{vent}}^* = -0.988$).

The flow front is circular for an isotropic material such as this, so a centrally located gate, $\lambda_{\text{gate}} = 0$, produces a front that reaches every point on the perimeter at the same time and $f_{\text{obj},2} = 1$. Any off center position, $\lambda_{\text{gate}} > 0$, yields a flow front that arrives at the perimeter at a single point, and its location along the perimeter increases monotonically with time from that point to the last point reached by the flow. However, the objective function, which includes perimeter regions with similar flow times, preferences gate locations near the edge that maximize flow velocity along the perimeter.

Inner Ring Tile

Figure 6.3 depicts results for the inner ring tile of the flank. Both λ_{gate} and Γ_{gate} were varied to produce the two-dimensional design space. The best designs occur along the inner and outer radii of the tile with the optimum solution found at the outer corner ($\lambda_{\text{gate}}^* = 0.996$, $\Gamma_{\text{gate}}^* = 0.003$) with $f_{\text{obj},2} = 0.20$. In that design, flow becomes nearly parallel approaching the inner edge, occurring between 1500 and 1600 sec in Figure 6.3(b). Thus, flow arrives all along the inner edge at nearly the same time making the angular location of the vent, Γ_{vent}^* , somewhat irrelevant, though the result from the simulation is indicated ($\lambda_{\text{vent}}^* = 0$, $\Gamma_{\text{vent}}^* = 0.893$). While similar arrival time along the inner edge may indicate risk of air entrapment, the overall volume blocked, if any, would be small.

Outer Ring Tile

Figure 6.4 depicts results for the outer ring tile. Like the inner ring tile, the best designs occur with the gate located along the inner and outer radii. The optimal gate location is again at the outer corner of the part ($\lambda_{\text{gate}}^* = 0.996$, $\Gamma_{\text{gate}}^* = 0.001$) where $f_{\text{obj},2} = 0.21$. Unlike the inner ring tile, the flow clearly converges to a single point at the vent location ($\lambda_{\text{vent}}^* = 0$, $\Gamma_{\text{vent}}^* = 1$).

Summary

In general, the worst designs, with the highest objective function value, occur with gate locations near the center of the tile ($\lambda_{\text{gate}} = 0.5$, $\Gamma_{\text{gate}} = 0.5$). In those designs, large regions of the mold are cut off from the vent by advancing flow and have a high likelihood of air entrapment causing partial saturation and voidage. The objective function value decreases

Table 6.4: Summary of optimal gate and vent positions and process parameters for each tile.

Category	Parameter	Units	Nose Tile	Inner Ring Tile	Outer Ring Tile
Mold Design	λ_{gate}^*	–	0.988	0.996	0.996
	Γ_{gate}^*	–	–	0.003	0.001
	λ_{vent}^*	–	–0.988	0	0
	Γ_{vent}^*	–	–	0.893	1
Process Parameters	Time to Fill	min	23.2	32.6	58.9
	Resin Consumption	L	11.38	9.35	17.00

as the gate shifts away from the center towards the edges indicating lower risk of air entrapment. Optimal gate, and corresponding vent, positions are summarized in Table 6.4 along with final process parameters, time to fill and resin consumption, generated for the three-dimensional parts. Time to fill and resin consumption are both highest for the largest tile (outer ring tile). Interestingly, fill time is longer for the inner ring tile than the nose tile. Though the inner ring tile is smaller in total volume, the flow length from gate to vent is

longer. Cumulative infusion time was 1395.7 min (≈ 23 hrs) though this could be reduced by infusing several parts simultaneously. Also, recall that other phases of processing (e.g., curing and drying) also contribute significantly to time but are not considered in this total. Total resin consumption was 406.6 L combined for all 31 tiles of the heatshield.

6.1.3 TPS Material Property Estimation

Table 6.5 compares nominal estimated TPS properties to a C-PICA material model from Milos, et al. [38]. Deviations from the reference material can be attributed in part to a difference in substrate densities, which are also included in the table, because substrates are more compressed in the VIP process leading to higher fiber fraction and lower resin loading. In this case, substrate density was predicted to be about 10% higher for the VIP-produced material, which results in slightly higher virgin density and lower resin mass fraction compared to the reference material. Predicted char yield was found to be slightly elevated, a difference attributed to both lower substrate density and a lower nominal resin char yield ($Y_R = 45.9\%$) in the reference material. The reference model based char yield on room temperature mass, capturing an additional reaction around 150°C which lowered the final yield. Here, char yield was computed relative to sample mass at 150°C , ignoring the earlier reaction which was believed to stem from additional solvent loss and not resin decomposition.

Table 6.5: Estimated final TPS properties compared to reference values.

Property	Units	Predicted	Reference**
$\rho_{\text{sub}}^{\text{post}}$	g/cc	0.101	0.092
ρ_{comp}	g/cc	0.275	0.273
w_{resin}	non-dimensional	0.63	0.66
Y_{comp}	%	69.7	64.2

**Material model parameters for C-PICA [38].

6.2 Design of Mold for Experimental Processing

The experimental mold of Chapter 3 was evaluated using the mold design approach in Section 5.3. Tile geometry, shown previously in Figure 3.8, was input directly into the mold filling simulation as an a priori input, bypassing tile layout. Material property inputs were identical to those outlined previously in Tables 6.1 and 6.2. Gate radius was slightly larger than the above example to match an available drill bit size ($R_{\text{gate}} = 0.166$ in). Simulated vent pressure was matched to the experimental setting in Table 3.2.

6.2.1 Mold Design

Figure 6.5(a) depicts the design space for the selected tile geometry with the optimal gate location highlighted at $\lambda_{\text{gate}}^* = 0.012$, $\Gamma_{\text{gate}}^* = 0.001$. Unlike the mold designs above, the optimal gate location is at the inner corner of the tile. Time to fill for the selected design is shown on the right (Figure 6.5(b)). Like the outer ring tile above, flow converges to a single point at the vent, in the opposite corner of the part. Note that time to fill is shown for Tile 2 with $P_{\text{vent}}^* = 1.5$. These results, summarized later in Table 6.6, vary between tiles due to differences in vent pressure. Gate and vent locations were translated to the tooling design, shown in Figure 6.6 rotated to match the orientation of the simulation result. The actual locations were offset slightly from the edge of the core to maintain a minimum wall thickness.

6.2.2 Time to Fill Results

Time to fill was obtained experimentally at four locations in the mold: the three pressure gauges located along the centerline of the part and at the vent, which was the last point reached by the flow. As explained in Chapter 3, some bubbles appeared at the vent prior to arrival of the main flow front. Flow front arrival was clearly distinguishable though, producing a continual flow of resin out of the vent and into the trap. It was this arrival

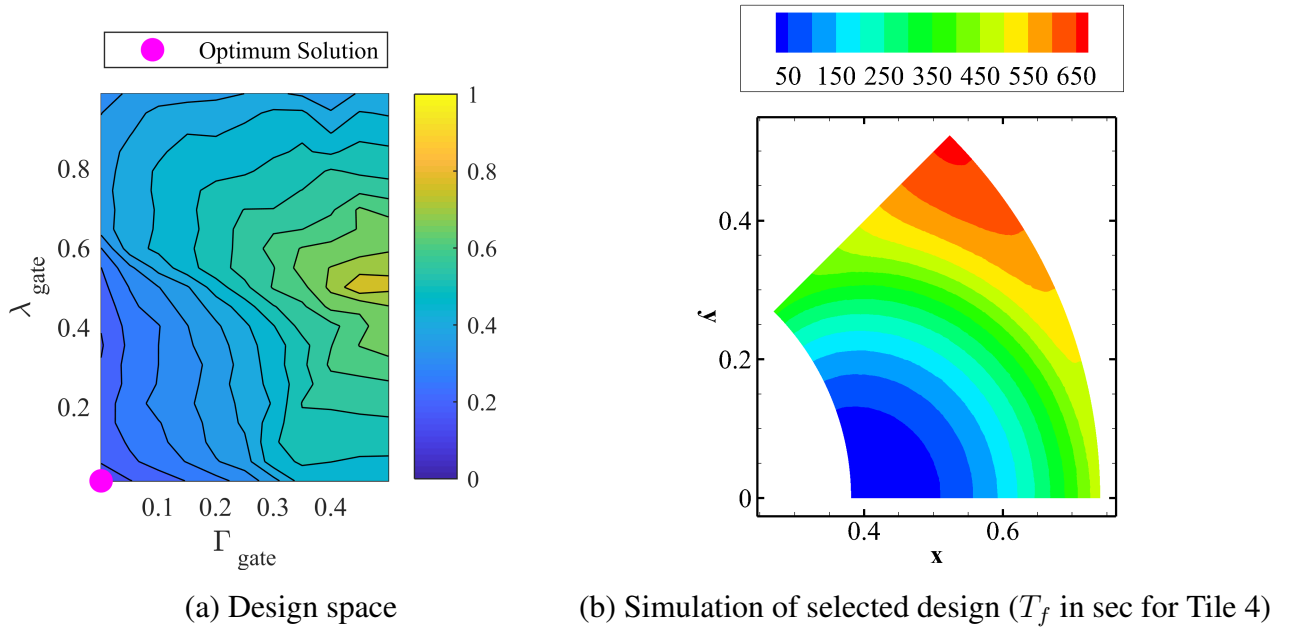


Figure 6.5: Mold design results for experimental tooling.

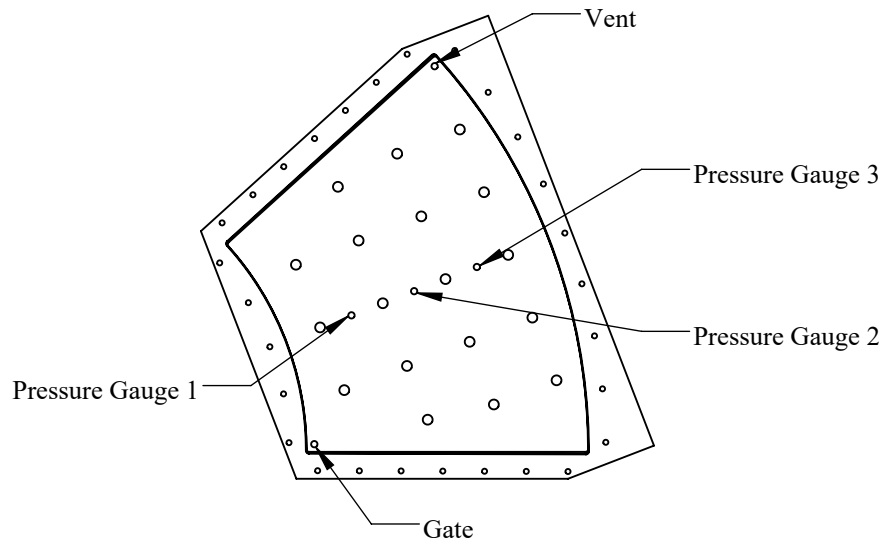


Figure 6.6: Mold top showing selected gate and vent placement, and pressure gauge locations.

time that was recorded as the total fill time. Arrival times at the centerline gauges, shown installed in the mold top in Figure 3.10, were identified by an increase in pressure. Table 6.6 compares experimental, T_f^{exp} , to simulated, T_f^{sim} , arrival times at each of these four locations with the relative difference between the two indicated. Pressure gauge locations, indicated in Figure 6.6, are numbered sequentially in order of flow arrival. Note that the first pressure gauge malfunctioned while infusing the first tile, and no reading was obtained.

Table 6.6: Time of flow arrival at pressure gauges and vent, experimental and simulated values.

Loc.	Tile 1			Tile 2			Tile 3			Tile 4		
	T_f^{exp} (sec)	T_f^{sim} (sec)	Diff. (%)	T_f^{exp} (sec)	T_f^{sim} (sec)	Diff. (%)	T_f^{exp} (sec)	T_f^{sim} (sec)	Diff. (%)	T_f^{exp} (sec)	T_f^{sim} (sec)	Diff. (%)
1	—	107	—	89	107	20	117	114	-3	134	108	-19
2	239	204	-15	173	203	17	192	218	14	253	207	-18
3	289	367	27	236	365	55	256	393	54	343	371	8
4	408	645	58	324	648	100	457	693	52	522	655	25

6.2.3 Discussion

The order of filling (Gauges 1, 2, and 3, then the vent) was correctly predicted by the simulation. Furthermore, material characterization, discussed previously in Chapter 3, demonstrated little, if any, air entrapment during filling. No significant in depth voidage was found in any locations, and nearly identical volumes of resin were delivered in all but the first run (which differed in its experimental setup). Together, these results indicate that the gate and vent placement generated by the methodology successfully avoided air entrapment as intended.

Arrival times at the first two gauges match reasonably well (within $\sim 20\%$ of the experimental results) but vary more significantly at Gauge 3 and the vent, which is overpredicted by up to 100%. Figure 6.5(b) shows the flow front interacting with the far walls of the cavity and changing shape between arrivals at Gauges 2 and 3. Initially, flow contours form concentric rings centered around the gate. Once flow reaches the far walls, the flow front

becomes more linear extending diagonally across the part. It is possible that the simulation does not capture the wall interaction precisely, particularly due to the presence of resin bubbles along the flow front which could influence behavior along the boundary.

Furthermore, the simulation relied on estimations of permeability, porosity and viscosity from Chapter 4 and did not account for variation in resin temperature (which was between 18°C and 23°C during testing). More accurate, experimentally-derived properties would likely improve simulation results. Indeed, the methodology allows input of known properties in place of estimations as material characterization improves. However, the use of estimated parameters here was consistent with the aim of the methodology — conceptual evaluation of new materials lacking that characterization. Estimated time to fill can also help guide processing. For example, in this work, estimated total fill times (~10–11 minutes) provided a useful order of magnitude approximation to the actual infusion (~5–9 minutes), allowing anticipation of vent arrival and subsequent valve closure to stop flow.

6.3 Summary

The design methodology was demonstrated on a 4.5-meter, 70 degree sphere-cone, conformal PICA heatshield. The optimal tile layout consisted of 31 tiles in total – a single nose tile and two rings of 15 tiles covering the flank. Mold design preferred gate locations on the edges of the part because central locations led to a large amount of blockage. Optimal gate locations were on the outer radius of the nose tile and at the outer corners of both flank tiles. The heatshield consumes around 400 L of resin in total with individual infusion times from 20–60 minutes. Predicted substrate density was slightly higher compared to a C-PICA reference model, leading to slightly higher virgin density and lower resin mass fraction. Predicted composite char yield was distinctly higher than the reference due to differences in the computation of the resin char yield.

Mold design was then applied, independently of the other tasks, to the prescribed tile geometry of Chapter 3. In this example, the optimal gate location was determined to be at

the inner corner of the part with the vent placed at the opposite outer corner. Experimental flow times, measured at four mold locations, agreed well at the nearest two pressure gauges but deviated more substantially at larger distances. Nonetheless, flow progression matched qualitatively (i.e. the sequence of flow front arrival at each location), and theoretical fill times were sufficiently accurate enough to inform actual processing. Significantly, processing yielded well-infused tiles with no observed air entrapment, which is itself a validation of the mold design.

While the optimal gate locations were somewhat trivial in these examples, always occurring on the perimeter of the parts, and specifically one of the corners for the conical tiles, other configurations necessitate the optimization approach developed here. More complex tile geometries such as asymmetric, and/or concave shapes yield more complicated flow patterns which are difficult to predict a priori. Furthermore, a two-dimensional line gate, suggested for future work in Chapter 7, would more or less require the numerical approach.

CHAPTER 7

SUMMARY AND FUTURE WORK

7.1 Summary of Contributions

This thesis developed a novel manufacturing process, VIP, that improves efficiency over the existing open process, reducing waste and other manufacturing byproducts, and allowing numerical simulation of the manufacturing process. A computational framework describing that process, and the materials used, optimized a conformal heatshield design for VIP. A short summary of each contribution is described below.

7.1.1 Formulation of A Constitutive Model of Fiber Substrate Ablators for Conceptual Design

A constitutive model of fiber substrate ablaters was developed in Chapter 2, combining a filamentary analog model of the substrate with known properties of the resin. Blending individual properties of the constituents yielded closed-form expressions describing the virgin density, resin mass fraction, and char yield of the composite TPS material. Predictions were compared to experimental results for two C-PICA variants, showing generally good agreement. Estimation of TPS properties reduces experimental burden and accelerates evaluation of alternative compositions during conceptual design. Property bounds formulated from the closed-form expressions quantified TPS variability, and a Monte Carlo simulation assessed the sensitivity to the input parameters that drive uncertainty. Results in Chapter 2 were central to the rest of the thesis – providing a check on experimental results in Chapter 3 and forming the foundation for material property estimation in the design methodology of Chapters 4 and 5 and the design example in Chapter 6.

7.1.2 Development and Demonstration of a Vacuum Infusion Process for Conformal Ablative

TPS Materials

Chapter 3 described the vacuum infusion process for conformal ablators. Compared to state-of-the-art processing, VIP reduces resin consumption and waste, simplifies clean up, eliminates the need for a vacuum oven (or chamber), and ultimately reduces labor and cost. VIP was demonstrated at a relevant scale, fabricating several large C-PICA tiles. Tiles were generally well infused in depth, and material properties compared favorably to theoretical predictions from Chapter 2. Deviations in properties between tiles were likely driven by differences in curing conditions and their effect on post-process resin density. Within each tile, resin loading was lower near the gate and higher elsewhere, but values remained within expected uncertainties.

7.1.3 Development of a Methodology to Optimize a Conformal Ablative Heatshield Design

Chapters 4 and 5 described a methodology for designing a conformal ablative heatshield that integrates material selection, tile layout, and processing. Chapter 4 outlined the methodology and its objectives, then laid out the inputs, extending the constitutive model of Chapter 2 to include estimation of substrate porosity and permeability, and resin viscosity and vapor pressure, which are required for the mold filling simulation. Chapter 5 paired that simulation with a tile layout procedure to produce a conformal heatshield design optimized for VIP. Symmetric tile designs minimizing the total number of tiles were generated for sphere-cone aeroshells. Mold filling was then simulated on the resulting tile geometries to select gate and vent positions that limited the risk of air entrapment during infusion. Finally, in the last step, properties of the fabricated TPS material were estimated using expressions from the constitutive model.

The methodology was demonstrated with two examples in Chapter 6. A complete design, based on the MSL forebody geometry, showed the fully integrated approach. Then, mold filling was simulated for the tile geometry in Chapter 3. Resulting gate and vent po-

sitions were used in the experimental mold design and yielded good results with consistent saturation of the material through the thickness.

7.2 Suggestions for Future Work

Improvements and extensions of this work are suggested in the following sections, organized by contribution.

7.2.1 Constitutive Model of Fiber Substrate Ablators

Suggested future work for the constitutive model includes expanding and improving estimations of material properties and updating the uncertainty analysis.

Properties of the Substrate

The filamentary analog simplified the substrate to randomly distributed, uniform density, cylindrical fibers, but actual substrate fibers possess non-circular cross sections and non-uniform density which may impact local properties. The model could be extended to account for this variation and its impact on material uncertainty. Fiber geometry and microstructure, discussed later, may also impact permeability and affect the flow simulation.

While substrates used in this work were flexible, they did resist shrinkage to some degree, and stiffness appeared to increase with compression. As a result, Case 2 (a partially compliant substrate) in Chapter 2 did not precisely capture the mechanical behavior, particularly for the compressed samples. Likewise, the tiles processed in Chapter 3 were highly compressed and shrunk less on average than the less compressed coupons of Chapter 2. A mechanical model that incorporates substrate stiffness and pre-process compression would likely improve prediction of material shrinkage and resulting TPS properties.

Properties of the Composite TPS

The constitutive model did not account for evaporation during curing and its effect on post-process resin density, necessitating the use of an experimentally obtained value. An extension of the model that accounts for solution evaporation, and resin loss, during curing could improve predictions.

Char yield varied substantially between the two felts investigated in Chapter 2, a result that was not anticipated by the current model. Experimental fits provided better agreement with the theoretical model but did not explain the discrepancy. Substrate mass, m_{sub} , was constant in the model, an assumption that could be checked by charring the dry felt alone. The two felts should be processed at the same in the same container to avoid variation in temperature profile and evaporation.

Finally, several more TPS properties relevant to thermal response modeling were outlined in Chapter 1. Extending the constitutive model to include some of these properties may be possible. Elemental composition of the virgin TPS may be deduced from known proportions of substrate and resin and their individual chemical compositions. Kinetics-based pyrolysis models (e.g., Wang, et al. [102], and Friedman, et al. [103]) may assist with obtaining composition and properties of the pyrolysis gas and resulting char. Other properties may be deduced from the microstructure of the materials. For example, Panerai, et al. used microscale modeling to estimate thermal conductivity and oxidative behavior of carbon-phenolic ablators [109, 110].

Uncertainty Analysis

Other input distributions (e.g., normal distributions) may be appropriate for the uncertainty analysis in Chapter 2. A mechanical model of composite shrinkage incorporating substrate stiffness and compression, also discussed above, may better capture uncertainty in the shrinkage.

7.2.2 Vacuum Infusion Process for Conformal Ablative TPS Materials

Several process improvements and extensions to further improve efficiency and consistency are identified below followed by suggestions for scaling the process to larger part sizes and volumes.

Process Improvements

Mold Design

Changes to surface coating can address resin build up and improve tool longevity. All surfaces in contact with the resin must be properly coated to prevent bonding. The secondary lid was not coated in this design, resulting in evaporated resin curing on its bottom surface. Expansion holes were coated for this work, but a deficiency in the application process led to poor coverage and exposed metal.

Mold closure (and opening) could be improved by using a slot, rather than through hole, design to allow quick installation and removal of bolts. Other closure mechanisms may yield similar improvements including temporary or built in clamps (which were depicted in Figure 1.13).

Other mold materials, such as rigid tooling foams used for prototyping, may be possible given small production quantities and the low working pressure of VIP. Release films could replace surface coating to seal tooling surfaces and facilitate part release. However, their compatibility with ablative resins would need to be evaluated. Flexible tooling (e.g., vacuum bags) may offer an even cheaper alternative, but rigid support would be necessary to prevent fiber compaction.

Infusion

Future investigations could evaluate even higher vent pressures to determine whether bubble formation can be completely suppressed and its impact, if any, on material quality and voidage. Other gating designs, such as larger diameter or line gates, could also be con-

sidered to speed up infusion. A channel could likely be machined along a perimeter edge to achieve the latter. In either case, vent placement would be crucial to ensure full evacuation throughout filling. Multiple gates are also possible, but not preferred here, because intersecting flow fronts can easily lead to air entrapment.

Curing and Drying

Passive flow regulation, perhaps using a back pressure regulating valve to maintain a fixed internal pressure, would improve consistency during curing. Larger diameter exhaust tubing would also help to avoid blockage from condensed resin solution. Locating the exhaust valve after the resin trap is preferred for the same reason. Low gas flow rates should be used to limit evaporation, and the size and number of expansion ports could potentially be reduced as well.

Less thermal mass, due to less resin volume in VIP, may allow faster temperature ramping and shorter hold times during curing. Drying could be accelerated using higher gas flow rates, which may be feasible given the small enclosed volume. In both cycles, cooling may be accelerated by opening the oven to the ambient room atmosphere at the end of the heating cycle, which was not possible in the open process due to the risk of resin oxidation. Temperature changes must not be too rapid, however, to avoid large thermal stresses which can cause material failure.

Size and Volume Scaling

Even larger tiles can further simplify aeroshell integration by reducing part counts and corresponding gap filling. The mold design in Chapter 3 could be easily scaled given a sufficiently large CNC machine, but fill times would increase. Given a sufficiently large substrate, small heatshields could even be fabricated from a single piece with a single mold, eliminating gaps altogether.

Other gating strategies, discussed above, as well as pressurizing and/or preheating the

resin could speed infusion. Bigger tiles require correspondingly larger, heavier tooling to maintain adequate stiffness, which would complicate handling. A large, walk-in oven would ease transfers during processing. Other mold materials may also mitigate the increase in weight.

Increased processing volumes would benefit both early TPS development (allowing multiple samples to be generated quickly) and later heatshield production (decreasing manufacturing time). Two approaches are possible: (1) processing multiple tiles with multiple molds or (2) processing multiple tiles in a single mold. The former could be easily implemented by fabricating several identical molds. Resin delivery and vacuum lines could be tied together to infuse parts at the same time, and a similar approach could be employed for curing and drying.

Multiple parts could be stacked vertically in a single mold, but IML/OML curvature would change through the stack, requiring additional post-process machining. Tolerances would be large without a rigid tool conforming the second surface. Alternatively, adjacent tiles could be laid out horizontally. This approach might allow several tiles to be joined during processing, eliminating some gap filling. In either case, mold flow would need to be investigated to ensure adequate saturation.

7.2.3 Design Methodology to Optimize a Conformal Ablative Heatshield Design

Suggestions for improving the design methodology are discussed within separate sections corresponding to Chapter 4 (Inputs) and to Chapter 5 (Design Tasks). They are further broken down based on the steps in the methodology presented earlier in Figure 4.1.

Inputs

Primary Inputs

TPS geometry could be extended to other shapes (e.g., spherical segments), shoulder tiles, and variable TPS thicknesses as well as asymmetric tile layouts and non-orthogonal seam

designs. Larger noses requiring multiple tiles could also be incorporated. All of these would require adaptation or modification of the current tile layout rules as well as additional files to define the subsequent mesh geometries. The tile layout for the MSL heatshield [26, 91], shown previously in Figure 1.7 and discussed further in Chapters 3 and 5, may provide a useful starting point for asymmetric layouts. That design somewhat mirrors the concentric rings in the present work but with extended tiles spanning multiple rings near the stagnation point.

Substrate draping was reduced to an a priori minimum radius of curvature constraint, but a draping simulation would better predict wrinkling behavior. It could also be used to evaluate local variation in porosity and permeability due to bending, and its effects on mold filling and TPS properties. The model proposed by Martinez-Hergueta, et al. likely represents the most promising approach for future study because of its similarity to the felts used in conformal ablators [99].

Secondary Inputs

Extending the permeability estimate to anisotropic materials would broaden the applicability of the mold filling simulation. In addition to the isotropic three-dimensional model used in Chapter 4, Tomadakis and Robertson developed models for one- and two-dimensional fiber structures [105]. Anisotropic permeability can be linked to distributions of pore size and direction, loosely described by the tortuosity tensor [111]. A recent NASA software, Porous Microstructure Analysis, computes tortuosity from microstructure and has direct applications to TPS materials [112].

Regarding resin properties, alternative blending rules, described in the review by Centeno, et al. [106] mentioned in Chapter 4, could also be considered for estimating viscosity. Raoult's law reasonably approximated the vapor pressure of the resin solution in this work but must be adapted for solutions deviating from ideal behavior [113].

Design Tasks

Tile Layout

In addition to other tile layouts and aeroshell geometries, tile layout could be improved by incorporating detailed seam design. In this work, seam geometry was assumed to be orthogonal, but other geometries, depicted in Figure 1.10, may be necessary. Tile size would also need to be adjusted to account for edge machining. Other potential modifications to the tile layout include allowing multiple substrate options and incorporating a dimensional constraint on the three-dimensional curved tile. The former would allow substrate selection when multiple variants are available. Such a capability would be useful for C-PICA, which has both thin and thick substrates to accommodate variable TPS sizing. A constraint on the three-dimensional tile can address size limitations due to the oven, shipping, and/or handling.

Mold and Process Design

Alternative gating was suggested for speeding up infusion, and the mold filling simulation could be adapted to those designs using the existing approach: embedding the gate geometry in the mesh (see Appendix D.2) and then selecting and applying the boundary condition to the corresponding nodes. A constant flow rate boundary condition could also be applied to mirror other processing setups (e.g., with a resin pump).

Tile geometry was simplified to a two-dimensional shell for computing the objective function, the blocked length. Thicker parts, with larger aspect ratios, may require adapting the simulation and objective function to the three-dimensional case. The perimeter would be a surface, rather than a line. A blocked area (or volume) could be computed, somewhat analogous to the blocked length here.

The fidelity of the three-dimensional simulation, which yielded total time to fill, could be improved by specifying resin viscosity as a function temperature, and improving estimation of substrate properties including local variation due to draping. Anisotropic permeabil-

ity estimation from the fiber structure, which was discussed above, would be particularly beneficial. Additional investigation is also needed to understand how bubbles along the flow front may impact flow, especially along mold walls, and its impact on fill time.

TPS Material Property Estimation

Extensions to TPS property estimation follow those discussed above for the constitutive model: approximating additional properties relevant to thermal response modeling and improving the uncertainty analysis. In addition, the methodology could be extended to other fibrous substrates (both carbon and non-carbon fiber materials) and alternative resin formulations (other phenolic-based solutions as well as other ablative resins such as silicone and cyanate ester).

Appendices

APPENDIX A

EVALUATION OF CONSTITUENT MATERIAL PROPERTIES

Experimental measurement of C-PICA constituent properties are reviewed in this section. Substrate measurements (permeability, porosity, and fiber density) are described first followed by the measurement of the resin viscosity. Measurement of the resin vapor pressure was described in Chapter 4. Results were used for comparison to property models in that chapter, then applied in the mold filling simulation described in Chapter 5 and demonstrated in Chapter 6. Fiber density, ρ_{fiber} , was used throughout the thesis.

A.1 Felt Substrate

Substrate measurements were obtained on 14 half-inch diameter cylindrical samples of Felt 1, which were approximately 1" long by 0.5" diameter. Samples spanned several locations across a single 41" by 12" piece. Eight samples were oriented in the through thickness direction; six samples were oriented in the in plane direction (Figure A.1).

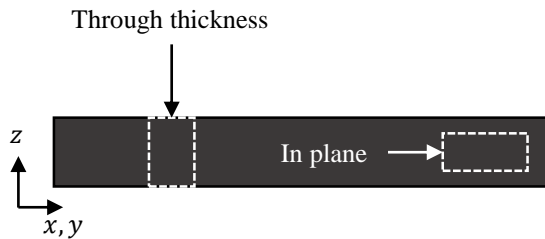


Figure A.1: Illustration of through thickness and in plane sample orientations.

A.1.1 Permeability

Sample permeabilities were obtained with an experimental setup and technique developed by Marschall and Milos [79], which is summarized here. Pressure drop was measured

across each sample while subjected to a steady, unidirectional flow of gas. A diagram of the experimental apparatus is shown in Figure A.2. Felt specimens were press fit into

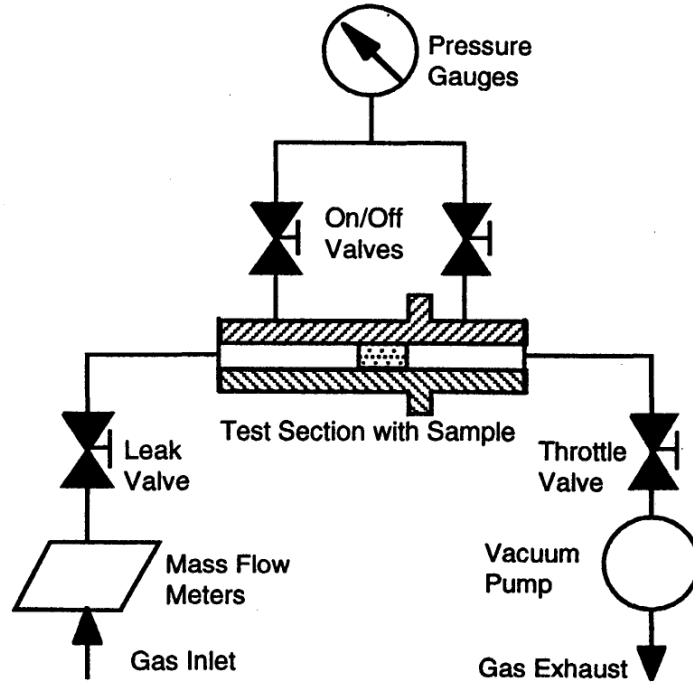


Figure A.2: Experimental setup for measuring permeability (Credit: Marschall and Milos [79]).

the cylindrical test section. The test section was then evacuated, and gas, controlled by two valves, was flowed through it. Upstream and downstream pressures were selected by opening and closing the corresponding on/off valves. Measurements were taken over a range of flow rates, from 1 sccm to 5000 sccm¹. Under these constraints, the Darcy flow approximation combined with mass conservation and the ideal gas law yields a relation for mass flow, \dot{m} , as a function of sample geometry (diameter, d , and length, L), test gas properties (viscosity, μ_g , temperature, T , gas constant, R , and molecular mass, M), and gas permeability, K_g :

$$\dot{m} = -\frac{\pi D^2 M}{4\mu_g RT} K_g P \frac{dP}{dx} \quad (\text{A.1})$$

¹Standard cubic centimeters per minute

Here, the pressure field, P , varies in one dimension only (along the length of the sample, x). Gas slippage along pore walls (i.e. along the fibers) requires the Klinkenberg correction [78]:

$$K_g = K \left(1 + \frac{b}{P} \right) \quad (\text{A.2})$$

to estimate permeability in the limit of continuum (or liquid) flow, K , which is the relevant parameter for modeling resin infusion. The other parameter, b , is a material-specific constant that is not relevant to the current investigation. Substituting and integrating over the length of the sample, the equation can be rearranged into a linear form:

$$F = \frac{4\mu_g \dot{m} R T L}{\pi d^2 M \Delta P} = K (P_{\text{av}} + b) \quad (\text{A.3})$$

where F has units of Newtons. Here, P_{av} is the average of the pressures upstream and downstream of the sample, and ΔP is the difference between them. Thus, K and b , both unknown, can be obtained by measuring the two pressures, immediately before and immediately after the sample, over a range of flow rates. A linear least squares fit of F vs. P_{av} yields a slope equivalent to the permeability K .

Results

Figure A.3 plots F against P_{av} for one such sample, an in plane specimen. The line (and equation) show the least squares fit with slope, $K = 2.7 \times 10^{-10} \text{ m}^2$. Based on the analysis by Marschall and Milos, K has an uncertainty of +11%/-16% (a range from $2.3 \times 10^{-10} \text{ m}^2$ to $3.0 \times 10^{-10} \text{ m}^2$ in this example), though nominal values were plotted in Figure 4.4.

A.1.2 Porosity and Fiber Density

Fiber density, ρ_{fiber} , was computed using a linear regression model based on Equation 2.1, which is repeated here:

$$\phi = 1 - \frac{\rho_{\text{sub}}}{\rho_{\text{fiber}}} \quad (\text{A.4})$$

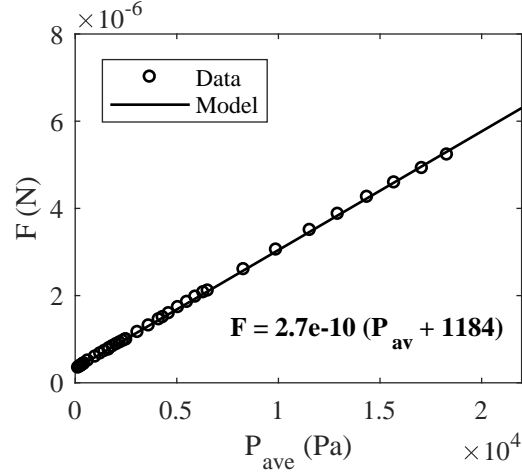


Figure A.3: Permeability results for a single felt sample.

This equation can be rearranged in terms of the fiber fraction, $1 - \phi$,

$$1 - \phi = \left(\frac{1}{\rho_{\text{fiber}}} \right) \rho_{\text{sub}} = \xi \rho_{\text{sub}} \quad (\text{A.5})$$

Plotting $(1 - \phi)$ vs. ρ_{sub} yields a line with slope, ξ , equal to the reciprocal of fiber density. As noted in Chapter 4, this fiber density ignores the central lumen (hollow space) characteristic of rayon-based carbon fibers [110]. Instead, the density computed can be interpreted as an average over the entire cross section. For the purposes of estimating pore volume in the constitutive model, this quantity is sufficient.

Sample porosities were obtained from three mass measurements: the unsaturated mass of the dry sample, m_{dry} ; the saturated mass of the sample infiltrated with a liquid, m_{sat} ; and the suspended mass, m_{sus} . The latter was the measured mass increase when the saturated sample was suspended in a beaker full of the infiltrant (Figure A.4). Note that the mass of the submerged sample was not being measured here, but rather the mass of the beaker. The buoyancy of the sample increased the apparent mass of the beaker (due to an equal and opposite reaction). Samples were infiltrated with water under vacuum to avoid trapping air within the sample.

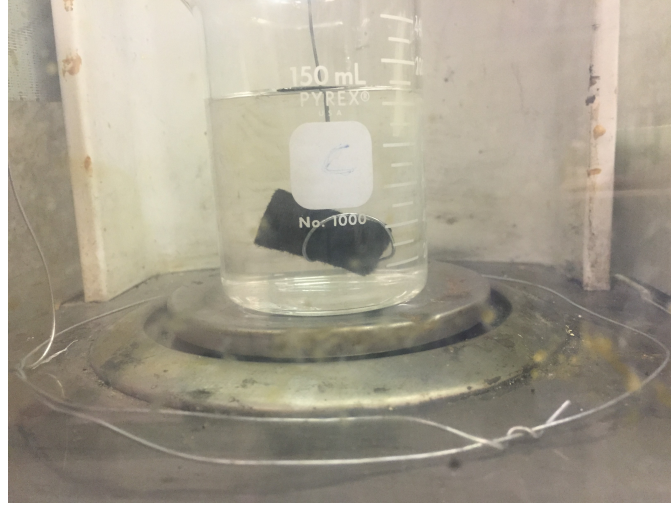


Figure A.4: Saturated sample suspended in infiltrating liquid.

From the first two masses, pore volume is simply,

$$V_{\text{pore}} = \frac{m_{\text{sat}} - m_{\text{dry}}}{\rho_{\text{liq}}} \quad (\text{A.6})$$

where ρ_{liq} is the density of the infiltrating liquid. The suspended mass is the sum of the infiltrant mass and the buoyant force acting on the fibers,

$$m_{\text{sus}} = (m_{\text{sat}} - m_{\text{dry}}) + \rho_{\text{liq}} V_{\text{fiber}} \quad (\text{A.7})$$

which when rearranged gives an expression for the volume of the fibers

$$V_{\text{fiber}} = \frac{m_{\text{sus}} - m_{\text{sat}} + m_{\text{dry}}}{\rho_{\text{liq}}} \quad (\text{A.8})$$

Finally, the (average) porosity of the sample is

$$\phi = \frac{V_{\text{pore}}}{V_{\text{pore}} + V_{\text{fiber}}} = \frac{m_{\text{sat}} - m_{\text{dry}}}{m_{\text{sus}}} \quad (\text{A.9})$$

Note that the dependence on infiltrant density is removed in this approach.

Substrate density was computed by measuring bulk volume (sample length and diame-

ter). Measurement uncertainty resulted in a relative error of $\pm 2\%$ on computed densities. Additionally, the samples were found to shrink slightly in length once infiltrated, so there exists a difference between dry and saturated substrate densities. This analysis used the saturated density (consistent with the porosity measurement based on saturated samples). However, the difference was less than 1%.

Results

Figure A.5(a) shows fiber fraction plotted against nominal density for each sample. The least squares model is indicated by the solid line with bounds depicting a 95% CI on the slope. Results are generally linear as predicted except for two potential outliers. Both through thickness and in plane samples appear to follow the same linear trend. Grouping by density is likely due to like samples being removed from the same region of the felt.

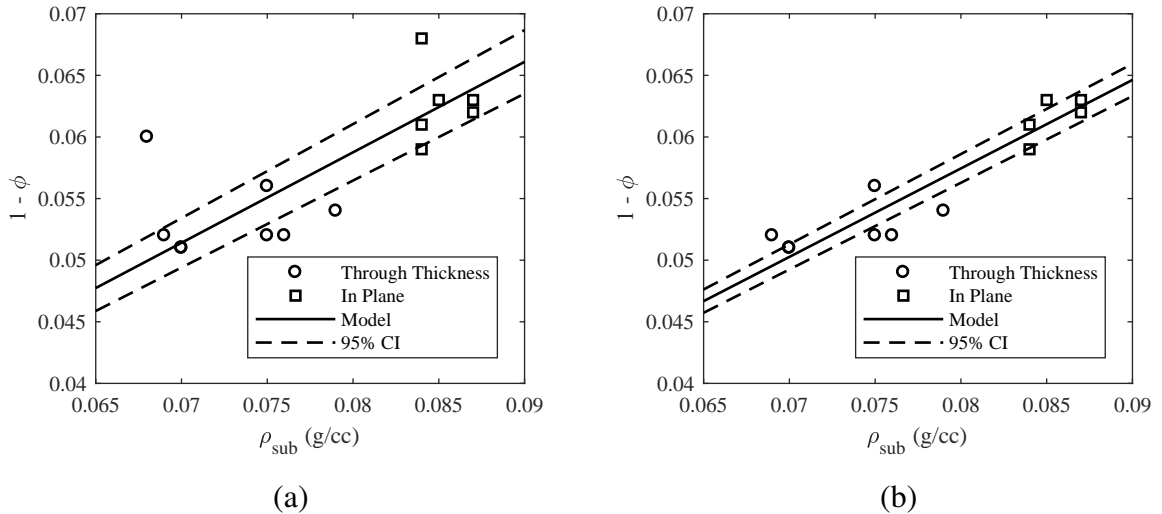


Figure A.5: Regression analysis on substrate samples (nominal densities).

Both outliers are biased toward higher values of $(1 - \phi)$ (and lower values of porosity, ϕ), which may indicate that these samples were not fully infiltrated. Data are plotted with outliers removed in Figure A.5(b). Removing the outliers produces a slight change in slope as well as a smaller variance. As performed, this single regression assumes no error in the independent variable, ρ_{sub} . To account for error in measured densities, regression

was repeated with ρ_{sub} adjusted to its maximum and minimum values (based on a relative error of $\pm 2\%$), which yields worst-case bounds on the slope. Results for these subsequent regression analyses are summarized in Table A.1. Recall that fiber density is the reciprocal of the slope. Therefore, based on maximum and minimum bounds across all analyses, fiber density lies between 1.34 g/cc and 1.45 g/cc, which was expressed as $\rho_{\text{fiber}} = 1.395 \pm 0.055$ g/cc in the thesis.

Table A.1: Results of regression analyses with 95% CIs.

Case	Regression Coefficient		Fiber Density	
	ξ	\pm (95% CI)	ρ_{fiber} (g/cc)	\pm (95% CI)
Nominal Density	0.718	0.015	1.39	0.03
Maximum Density	0.704	0.014	1.42	0.03
Minimum Density	0.733	0.015	1.37	0.03

A.2 Resin

A.2.1 Dynamic Viscosity

Viscosity was obtained using a Brookfield rotational viscometer (Figure A.6), which measures torque on a rotating spindle immersed in a test fluid. Based on recommendations in the manufacturer’s reference manual, measurements were taken in a 600 mL low form Griffin beaker using an LV-1 spindle rotating at 60 rpm, yielding ± 1 cP accuracy over a range from 15 cP to 100 cP [114]. Note that a smaller beaker, different from that used here, is shown in the figure.

Viscosity was measured at several temperatures between 16°C and 29°C. The lower range was obtained as the resin warmed to room temperature after removal from cold storage while the upper range was obtained by heating the solution and then allowing it to cool. Resin temperature was recorded with a thermometer ($\pm 0.2^\circ\text{C}$ accuracy) inserted into the solution. However, the thermometer was immediately removed after recording the temperature to avoid altering the viscosity reading.



Figure A.6: Experimental set up with rotational viscometer.

An exponential model, first proposed by Reynolds [115], was used to estimate viscosity as a function of temperature,

$$\mu(T) = \mu_0 \exp\left(-\frac{T}{T'}\right) \quad (\text{A.10})$$

with model parameters μ_0 (reference viscosity) and T' (reference temperature). The reference viscosity corresponds to fluid viscosity at $T = 0$, which depends on the temperature scale. The parameter T' corresponds to the temperature at which $\mu = \mu_0/e$ and is related to how quickly viscosity decreases with temperature. Taking the logarithm of both sides yields a linear equation:

$$\ln \mu = \left(-\frac{1}{T'}\right) T + \ln \mu_0 \quad (\text{A.11})$$

A linear least squares fit of $\ln \mu$ vs. T yields the parameters, μ_0 and T' .

Results

Measurements were obtained for two resin samples, approximately 500 mL each, taken from larger batches used during processing of Tiles 1–3 (Chapter 3). Figure A.7 depicts

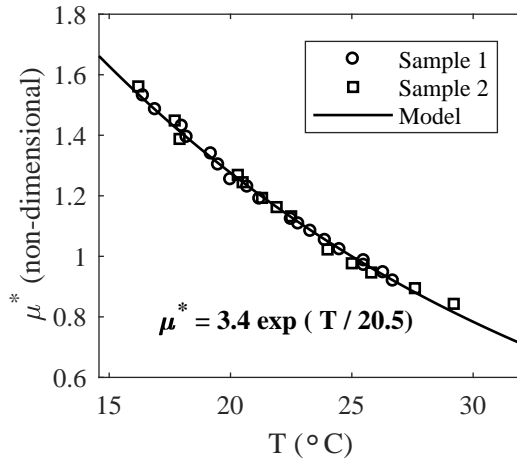


Figure A.7: Viscosity results.

nondimensional viscosity, μ^* , for both of these samples along with the least squares solution of Equation A.11. As was indicated in Chapter 4, results were normalized by the

viscosity at 25°C to protect details of the resin formulation. The equation of the fitted model is also shown. The exponential model provides an excellent fit of the experimental results in this range.

APPENDIX B

APPLICABILITY OF THE VACUUM INFUSION PROCESS

This appendix explores the limits of VIP relative to substrate density and resin viscosity, supplementing the discussion in Chapter 3. Time to fill results were generated across a range of densities and viscosities using the outer ring tile geometry in Chapter 6. Increased tile thicknesses were also investigated.

B.1 Methodology

B.1.1 Geometry and Mold Design

The outer ring tile geometry was selected because its size, an approximately 1 m x 1 m footprint, represents a notional goal for conformal ablators [40]. TPS thickness was 0.75 inches in the example, with $t_{\text{sub}}^{\text{pre}} = 1$ in. This study evaluated several additional substrate thicknesses ($t_{\text{sub}}^{\text{pre}} = 1.5$ in, 2 in, and 3 in). Gate location was fixed to the optimal solution ($\lambda_{\text{gate}}^* = 0.996$, $\Gamma_{\text{gate}}^* = 0.001$) found in Chapter 6 and the same gate radius, $R_{\text{gate}} = 0.125$ in.

B.1.2 Properties

Substrate

A rayon-based substrate was assumed with $\rho_{\text{fiber}} = 1.395$ g/cc and $d_{\text{fiber}} = 11$ μm , reflecting the nominal properties for Felt 1 used previously in Chapter 6. Porosity, ϕ , and permeability, K were estimated from Equations 4.4 and 4.5, respectively. Figure B.1 depicts these properties as functions of substrate density, $\rho_{\text{sub}}^{\text{pre}}$, ranging from zero to ρ_{fiber} (spanning the full range of porosities). Permeability decreases with substrate density — more densely packed fibers lead to more flow resistance. At the extremes, K becomes very large as $\rho_{\text{sub}}^{\text{sub}}$

approaches zero ($K \rightarrow \infty$ as $\rho_{\text{sub}} \rightarrow 0$), and becomes very small as $\rho_{\text{sub}}^{\text{pre}}$ approaches the fiber density ($K \rightarrow 0$ as $\rho_{\text{sub}}^{\text{pre}} \rightarrow \rho_{\text{fiber}}$). These cases correspond to no substrate (empty space) and a fully dense substrate (with no open porosity), respectively.

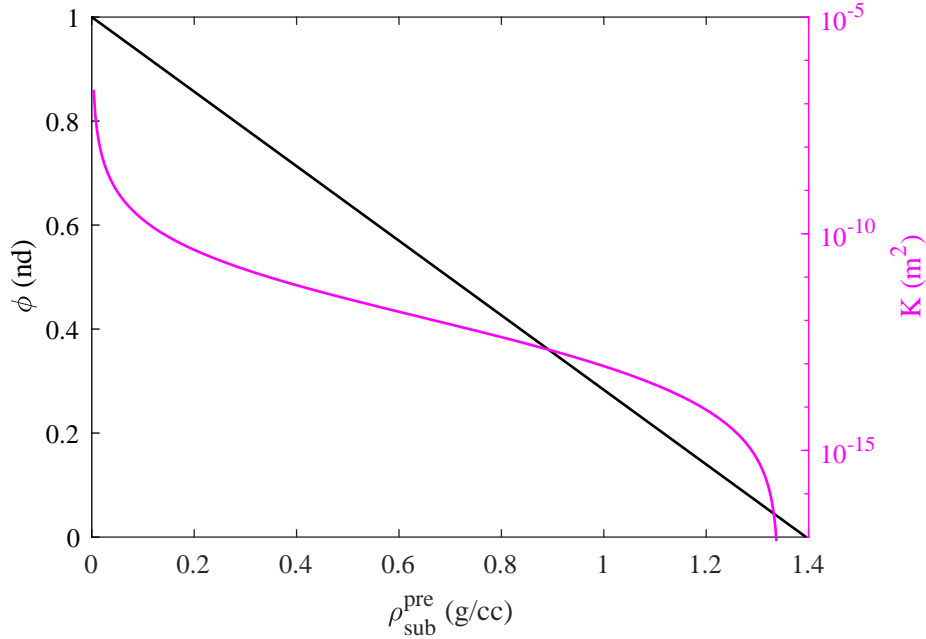


Figure B.1: Variation of porosity and permeability with rayon-based substrate density.

Resin

Resin properties were based on the C-PICA resin formulation used in this work. Resin dilution was varied, by altering the amount of solvent, to obtain viscosity (from Equation 4.9) as a function of vapor pressure (from Equation 4.10). Figure B.2 shows relative changes in the two properties, normalized by values for the standard formulation ($\mu_{\text{sol}}^* = 1$, $P_{\text{vap,sol}}^* = 1$). Viscosity was varied between $\mu_{\text{sol}}^* = 0.7$ and 8.4. The upper bound reflects the base resin without additional solvent. Thus, in the figure, dilution increases moving from right to left, i.e., adding solvent reduces both viscosity and vapor pressure. While the correlation is specific to this resin formulation, a similar approach could be used for other resin mixtures.

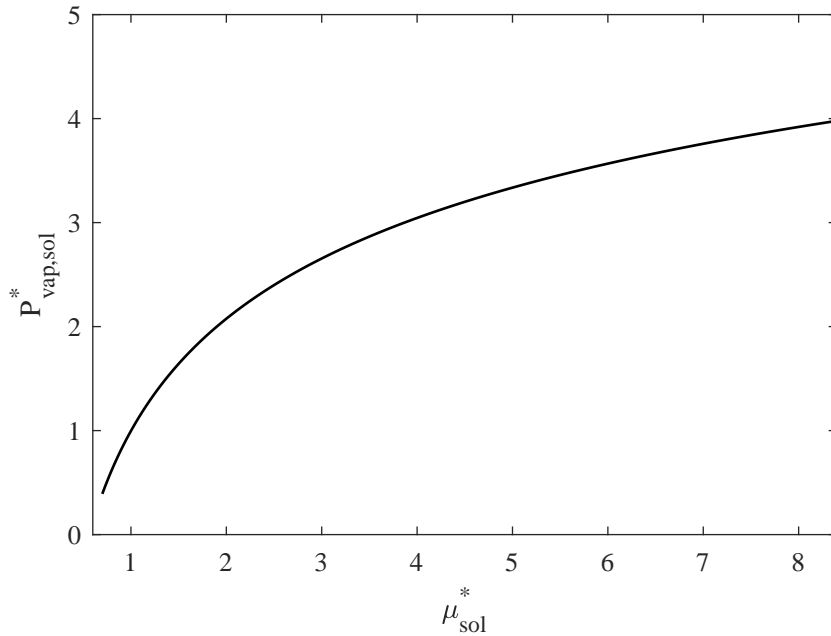


Figure B.2: Correlation between viscosity and vapor pressure for a diluted phenolic resin solution (based on the C-PICA formulation).

B.1.3 Simulation

Mold filling was simulated in LIMS using the approach in Chapters 5 and 6. Total time to fill was generated on the full three-dimensional geometries, with $t_{\text{sub}}^{\text{pre}}$ equal to 1 in, 1.5 in, 2 in, and 3 in. Resin properties (μ_{sol}^* and $P_{\text{vap,sol}}^*$) and substrate density ($\rho_{\text{sub}}^{\text{pre}}$) were varied using the functional relationships depicted in Figures B.1 and B.2. Vent pressure, P_{vent} , was set equal to $P_{\text{vap,sol}}$ following the approach in Chapters 5 and 6.

B.2 Results

Figures B.3(a)–(d) depict the viscosity-density design space for each of the substrate thicknesses. Time to fill, denoted by the contours, is expressed in hours, with the upper contour (yellow) indicating infusion times greater than 8 hours, reflecting the length of a standard work day. Longer infusions could perhaps be accommodated, but become increasingly impractical especially considering that manual intervention is required to stop resin flow in

the current implementation. In the figures, substrate density was limited to a maximum of 0.4 g/cc because the time to fill far exceeded the 8 hour limit for those configurations. The current C-PICA formulation, used in the example in Chapter 6, is highlighted for reference ($\rho_{\text{sub}}^{\text{pre}} = 0.095 \text{ g/cc}$, $\mu_{\text{sol}}^* = 1$).

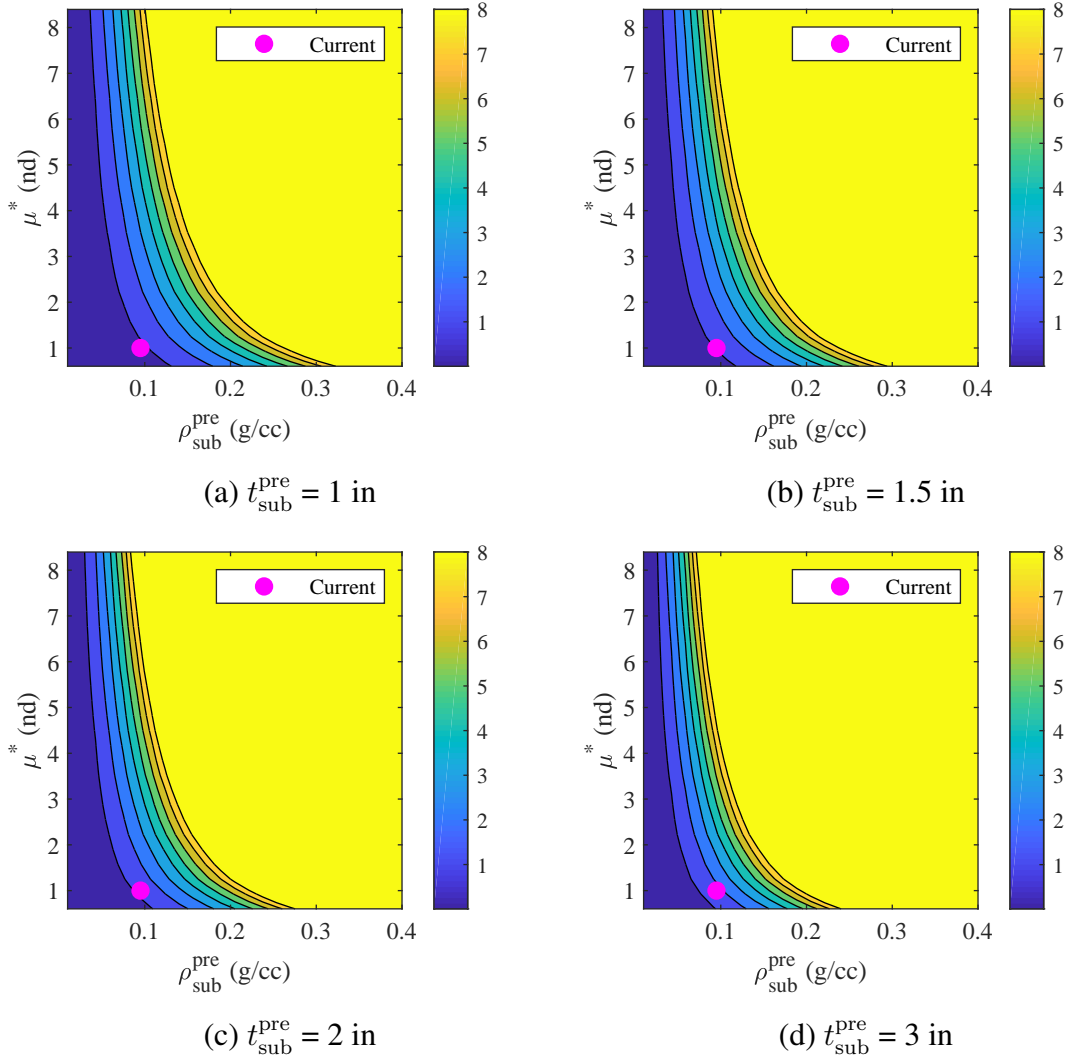


Figure B.3: Time to fill (in hours) for example designs.

B.3 Discussion

Figure B.3(a) depicts the current substrate thickness ($t_{\text{sub}}^{\text{pre}} = 1 \text{ in}$). In that case, with the current resin formulation ($\mu_{\text{sol}}^* = 1$), VIP is feasible up to $\rho_{\text{sub}}^{\text{pre}} \approx 0.25 \text{ g/cc}$. Decreasing

viscosity by increasing resin dilution slightly extends that range (~ 0.3 g/cc). Moving the other direction (decreasing dilution and increasing viscosity) shrinks the viable density range, approaching $\rho_{\text{sub}}^{\text{pre}} = 0.1$ g/cc with no resin dilution (and the highest viscosity). Note that vapor pressure (and, thus, vent pressure) also increases with viscosity contributing to longer infusion times. Given a fixed substrate density, $\rho_{\text{sub}}^{\text{pre}}$, time to fill increases rapidly with viscosity below approximately $\mu_{\text{sol}}^* < 4$. Above that value, the increase in T_f is less pronounced due to smaller changes in the vapor pressure (Figure B.2).

Infusion time increases with substrate thickness, due to an increase in fill volume, demonstrated by a leftward shift in the limiting contour in Figures B.3(b)–(d). This result further limits the range of feasible densities. With the current resin formulation, VIP is feasible up to $\rho_{\text{sub}}^{\text{pre}} = 0.2$ g/cc for the thickest substrate shown in Figure B.3(d), a 20% decrease from above. Similarly, the upper limit at the highest viscosity decreases to 0.07 g/cc in this configuration.

Recall that these results pertain to a specific tile geometry (approximately 1 m x 1 m), substrate (rayon-based carbon fiber), and resin formulation (diluted phenolic resin) and, thus, serve as only a reference point for future investigations. Changes to these assumptions will alter the resulting time to fill (e.g, reducing the tile size shortens infusion and extends the range of suitable substrate densities). Also, experimental times were generally shorter than predicted for the mold design in this work (Chapter 6), so the numerical results are likely conservative. Infusion could also be accelerated, if necessary, using one of the approaches suggested in Chapter 7: investigating other, larger gate designs as well as pressurizing and/or preheating the resin delivery.

APPENDIX C
COMPUTATION OF THE MINIMUM SEAM ANGLE

The seam angle constraint, described in Section 5.2.3, defines a minimum angular offset between radial seams of adjacent rings in the tile layout. As discussed in that section, multiple adjacent seam angles, γ_j exist, up to $2N_j$ total, where N_j is the number of tiles in the inner ring, and the minimum seam angle in a layout, $\beta_{j,j+1}^{\min}$, depends on the relative positioning between the two rings. It is necessary to find the largest possible (maximum) minimum seam angle between adjacent rings, which is the best-case configuration.

The example in Section 5.2.3, $N_j = N_{j+1}$, where N_{j+1} is the number of tiles in the outer ring, yields a minimum seam angle of zero (with all seams aligned) or a maximum of $\frac{\pi}{N_j}$ (half the angular span of each tile). Other configurations where $N_j \neq N_{j+1}$ pose more of a challenge due to the presence of multiple different seam angles. This appendix describes the computational approach in more detail.

C.1 Methodology

The solution approach relies on, first, enumerating the angles of all seams in the inner ring, β_i ,

$$\beta_i = \frac{2\pi}{N_j}, \quad i \in [1, N_j] \quad (\text{C.1})$$

and in the outer ring, β_k ,

$$\beta_k = \frac{2\pi}{N_{j+1}}, \quad k \in [1, N_{j+1}] \quad (\text{C.2})$$

Equations C.1 and C.2 assume an initial orientation where one seam in each ring falls at an angle of 2π radians, i.e. seams at $i = N_j$ and $k = N_{j+1}$. Therefore, in this initial configuration, there is at least one seam aligned. Next, the difference between every β_i and

every β_k is computed, yielding the seam angle between every combination of seams in the layout (not just adjacent ones). Finally, the smallest positive angle is selected from this result — a quantity describing the minimum angle through which one ring must be rotated (relative to the other) from the initial configuration to produce the next seam alignment. (Note that, due to symmetry, selecting the largest negative angle would be analogous.) In either case, the minimum seam angle is maximized by taking half of this rotation, halfway between the two seam alignments, to obtain $\beta_{j,j+1}^{\min}$, the result used by the methodology.

C.2 Code

Figure C.1 shows the MATLAB function used to compute the largest minimum seam angle between two adjacent rings, j and $j + 1$, comprised of N_j and N_{j+1} tiles, respectively. Equations C.1 and C.2 are implemented in Lines 6 and 7. All seam angle combinations are

```

1 function beta_min = max_minseamangle(Nj,Njp1)
2
3     % This function computes the maximum minimum seam angle
4     % between two adjacent rings with N_j and N_(j+1) tiles
5
6     betai = (2*pi/Nj(k))*(1:Nj(k)); % inner layer
7     betak = (2*pi/Njp1(k))*(1:Njp1(k)); % outer layer
8
9     betai_mat = repmat(beta_i',[1,length(beta_k)]);
10    betak_mat = repmat(beta_k',[length(beta_i),1]);
11
12    diff = betai_mat - betak_mat;
13
14    tol = 1e-6;
15    beta_min = min(diff(diff > tol)) / 2;
16
17 end

```

Figure C.1: MATLAB code used to compute the largest minimum seam angle between two adjacent rings in the tile layout.

computed in Lines 9–12, by duplicating each vector of angles into matrices, `betai_mat` and `betak_mat`, then subtracting to form the matrix of differences, `diff`. Thus, `diff` contains all seam angles. Finally, the minimum seam angle is computed in Lines 14–15

by taking half of the smallest positive angle in `diff`. The tolerance, `tol`, accounts for rounding errors in the subtraction operation in Line 12 due to machine precision.

APPENDIX D
FURTHER DETAILS ON THE MOLD FILLING SIMULATION

This appendix provides additional details on the mold filling simulation described in Chapter 5 and applied in Chapter 6. In those chapters, mold designs were evaluated according to Equation 5.5, which is repeated here:

$$f_{\text{obj},2} = \frac{p'}{p_{\text{total}}} \quad (\text{D.1})$$

This equation quantifies the fraction of the perimeter, p_{total} , blocked by advancing flow during infusion, i.e., the length of unfilled regions, p' , with no path for air removal through the vent. Section 5.3 described the blocked length, p' , computation as follows:

Blocked regions correspond to a pair of perimeter points with the same time to fill $T_f(p_{j+1}^*) = T_f(p_j^*)$, where $p_{j+1}^* > p_j^*$. That is, the flow front has reached two different locations on the perimeter at the same time. The length of all blocked regions are summed to yield the total blocked length.

The blocked length was notionally depicted in Figure 5.7. Programatically, such a computation is straightforward once the time to fill is extracted along the perimeter of the part. The calculation is carried out separately for each direction around the perimeter (two segments in total), starting at the first perimeter point reached by the flow, $p_0 = 0$, and ending at the last point reached, p_n . The set of perimeter points, \mathcal{P} , ordered sequentially, are thus defined:

$$\mathcal{P} = \{p_0 \cup p_i \mid p_i > p_{i-1}, i \in [1, 2, \dots, n_p]\} \quad (\text{D.2})$$

where p_i is the distance along the perimeter from p_0 . Thus, there are $n_p + 1$ points in total defining the perimeter segment. The n_b points bounding the blocked regions are denoted

by:

$$p_j^*, \quad j = [1, \dots, n_b], \quad p_j^* \in \mathcal{P} \quad (\text{D.3})$$

where n_b is even. During iteration, one perimeter point, denoted p_c , is selected for comparison to other points:

$$p_c \in \mathcal{P}, \quad c \in [0, \dots, n_p] \quad (\text{D.4})$$

where index c equals the corresponding index in the set of perimeter points.

The algorithm starts at the first perimeter point, initializing $i = 0$ and $j = 1$ and setting $p_c = p_i$. Time to fill at this point is compared to all following points according to the inequality:

$$T_f(p_i) \leq T_f(p_c) \quad , \quad i \in [c + 1, \dots, n_p] \quad (\text{D.5})$$

If this condition is satisfied by one or more points, $p_k \in \mathcal{P}$, then p_c forms the lower bound on the blocked region,

$$p_j^* = p_c \quad (\text{D.6})$$

while the upper bound is the farthest point in p_k , that is,

$$p_{j+1}^* = \max(p_k) \quad (\text{D.7})$$

and, the blocked length is $p_{j+1}^* - p_j^*$. The selected comparison point is then updated, $p_c = p_{k+1}$. Otherwise, if no points satisfy Equation D.5, then the algorithm moves to the next point on the perimeter, setting $p_c = p_{i+1}$. The process is repeated for the selected point, p_c , again applying Equation D.5 and updating according to Equations D.6 and D.7 if a blocked region is found. Iteration terminates when the last point, p_n , is reached. Figure D.1 depicts the algorithm. Note again that there are two directions around the perimeter, so this procedure is carried out twice, summing both p' computed.

This basic formulation, though qualitatively useful, does not account for regions where flow reaches two points on the perimeter at very nearly the same time. In actual processing,

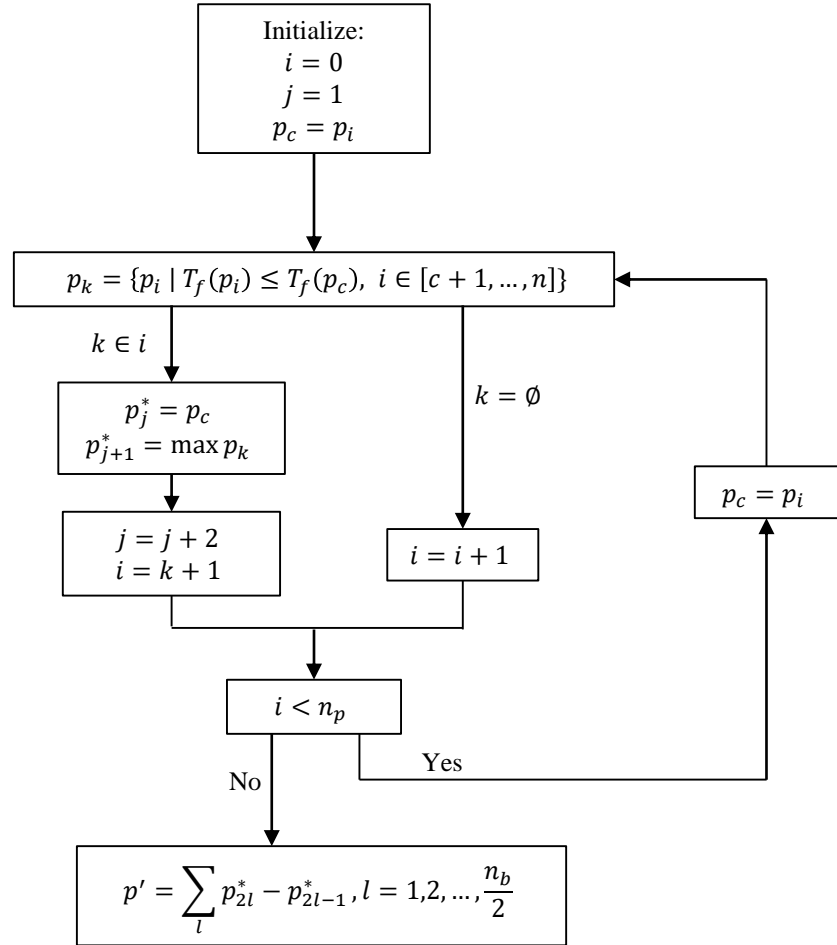


Figure D.1: Algorithm for computing the blocked length, p' , for one segment.

local variation in material properties may produce a nonsmooth flow front. Thus, while the simulation may satisfy $T_f(p_{i+1}) > T_f(p_i)$ for adjacent perimeter points, p_i and p_{i+1} , the actual process may not if $T_f(p_{i+1}) - T_f(p_i)$ is sufficiently small. In addition, this formulation can lead to a poorly shaped objective function with little differentiation between similar designs.

D.1 Modified Mold Design Objective Function

An additional term, p'_{vel} , was added to the objective to capture regions with similar time to fill. A small difference in fill time between adjacent points, $T_f(p_{i+1}) - T_f(p_i)$, yields a correspondingly high apparent flow velocity along the perimeter, u^{perim} . Thus, p'_{vel} , was formulated to capture regions where u^{perim} is above a critical value, u^{crit} :

$$p'_{\text{vel}} = \sum_s (p_{s+1} - p_s), \quad u_s^{\text{perim}} > u^{\text{crit}}, \quad p_s \in \mathcal{P}, \quad s \in [1, \dots, n_p], \quad (\text{D.8})$$

which is added to the previously computed blocked length

$$p^l = \sum_l (p_{2l}^* - p_{2l-1}^*) + p'_{\text{vel}}, \quad l = 1, 2, \dots, \frac{m}{2} \quad (\text{D.9})$$

The additional term penalizes designs where flow reaches adjacent perimeter points at around the same time.

D.1.1 Perimeter Velocity

Flow velocity along the perimeter was approximated by a forward finite difference at each point:

$$u_i^{\text{perim}} \approx \frac{p_{i+1} - p_i}{T_f(p_{i+1}) - T_f(p_i)}, \quad i = 0, \dots, n_p - 1 \quad (\text{D.10})$$

D.1.2 Critical Velocity

The velocity criterion, u^{crit} , was based on a solution of Darcy's law for two-dimensional radial flow [61]. Flow velocity, u_r , a radial distance R_{eq} from the gate is given by:

$$u_r = \frac{K P_{\text{gate}}}{\phi^{\text{pre}} \mu R_{\text{eq}} \ln \frac{R_{\text{eq}}}{R_{\text{gate}}}} \quad (\text{D.11})$$

where R_{gate} and P_{gate} are the radius of the gate and injection pressure, respectively. Material properties: permeability, K , porosity, ϕ^{pre} , and viscosity, μ , are those defined earlier in the thesis. Here, Equation D.11 was generalized to arbitrary part geometries by computing an equivalent radius given perimeter, p_{total} ,

$$R_{\text{eq}} = \frac{1}{2\pi} p_{\text{total}} \quad (\text{D.12})$$

The velocity, u_r , thus scales with part size, material properties, and gate pressure. Dividing u_r by a scaling parameter r_p yields the critical value,

$$u^{\text{crit}} = \frac{1}{r_p} u_r \quad (\text{D.13})$$

As $r_p \rightarrow 0$, $u^{\text{crit}} \rightarrow \infty$ and $p'_{\text{vel}} \rightarrow 0$, and the algorithm reverts to the unmodified, basic formulation. Increasing r_p increases the penalty on designs where the flow front arrives at the perimeter around the same time.

D.1.3 Scaling Parameter Study

The effect of the scaling parameter, r_p , was studied on tile geometries from Chapter 6. All substrate, resin, and process parameters were maintained from that example. Results are presented below for the nose tile and the outer ring tile.

Nose Tile

The nose tile represents an extreme case because both the tile and the flow front are circular (assuming isotropic permeability). Thus, for a centrally located gate, $\lambda_{\text{gate}} = 0$, the front reaches every point on the perimeter at the same time and $f_{\text{obj},2} = 1$. Any off center position, $\lambda_{\text{gate}} > 0$, produces a flow front that arrives at the perimeter at a single point and progresses monotonically with time yielding $f_{\text{obj},2} = 0$. Logically, however, it is obvious that small λ_{gate} are undesirable because the flow front will reach everywhere on the perimeter at very nearly the same time.

Figure D.2 shows the design space, generated by a sweep across radial gate position, λ_{gate} , for several values of r_p . The unmodified objective function ($r_p = 0$) demonstrates the severity of the problem: $f_{\text{obj},2}$ equals 1 at $\lambda_{\text{gate}} = 0$ and then declines steeply to near zero for $\lambda_{\text{gate}} > 0$. (The objective is not exactly zero due to small errors inherent in the numerical approximation of the problem.) Identifying the optimal gate position is impossible because all offcenter locations are effectively equivalent.

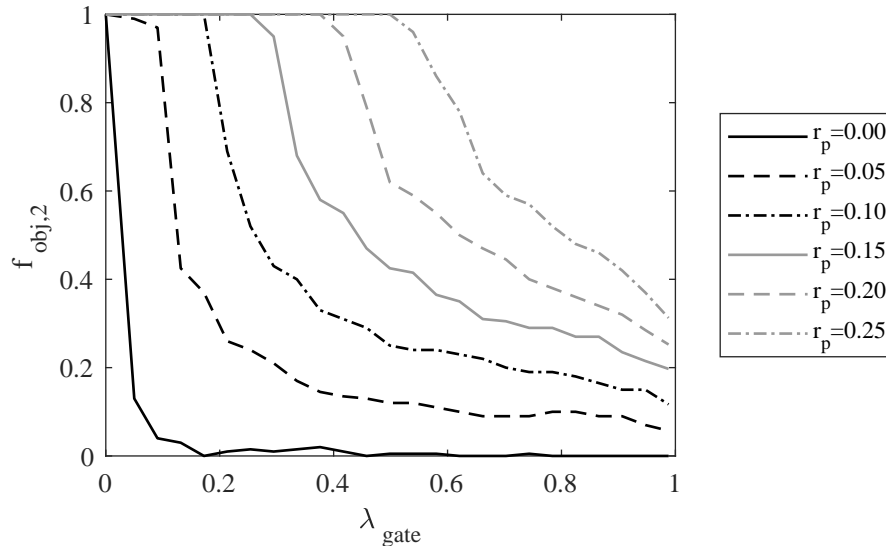


Figure D.2: Scaling of objective function with increasing r_p

Increasing r_p decreases the slope at $\lambda_{\text{gate}} = 0$, effectively spreading out the peak, and a single optimum becomes clear at $\lambda_{\text{gate}} = 0.99$. However, there is a corresponding loss in

fidelity at low values of λ_{gate} , which all possess the same objective value ($f_{\text{obj},2} = 1$).

Outer Ring Tile

Figure D.3 shows the design space for the outer ring again for several values of r_p . The two-dimensional design space was generated by sweeps across both gate coordinates, λ_{gate} and Γ_{gate} . Results appear somewhat analogous to those of the nose tile, extended to two dimensions. For the unmodified objective, Figure D.3(a), function value decreases rapidly as position shifts away from the center of the part ($\lambda_{\text{gate}} = 0.5, \Gamma_{\text{gate}} = 0.5$). Identifying the best design is again difficult because several areas along the sides of the part are largely equivalent ($f_{\text{obj},2} \approx 0.05$). As r_p increases, objective function values tend to increase across the space, smoothing out and expanding the peak. Like the nose tile example, there is a corresponding loss in fidelity in those regions. Areas of minimum $f_{\text{obj},2}$ become smaller and are localized to the corners of the part. Increasing r_p beyond a certain point is counter-productive, yielding a wide, poorly differentiated region in the center with high $f_{\text{obj},2}$ and a steep gradient at the edges.

Selection of Scaling Parameter

A fixed scaling parameter, $r_p = 0.1$, was selected based on these results. This value appeared to provide sufficient differentiation in objective function across the design space without overcompensating.

D.2 Mesh Generation

Sufficient perimeter resolution is required to accurately compute the objective function. In this work, element size was specified by a characteristic length, l_c , scaling with the length of the perimeter, p_{total} ,

$$l_c = \frac{p_{\text{total}}}{n_{\text{el}}} \tag{D.14}$$

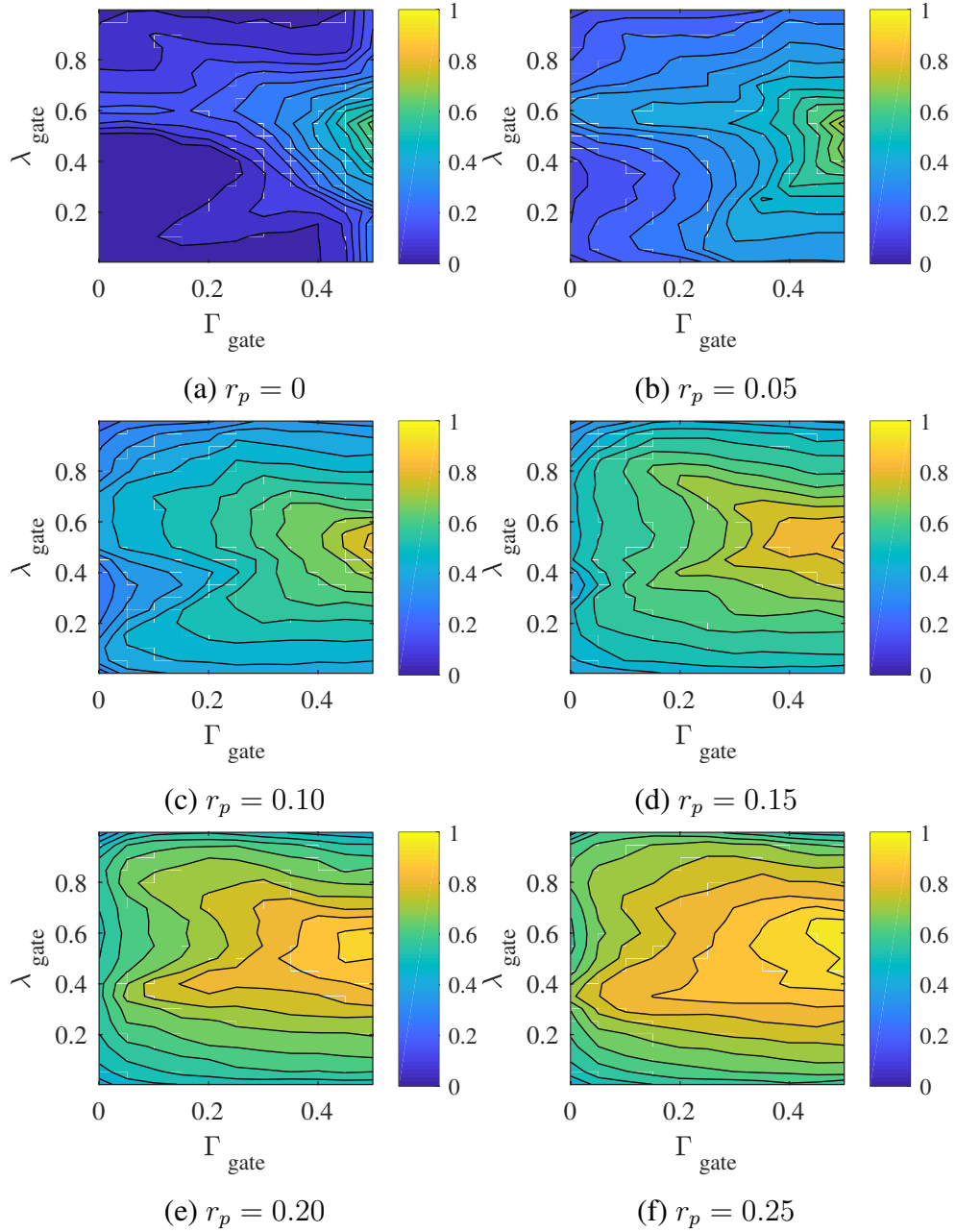


Figure D.3: Scaling of objective function with increasing r_p

where n_{el} specifies the desired number of elements on the perimeter. A second characteristic length, describing element size near the gate, $l_{c,gate}$, was set to

$$l_{c,gate} = \frac{l_c}{c_{el}}, \quad c_{el} > 1 \quad (\text{D.15})$$

which clusters elements near the gate to capture rapid flow advancement in that region. A fixed value of $c_{el} = 4$ was used here. While other scaling is certainly possible, this quantity yielded acceptable fidelity in this work. Thus, a single parameter, n_{el} , controlled element sizing and simulation accuracy. Selection of n_{el} is discussed below after a brief discussion of the mesh generation procedure.

D.2.1 Mesh Generation

Meshes were dynamically generated using built-in geometry functions. Commands referenced here are described in the gmsh manual¹. The perimeter of the part was generated first followed by the gate, which was embedded into the part surface by,

```
Line { expression-list } In Surface { expression };
```

Two Field parameters specified characteristic element sizes across the part:

```
Field[1] = Attractor;
Field[1].EdgesList = {13,14,15,16};

Field[2] = Threshold;
Field[2].DistMin = R_gate;
Field[2].DistMax = 2*R_gate;
Field[2].IField = 1;
Field[2].LcMax = lc;
Field[2].LcMin = lc_gate;
```

¹Gmsh Reference Manual, available at: <http://gmsh.info/doc/texinfo/gmsh.html>.

Background Field = 2;

The first field, `Field[1]` specifies the edges corresponding to the gate. The second field, `Field[2]`, clusters elements near those edges using a `Threshold` operator. This specifies the element size near the gate, `lc_gate`, and the nominal size elsewhere, `lc`. The radial distance parameters, `DistMin` and `DistMax`, specify a region around the gate where element size transitions from `lc_gate` to `lc`. The function `Background Field` selects `Field[2]` for subsequent mesh generation.

D.2.2 Mesh Parameter Study

The mesh parameter was varied to study convergence in the objective function for example tile geometries from Chapter 6. Convergence was measured by the following criteria:

$$f_{\text{diff}}^j = \frac{1}{n_d} \sum_{i=1}^{n_d} |f_{\text{obj},2}^{i,j} - f_{\text{obj},2}^{i,\text{final}}| \quad (\text{D.16})$$

which computes the difference in objective function at a given iteration, j , compared to its value at the final iteration and averaged across all points, n_d , in the discretization of the design space. Mesh resolution was varied over the range $n_{\text{el}} = [40,400]$ in increments of 20. Figure D.4 depicts three stages of mesh refinement for the outer ring tile between $n_{\text{el}} = 150$ and $n_{\text{el}} = 250$. In below results, the convergence criterion, f_{diff} , was compared to the theoretical resolution in the objective function, which is the inverse of the number of elements on the perimeter, $\frac{1}{n_{\text{el}}}$. Simulation time, which was also recorded, reflects the average time for one simulation at the given mesh resolution with the processor noted previously².

²A single 6-core Intel Xeon E5-1650 v4 processor

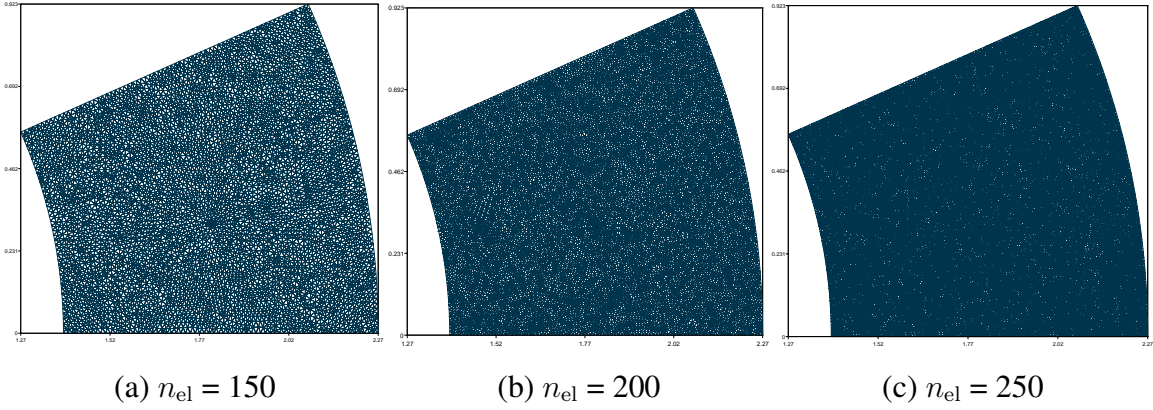


Figure D.4: Mesh refinement for outer ring tile.

Nose Tile

Figure D.5 shows results for the nose tile with f_{diff} on the lefthand y-axis and simulation time on the righthand y-axis. The design space was discretized into $n_d = 25$ points spanning the feasible range of λ_{gate} . The objective function converges relatively quickly between $n_{\text{el}} = 40$ and $n_{\text{el}} = 200$, though it deviates somewhat from the theoretical resolution. Beyond $n_{\text{el}} = 200$, f_{diff} remains fairly constant, but simulation time increases significantly by over an order of magnitude.

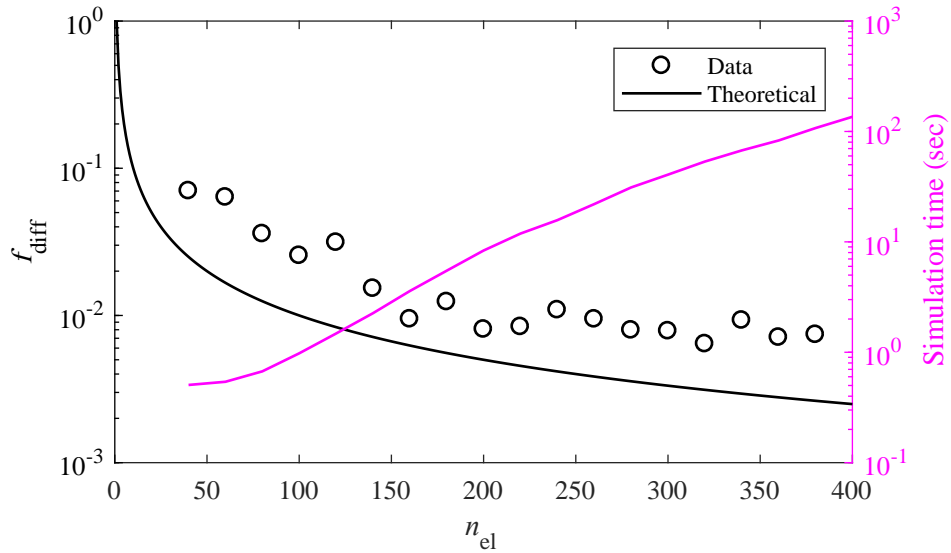


Figure D.5: Convergence of the objective function for the nose tile.

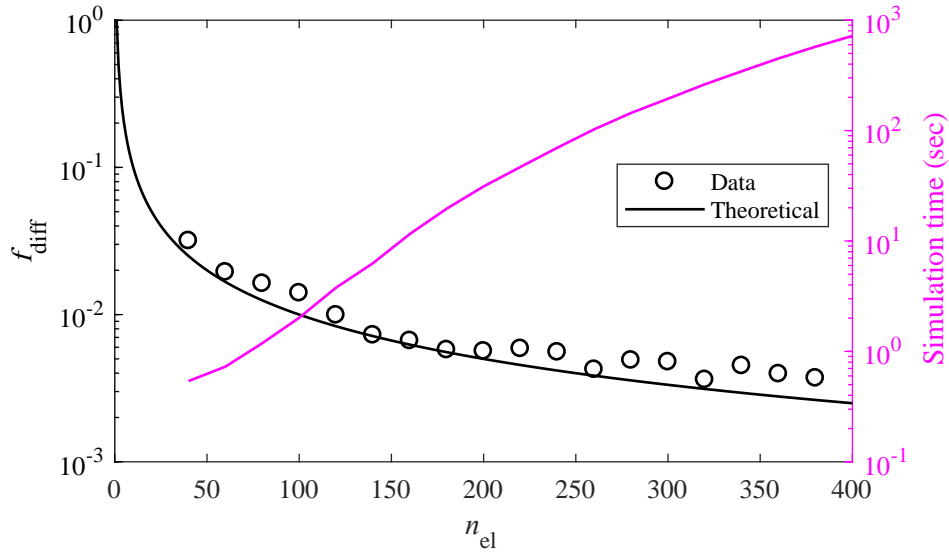


Figure D.6: Convergence of objective function for the outer ring tile.

Outer Ring Tile

Figure D.6 shows results for the outer ring tile. Here, the design space was discretized into $n_d = 66$ points (11 points spanning λ_{gate} and 6 points spanning Γ_{gate}). The convergence criterion, f_{diff} , mirrors the theoretical resolution more closely, converging to a value of 10^{-2} around $n_{el} = 120$. At $n_{el} = 200$, $f_{diff} = 0.006$ with little change beyond that. Simulation time again ramps up significantly at higher mesh resolutions.

D.2.3 Selection of Mesh Parameter

Based on these results, a mesh parameter of $n_{el} = 200$ was selected for the current work. In both examples, the convergence criterion, f_{diff} , changed little beyond this resolution, yet simulation time increased dramatically. With $n_{el} = 200$, a single mold filling simulation using the current hardware required on the order of 10^1 seconds, which allowed solution of the optimal gate location within a few minutes (using parallel operation). The selected mesh sizing thus balances objective function resolution ($<10^{-2}$) and computation time for the current methodology.

REFERENCES

- [1] W. G. Vincenti, J. W. Boyd, and G. E. Bugos, “H. Julian Allen: An Appreciation,” *Annual Review of Fluid Mechanics*, vol. 39, no. 1, pp. 1–17, 2007.
- [2] H. J. Allen and A. J. Eggers, “A Study of the Motion and Aerodynamic Heating of Missiles Entering the Earth’s Atmosphere at High Supersonic Speeds,” NACA RM A53D28, Tech. Rep., 1953.
- [3] B. Laub and E. Venkatapathy, “Thermal protection system technology and facility needs for demanding future planetary missions,” in *International Workshop on Planetary Probe Atmospheric Entry and Descent Trajectory Analysis and Science*, Lisbon, Portugal, 2003.
- [4] M. Natali, J. M. Kenny, and L. Torre, “Science and technology of polymeric ablative materials for thermal protection systems and propulsion devices: A review,” *Progress in Material Science*, vol. 84, pp. 192–275, 2016.
- [5] C. Tang and M. J. Wright, “Analysis of the forebody aeroheating environment during Genesis sample return capsule reentry,” in *45th AIAA Aerospace Sciences Meeting and Exhibit*, Reno, NV, 2007.
- [6] D. M. Curry, “Space Shuttle Orbiter Thermal Protection System Design and Flight Experience,” NASA TM 104773, Tech. Rep., 1993.
- [7] J. S. Tate, S. Gaikwad, N. Theodoropoulou, E. Trevino, and J. H. Koo, “Carbon/Phenolic Nanocomposites as Advanced Thermal Protection Material in Aerospace Applications,” *Journal of Composites*, vol. 2013, 2013.
- [8] D. J. Rasky and H. K. Tran, “Low-cost entry systems for future planetary exploration missions,” *Acta astronautica*, vol. 45, no. 99, pp. 347–355, 1999.
- [9] H. K. Tran, D. J. Rasky, and L. Esfahani, “Thermal Response and Ablation Characteristics of Lightweight Ceramic Ablators,” *Journal of Spacecraft and Rockets*, vol. 31, no. 6, pp. 993–998, 1994.
- [10] H. K. Tran, “Development of Light Weight Ceramic Ablators and Arc-jet Test Results,” NASA TM 108798, Tech. Rep., 1994.
- [11] H. K. Tran, C. E. Johnson, D. J. Rasky, F. C. L. Hui, Y. Chen, and M.-T. Hsu, “Phenolic impregnated carbon ablators (PICA) for Discovery Class missions,” in *31st AIAA Thermophysics Conference*, New Orleans, Jun. 1996.

- [12] H. K. Tran, W. D. Henline, D. J. Rasky, and S. R. Riccitiello, *Low-density resin impregnated ceramic article having an average density of 0.15 to 0.40 g/cc*, 1996.
- [13] G. W. Sutton, “The Initial Development of Ablation Heat Protection, An Historical Perspective,” *Journal of Spacecraft and Rockets*, vol. 19, no. 1, pp. 3–11, 1982.
- [14] T. J. Kowal, “Thermal Protection System (Heat shield) Development – Advanced Development Project,” *JSC Commercial Human Space Flight Symposium*, 2010.
- [15] E. Venkatapathy and D. Ellerby, “Heat Shield for Extreme Entry Environment Technology for Near-Term Robotic Science Missions and Longer Term Human Missions,” in *11th International Planetary Probe Workshop*, Pasadena, CA, 2014.
- [16] M. Gasch, M. Stackpoole, S. White, and T. Boghozian, “Development of Advanced Conformal Ablative TPS Fabricated from Rayon- and Pan-Based Carbon Felts,” in *57th AIAA/ASCE/AHS/ASC Structures, Structural Dynamics, and Materials Conference*, San Diego, CA, 2016.
- [17] P. Zell, E. Venkatapathy, and J. Arnold, “The block-ablator-in-a-honeycomb heat shield architecture overview,” in *7th International Planetary Probe Workshop*, Barcelona, Spain, 2010.
- [18] J. E. Pavlosky and L. G. St. Leger, “Apollo experience report: Thermal protection subsystem,” NASA D-7564, Tech. Rep., 1974.
- [19] J. Kowal, “Overview of the Orion Thermal Protection System Development,” in *7th International Planetary Probe Workshop*, 2010.
- [20] E. L. Strauss, “Superlight ablative systems for Mars lander thermal protection,” *Journal of Spacecraft and Rockets*, vol. 4, no. 10, pp. 1304–1309, 1967.
- [21] C. Szalai, E. Slimko, and P. Hoffman, “Mars Science Laboratory Heatshield Development, Implementation, and Lessons Learned,” *Journal of Spacecraft and Rockets*, vol. 51, no. 4, pp. 1167–1173, 2014.
- [22] K. E. Parmenter, K. Shuman, F. Milstein, C. E. Szalai, H. K. Tran, and D. J. Rasky, “Compressive response of lightweight ceramic ablators: phenolic impregnated carbon ablator,” *Journal of Spacecraft and Rockets*, vol. 38, no. 2, pp. 231–236, 2001.
- [23] J. Feldman, D. Ellerby, K. Peterson, M. Stackpoole, and E. Venkatapathy, “3D Woven Thermal Protection Systems,” in *South Texas SAMPE Chapter Meeting*, Austin, TX, 2015.
- [24] K. H. Peterson, B. Yount, N. R. Schneider, D. K. Prabhu, J. O. Arnold, T. H. Squire, P. F. Wercinski, J. F. Chavez-Garcia, and E. Venkatapathy, “Thermal and Structural

Performance of Woven Carbon Cloth For Adaptive Deployable Entry and Placement Technology,” in *AIAA Aerodynamic Decelerator Systems (ADS) Conference*, Daytona Beach, FL, 2013.

- [25] W. H. Willcockson, “Stardust Sample Return Capsule Design Experience,” *Journal of Spacecraft and Rockets*, vol. 36, no. 3, pp. 470–474, May 1999.
- [26] R. Beck, D. Driver, M. Wright, B. Laub, H. Hwang, E. Slimko, K. Edquist, S. Sepka, W. Wilcockson, and T. Thames, “Development of the Mars Science Laboratory Heatshield Thermal Protection System,” *Journal of Spacecraft and Rockets*, vol. 51, no. 4, pp. 1139–1150, 2014.
- [27] M. J. Wright, R. A. Beck, K. T. Edquist, D. Driver, S. A. Sepka, E. M. Slimko, and W. H. Willcockson, “Sizing and Margins Assessment of the Mars Science Laboratory Aeroshell Thermal Protection System,” *Journal of Spacecraft and Rockets*, vol. 51, no. 4, pp. 1125–1138, 2014.
- [28] T. Ajluni, D. Everett, T. Linn, R. Mink, W. Willcockson, and J. Wood, “OSIRIS-REx, Returning the Asteroid Sample,” in *IEEE Aerospace Conference Proceedings*, Big Sky, MT, 2015.
- [29] S. Berry, T. Horvath, N. Langley, R. Lillard, B. Kirk, and N. Johnson, “Aerothermal Testing for Project Orion Crew Exploration,” in *41st AIAA Thermophysics Conference*, AIAA Paper 2009-3842, 2009.
- [30] A. Chambers and D. Rasky, “NASA + SpaceX Work Together,” *ASK Magazine*, pp. 5–8, 2010.
- [31] F. S. Milos, Y.-K. Chen, W. M. Congdon, and J. M. Thornton, “Mars Pathfinder Entry Temperature Data, Aerothermal Heating, and Heatshield Material Response,” *Journal of Spacecraft and Rockets*, vol. 36, no. 3, pp. 380–391, 1999.
- [32] C. Szalai, Y. K. Chen, M. Loomis, F. Hui, B. Thoma, S. Buck, and L. Scrivens, “Mars Exploration Rover TIRS Cover Thermal Protection System Design Verification,” in *36th AIAA Thermophysics Conference*, Orlando, FL, 2003.
- [33] R. A. Mitcheltree, M. DiFulvio, T. J. Horvath, and R. D. Braun, “Aerothermal Heating Predictions for Mars Microprobe,” *Journal of Spacecraft and Rockets*, vol. 36, no. 3, pp. 405–411, May 1999.
- [34] F. S. Milos, “Galileo Probe Heat Shield Ablation Experiment,” *Journal of Spacecraft and Rockets*, vol. 34, no. 6, pp. 705–713, Nov. 1997.
- [35] W. H. Willcockson, “Mars Pathfinder Heatshield Design and Flight Experience,” *Journal of Spacecraft and Rockets*, vol. 36, no. 3, pp. 374–379, 1999.

- [36] J.-M. Bouilly, “Thermal protection of the HUYGENS probe during TITAN entry: last questions,” in *2nd International Planetary Probe Workshop*, 2004, pp. 113–120.
- [37] “Composite Production,” in *Missile Technology Control Regime Annex Handbook*, Federation of American Scientists, 1996, Item 6:1–13.
- [38] F. S. Milos, M. J. Gasch, and D. K. Prabhu, “Conformal Phenolic Impregnated Carbon Ablator Arcjet Testing, Ablation, and Thermal Response,” *Journal of Spacecraft and Rockets*, vol. 52, no. 3, pp. 804–812, 2015.
- [39] G. Pulci, J. Tirillò, F. Marra, F. Fossati, C. Bartuli, and T. Valente, “Carbon–phenolic ablative materials for re-entry space vehicles: Manufacturing and properties,” *Composites Part A: Applied Science and Manufacturing*, vol. 41, no. 10, pp. 1483–1490, 2010.
- [40] R. A. S. Beck, J. O. Arnold, M. J. Gasch, M. Stackpoole, P. Wercinski, E. Venkatapathy, W. Fan, J. Thornton, and C. E. Szalai, “Conformal Ablative Thermal Protection System for Planetary and Human Exploration Missions,” in *9th International Planetary Probe Workshop*, Toulouse, France, 2012.
- [41] R. A. S. Beck, M. J. Gasch, and A. Calomino, “An overview of NASA’s current materials development efforts for Mars EDL,” in *8th International Planetary Probe Workshop*, Portsmouth, VA, 2011.
- [42] J. O. Arnold, E. Venkatapathy, and R. A. S. Beck, “Flexible Ablators: Applications and Arcjet Testing,” in *8th International Planetary Probe Workshop*, Portsmouth, VA, 2011.
- [43] R. A. S. Beck, J. O. Arnold, M. J. Gasch, M. Stackpoole, D. Prabhu, C. E. Szalai, P. Wercinski, and E. Venkatapathy, “Conformal Ablative Thermal Protection System for Planetary and Human Exploration Missions: An Overview of the Technology Maturation Effort,” in *10th International Planetary Probe Workshop*, San Jose, CA, 2013.
- [44] M. Gasch, P. Agrawal, and R. Beck, “Testing of Advanced Conformal Ablative TPS,” in *10th International Planetary Probe Workshop*, San Jose, CA, 2013.
- [45] E. Venkatapathy, J. Feldman, R. Beck, P. Gage, P. Wercinski, D. Ellerby, and M. Munk, “Development Challenges of Game-Changing Entry System Technologies From Concept to Mission Infusion,” in *IEEE Aerospace Sciences*, Big Sky, MT, 2016.
- [46] R. A. S. Beck, J. O. Arnold, M. J. Gasch, M. Stackpoole, and E. Venkatapathy, “Development of a Conformal Ablative Backshell Thermal Protection System for Outer

Planetary Exploration Missions,” in *Outer Planets Assessment Group*, Bethesda, MD, 2014.

- [47] R. Beck, M. Gasch, M. Stackpoole, M. Wilder, T. Boghuzian, D. Prabhu, C. Kazemba, and E. Venkatapathy, “Conformal Ablative Thermal Protection Systems (CA-TPS) for Venus and Saturn Backshells,” in *Outer Planets Advisory Group Annual Meeting*, San Antonio, TX, 2016.
- [48] R. A. S. Beck, M. J. Gasch, F. S. Milos, M. M. Stackpoole, B. P. Smith, E. Venkatapathy, M. C. Wilder, T. Boghuzian, D. K. Prabhu, G. T. Swanson, D. Kazemba, W. Congdon, B. A. Woollard, and A. Sidor, “Conformal Ablative Thermal Protection System for Small and Large Scale Missions: Approaching TRL 6 for Planetary and Human Exploration Missions and TRL 9 for Small Probe Missions,” in *12th International Planetary Probe Workshop*, Cologne, Germany, 2017.
- [49] I. Cozmuta, M. J. Wright, B. Laub, and W. H. Willcockson, “Defining Ablative Thermal Protection System Margins for Planetary Entry Vehicles,” in *42nd AIAA Thermophysics Conference*, Honolulu, HI, 2011.
- [50] J. A. Dec and R. A. Mitcheltree, “Probabilistic Design Of A Mars Sample Return Earth Entry Vehicle Thermal Protection System,” in *40th Aerospace Sciences Meeting and Exhibit*, Reno, NV: AIAA Paper 2002-0910, 2002.
- [51] Y.-K. Chen, T. Squire, B. Laub, and M. Wright, “Monte Carlo Analysis for Spacecraft Thermal Protection System Design,” in *9th AIAA/ASME Joint Thermophysics and Heat Transfer Conference*, San Francisco, CA, 2006.
- [52] M. J. Wright, D. Bose, and Y. K. Chen, “Probabilistic Modeling of Aerothermal and Thermal Protection Material Response Uncertainties,” *AIAA Journal*, vol. 45, no. 2, pp. 399–410, 2007.
- [53] B. Laub and D. M. Curry, “Tutorial on Ablative TPS,” in *2nd International Planetary Probe Workshop*, Mountain View, CA, 2004.
- [54] F. S. Milos and Y.-K. Chen, “Ablation and Thermal Response Property Model Validation for Phenolic Impregnated Carbon Ablator,” *Journal of Spacecraft and Rockets*, vol. 47, no. 5, pp. 786–805, 2010.
- [55] M. Gasch, R. Beck, and P. Agrawal, “Arcjet Testing of Advanced Conformal Ablative TPS,” in *38th Annual Conference on Composites, Materials and Structures*, Cocoa Beach, FL, 2014.
- [56] M. J. Wright, M. Hughes, A. Calomino, and M. D. Barnhardt, “An Overview of Technology Investments in the NASA Entry Systems Modeling Project,” in *53rd AIAA Aerospace Sciences Meeting*, Kissimmee, FL, 2015.

- [57] E. Venkatapathy, “EDL Systems Short Course: Modern Advances in Ablative TPS,” in *10th International Planetary Probe Workshop*, San Jose, CA, 2013.
- [58] I. Muskat, *Method of Molding*, 1950.
- [59] K. Potter, “The early history of the resin transfer moulding process for aerospace applications.,” *Composites Part A: Applied Science and Manufacturing*, vol. 30, no. 5, pp. 619–621, 1999.
- [60] C. Williams, J. Summerscales, and S. Grove, “Resin infusion under flexible tooling (RIFT): a review,” *Composites Part A: Applied Science and Manufacturing*, vol. 27, no. 7, pp. 517–524, 1996.
- [61] C. D. Rudd, A. C. Long, K. N. Kendall, and C. G. E. Mangin, *Liquid Moulding Technologies*. Cambridge, England: Elsevier, 1997.
- [62] R. S. Parnas, *Liquid Composite Molding*. Cincinnati, Ohio: Hanser Gardner, 2000.
- [63] P. Ermanni, C. D. Fratta, and F. Trochu, “Molding: Liquid Composite Molding (LCM),” in *Wiley Encyclopedia of Composites*, 2012.
- [64] H. Darcy, *Les fontaines publiques de la ville de Dijon*, V. Dalmont, Ed. Paris, 1856.
- [65] A. W. Chan and S.-T. Hwang, “Modeling of the impregnation process during resin transfer molding,” *Polymer Engineering and Science*, vol. 31, no. 15, pp. 1149–1156, 1991.
- [66] N. Correia, F. Robitaille, A. Long, C. Rudd, P. Šimáček, and S. Advani, “Use of Resin Transfer Molding Simulation to Predict Flow, Saturation, and Compaction in the VARTM Process,” *Journal of Fluids Engineering*, vol. 126, no. 2, pp. 210–215, 2004.
- [67] N. Correia, F. Robitaille, A. Long, C. Rudd, P. Šimáček, and S. Advani, “Analysis of the vacuum infusion moulding process: I. Analytical formulation,” *Composites Part A: Applied Science and Manufacturing*, vol. 36, no. 12, pp. 1645–1656, 2005.
- [68] K. Han, S. Jiang, C. Zhang, and B. Wang, “Flow modeling and simulation of SCRIMP for composites manufacturing,” *Composites Part A: Applied Science and Manufacturing*, vol. 31, no. 1, pp. 79–86, 2000.
- [69] S. Jiang, C. Zhang, and B. Wang, “Optimum arrangement of gate and vent locations for RTM process design using a mesh distance-based approach,” *Composites Part A: Applied Science and Manufacturing*, vol. 33, no. 4, pp. 471–481, 2002.

- [70] A. Gokce, K.-T. Hsiao, and S. G. Advani, "Branch and bound search to optimize injection gate locations in liquid composite molding processes," *Composites Part A: Applied Science and Manufacturing*, vol. 33, no. 9, pp. 1263–1272, 2002.
- [71] R. Mathur, S. G. Advani, and B. K. Fink, "Use of genetic algorithms to optimize gate and vent locations for the resin transfer molding process," *Polymer Composites*, vol. 20, no. 2, pp. 167–178, 1999.
- [72] B. Liu, S. Bickerton, and S. G. Advani, "Modelling and simulation of resin transfer moulding (RTM) - Gate control, venting and dry spot prediction," *Composites Part A: Applied Science and Manufacturing*, vol. 27, no. 2, pp. 135–141, 1996.
- [73] D. K. Todd and L. W. Mays, *Groundwater Hydrology*, 3rd. Wiley, 2004.
- [74] S. Whitaker, "Flow in porous media I: A theoretical derivation of Darcy's law," *Transport in Porous Media*, vol. 1, pp. 3–25, 1986.
- [75] R. Panton, "Flow at Low Reynolds Numbers," in *Incompressible Flow*, Wiley, 2013, ch. 21, pp. 607–649.
- [76] P. Forchheimer, "Wasserbewegung durch boden," *Zeitschrift des Vereines Deutscher Ingenieure*, no. 45, pp. 1782–1788, 1901.
- [77] Z. Zeng and R. Grigg, "A criterion for non-darcy flow in porous media," *Transport in Porous Media*, vol. 63, pp. 57–69, 2006.
- [78] L. J. Klinkenberg, "The permeability of porous media to liquids and gases," in *Drilling and Production Practice*, American Petroleum Institute, 1941.
- [79] J. Marschall and F. S. Milos, "Gas Permeability of Rigid Fibrous Refractory Insulations," *Journal of Thermophysics and Heat Transfer*, vol. 12, no. 4, pp. 528–535, 1998.
- [80] H. C. Brinkman, "A calculation of the viscous force exerted by a flowing fluid on a dense swarm of particles," *Applied Scientific Research*, vol. A, no. 1, pp. 27–34, 1949.
- [81] D. A. Nield and A. Bejan, "Mechanics of Fluid Flow Through a Porous Medium," in *Convection in Porous Media*, 4th ed., New York: Springer, 2013, ch. 1.
- [82] M. V. Brusckke and S. G. Advani, "A finite element/control volume approach to mold filling in anisotropic porous media," *Polymer Composites*, vol. 11, no. 6, pp. 398–405, 1990.

- [83] A. Barney, C. Anton, J. Crumpler, J. S. Jones, and B. Brewer, *Low density ablator composition*, 2003.
- [84] C. S. Thatcher, J. S. Jones, J. D. Eichinger, B. L. Muench, T. H. Crooks, and E. B. Curry, *Heatshield having strain compliant matrix and method of forming same*, 2011.
- [85] W. M. Congdon, “Family Systems of Advanced Charring Ablators for Planetary Aerocapture and Entry Missions,” in *1st NASA Science Technology Conference*, College Park, MD, 2007.
- [86] R. Carta, S. Palmas, A. M. Polcaro, and G. Tola, “Behaviour of a carbon felt flow by electrodes, Part I: Mass transfer characteristics,” *Journal of Applied Electrochemistry*, vol. 21, no. 9, pp. 793–798, 1991.
- [87] J. González-García, P. Bonete, E. Expósito, V. Montiel, A. Aldaz, and R. Torregrosa-Maciá, “Characterization of a carbon felt electrode: structural and physical properties,” *Journal of Materials Chemistry*, vol. 9, no. 2, pp. 419–426, 1999.
- [88] H. O. Pierson, “Carbon Fibers,” in *Handbook of Carbon, Graphite, Diamonds and Fullerenes*, Elsevier, 1994, ch. 8, pp. 166–197.
- [89] P. Morgan, “Properties of Carbon Fibers,” in *Carbon Fibers and Their Composites*, CRC Press, 2005, ch. 20, pp. 791–859.
- [90] A. T. Sidor, R. D. Braun, R. A. Beck, and M. M. Stackpoole, “Vacuum Infusion Process Development for Conformal Ablative Thermal Protection System Materials,” in *AIAA Space Conference & Exposition*, Orlando, FL, 2017.
- [91] A. Dyakonov, M. Schoenenberger, and J. Van Norman, “Hypersonic and Supersonic Static Aerodynamics of Mars Science Laboratory Entry Vehicle,” in *43rd AIAA Thermophysics Conference*, New Orleans, LA, Jun. 2012.
- [92] W. Umrath, *Fundamentals of Vacuum Technology*. Cologne, Germany: Oerlikon Leybold Vacuum, 2007.
- [93] E. W. Washburn, “The dynamics of capillary flow,” *Physical Review*, vol. 17, no. 3, pp. 273–283, 1921.
- [94] A. Marmur and R. D. Cohen, “Characterization of porous media by the kinetics of liquid penetration: The vertical capillaries model,” *Journal of Colloid and Interface Science*, vol. 189, no. 2, pp. 299–304, 1997.
- [95] I. Pezron, G. Bourgain, and D. Quéré, “Imbibition of a Fabric,” *Journal of Colloid And Interface Science*, vol. 173, no. 2, pp. 319–327, 1995.

- [96] A. Prodromou and J. Chen, "On the relationship between shear angle and wrinkling of textile composite preforms," *Composites Part A: Applied Science and Manufacturing*, vol. 28, no. 5, pp. 491–503, Jan. 1997.
- [97] S. Bickerton, E. Sozer, P. Šimáček, and S. Advani, "Fabric structure and mold curvature effects on preform permeability and mold filling in the RTM process. Part II. Predictions and comparisons with experiments," *Composites Part A: Applied Science and Manufacturing*, vol. 31, no. 5, pp. 439–458, 2000.
- [98] A. Cherouat and H. Borouchaki, "Geometrical Draping of Nonwoven Fabrics," in *Non-woven Fabrics*, IntechOpen, 2016, ch. 5.
- [99] F. Martínez-Hergueta, A. Ridruejo, C. González, and J. LLorca, "A multiscale micromechanical model of needlepunched nonwoven fabrics," *International Journal of Solids and Structures*, vol. 96, pp. 81–91, 2016.
- [100] S. D. Williams and D. M. Curry, "Thermal protection materials: Thermophysical property data," NASA RP 1289, Tech. Rep., 1992.
- [101] J. A. Parker and E. L. Winkler, "The effects of molecular structure on the thermochemical properties of phenolics and related polymers," NASA TR R-276, Tech. Rep., 1967.
- [102] Y. Wang, S. Wang, C. Bian, Y. Zhong, and X. Jing, "Effect of chemical structure and cross-link density on the heat resistance of phenolic resin," *Polymer Degradation and Stability*, vol. 111, pp. 239–246, 2015.
- [103] H. L. Friedman, "Kinetics of thermal degradation of char-forming plastics from thermogravimetry. Application to a phenolic plastic," *Journal of Polymer Science Part C: Polymer Symposia*, vol. 6, no. 1, pp. 183–195, 1964.
- [104] P. C. Carman, *Flow of gases through porous media*. Academic Press, 1956.
- [105] M. M. Tomadakis and T. J. Robertson, "Viscous Permeability of Random Fiber Structures: Comparison of Electrical and Diffusional Estimates with Experimental and Analytical Results," *Journal of Composite Materials*, vol. 39, no. 2, pp. 163–188, 2005.
- [106] G. Centeno, G. Sánchez-Reyna, J. Ancheyta, J. A. Muñoz, and N. Cardona, "Testing various mixing rules for calculation of viscosity of petroleum blends," *Fuel*, vol. 90, no. 12, pp. 3561–3570, 2011.
- [107] E. A. Guggenheim, "The theoretical basis of Raoult's law," *Transactions of the Faraday Society*, vol. 33, pp. 151–156, 1937.

- [108] P. Šimáček and S. G. Advani, “Desirable features in mold filling simulations for Liquid Composite Molding processes,” *Polymer Composites*, vol. 25, no. 4, pp. 355–367, 2004.
- [109] F. Panerai, J. Ferguson, J. Lachaud, A. Martin, M. J. Gasch, N. N. Mansour, M. Field, and S. Cruz, “Analysis of Fibrous Felts for Flexible Ablators Using Synchrotron Hard X-Ray Micro-Tomography,” in *8th European Symposium on Aerothermodynamics for Space Vehicles*, 2015.
- [110] F. Panerai, J. C. Ferguson, J. Lachaud, A. Martin, M. J. Gasch, and N. N. Mansour, “Micro-tomography based analysis of thermal conductivity, diffusivity and oxidation behavior of rigid and flexible fibrous insulators,” *International Journal of Heat and Mass Transfer*, vol. 108, pp. 801–811, 2017.
- [111] P. Guo, “Dependency of Tortuosity and Permeability of Porous Media on Directional Distribution of Pore Voids,” *Transport in Porous Media*, vol. 95, no. 2, pp. 285–303, 2012.
- [112] J. C. Ferguson, F. Panerai, A. Borner, and N. N. Mansour, “PuMA: the Porous Microstructure Analysis software,” *SoftwareX*, vol. 7, pp. 81–87, 2018.
- [113] M. L. McGlashan, “Deviations from Raoult’s law,” *Journal of Chemical Education*, vol. 40, no. 10, pp. 516–518, 1963.
- [114] *Brookfield DV-II+Pro Viscometer: Operating Instructions*. Manual No. M/85-150-P700, Brookfield Engineering Laboratories.
- [115] O. Reynolds, “On the Theory of Lubrication and Its Application to Mr. Beauchamp Tower’s Experiments, Including an Experimental Determination of the Viscosity of Olive Oil,” *Philosophical Transactions of the Royal Society of London*, vol. 177, pp. 157–234, 1886.